Turbulence, Particles and Magnetic fields

Rémi Zamansky

Université de Toulouse

Mémoire présenté en vue de l'obtention de

l'**Habilitation à Diriger des Recherches**

par

Rémi Zamansky

Maître de Conférences à l'Institut National Polytechnique de Toulouse
Institut de Mécanique des Fluides de Toulouse (IMFT)

Turbulence, particles and magnetic fields

Soutenance : 7 novembre 2023

Composition du jury :

Alain Pumir	Directeur de recherche (CNRS - ENS Lyon)	Rapporteur
Olivier Simonin	Professeur des Universités (INPT - IMFT)	Rapporteur
John Christos Vassilicos	Directeur de recherche (CNRS - LMFL)	Rapporteur
Aurore Naso	Directrice de recherche (CNRS - LMFA)	Examinatrice
Joachim Peinke	Professor (University Oldenburg)	Examinateur
Nicolas Rimbert	Professeur des Universités (ENSEM - LEMTA)	Examinateur
Dominique Legendre	Professeur des Universités (INPT - IMFT)	Correspondant

Contents

1 About this manuscript

This manuscript describes my recent work related to the Lagrangian modeling of turbulent flows, to the modeling of particle motion in turbulent flows and the generation of turbulence induced by a dispersed phase, and finally on flows involving a liquid metal with non-conducting particles subjected to an alternating magnetic field. It is clear that the content of the manuscript is not as general as the title might suggest, and this title rather gives the keywords associated with the work presented in this dissertation.
In the first chapter, after an introduction on energy cascade of turbulent flow and intermittency, I present recent development on the statistical analysis of the material derivative of the velocity in isotropic turbulence and on the stochastic modeling of the fluid particles dynamics. Obtaining numerical solutions of the Navier-Stokes equation with supercomputers, I highlight a relationship between the force on a fluid particle (the acceleration), the kinetic energy and the dissipated power. This relation connects the idea of the energy cascade, and its intrinsic multi-scale character to the dynamics of the tracer in turbulent flows. By relying on this relation, I propose a vectorial stochastic model that effectively describes the interaction of fluid particles with all other fluid particles of the flow. This model presents some of the remarkable features of the fluid particle dynamics, in particular the occurrence of extreme events, the temporal asymmetry and the emergence of anomalous scaling law.
The second chapter starts with a discussion on the Euler-Lagrange approach used to model dispersed phase flows and on the coarse graining implied by this framework. Then, statistical descriptions of the acceleration and hydrodynamic forces of particles that are heavy or light, small or large is presented. Subsequently, we consider stochastic modeling of the high frequency part of the dynamics of these particles, as well as its coupling with the large eddy simulation approaches. Finally, the last part of the chapter focus on the numerical modeling of the turbulent agitation induced by the rising of a swarm of bubbles, and to the analysis of the specific properties of this flow resulting from the interactions between wakes.
In the last chapter, we discuss our work on the magnetohydrodynamic of liquid metal subjected to an alternating magnetic field. In the first part, I present the experimental setup and the numerical simulations developed to study thermo-magneto-convection flows induced by the Joule heating and the Laplace force. The second part focus on a modeling approach, confronted to an experimental approach, of the perturbation of an alternating magnetic field caused by the presence of bubbles in a liquid metal.

The common thread between these three chapters is the focus on the modeling of the physical phenomena. I find that the 11 successive states of lithography "Le Taureau", realized by Pablo Picasso in 1945, reproduced in the figure 1.1, illustrates quite well the process of proposing an adequate model, as simple and smart as possible.[1] How many

[1] Frederic Risso indicated to me that Christophe Clanet had used this same artwork to discuss the role of modeling during a plenary Lecture at the international conference on multiphase flows and Wladimir

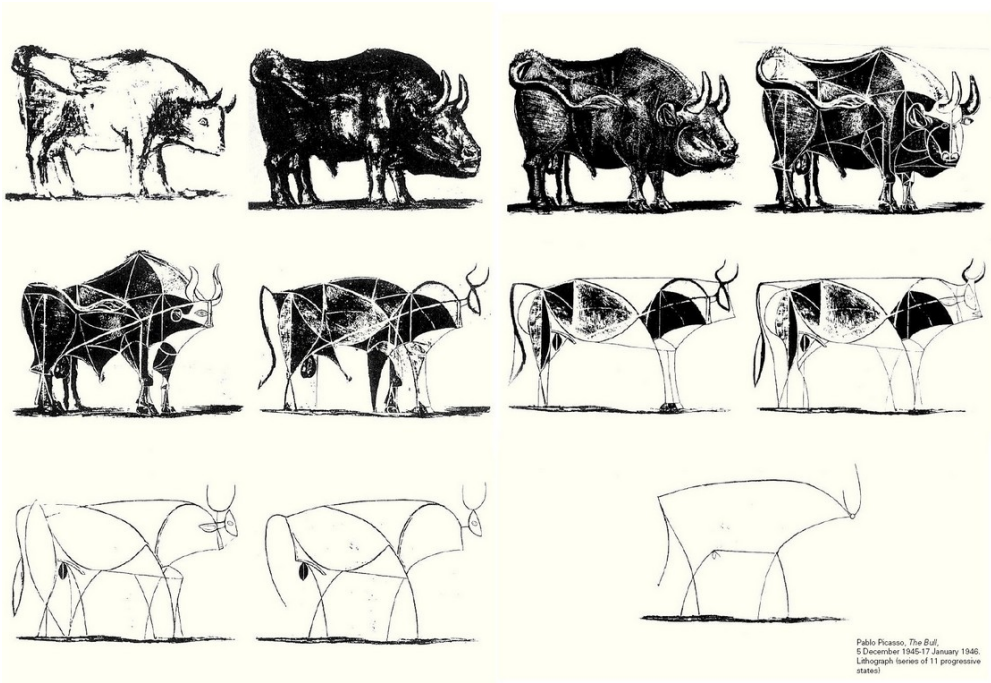

Figure 1.1: Pablo Picasso, The 11 successive states of lithography "Le Taureau", 1945.

pencil strokes are needed to instantly recognize a bull or how many degrees of freedom are needed to describe a system? The answer obviously depends on the level of detail one want to reproduce: Is it an animal? Is it a cow or a bull? What is the color of the animal's coat? Is it wounded?... I reproduce an excerpt from Fernand Mourlot's text, "Gravés dans ma mémoire", Ed. Robert Laffont, 1979, which details Picasso's creative process for his engraving of the Bull, and which underlies the necessity to well grasp the physical behavior of the system under study to propose an adequate model: *"L'opération a duré quinze jours. Le 5 décembre 1945, un mois après son arrivée rue de Chabrol, Picasso a dessiné au lavis un taureau. Un taureau magnifique, très bien fait, gentil même. Et puis on lui a donné l'épreuve; nous en avons tiré à peine deux ou trois, ce qui fait que ce taureau est extrêmement rare. Une semaine après, il revient et il demande une nouvelle pierre; il reprend son taureau au lavis et à la plume; il recommence le 18. Troisième état, le taureau est repris au grattage à plat, puis à la plume en accentuant fortement les volumes; le taureau est devenu un animal terrible avec des cornes et des yeux effroyables. Bon, ça n'allait pas, Picasso exécute un quatrième état, le 22 décembre, et un cinquième, le 24; à chaque fois il simplifie le dessin qui devient de plus en plus géomètrique avec des aplats noirs.*

Sixième et septième états, les 26 et 28 décembre, puis, après le retour de Picasso, quatre autres états, onze en tout, les 5, 10 et 17 janvier. Le taureau est réduit à sa plus simple expression; quelques traits d'une maîtrise exceptionnelle qui symbolisent comme un jeu de signes ce malheureux taureau avec sa petite tête d'épingle et ses cornes ridicules en forme d'antenne. Les ouvriers se désolaient d'avoir vu un taureau aussi magnifique transformé

Bergez also reported to me that Lydéric Bocquet had also shown it to illustrate the reduction of complexity during his inaugural lesson at the Collège de France. Although it is not as original as I thought, I left it because I think it has its place here.

en une espèce de fourmi...
... C'est Célestin qui a trouvé le mot de la fin : "Picasso, il a fini par là où, normalement, il aurait dû commencer." C'est vrai, seulement pour arriver à son taureau d'une seule ligne, il a fallu qu'il passe par tous les taureaux précédents. Et quand on voit son onzième taureau on ne peut s'imaginer le travail qu'il lui a demandé".

2 Turbulence

Contents

2.1 Universality, cascade and intermittency

Turbulence is fascinating with all its eddies and vortices forming, deforming and dancing together. As beautiful is the theoretical analysis of turbulent flows, looking for order and coherence in this apparently erratic motion. Everything indicates that the spatio-temporal evolution of turbulent flows can be described by the Navier-Stokes equation, and in particular the numerical simulations which, in this context, are called "direct numerical simulation" (or DNS). Nevertheless, bringing into play nonlinear and nonlocal interactions, it still resists complete analytical method, despite having been proposed 200 years ago [190]. So understanding all the details of turbulent flow remains, to say the least, a formidable problem. The situation bears similarity with critical phenomena, in which the interactions among the large numbers of degrees of freedom induce collective organization at macroscopic scales that cannot be figured out from the behavior of individual particles. The connection between the small-scale velocity fluctuations in turbulence and the large-scale flow properties implies scaling relations. The cornerstone of the statistical description of turbulent flows was advanced in the 40's by Kolmogorov proposing a universal picture of turbulence based on the idea of a cascade of kinetic energy and its dissipation into heat. Completing the Kolmogorov statistical description approach and in particular its bridging with the Navier-Stokes equations, remains one of the great challenges in the study of turbulence.

Cascade

Following the idea of the energy cascade due to Richardson [221], Taylor [250, 251] and Kolmogorov [126, 125, 124], energy is injected at some length scale L where it causes vortices of size L. As these large vortices do not dissipate energy, structures on smaller scales must form. It is convenient to imagine these new length scales appearing as the large vortices break up into smaller ones, giving rise to eddies of all possible sizes, at least in an interval between L and η, the dissipative scale. The vortices at a given scale ℓ are supplied with energy by the larger ones, at the same time they lose energy by disintegrating themselves, after a time τ_ℓ into smaller vortices. The key assumption here is that the viscosity is not relevant for this process, and so if no dissipation occurs the energy transfer rate (per unit of mass) ε_ℓ is constant across scales in a steady regime. Assuming that the eddies of size ℓ are characterized be a velocity u_ℓ, we find scale invariance in the energy cascade:

$$\frac{u_\ell^2}{\tau_\ell} = \frac{u_\ell^3}{\ell} = \varepsilon_\ell = \text{cst} = \langle\varepsilon\rangle \ . \tag{2.1}$$

This inertial cascade takes place in a range of scales in which the viscosity has negligible effect, that is to say as long as $Re_\ell \gg 1$, where $Re_\ell = u_\ell \ell/\nu$ the Reynolds number of the flow at scale ℓ. From this Reynolds number, one defines the dissipative length scale $\eta = \nu^{3/4}\langle\varepsilon\rangle^{-1/4}$ which correspond to $Re_\eta = 1$, corresponding to the end of the inviscid cascade. And by conservation, in the original Kolmogorov theory, the characteristic energy transfer rate is taken to be the average rate of dissipation of kinetic energy into heat $\langle\varepsilon\rangle$. This cascade scaling finds a remarkable confirmation in the "4/5 law", one of the few exact results in turbulence, which relates the third moment of the velocity increments ($\delta_r u = u(x+r) - u(x)$) to the average dissipation rate [125]: $\langle(\delta_r u)^3\rangle = -\frac{4}{5}\langle\varepsilon\rangle r + \ldots$.
For the second moment of the velocity increments, Kolmogorov also proposed an empirical relation derived from similarity hypotheses [126]. From dimensional analysis we have

$$\langle(\delta_r u)^2\rangle = \text{f}ct(r, \nu, \langle\varepsilon\rangle, L, \ldots) = (\langle\varepsilon\rangle r)^{2/3}\, \Phi(r/L, r/\eta) \ . \tag{2.2}$$

The first hypothesis proposed that for high enough Reynolds numbers, turbulence is universal. For $r \ll L$, it is assumed that the velocity increment statistics are independent of the specific forcing mechanism which can be expressed mathematically as $\lim_{r/L\to 0} \Phi(r/L, r/\eta) = \phi(r/\eta)$. And in the second hypothesis, it is proposed that for $r \gg \eta$ velocity increment statistics become independent of the viscosity ($\lim_{r/\eta\to\infty} \phi(r/\eta) = cst$). With these two hypotheses, which correspond to a complete similarity hypothesis using the Barenblatt terms [14], the variance of the velocity increments scales like

$$\langle(\delta_r u)^2\rangle \sim (\langle\varepsilon\rangle r)^{2/3} \tag{2.3}$$

for $\eta \ll r \ll L$. Although this relation is not derived from the Navier-Stokes equation, it received many experimental confirmations.

Intermittency

Actually with similar arguments, one could generalize the previous scaling relation (2.3) to higher moments of the velocity increment and obtain: $\langle|\delta_r u|^p\rangle \sim (\langle\varepsilon\rangle r)^{p/3} \sim \langle(\delta_r u)^2\rangle^{p/2}$. Such a scaling relation would imply that $\delta_r u$ presents a Gaussian distribution with variance $\sigma^2 \sim (\langle\varepsilon\rangle r)^{2/3}$. The problem is that although for very large separation r, $\delta_r u$ presents a

Gaussian distribution, experiments and numerical simulations have reported systematic deviations from the Gaussian distribution when r is reduced [7, 49, 111]. This is known as intermittency, because on small scales turbulent flows present weak fluctuations with intermittent bursts of much larger fluctuations. And indicates that the large scales of the flow keep influencing small-scale motion of the flow, or equivalently, that the structure of the flow on small scales presents a Reynolds number dependence.
This observation is directly related to the Landau's remark [138], which pointed out that the 1941 picture of a universal inertial range depending only on the mean energy dissipation rate is flawed, because the dissipation rate presents very large, intermittent, spatiotemporal fluctuations. Therefore, the global average of ε is not the relevant scale, since locally it can take values hundreds of times smaller or larger than $\langle\varepsilon\rangle$.
These remarks led Kolmogorov and Oboukhov to the refined similarity hypothesis by introducing a local scale for the energy transfer rate based on a locally averaged dissipation rate on a sphere of radius r [128, 192]

$$\varepsilon_r(\mathbf{x}) = \frac{3}{4\pi r^3}\int_{|h|<r} \varepsilon(\mathbf{x}+\mathbf{h})d\mathbf{h} \ . \tag{2.4}$$

Keeping the idea of the central role of the transfer rate, a local velocity scale is derived $v_r = (\varepsilon_r r)^{1/3}$ as well as a local Reynolds number $Re_r = v_r r/\nu$.
Using these local scales, they proposed local similarity hypothesis, that states that $\delta_r u/v_r$ presents universal distribution, only dependent on Re_r. Further, it was proposed that for $Re_r \gg 1$ the distribution of $\delta_r u/v_r$ does not dependent on Re_r. This translates in the following scaling relation for the structure function when $Re_r \gg 1$:

$$\langle(\delta_r u)^p\rangle \sim r^{p/3}\langle\varepsilon_r^{p/3}\rangle \ . \tag{2.5}$$

Further assuming a log-normal distribution of ε_r, with parameters that are scale-dependent, for $\eta \ll r \ll L$ the structure function can be expressed as:

$$\langle(\delta_r u)^p\rangle = c_p(r\langle\varepsilon\rangle)^{p/3}(L/r)^{\alpha_p} \tag{2.6}$$

where c_p is a prefactor that depends on p and possibly on the large-scale features of the flow, and α_p is called intermittency exponent or anomalous exponent by analogy with so-called critical points in phase transitions [90, 73, 16]. The later characterizes the absence of scale separation that manifests as an influence of the large scales on the small ones through the intermittency. This refined scaling of the velocity increments and the intermittency exponent has been studied in much detail, in particular within the framework of multifractal analysis [129, 79, 188, 49, 83, 262, 243].
With these refined hypotheses, the structure of the velocity field loses it universal behavior as it depends on the large scales through the long-range correlation of ε which is set by the specific forcing mechanism. However, in this view, what remains universal is the cascade mechanism itself, which, as fragmentation processes, presents scale-to-scale transformations with local similarities [51, 50, 48, 83, 37, 93, 235].
To summarize, the small-scale quantities, typically the velocity derivatives, present a Reynolds number dependence[1]. They primarily depend on the local dissipation rate whose statistics depend on the Reynolds number through the intermittency of the cascade (the

[1]Taking $r = \eta$ in (2.6) we have $\langle(\partial_x u_x)^p\rangle \approx \langle(\delta_\eta u)^p/\eta^p\rangle \approx c_p(\langle\varepsilon\rangle/\nu)^{p/2}Re^{3\alpha_p/4}$ with $L/\eta = Re^{3/4}$.

depth of the cascade varies like $\ln Re_\lambda$, as discussed in the next subsection). This scaling theory has been proposed in an Eulerian framework as it focuses on the length scale and the question of the dynamics (time evolution) is not a central aspect of this description. Conversely, the Lagrangian description of the turbulence naturally focuses on the dynamics and could be a bridge between Navier-Stokes theory and cascade scaling. More specifically, the acceleration of fluid particles (*i.e.* the material derivative of the velocity) is classically considered as a small-scale quantity [178, §21.5], meaning that it is determined by the dissipative scales of the turbulence. Indeed, it is intimately linked to the dissipation rate of turbulence. However, various experimental and numerical works have also reported its dependence on the kinetic energy (a quantity carried by the large scales). This is generally attributed to long-range correlations, or intermittency, of the dissipation rate, as discussed above. Bellow, in sections 2.2-2.3, we show that in addition to this intermittency effect, there is a direct effect of the large scales of the flow structure on the acceleration. This questions the pertinence of considering the acceleration as a small-scale quantity only, and open the possibility of modeling the dynamics of a tracer in a turbulent flow as presented in section 2.4.
Before presenting this aspect of the Lagrangian dynamics, we briefly present the multiplicative cascade model for the energy transfers rate, and the stochastic modeling of the dissipation rate in the Lagrangian framework, which has been proposed consistently with the cascade picture. Note that the reminder of this chapter is largely based on the paper [274] published last year, with just minor additions and corrections[2].

Dissipation as multiplicative cascade process

The image of the energy cascade is naturally associated with multiplicative processes [191, 270, 127, 178, 157, 25, 80]. Such a model proposes to express the locally averaged dissipation ε_n over a volume of size $\ell = L\lambda^n$, with L the large-scale of the flow and $\lambda < 1$, as:

$$\varepsilon_n = \varepsilon_0 \frac{\varepsilon_1}{\varepsilon_0} \cdots \frac{\varepsilon_n}{\varepsilon_{n-1}} = \varepsilon_0 \prod_{i=1}^{n} \xi_i \ . \tag{2.7}$$

Assuming that $\xi_i = \varepsilon_i/\varepsilon_{i-1}$ are independent positive random numbers with identical distribution across scales we write:

$$\ln \frac{\varepsilon_n}{\varepsilon_0} = \sum_{i=1}^{n} \ln \xi_i \ . \tag{2.8}$$

Therefore according to the central limit theorem the term on the right tends to a normal distribution with parameters $\mu = n\mu_\xi$ and $\sigma^2 = n\sigma_\xi^2$. The parameters μ_ξ and σ_ξ^2 appear as fundamental unknowns[3]. Setting $\ell = \eta$ (*i.e.* $n = \ln(\eta/L)/\ln\lambda \sim \ln Re_\lambda$) we obtain a model for the local dissipation rate. The log-normal distribution for ε has been confirmed for example by DNS of [271] or experiments [188] and is shown in figure 2.1.
Moreover the variance of the logarithm of the local dissipation rate is then given by $\sigma^2 = \dfrac{\sigma_\xi}{\ln\lambda} \ln \eta/L = A + B \ln Re_\lambda$ as predicted by Kolmogorov and Oboukhov [128, 192].

[2] Actually it is the preparation of this chapter of the memoir that initiated the work published in Ref. [274].

[3] Nevertheless, they are related by this relation $\mu_\xi = -\sigma_\xi^2/2$ obtained from the moments of a log-normal variable in order to guarantee that the average energy flux is conserved throughout the cascade.

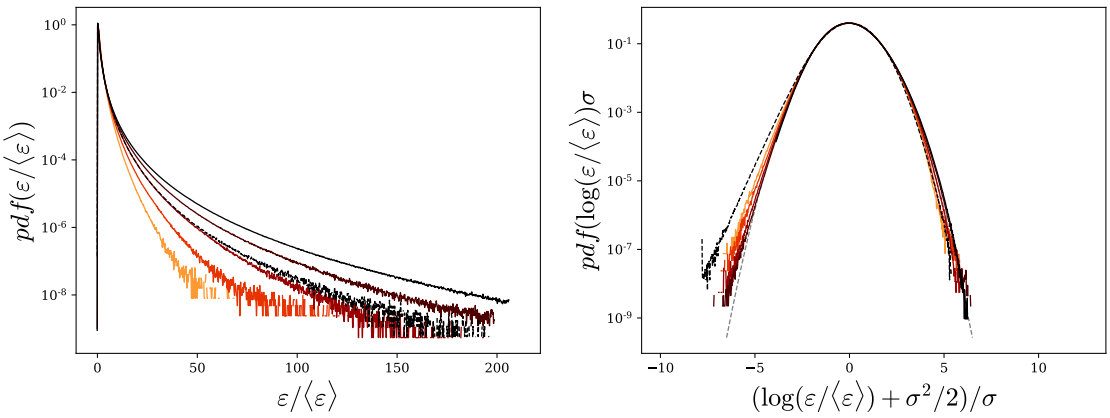

Figure 2.1: PDF of pseudodissipation (solid line) (left) and log of pseudodissipation (solid line) (right) centered and normalized by $\mu = \log(\varepsilon/\langle\varepsilon\rangle) = -\sigma^2/2$ and $\sigma^2 = \langle\log^2\varepsilon\rangle - \langle\log\varepsilon\rangle^2$ for $Re_\lambda = 50$, 90, 150, 230 and 380 from orange to black. Comparison with the actual dissipation for $Re_\lambda = 380$ in black dashed line and with $\exp(-x^2/2)/\sqrt{2\pi}$ in gray dashed lines on the right panel.

Such evolution for σ^2 has been also confirmed by the DNS of Ref. [271] showing that $\sigma^2 \approx 3/8 \ln Re_\lambda/10$. Note that alternative Reynolds number dependence have been proposedin Ref. [49].

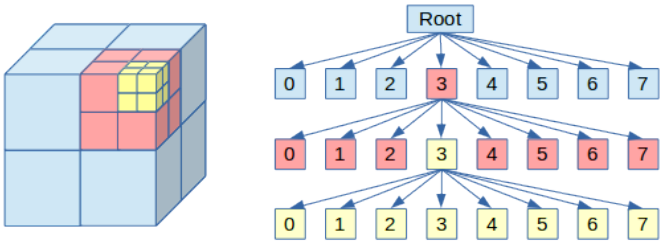

Figure 2.2: Schematic representation of multiplicative cascades (image from geidav.wordpress.com)

Implicitly the discrete model presented above assumes that the scale ratio λ is large enough, so that successive values of the scaling factor ξ_i can be considered as statistically independent. A continuous description of the evolution of energy transfer rate ε_r across scales, *i.e.* for infinitesimal λ, by a Markovian stochastic process has been proposed in Ref. [189], or similarly for the evolution of the velocity increments through scale r in Ref. [81].

Such a multiplicative process, that assumed that the coupling is local in scale, also implies a logarithmic evolution of the spatial correlation of the dissipation rate as explained by Mandelbrot [156]. To show that we consider the transfer rate at two points A and B, ε_n^A and ε_n^B, both defined on the same scale n. The points A and B are separated by a distance r (with r in the inertial range $L > r > \eta$) from each other and we note $k = \ln(r/L)/\ln\lambda$, then $0 < k < n$. Clearly, as illustrated in the figure 2.2, the greater the distance between

the two points, the larger the scale of their common root in the cascade:

$$\varepsilon_n^A = \varepsilon_0^{AB} \frac{\varepsilon_1^{AB}}{\varepsilon_0^{AB}} \cdots \frac{\varepsilon_k^{AB}}{\varepsilon_{k-1}^{AB}} \frac{\varepsilon_{k+1}^{A}}{\varepsilon_k^{A}} \cdots \frac{\varepsilon_n^{A}}{\varepsilon_{n-1}^{A}} \tag{2.9}$$

$$\varepsilon_n^B = \varepsilon_0^{AB} \frac{\varepsilon_1^{AB}}{\varepsilon_0^{AB}} \cdots \frac{\varepsilon_k^{AB}}{\varepsilon_{k-1}^{AB}} \frac{\varepsilon_{k+1}^{B}}{\varepsilon_k^{B}} \cdots \frac{\varepsilon_n^{B}}{\varepsilon_{n-1}^{B}} \ . \tag{2.10}$$

In the two previous equations, we have distinguished by the exponents A and B the variables which are specific to points A and B and by AB those which are common. This can be expressed as:

$$\ln \frac{\varepsilon_n^A}{\varepsilon_0} = \sum_{i=1}^{k} \ln \xi_i^{AB} + \sum_{i=k+1}^{n} \ln \xi_i^A \tag{2.11}$$

$$\ln \frac{\varepsilon_n^B}{\varepsilon_0} = \sum_{i=1}^{k} \ln \xi_i^{AB} + \sum_{i=k+1}^{n} \ln \xi_i^B \ . \tag{2.12}$$

The correlation between $\ln \varepsilon_n^A$ and $\ln \varepsilon_n^B$ is defined as

$$R_{\ln \varepsilon}(r) = \langle (\ln \frac{\varepsilon_n^A}{\varepsilon_0} - \mu)(\ln \frac{\varepsilon_n^B}{\varepsilon_0} - \mu) \rangle = \langle \ln \frac{\varepsilon_n^A}{\varepsilon_*} \ln \frac{\varepsilon_n^B}{\varepsilon_*} \rangle \ , \tag{2.13}$$

where we noted $\varepsilon_* = \varepsilon_0 e^{\mu}$. Introducing similarly $\xi_* = e^{\mu_\chi}$ and $\xi' = \xi/\xi_*$ we express the correlation as:

$$\begin{aligned} R_{\ln \varepsilon} &= \langle \sum_{i=1}^{n} (\ln \xi_i^A - \mu_\xi) \sum_{j=1}^{n} (\ln \xi_i^B - \mu_\xi) \rangle = \langle \sum_{i=1}^{n} \ln \xi_i'^A \sum_{j=1}^{n} \ln \xi_j'^B \rangle \\ &= \langle \left(\sum_{i=1}^{k} \ln \xi_i'^{AB} + \sum_{i=k+1}^{n} \ln \xi_i'^A \right) \left(\sum_{j=1}^{k} \ln \xi_j'^{AB} + \sum_{j=k+1}^{n} \ln \xi_j'^B \right) \rangle \\ &= \sum_{i=1}^{k} \sum_{j=1}^{k} \delta_{ij} \sigma_\xi^2 = k \sigma_\xi^2 \ . \end{aligned} \tag{2.14}$$

To obtain this results we used the hypothesis that within the same branch, the events at a given scale are independent of those at another scale, $\langle \ln \xi_i'^{AB} \ln \xi_j'^{AB} \rangle = \delta_{ij} \sigma_\xi^2$, as well as the absence of correlation between branches A and B: $\langle \ln \xi_i'^A \ln \xi_j'^B \rangle = 0$. This gives a logarithmic evolution of the correlation coefficient $\rho_{\ln \varepsilon} = R_{\ln \varepsilon}/\sigma^2$, in the range $\eta < r < L$:

$$\rho_{\ln \varepsilon} = \frac{\langle \ln \frac{\varepsilon_n^A}{\varepsilon_*} \ln \frac{\varepsilon_n^B}{\varepsilon_*} \rangle}{\langle \ln^2 \frac{\varepsilon_n}{\varepsilon_*} \rangle} = \frac{k}{n} = \frac{\ln L/r}{\ln L/\eta} = 1 - \frac{\ln r/\eta}{\ln L/\eta} \ . \tag{2.15}$$

Stochastic modeling of the dissipation

Although not trivial, this result can be transposed for the temporal correlation along a particle path [240, 107, 169, 35]. The logarithmic behavior of the correlation is confirmed by DNS, as it can be seen in Ref. [146] or in figure 2.3, where the evolution of the

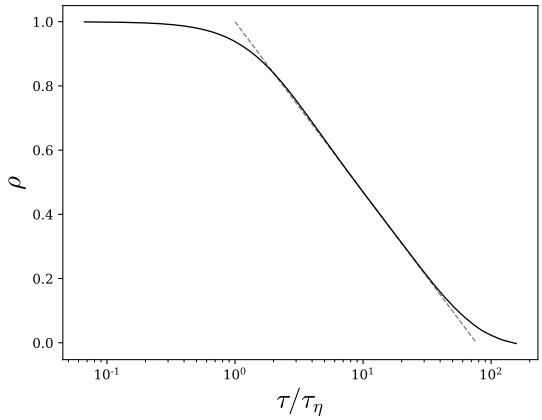

Figure 2.3: Autocorrelation of the log of the dissipation rate along the path of fluid particles from the database of Refs. [21, 140] at $Re_\lambda = 420$, comparison with $\rho_{\ln\varepsilon} = 1 - \ln(\tau/\tau_\eta)/\ln(\tau_\varepsilon/\tau_\eta)$.

Lagrangian correlation of the logarithm of the dissipation is plotted from the DNS data of [21, 140].
It has been proposed to model the dissipation rate as a stochastic multiplicative process. Such a process can be generically expressed as :

$$d\varepsilon = \varepsilon\Pi dt + \varepsilon\Sigma dW \tag{2.16}$$

with dW the increment of the Wiener process ($\langle dW\rangle = 0$ and $\langle dW^2\rangle = dt$) and where Π and Σ are to be determined.
Considering that ε follows a log-normal distribution with parameter σ^2 and $\mu = -\sigma^2/2$, we define the standard normal variable χ (Gaussian random variable with zero mean and unit variance) as:

$$\frac{\varepsilon}{\langle\varepsilon\rangle} = \exp\left(\sigma\chi - \sigma^2/2\right) \ . \tag{2.17}$$

A stochastic process for χ has to be given in order to obtain the stochastic process for ε, via the Ito transformation.
Pope and Chen [203] proposed to obtain χ from an Orstein-Uhnlebbeck process with a characteristic time τ_ε:

$$d\chi = -\frac{\chi}{\tau_\varepsilon}dt + \sqrt{\frac{2}{\tau_\varepsilon}}dW \ . \tag{2.18}$$

According to the Ito formula, this gives for Π and Σ :

$$\Pi = -\left(\ln\varepsilon/\langle\varepsilon\rangle - \sigma^2/2\right)/\tau_\varepsilon \ , \tag{2.19}$$

$$\Sigma = \sqrt{2\sigma^2/\tau_\varepsilon} \ . \tag{2.20}$$

This process gives, as expected, a log-normal distribution for ε (normal distribution for χ) as well as an exponential decrease of the correlation of $\ln\varepsilon$ with a characteristic time τ_ε. This exponential behavior is not consistent with the multiplicative cascade model as

discussed above. It rather corresponds to a direct energy transfer from large to small-scales.

To ensure a logarithmic decorrelation of the dissipation, Chevillard [54] proposed to adapt the Gaussian multiplicative chaos introduced by Mandelbrot [156]. This leads to a multifractal model in which the increment of the Wiener process in Eq. (2.18) is replaced by a fractional Gaussian noise:

$$d\chi = -\frac{\chi}{\tau_\varepsilon}dt + \frac{1}{\Lambda}dW^0_{\tau_c} \ , \tag{2.21}$$

where, $dW^0_{\tau_c}$ is formally a fractional Gaussian noise with a 0 Hurst exponent, regularized at a timescale τ_c, and Λ is a normalization factor ensuring unit variance for χ. The value of Λ is dependent on the specific regularization of $dW^0_{\tau_c}$. As explained in Ref. [54], this process can be reexpressed as

$$d\chi(t) = \left(-\frac{\chi}{\tau_\varepsilon} + \frac{\Gamma}{\Lambda}\right)dt + \frac{1}{\sqrt{\Lambda^2\tau_c}}dW \tag{2.22}$$

with dW the increments of a standard Wiener process and Γ corresponds to a convolution of the Wiener increments:

$$\Gamma = -\frac{1}{2}\int_{-\infty}^{t}(t-s+\tau_c)^{-3/2}dW(s) \tag{2.23}$$

where $dW(s)$ are the increments of the same realization of the Wiener process as in Eq. (2.22). In Eq. (2.23), the regularization time τ_c prevents the divergence of the kernel when $s \to t$. The normalization factor Λ is estimated as $\Lambda = \langle X^2 \rangle$ where X obey the stochastic Eq. (2.22) in which Λ has been set to 1.

The stochastic process (2.22) gives a logarithmic correlation for χ: $\langle \chi(t)\chi(t-s)\rangle \sim \ln \frac{\tau_\varepsilon}{s}$ for $\tau_c \ll s \ll \tau_\varepsilon$, as illustrated in the Fig. 2.4.

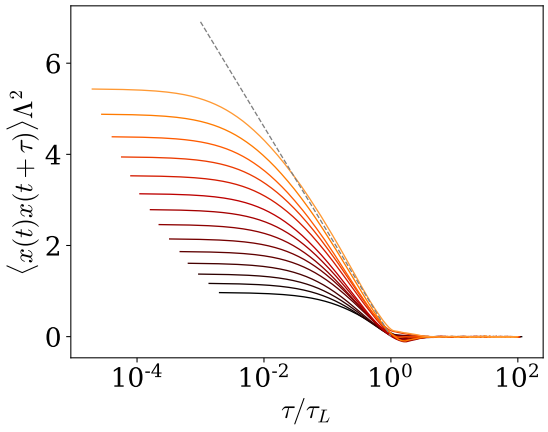

Figure 2.4: Correlation of χ for various values of τ_ε/τ_c.

With the Ito transformation, we obtain the process for ε from (2.22). This gives for Π and Σ :

$$\Pi = \left(-\ln\frac{\varepsilon}{\langle\varepsilon\rangle} + \frac{\sigma^2}{2\Lambda^2}\left(\frac{\tau_\varepsilon}{\tau_c} - \Lambda^2\right) + \frac{\sigma}{\Lambda}\Gamma\tau_\varepsilon\right)/\tau_\varepsilon \ , \tag{2.24}$$

$$\Sigma = \sqrt{\frac{\sigma^2}{\Lambda^2\tau_c}} \ . \tag{2.25}$$

2.2 Lagrangian dynamics

With the advances of experimental techniques and the increase in computing power of the last decades, remarkable features of the dynamics of fluid particles in turbulent flows have been discovered. Among them, the measurement of the probability distribution of the acceleration of these tracers has been shown to be clearly non Gaussian with a high frequency of observing very intense events [134, 264, 181, 180]. Even for moderate Reynolds numbers, it is relatively common to observe accelerations more than 100 times greater than their standard deviation. In addition, the components of acceleration and its norm present very different correlation times, the ratio of these characteristic times increasing with the Reynolds number [199, 182, 183] showing that the dynamics of the tracers is influenced by the full spectrum of turbulence scales. On the one hand, the short-time correlation of the acceleration component is connected to the centripetal forces in intense vorticity filaments [30, 183]. On the other hand, the acceleration norm has been shown to be directly correlated with the local dissipation rate of turbulence [217, 271, 106, 31], in accordance with Kolmogorov's hypotheses. Nevertheless, various experimental and numerical works have also reported its dependence on the local kinetic energy [180, 241, 29, 62, 36, 217, 8], which is generally attributed to nonindependence of the small-scale dynamics from those of the large-scales. In this view, the Lagrangian acceleration is essentially given by the local gradients of the velocity, but the latter present correlation with the kinetic energy caused by direct energy transfers between large- and small-scales in the energy cascade [258]. The absence of a proper scale separation explains that the Lagrangian correlation functions present power-laws with anomalous exponents which can be described by the multifractal formalism [55, 9, 28, 239, 139] as the signature of intermittency and persistence of viscous effects. To end this list, we mention the asymmetry of the fluctuations of the mechanical power received or given up by a fluid particle reflecting the temporal irreversibility of its dynamics [198, 75, 268, 208, 68, 66].

Such a complex phenomenology must be attributed to the collective and dissipative effects. Indeed according to the Navier-Stokes equation, the acceleration of a fluid particle is essentially given by the pressure field which is determined by the motion of all the other particles [65, 259]. Moreover, although the Laplacian term in the Navier-Stokes equation is of order Re^{-1} smaller than the pressure gradient term, the viscosity cannot be neglected. Indeed, as a small force integrated over a long period could be significant, the viscosity insidiously affects the fluid tracer velocity. Which in turn influences the particle acceleration through modifications of the pressure gradient, and local interactions are intrinsically inseparable from the nonlocal ones. This is manifested by the persistence of the effect of the Reynolds number on the acceleration statistics, even for very large Reynolds numbers. Such a scenario is supported by Refs. [61, 196, 56] who showed that adding some noise to an inviscid Lagrangian flow causes the irreversibility of the dynamics.

Following the Kolmogorov first hypothesis [128, 126] stating that locally homogenous turbulent flows are universal, it should be possible, in principle, to propose a stochastic model that reproduces the dynamics of a single fluid particle by effectively accounting for the interactions with all the other fluid particles. Let us note that the Kolmogorov first hypothesis received some support from recent studies [249, 143, 37]. To propose such a stochastic model, our main assumption is to write the increments of the acceleration vector of a fluid particle as $da_i = M_i dt + D_{ij} dW_j$. Both M and D depend on particle acceleration a and velocity u. The latter is simply given by the kinematic relation of

a fluid particle $u_i = \int a_i dt$. It is indeed a necessary condition that a depends on u to present a restoring effect that can counteract the diffusion in the velocity space and get a statistically stationary dynamics of the fluid particle. We will propose closed expressions for M and D from basic considerations using, as a starting point the acceleration statistics conditioned on both the local values of the dissipation rate and the kinetic energy observed from direct numerical simulations (DNS), which are presented bellow. It will be shown that introducing a "maximal winding hypothesis" associated with a nondiagonal diffusion tensor, this simple stochastic model reproduces all the statistical features of the Lagrangian dynamics presented above, without any adjustable parameter.

Let us first review some previous works on the stochastic modeling of the Lagrangian dynamics (see also Ref. [8]). Among the pioneering works, Sawford [237] proposed a scalar Gaussian model for the acceleration presenting a feedback term proportional to the velocity. Pope and Chen [203] devised a Langevin-like equation for the velocity coupled with a log-normal model for the dissipation through the introduction of conditional statistics. Similarly, Refs. [216, 215, 23] proposed an extension of the Sawford model leading to a non-Gaussian scalar model for the acceleration. This work was further refined by Ref. [136] who also advanced a non-Gaussian scalar model for the dynamics by prescribing an ad hoc shape of the conditional acceleration statistics with the dissipation along with a linear dependence on the velocity. The model introduced in Ref. [218] describes the increments of the derivative of the acceleration in a so-called third-order model to better account for the Reynolds number dependence on the acceleration statistics. Recently, Ref. [261] proposed generalization to an infinite number of layers leading to smooth 1D trajectory along with a multifractal correction to account for intermittency, as introduced in Refs. [10, 157, 118]. An acceleration vector model has been proposed in Ref. [214] by imposing an empirical correlation between velocity and acceleration, with additive noise leading to Gaussian statistics for the acceleration. Likewise, Ref. [202] presented a 3D Gaussian model, with a linear dependence on the velocity as well as an extension to non-homogenous flows. To account for intermittency effect, in Refs. [92, 230, 279, 228, 17, 91] the 3D acceleration vector is given by the product of two independent stochastic processes, one for the acceleration norm and the other for its orientation. In these models, the velocity feedback on the dynamics is realized by a coupling with a large eddy simulation framework. To summarize, to our knowledge, a 3D vectorial model for the tracer dynamics that is autonomous and reproducing the essential features of Lagrangian turbulence (irreversibility, non-Gausianty, multifractality) has not yet been proposed.

The essential building block of previously cited models is the conditional acceleration statistics. Previous studies have focused on conditional statistics with either the velocity or the dissipation rate separately. From the extensive analysis of Ref. [271], one can conclude that the acceleration variance conditioned on the dissipation rate ε presents a power-law behavior at large values of ε with a Reynolds-number-dependent exponent reflecting that the small-scale dynamics are not independent of large scales.

Regarding the links between the fluid particle acceleration and their velocity, Biferale *et al.* [29] argued that according to the Heisenberg-Yaglom scaling for the acceleration $\langle a^2 \rangle \sim a_\eta^2 = \langle \varepsilon \rangle^{3/2} \nu^{-1/2} = \langle K \rangle^{9/4} L^{-3/2} \nu^{-1/2}$, with ν the kinematic viscosity, $K = 1/2 u_i u_i$ the kinetic energy and L the characteristic size of the large structures, one should expect that the variance of the velocity-conditioned acceleration behaves like $\langle a^2 | K \rangle \propto K^{9/4}$. Then on the basis of the multifractal formalism, they proposed a very close scaling law, $\langle a^2 | K \rangle \sim K^{2.3}$. The proposed relation was observed to be in agreement with DNS for

large velocity, typically $|u| > 3\sigma_u$ with $\sigma_u = \sqrt{2/3\langle K\rangle}$. These events remain very rare since the PDF of the fluid velocity is Gaussian so the range of validity of the power-law is, at best, very limited. Alternatively, Sawford et al. [241] propose that $\langle a_x^2|u_x\rangle \sim u_x^6$ based on a mechanism involving vorticity tubes. This scaling law which seems compatible with the first measurements of the acceleration conditioned on velocity in Ref. [180], is confirmed neither by the DNS of Ref. [29] nor in a second experimental paper by Crawford et al. [62] which gave more credit to the $K^{9/4}$ law. As mentioned above, it has been proposed that the dependence of the acceleration on the velocity arises through the dependence of the dissipation rate on the kinetic energy due to intermittency effect [29]. Additionally, Ref. [258] proposed that the dependence on velocity is a consequence of direct and bidirectional coupling of large and small scales caused by kinematic relations related to nonlocal interactions.

Here, we study the acceleration statistics conditional on both the kinetic energy and the dissipation rate. To our knowledge such doubly conditional statistics of the acceleration have never been presented. It will be shown that the variance can be expressed as $\langle a^2|\varepsilon, K\rangle \sim \exp(\alpha K/\langle K\rangle + \gamma \ln \varepsilon/\langle\varepsilon\rangle)$. This result is clearly in contrast with the previously proposed power-law dependence on velocity. It shows that the influence of the large-scales through the intermittent distribution of the dissipation rate, which manifests through the Reynolds number dependence of the coefficient γ, is supplemented by an explicit dependence on the local kinetic energy. This direct dependence on the large-scale characteristics is of a kinematic nature as it appears independent of the Reynolds number. The behavior of the doubly conditional acceleration can be interpreted as a consequence of a scaling symmetry for the fluid-particle acceleration incorporating both the intermittency and the kinematic effects of the flow structure. We also propose to apply the incomplete similarity framework introduced by Barenblatt to explain the dependence of the statistics of the acceleration conditioned to the dissipation rate on the Reynolds number and to account for the intermittency effect. That enables us to provide as well new scaling relations for the unconditional variance in good agreement with the DNS. Eventually the doubly conditional statistics of the acceleration which gives a relation between the force, the energy, and the power will serve as a corner stone to build the stochastic model for the dynamics of a fluid particle mentioned above. Although such a model could be of interest for practical applications, its construction is relevant to study the specificities of the Lagrangian description of turbulence by linking the cascade picture to the fluid particles dynamics on the basis of the behavior of the conditional statistics obtained by the DNS of the Navier-Stokes equations.

In Sec. 2.3 we present the statistics of the acceleration conditioned on the local values of the dissipation rate and kinetic energy obtained from DNS. Then we show that the Reynolds number dependence on the acceleration conditioned on the dissipation rate can be described using the Barenblatt incomplete similarity. We deduce a new relation for the unconditional acceleration variances. To end this section, we show that these new results can be interpreted as a multiplicative cascade for the acceleration with scale dependent kinematic effects. Then in Sec. 2.4 we give the derivation of the stochastic model for a single fluid-particle dynamics taking as an initial step the doubly conditional acceleration variance, and present the outcome of the model for the Reynolds number up to $Re_\lambda = 9000$, along with comparison with DNS results when available.

2.3 Scaling laws of the acceleration

2.3.1 Methodology

We present in this section results concerning the statistics of the acceleration of a fluid particle. These results have been obtained from five direct numerical simulations (DNS) of isotropic turbulence in a periodic box with Taylor-scale Reynolds numbers of $Re_\lambda = 50$, 90, 150, 230 and 380. We used pseudospectral code as detailed in Refs. [275, 279, 144]. The DNS was carried with resolutions of 128^3, 256^3, 512^3, 1024^3 and 2048^3 with the large scale forcing proposed by Ref. [131]. For each simulation we have $\eta/\Delta x = 1$ with $\eta = \langle\varepsilon\rangle^{-1/4}\nu^{3/4}$ the Kolmogorov length scale and Δx the grid size. The statistics are computed from 40 3D fields sampled at roughly each large-eddy-turnover time.
We will show statistics of the acceleration conditioned by the dissipation rate and the kinetic energy. Note that we consider here the pseudodissipation $\tilde{\varepsilon} = \nu(\partial_j u_i)^2$, which is the second invariant of the velocity gradient tensor multiply by the viscosity rather than the dissipation $\varepsilon = \frac{1}{2}\nu(\partial_j u_i + \partial_i u_j)^2$. We prefer to show here the statistics of the pseudodissipation to be consistent with the next section, in which we will use the log-normal distribution hypothesis for the dissipation. Indeed, this property is very well verified for the pseudodissipation whereas it is only approximate for the dissipation [271]. Nevertheless, the statistics presented below have also been computed considering the dissipation, ε, and no significant differences were observed. To lighten the writing, in the sequel, we will drop the tilde in the notation of the pseudodissipation, as well, in the text, we will write dissipation instead of pseudodissipation.

2.3.2 Conditional statistics given the dissipation and the kinetic energy

To illustrate the relationships between acceleration, energy dissipation and kinetic energy, we show in Fig. 2.5 visualizations of these quantities at the same instant obtained from our DNS. We notice that $\ln a^2/\langle a^2\rangle$ and $\ln\varepsilon/\langle\varepsilon\rangle$ show a fairly marked correlation although the acceleration appears more diffuse than dissipation. We also notice that to some extent the kinetic energy and the dissipation rate appears correlated. In addition, it seems that some areas of the flow where the kinetic energy is high also correspond to regions of high acceleration magnitude.
Figure 2.6 presents the variance of the acceleration of a fluid particle conditioned to the local values of the kinetic energy and the dissipation rate: $\langle a^2|\varepsilon, K\rangle$. In Fig. 2.6 (top), the levels of the logarithm of the conditional variance are shown as a function of K and of ε. We see that the conditional variance of the acceleration depends on these two quantities and that the dependence on K seems somewhat similar to that of $\ln\varepsilon$. In a more quantitative way, we show in Fig. 2.6 (left) the variance of the acceleration as a function of ε for different values of K. We can see that the shape of the curves remains globally unchanged when K varies and also presents the same shape as the variance conditioned by ε only as also presented in this figure. Essentially, it is observed that the conditional variance presents power-law behavior for $\varepsilon \gg \langle\varepsilon\rangle$ with an exponent close to 3/2 and a prefactor depending on K. As discussed in more detail below, we observe a slight deviation of the scaling law compared to the acceleration conditioned only by the dissipation.
Figure 2.6 (right) shows the variance of the acceleration as a function of K for different values of ε. As expected, we find that the variance of the acceleration increases with K.

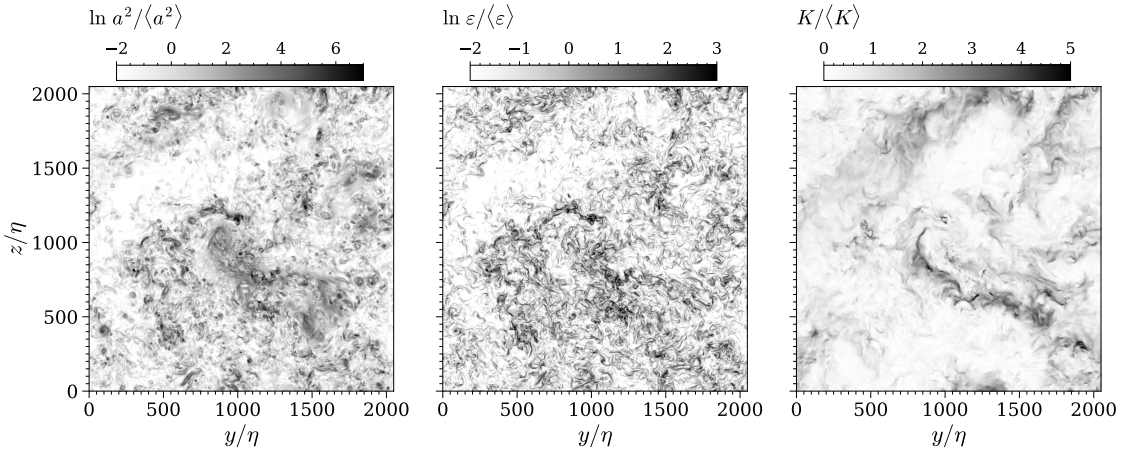

Figure 2.5: Visualization of the instantaneous fields of the square of the acceleration, of the dissipation and of the kinetic energy in a cut $y-z$ of the flow by DNS at $Re_\lambda = 380$. Left: $\ln(a^2/ < a^2 >)$; middle: $\ln(\varepsilon/ < \varepsilon >)$ and right: $K/ < K >$.

We clearly notice an exponential growth of the variance over the whole range of K with a growth rate α which appears independent of ε:

$$\langle a^2|\varepsilon, K\rangle = c_\varepsilon a_\eta^2 \exp(\alpha K/\langle K\rangle) \tag{2.26}$$

with $a_\eta^2 = \langle\varepsilon\rangle^{3/2}\nu^{-1/2} = \langle\varepsilon\rangle/\tau_\eta$ the so-called Kolmogorov acceleration and the prefactor c_ε depending on ε. From our DNS it appears that $\alpha \approx 1/3$ for all the Reynolds numbers considered here. We also find the same value of α from the database of [21, 140] obtained for $Re_\lambda = 400$ suggesting that the value of α is independent of the Reynolds number.
This exponential behavior contrasts with the references mentioned in the introduction in which power-laws behavior for the variance conditioned on K solely had been proposed. Nevertheless, we can notice that exponential growth does not seem to disagree with the data presented in these references. Interestingly, this relationship only depends on a characteristic velocity, (not a time and a length scale separately). The absence of characteristic time is attributed to the scale separation between large structures and small ones (the large structures of the flows appear as quasi stationary and infinite to the smallest ones such that only their relative velocity matters). The independence of the coefficient α on the Reynolds number tends to confirm that the velocity scale used for the nondimensionalization of the argument of the exponential is appropriate.
In appendix of [274] we propose to estimate the factor c_ε as:

$$c_\varepsilon \approx A\,\langle a^2|\varepsilon\rangle/a_\eta^2 \tag{2.27}$$

where $A = \left(1 - \frac{2}{3}\alpha\right)^{3/2}$, which is equal to $A = 7\sqrt{7}/27 \approx 0.686$, for $\alpha = 1/3$, neglecting a small logarithmic dependence on $\varepsilon/\langle\varepsilon\rangle$.
Consequently, for large Reynolds numbers, the doubly-conditioned variance of the fluid-particle acceleration is expressed as

$$\langle a^2|\varepsilon, K\rangle = A\,\langle a^2|\varepsilon\rangle \exp(\alpha K/\langle K\rangle)\,. \tag{2.28}$$

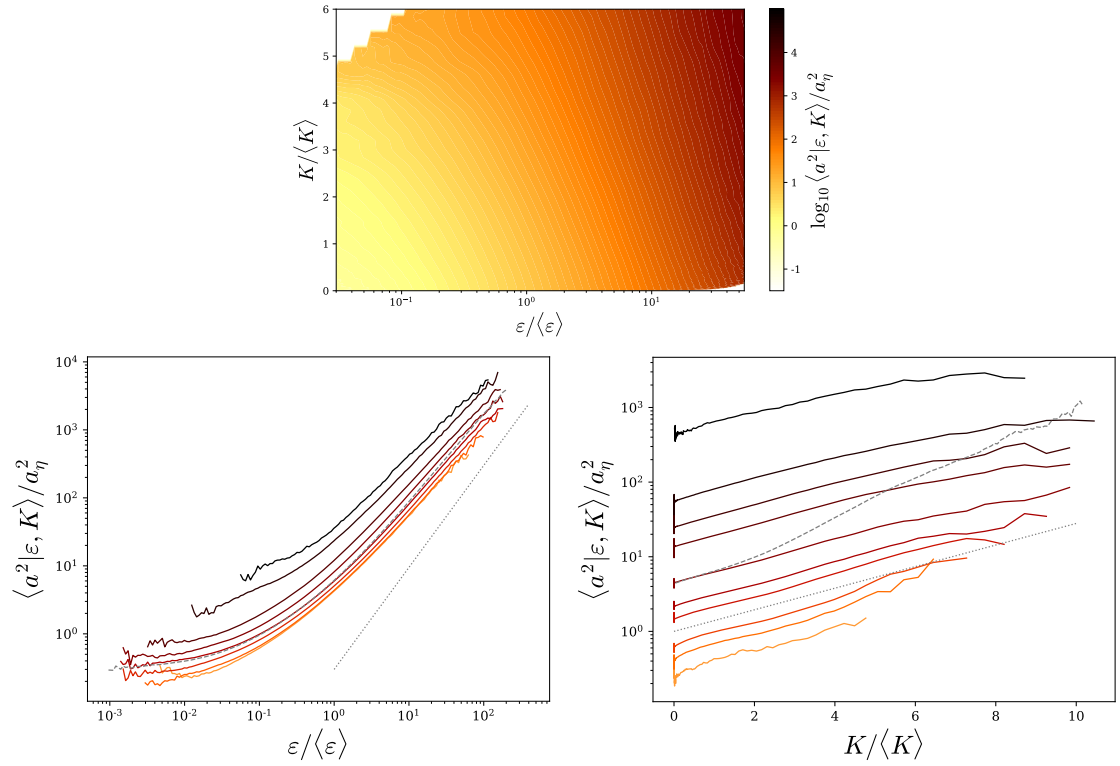

Figure 2.6: Variance of acceleration conditioned on the local dissipation rate and kinetic energy obtained from DNS at $Re_\lambda = 380$. Top: Map of $\ln\langle a^2|\varepsilon,K\rangle/a_\eta^2$ versus $\ln\varepsilon/\langle\varepsilon\rangle$ and $K/\langle K\rangle$. Left: Plot, in logarithmic scales, of $\langle a^2|\varepsilon,K\rangle/a_\eta^2$ against $\varepsilon/\langle\varepsilon\rangle$ for $K/\langle K\rangle = 0.025, 0.1, 0.5, 1, 2, 3, 5, 6.5 \pm 30\%$ from orange to black. Comparison with $\langle a^2|\varepsilon\rangle/a_\eta^2$ in gray dashed line and with the power-law $(\varepsilon/\langle\varepsilon\rangle)^{3/2}$ in gray dotted line. Right: Plot, in semilogarithmic scales, of $\langle a^2|\varepsilon,K\rangle/a_\eta^2$ against $K/\langle K\rangle$ for $\varepsilon/\langle\varepsilon\rangle = 0.01, 0.05, 0.1, 0.3, 0.5, 1, 3, 5, 10, 50 \pm 30\%$ from orange to black. Comparison with $\langle a^2|K\rangle/a_\eta^2$ in gray dashed line and with $\exp(\alpha K/\langle K\rangle)$ with $\alpha = 1/3$ in gray dotted line.

This relation is confirmed in Fig. 2.7 which presents the conditional variance of the acceleration normalized by $Aa_\eta^2\exp(\alpha K/\langle K\rangle)$ as a function of ε for different values of K as well as normalized by $A\langle a^2|\varepsilon\rangle = \langle a^2|\varepsilon, K=0\rangle$ as a function of K for different values of ε. It can be seen that a fairly good overlap of the various curves is obtained, confirming the self-preserving character of the acceleration conditioned on both the kinetic energy and the dissipation rate. We see in this relation an explicit effect of the local kinetic energy on the acceleration. Since the argument of the exponential depends on $K/\langle K\rangle$ not on a local Reynolds number, it suggests pure kinematic effects for the acceleration which is likely associated to the divergence free constrain and the nonlocality of the pressure gradient. There is also an indirect effect through the dependence of the dissipation rate on the large-scale structures. The later is manifested as Reynolds number dependence of the conditional acceleration on the dissipation rate solely. This intermittency effect is analyzed further in the next section. We postpone to Sec. 2.3.5 further comments on the behavior of the doubly-conditioned variance.

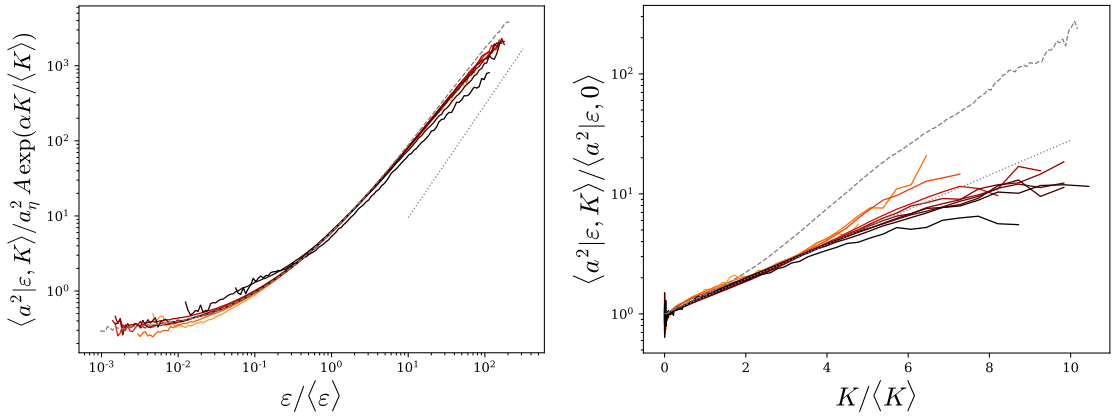

Figure 2.7: Normalized variance of acceleration conditioned on the local dissipation rate and kinetic energy obtained from DNS at $Re_\lambda = 380$. (Left) Plot of $\langle a^2|\varepsilon,K\rangle/Aa_\eta^2\exp(\alpha K/\langle K\rangle)$ against $\varepsilon/\langle\varepsilon\rangle$ for various values of K. Comparison with $\langle a^2|\varepsilon\rangle/a_\eta^2$ in gray dashed line and with the power-law $(\varepsilon/\langle\varepsilon\rangle)^{3/2}$ in gray dotted line. (Right) Plot of $\langle a^2|\varepsilon,K\rangle/\langle a^2|\varepsilon,K=0\rangle$ against $K/\langle K\rangle$ for various values of $\varepsilon/\langle\varepsilon\rangle$. Comparison with $\langle a^2|K\rangle/a_\eta^2$ in gray dashed line and with $\exp(\alpha K/\langle K\rangle)$ with $\alpha = 1/3$ in gray dotted line The ranges of the fixed values of K and ε for both plots are the same as in Fig. 2.6.

2.3.3 Similarity of the conditional statistics given the dissipation

We propose now to focus with more details on the scaling law of the acceleration variance conditioned on the dissipation rate only, $\langle a^2|\varepsilon\rangle$. For that we consider the DNS data from Yeung et al. [271], along with our DNS data. Figure 2.8 (Left) presents the conditional acceleration variance for Reynolds numbers in the range $Re_\lambda = 40$ to 680. We first notice that for weak values of the dissipation rate ($\varepsilon \ll \langle\varepsilon\rangle$) the value of the conditional acceleration variance tends towards an asymptotic value, which depends on the Reynolds number. The saturation of the conditional acceleration shows that the local acceleration is not only determined by the microstructure of the flow, and that it presents somehow effects of the large structures of the flow which dominates in low dissipative regions. We denote by a_0^2 the asymptotic value of the conditional variance:

$$a_0^2 = \lim_{\varepsilon\to 0}\langle a^2|\varepsilon\rangle\,. \tag{2.29}$$

Assuming that the acceleration of fluid particles in low dissipative regions is mainly influenced by large scales, we can estimate a_0^2 as $a_0^2 \sim \langle K\rangle/\tau_L^2$ with τ_L the integral timescale of the flow. This leads to the following estimate:

$$a_0^2/a_\eta^2 \sim \tau_\eta/\tau_L \sim Re_\lambda^{-1}\,. \tag{2.30}$$

We test this scaling law for a_0 in Fig. 2.8(right) by presenting a_η^2/a_0^2 as a function of Re_λ from the different DNS datasets. We observe a linear growth rate of a_0^2/a_η^2 with $1/Re_\lambda$. For large values of ε, we notice in Fig. 2.8(Left), as already reported in [271], that the conditional variance presents a power-law behavior with ε. The exponent of this scaling law is seen to evolve continuously with the Reynolds number, and seems to tend asymptotically

towards $\varepsilon^{3/2}$. From dimensional analysis we define f as:

$$\frac{\langle a^2|\varepsilon\rangle}{\varepsilon^{3/2}\nu^{-1/2}} = f(\varepsilon/\langle\varepsilon\rangle, Re_\lambda)\,. \tag{2.31}$$

In the inset of Fig. 2.8(Left), it is seen that f seems to admit an asymptotic constant value for $\varepsilon \gg \langle\varepsilon\rangle$ only in the limit of a very large Reynolds number. For intermediate Reynolds numbers, f presents power-law behavior with ε for $\varepsilon \gg \langle\varepsilon\rangle$ but with a Reynolds number dependent exponent. This implies an absence of similarity of the flow when the Reynolds number is changed and the persistence of the Reynolds number effect, even for large Reynolds numbers, which highlights an absence of proper scale separation suggesting direct coupling between large- and small-scales. This is reminiscent of the incomplete similarity framework proposed by Barenblatt [15, 14, 13]. Following Barenblatt, we assume that f presents an incomplete similarity in $\varepsilon/\langle\varepsilon\rangle$ and absence of similarity in Re_λ. Accordingly we write

$$f(\varepsilon/\langle\varepsilon\rangle, Re_\lambda) = B\,(\varepsilon/\langle\varepsilon\rangle)^\beta \tag{2.32}$$

where the anomalous exponent β, and the prefactor B are both functions of Re_λ. Arguing for a vanishing viscosity principle, it can be assumed that the critical exponent becomes independent of the Reynolds number in the limit of asymptotically large Reynolds number. Finally arguing that the dependence of B and β on the Reynolds number is small, Barenblatt further proposed that they present inverse logarithmic dependence on Re_λ, which is also in agreement with the log-similarity proposed by Refs. [51, 82]. Expending β and B in power of $1/\ln(Re_\lambda)$ yields, keeping only the leading-order term in Re_λ:

$$\beta = \beta_0 + \beta_1/\ln Re_\lambda \tag{2.33}$$

$$B = B_0 + B_1/\ln Re_\lambda\ . \tag{2.34}$$

To have a finite limit, consistently with the vanishing viscosity principle, we need $\beta_0 = 0$. The remaining constants B_0, B_1 and β_1 are then determined by comparison with the DNS data. From the inset of Fig. 2.8(Left) we see that both β and B are increasing functions of Re_λ implying that both B_1 and β_1 are negative. In Fig. 2.9(Left) we assess the relations (2.32)-(2.34) by plotting

$$\chi = \frac{1}{\gamma}\ln(1/B\,\langle a^2|\varepsilon\rangle/a_\eta^2)\,, \tag{2.35}$$

with

$$\gamma = 3/2 + \beta\,, \tag{2.36}$$

against $\ln(\varepsilon/\langle\varepsilon\rangle)$ for various Reynolds numbers. It is observed that with $B_0 = 17.1$, $B_1 = -54.7$ and $\beta_1 = -1$, all the DNS data collapse on the line $\chi = \ln(\varepsilon/\langle\varepsilon\rangle)$ (the bisectrix of the graph) for $\varepsilon \gg \langle\varepsilon\rangle$, validating the scaling relation.
We can go a step further by using the low dissipative limit of the conditional acceleration. For that we introduce $\chi_0 = \lim_{\varepsilon\to 0}\chi = \frac{1}{\gamma}\ln(1/B\,a_0^2/a_\eta^2)$. With this definition, $\chi - \chi_0 = \ln\left[\left(\langle a^2|\varepsilon\rangle/a_0^2\right)^{1/\gamma}\right]$ tends to 0 in the low dissipative regions ($\varepsilon \ll \langle\varepsilon\rangle$). On the other hand, for $\varepsilon \gg \langle\varepsilon\rangle$, $\chi - \chi_0$ should be equal to $\chi - \chi_0 = \ln(\varepsilon/\langle\varepsilon\rangle) - \chi_0 = \ln\left[\varepsilon/\langle\varepsilon\rangle\left(Ba_\eta^2/a_0^2\right)^{1/\gamma}\right]$. This is seen in Fig. 2.9 (right) that presents the evolution of $\left(\langle a^2|\varepsilon\rangle/a_0^2\right)^{1/\gamma}$ against

$$\zeta = \varepsilon/\langle\varepsilon\rangle\left(Ba_\eta^2/a_0^2\right)^{1/\gamma} \tag{2.37}$$

for the various Reynolds numbers considered here.
It is interesting to note that the curves are all overlapping even for intermediate values of ε, suggesting that the conditional acceleration variance can be cast in a self-similar form:

$$\langle a^2|\varepsilon\rangle = a_0^2\,(\phi(\zeta))^\gamma \tag{2.38}$$

with ϕ a universal function of only one argument $\phi = \phi(\zeta)$ with the asymptotics $\phi(\zeta) = 1$ for $\zeta \ll 1$ and $\phi(\zeta) = \zeta$ for $\zeta \gg 1$. Making a Taylor expansion of ϕ around $\zeta = 0$ and using a matching asymptotic argument, simply yields

$$\phi(\zeta) = 1 + \zeta\,. \tag{2.39}$$

It is seen in the inset of the Fig. 2.9 (right) that the proposed expression for ϕ gives a good approximation of the data over the whole range of ε and Re_λ. We can indeed observe more than 5 decades of quasilinear growth of $\left(\langle a^2|\varepsilon\rangle/a_0^2\right)^{1/\gamma} - 1 = \exp(\chi - \chi_0) - 1$ with ζ. The nondimensional function f introduced in Eq. (2.31) can, in consequence, be expressed as:

$$f(\varepsilon/\langle\varepsilon\rangle, Re_\lambda) = B\,(\varepsilon/\langle\varepsilon\rangle)^\beta \left(1 + \frac{1}{\zeta}\right)^{3/2+\beta}\,, \tag{2.40}$$

where the term within the brackets is interpreted as a correction factor for small dissipative regions. Accordingly, we obtain the following expression for the conditional acceleration variance:

$$\langle a^2|\varepsilon\rangle = B a_\eta^2 \left(\left(\frac{1}{B}\frac{a_0^2}{a_\eta^2}\right)^{1/\gamma} + \frac{\varepsilon}{\langle\varepsilon\rangle}\right)^\gamma\,. \tag{2.41}$$

As $\gamma = 3/2 + \beta$ and B evolve slowly with Re_λ, their expressions remain speculative and would require a much larger range of Reynolds numbers to be validated.

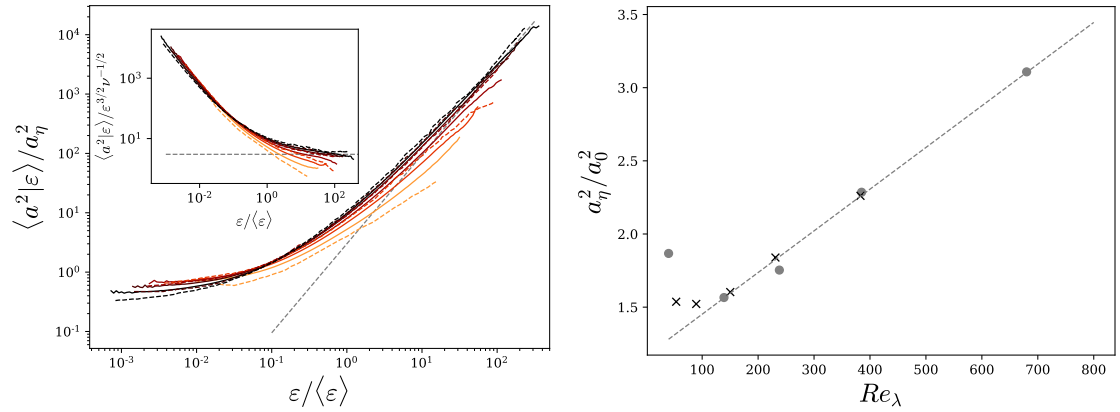

Figure 2.8: (Left) Acceleration variance conditioned on the local dissipation rate normalized by the Kolmogorov acceleration $\langle a^2|\varepsilon\rangle/a_\eta^2$. The continuous line are for our DNS for $Re_\lambda = 50$, 90, 150, 230 and 380 from orange to black; the dashed lines correspond to the DNS of Yeung et al. [271] for $Re_\lambda = 40$, 139, 238, 385, 680, from orange to black. Comparison with the power-law $(\varepsilon/\langle\varepsilon\rangle)^{3/2}$. Inset conditional acceleration normalized by $\varepsilon^{3/2}\nu^{-1/2}$. (Right) a_η^2/a_0^2 as a function of Re_λ with $a_0^2 = \lim_{\varepsilon\to 0}\langle a_i^2|\varepsilon\rangle$ the acceleration variance in low dissipative regions. Gray dots for the DNS of Yeung et al., black crosses for our DNS. Comparison with the line $0.0028Re_\lambda + 1.16$ in dashed lines.

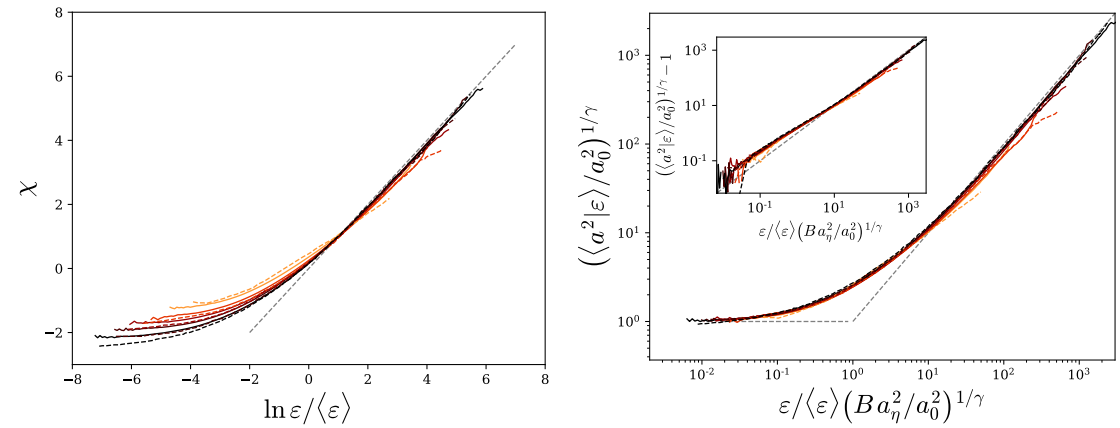

Figure 2.9: (Left) Evolution of $\chi = \dfrac{1}{\gamma}\ln(1/B\,\langle a^2|\varepsilon\rangle/a_\eta^2)$, with $\gamma = 3/2+\beta$ versus $\ln\varepsilon/\langle\varepsilon\rangle$ with $B = B_0 + B_1/\ln(Re_\lambda)$ and $\beta = \beta_1/\ln(Re_\lambda)$ and $B_0 = 17.1$, $B_1 = -54.7$ and $\beta_1 = -1$, for various Re_λ: continuous line for our DNS at $Re_\lambda = 50$, 90, 150, 230 and 380 from orange to black; and dashed lines correspond to the DNS of Yeung et al. [271] for $Re_\lambda = 40$, 139, 238, 385, 680, from orange to black. Comparison with the line $\chi = \ln\varepsilon/\langle\varepsilon\rangle$ in gray dashed line. (Right) Evolution of $\left(\langle a^2|\varepsilon\rangle/a_0^2\right)^{1/\gamma} = \exp(\chi-\chi_0)$ against $\zeta = \varepsilon/\langle\varepsilon\rangle\left(Ba_\eta^2/a_0^2\right)^{1/\gamma}$ for the various Reynolds numbers. Inset: plot of $\left(\langle a^2|\varepsilon\rangle/a_0^2\right)^{1/\gamma}-1$ against $\zeta = \varepsilon/\langle\varepsilon\rangle\left(Ba_\eta^2/a_0^2\right)^{1/\gamma}$.

2.3.4 Reynolds number dependence of the unconditional acceleration variance

Assuming the distribution of the dissipation, we can integrate relation (2.41) to obtain the unconditional variance

$$\langle a^2 \rangle = \int \langle a^2 | \varepsilon \rangle P(\varepsilon) d\varepsilon \ , \tag{2.42}$$

and thus propose an alternative formula to the empirical relations proposed in Refs. [271, 241, 103]. We consider that $\varepsilon/\langle\varepsilon\rangle$ presents a log-normal distribution with parameter $\sigma^2 \approx 3/8 \ln Re_\lambda/R_c$ with $R_c = 10$ as shown by Ref. [271] from DNS data, consistently with the proposition of Kolmogorov and Oboukhov [128, 192]. Notice nevertheless that other expressions for σ^2 have been proposed in the literature reflecting the vanishing viscosity limits [49]. Taking for $\langle a^2|\varepsilon\rangle$ the expression (2.41), we perform the integration numerically with the expression (2.33) and (2.34) for β and B with the values of B_0, B_1 and β_1 and the expression of a_0^2/a_η^2 proposed above. The resulting evolution of the acceleration variance with the Reynolds number is presented in Fig. 2.10. It is seen that the predicted acceleration variance is in very good agreement with the DNS of Ref. [271], our DNS, as well as the DNS of [42][4] and is also very close to the relation proposed by Ref. [241] for $Re_\lambda < 1000$.

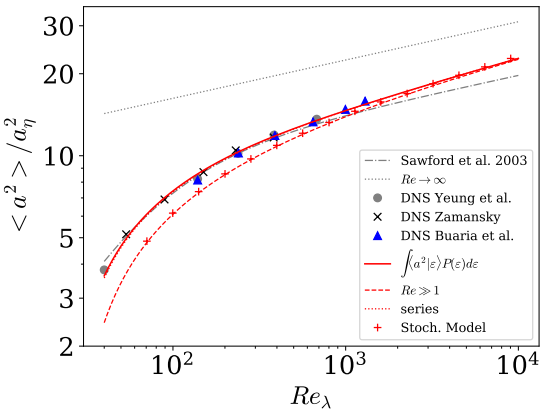

Figure 2.10: Evolution of the acceleration variance normalized by the Kolmogorov acceleration with the Reynolds number. From our DNS data (black crosses), the DNS data from [271] (gray dots), the DNS data from [42] (blue triangles) and from the stochastic model (red plus) and comparison with the relation $3 \times 1.9 Re_\lambda^{0.135}(1 + 85 Re_\lambda^{-1.35})$ from [241] (gray dash dot line), with the numerical integration of $\langle a^2 \rangle = \int \langle a^2|\varepsilon\rangle P(\varepsilon) d\varepsilon$ with $\langle a^2|\varepsilon\rangle$ given by (2.41) and $P(\varepsilon)$ log-normal (continuous red line), with its approximation of (2.45) (red dotted lines), with the large-Reynolds number limit relation (2.44) (red dashed line) and with the asymptotic power-law (2.46) (gray dotted lines).

The first term within the brackets in Eq. (2.41) is the footprint of the large-scale structures whose effects are vanishing if the local dissipation rate is larger than $\varepsilon/\langle\varepsilon\rangle \gg (B\, a_\eta^2/a_0^2)^{-1/\gamma}$ and therefore can be neglected when the Reynolds number is large since $a_\eta^2/a_0^2 \sim Re_\lambda$.

[4] It worth noting that the Ref. [42] was published after the presentation of results in Ref. [274]. We can thus see a stronger validation in the agreement between the model and the DNS of Ref. [42] over a larger range of Reynolds number than the one initially available.

Hence, for large Reynolds numbers, Eq. (2.41) reduces to:

$$\langle a^2|\varepsilon\rangle/a_\eta^2 = B\left(\frac{\varepsilon}{\langle\varepsilon\rangle}\right)^\gamma . \tag{2.43}$$

With this expression, the acceleration variance is simply estimated from the moments of the log-normal distribution as:

$$\frac{\langle a^2\rangle}{a_\eta^2} = B\left(Re_\lambda/R_c\right)^{9/64+3\beta(1+\beta/2)/8} . \tag{2.44}$$

This expression, also presented in Fig. 2.10, is shown to converge to the previous estimate as the Reynolds number increases.
In appendix of [274], we show that the integral (2.42) can be expressed from the generalized binomial series expansion. We further obtain the following estimation for the acceleration variance keeping only the first two terms:

$$\frac{\langle a^2\rangle}{a_\eta^2} = B\left(\frac{Re_\lambda}{R_c}\right)^{3/16\gamma(\gamma-1)}\left(1+\gamma\left(\frac{1}{B}\frac{a_0^2}{a_\eta^2}\right)^{1/\gamma}\left(\frac{Re_\lambda}{R_c}\right)^{-3/8(\gamma-1)}\right) . \tag{2.45}$$

In Fig. 2.10, it is seen that this relation almost overlaps with the direct numerical calculation of the variance through Eq. (2.42). The term within the brackets enables us to measure the contribution from small Reynolds number effects. At $Re_\lambda \approx 100$, the two estimates (2.44) and (2.45) for the variance differ by about 20%, while there is about 8% in difference at $Re_\lambda \approx 500$. That confirms that the term containing a_0^2 is indeed vanishing at large Reynolds numbers.
The previous estimations of the acceleration variance tend asymptotically to the following power-law:

$$\langle a^2\rangle/a_\eta^2 = 7.62 Re_\lambda^{9/64} , \tag{2.46}$$

where we have used Eq. (2.33) to obtain the value of the prefactor, $R_c^{-9/64} B_0 \exp(3\beta_1/8) \approx 7.62$. This expression is presented as well in Fig. 2.10, confirming that the convergence toward the power-law is very slow, and that Eq. (2.44) should be considered as an intermediate asymptotic expression for the acceleration variance.

2.3.5 Multiplicative cascade for the acceleration

Substituting Eq. (2.43) into Eq. (2.28), we can eventually estimate the doubly conditional acceleration variance for large Reynolds numbers as:

$$\langle a^2|\varepsilon, K\rangle/a_\eta^2 = C\exp(\alpha K/\langle K\rangle)\left(\frac{\varepsilon}{\langle\varepsilon\rangle}\right)^\gamma , \tag{2.47}$$

where $C = A\,B$, with expressions of A and B determined above.
As mentioned above and apparent in the previous formula, the acceleration depends on the local value of the kinetic energy, along with the local dissipation rate. The acceleration, being mainly due to the pressure gradient, it presents a nonlocal behavior. The fact that the acceleration depends on the local kinetic energy but not on a local Reynolds number reflects that its nonlocality is a purely kinematic effect. Further, the exponential dependence on the kinetic energy suggests that the acceleration can respond to the structures of all sizes.

To illustrate this point, we discuss a multiplicative cascade model for the acceleration that incorporates the effect of the full spectrum of the flow structure. Fluctuations of the locally-space-averaged dissipation rate can be modeled by multiplicative cascades [270, 127, 178, 157, 25, 80]. Such model proposes to express the local dissipation over a volume of size $\ell = L\lambda^n$, with $\lambda < 1$ and L being the large-scale of the flow, as the product of n random numbers ξ_i:

$$\varepsilon_\ell = \langle\varepsilon\rangle \prod_{i=1}^{n} \xi_i \,. \tag{2.48}$$

Typically, for large n, this yields log-normal distribution of ε_ℓ assuming the ξ_i are independent and identically distributed (and have as well finite variance).
We propose likewise to write the squared acceleration, coarse-grained at scale ℓ, as :

$$a_\ell^2 = a_0^2 \prod_{i=1}^{n} \theta_i \,. \tag{2.49}$$

The scale-to-scale factor θ_i is given by:

$$\theta_i = \exp\left(\frac{\alpha}{\langle K\rangle}\frac{1}{2}v_i^2\right)(\xi_i)^\gamma = \exp\left(\frac{\alpha}{\langle K\rangle}\frac{1}{2}v_i^2 + \gamma\ln\xi_i\right) , \tag{2.50}$$

where v_i is here the velocity of eddies of size $\ell_i = L\lambda^i$, which is also a fluctuating quantity. The exponential modulation is then interpreted as an entrainment acceleration due to these structures.
With this expression we obtain:

$$a_\ell^2 = a_0^2 \exp\left(\frac{\alpha}{\langle K\rangle}\sum_{i=1}^{n}\frac{1}{2}v_i^2 + \gamma\sum_{i=1}^{n}\ln\xi_i\right) . \tag{2.51}$$

Setting $n = \ln(\eta/L)/\ln(\lambda) \sim \ln Re_\lambda$, η being the Kolmogorov length scale, we have $K = \sum_{i=1}^{n}\frac{1}{2}v_i^2$ due to the additive nature of the kinetic energy. Thereby using Eq. (2.48), we obtain back Eq. (2.47) by taking the conditional average of Eq. (2.51). The order of magnitude of the eddy velocities can be estimated from the Kolmogorov relation, $(\varepsilon_\ell\ell)^{1/3}$, showing that the sum is *a priori* dominated by the large-scales but, on the other hand, because of the intermittent behavior of ε_ℓ, it may well happen that the inertial-scale structures can be dynamically important.
Note that in this multiplicative model, we have transposed the statistical relation (2.47) to an instantaneous version. Such idealization, find support in the invariance of the conditional PDF, which is shown in appendix of [274]. Another important point to mention is that although we assume that the local acceleration depends both on K and ε it is not assumed that those two variables are independent.
The dissipation presents large fluctuations leading to very important accelerations and, even if the acceleration orientation is changing rapidly, it can cause a local increase of the velocity. When the kinetic energy becomes significantly larger than its averaged value, then the modulation of the acceleration by the exponential term becomes preponderant, thus offering a feedback mechanism allowing obtaining the normal fluctuations of the velocity. This dynamic scenario appears consistent with the recent DNS analysis of Ref. [197] showing that the fluid-particles can undergo energy gains in intense dissipative regions and is developed in the next section.

2.4 Stochastic modeling of the fluid-particle dynamics

2.4.1 Model formulation

The foregoing multiplicative model suggests that the acceleration norm can be determined from the local kinetic energy and dissipation rate. The relation (2.47) is pointwise and so it applies equally well to both Lagrangian and Eulerian descriptions. However, in the Lagrangian framework, the kinematic relation between velocity and acceleration allows proposing a model for the acceleration depending only on the local dissipation rate. The evolution of the later along the particle path is to be obtained from a stochastic process. For the derivation of this model, we will rely on the relation (2.47), in which the contribution from low dissipative events is neglected:

$$a^2 = f(K,\varepsilon) = a_\eta^2 C \left(\frac{\varepsilon}{\langle\varepsilon\rangle}\right)^\gamma \exp\left(\alpha\frac{K}{\langle K\rangle}\right) . \tag{2.52}$$

We express the increments of a^2 as a second order Taylor expansion in K and ε,

$$da^2 = a^2\left(\alpha\frac{dK}{\langle K\rangle} + \gamma\frac{d\varepsilon}{\varepsilon} + \frac{\alpha^2}{2}\frac{dK^2}{\langle K\rangle^2} + \frac{\gamma(\gamma-1)}{2}\frac{d\varepsilon^2}{\varepsilon^2} + \gamma\alpha\frac{dK}{\langle K\rangle}\frac{d\varepsilon}{\varepsilon}\right) . \tag{2.53}$$

We consider ε as stochastic variable reflecting the very large number of degrees of freedom that control them. In a fairly general way, we consider that the dissipation ε follows a multiplicative stochastic process:

$$d\varepsilon = \varepsilon\Pi dt + \varepsilon\Sigma dW , \tag{2.54}$$

where dW are the increments of the Wiener process ($\langle dW\rangle = 0$; $\langle dW^2\rangle = dt$). We specify the terms Π and Σ below. Substituting Eq. (2.54) into Eq. (2.53) one obtains, following the Ito calculus, at first order in dt :

$$da^2 = a^2\left[\frac{\alpha}{\langle K\rangle}P + \gamma\Pi + \frac{\gamma(\gamma-1)}{2}\Sigma^2\right]dt + \gamma a^2\Sigma dW . \tag{2.55}$$

We used the identity $dK = u_i du_i = u_i a_i dt = Pdt$, where P is the mechanical power per unit of mass exchanged by the fluid particle. Even if Π and Σ are given, eq. (2.55) is not closed, as it remains to estimate $P = a_i u_i$, which requires the knowledge of a_i and u_i.
As mentioned in the introduction, we introduce a vectorial stochastic model for the dynamics of a fluid particle. We are looking for a stochastic process of the form:

$$du_i = a_i dt , \tag{2.56}$$
$$da_i = M_i dt + D_{ij} dW_j , \tag{2.57}$$

where dW_j are the increments of the jth component of a tridimensional Wiener process ($\langle dW_j\rangle = 0$; $\langle dW_i dW_j\rangle = dt\delta_{ij}$). *a priori*, the vector M and the tensor D depend on the vectors a and $u = \int a dt$. Indeed, M must depend on u to allow the particle velocity to reach a statistically steady state.
Now, we propose expressions for M_i and D_{ij}. For this, we want to impose, on the one hand, that the model is isotropic ($\langle a_i a_j\rangle = 0$ for $i \neq j$) and, on the other hand, that

its norm $a^2 = a_i a_i$ is compatible with the Eq. (2.55). We therefore write the stochastic equation for $a_{ij}^2 = a_i a_j$ derived from Eq. (2.57), thanks to the Ito formula:

$$\begin{aligned} da_{ij}^2 &= a_j da_i + a_i da_j + da_i da_j \\ &= (M_i a_j + M_j a_i + D_{ik} D_{jk})\, dt + (a_j D_{ik} + a_i D_{jk})\, dW_k \,. \end{aligned} \tag{2.58}$$

For the square of the norm $a^2 = a_i a_i$, we have:

$$da^2 = (2a_i M_i + D_{ij} D_{ij})\, dt + 2a_i D_{ij} dW_j \,. \tag{2.59}$$

We then proceed by identification between Eqs. (2.59) and (2.55), in a similar way as Refs. [89, 195], by identifying first the square of the diffusion term and then the drift term.

Identification of the diffusion term and the maximum winding hypothesis

Quite generally, we can decompose the diffusion tensor into:

$$D_{ij} = c_1 \delta_{ij} + S_{ij} + \Omega_{ij} \,, \tag{2.60}$$

where S_{ij} is a zero-trace symmetric tensor and Ω_{ij} is an antisymmetric tensor. The latter can be written as $\Omega_{ij} = \epsilon_{ijk}\omega_k$ with ϵ_{ijk} the Levi-Civita permutation symbol and ω_k a pseudovector. S_{ij} must be zero in order to guarantee the statistical isotropy of the acceleration. But Ω_{ij} can be different from 0. Indeed, the experimental results of Ref. [181] and numerical results of Ref. [199] have shown that the acceleration presents a scale separation between the evolution of the components and its norm, and that this separation can be modeled using processes for the acceleration norm and its orientation vector [276, 92, 228]. A stochastic model for orientation can be formulated as a diffusion process with a rotational part in the diffusion tensor [92, 266]. Since the model for the dynamics (2.56) - (2.57) involves only two vectors, a and u, we propose to form the pseudovector ω from these two vectors in order to get a closed model: $\omega_k = c_2 \epsilon_{klm} a_l u_m$. The model remains statistically isotropic and the chirality of the flow is not broken either since the odd moments of dW_j are zero (Gaussian with zero mean). In other words, the sign of c_2 does not matters. We then have:

$$D_{ij} = c_1 \delta_{ij} + c_2 (a_i u_j - a_j u_i) \,. \tag{2.61}$$

It is to be noted that c_1 and c_2 are not constant.
By identifying the square of the diffusion term between (2.55) and (2.59) we find

$$\gamma^2 (a^2)^2 \Sigma^2 = 4 a_i a_j D_{ik} D_{jk} \,. \tag{2.62}$$

Expanding it by using expression (2.61), we find

$$\gamma^2 (a^2)^2 \Sigma^2 = 4a^2 (c_1^2 + c_2^2 (2a^2 K - P^2)) \,, \tag{2.63}$$

which gives for c_1:

$$c_1^2 = \frac{\gamma^2}{4} a^2 \Sigma^2 - c_2^2 (2a^2 K - P^2) = a^2 \left(\frac{\gamma^2}{4} \Sigma^2 - 2c_2^2 K \left(1 - \frac{a_T^2}{a^2} \right) \right) \,, \tag{2.64}$$

where we have introduced the tangential acceleration a_T, as the projection of the acceleration vector in the direction of the velocity vector: $a_T = a_i u_i/\sqrt{u^2} = P/\sqrt{2K}$. Equation (2.64) imposes a constraint on c_2 to guarantee the positivity of c_1^2:

$$c_2^2 2K \leq \frac{\gamma^2}{4}\Sigma^2\,, \tag{2.65}$$

since $0 \leq 1 - \dfrac{a_T^2}{a^2} \leq 1$. So, to guarantee the positivity of c_1^2 whatever K, c_2^2 must be proportional to $1/K$. Introducing a parameter c_R as $c_2^2 = \dfrac{\gamma^2}{4}\Sigma^2\dfrac{c_R^2}{2K}$, with the constraint $c_R^2 \leq 1$, we obtain

$$c_1^2 = \frac{\gamma^2}{4}\Sigma^2\left(a^2(1-c_R^2) + c_R^2 a_T^2\right)\,. \tag{2.66}$$

Subsequently, we only consider the limit $c_R = 1$ that corresponds to the maximum rotational part of the diffusion tensor. We will discuss this choice in more detail below in Sec. 2.4.3, when presenting the results.
Finally, from Eq. (2.61) and the expressions of c_1 and c_2, we write the components of the diffusion tensor as

$$D_{ij} = \sqrt{\frac{\gamma^2}{4}\Sigma^2}\left[\sqrt{a_T^2}\delta_{ij} + \sqrt{a_N^2}\epsilon_{ijk}b_k\right]\,, \tag{2.67}$$

where we introduced the normal component a_N of the acceleration $a_N^2 = a^2 - a_T^2$, and the bi-normal unit vector[5] $b_k = \epsilon_{klm}u_l a_m/|\epsilon_{hij}u_i a_j|$.
Note that b_k, a_T and a_N are not well defined when $K = 0$. However, c_2 must vanish when $u = 0$ and we can therefore consider that $c_R = 0$ in that case.

Determination of the drift term

Identifying the drift term between Eqs. (2.59) and (2.55), we get:

$$2a_i M_i + D_{ij}D_{ij} = a^2\left(\frac{\alpha}{\langle K\rangle}P + \gamma\Pi + \frac{\gamma(\gamma-1)}{2}\Sigma^2\right)\,. \tag{2.68}$$

From Eq. (2.67) the term $D_{ij}D_{ij}$ is computed as [6]

$$D_{ij}D_{ij} = \frac{\gamma^2}{4}\Sigma^2\left(2a^2 + a_T^2\right)\,. \tag{2.69}$$

We then have

$$a_i M_i = a^2\left(\frac{\alpha}{2\langle K\rangle}P + \frac{\gamma}{2}\Pi - \frac{\gamma}{4}\Sigma^2\right) - a_T^2\frac{\gamma^2}{8}\Sigma^2\,. \tag{2.70}$$

[5] To obtain this relation we notice that $a_i u_j - a_j u_i = \epsilon_{ijk}\epsilon_{klm}a_l u_m$ and that the vector b_k is the unit vector collinear to $\epsilon_{klm}a_l u_m$: $b_k = \epsilon_{klm}a_l u_m/|\epsilon_{hij}a_i u_j|$. By expanding the norm, we have: $(\epsilon_{hij}a_i u_j)^2 = 2a^2K - P^2$. We therefore write: $\epsilon_{klm}a_l u_m = b_k\sqrt{2a^2K - P^2} = b_k\sqrt{2K}\sqrt{a^2 - a_T^2} = b_k\sqrt{2K}\sqrt{a_N^2}$.

[6] $D_{ij}D_{ij} = \dfrac{\gamma^2}{4}\left(a_T^2\underbrace{\delta_{ij}\delta_{ij}}_{3} + a_N^2\underbrace{\epsilon_{ijk}b_k\epsilon_{ijl}b_l}_{2\delta_{kl}b_k b_l}\right)$, $\delta_{kl}b_k b_l = 1$ since b is a unit vector and with $a^2 = a_T^2 + a_N^2$, we obtain the result.

To go further we must now specify the terms Π and Σ used for the stochastic process for ε. Various models for the dissipation have been proposed. Pope and Chen [203] proposed a simple model based on the exponential of an Orstein-Uhlenbeck process (see (2.18)). Here, we rely on the model proposed in Refs. [54, 195]. This non-Markovian log-normal model presents a logarithmic decrease in the correlation of ε which is consistent with the idea of a turbulent cascade and a multiplicative process (see (2.22)), unlike the Pope and Chen model which gives an exponential decrease, see also the discussion in Ref. [146]. As presented in (2.24)-(2.25), the drift and diffusion terms are written, respectively, as:

$$\Pi = \frac{1}{\tau_\varepsilon}\Big(- \ln \frac{\varepsilon}{\langle\varepsilon\rangle} + \frac{\sigma^2}{2\Lambda^2}(\frac{\tau_\varepsilon}{\tau_c} - \Lambda^2) + \frac{\sigma}{\Lambda}\hat{\Gamma}\tau_\varepsilon\Big)\,, \tag{2.71}$$

and

$$\Sigma = \sqrt{\frac{\sigma^2}{\Lambda^2\tau_c}}\,, \tag{2.72}$$

with σ^2 the variance of the logarithm of ε, τ_ε the correlation time of ε, τ_c the regularization timescale of the process (taken equal to the Kolmogorov dissipative time τ_η), Λ^2 a normalization factor, and $\hat{\Gamma}$ the convolution of the Wiener increments with a temporal kernel, ensuring the non-markovian property of the process. In the process for ε proposed by Refs. [54, 195], the latter corresponds to a fractional Gaussian noise with 0 Hurst exponent [159] regularized at scale τ_c. The expression of the convolution kernel proposed by Refs. [54, 195], (see (2.23)), applies to a scalar noise since the dissipation rate is a scalar, whereas the acceleration model involves a vectorial noise. Therefore, the kernel in $\hat{\Gamma}$ includes a projection in order to apply to the vectorial Wiener increments:

$$\hat{\Gamma} = -\frac{1}{2}\int_{-\infty}^{t} \frac{1}{(t-s+\tau_c)^{3/2}}\mathcal{P}_j dW_j(s)\ . \tag{2.73}$$

By proceeding in a similar way as Ref. [195], the projection operator is obtained by identification between the diffusion terms of Eqs. (2.55) and (2.59):

$$\mathcal{P}_j = \frac{2a_i D_{ij}}{\gamma a^2 \Sigma} = \frac{\sqrt{a_T^2} - a_T}{a^2}a_j + e_j \tag{2.74}$$

where we have used the relation recall in footnote 5 and where e_j is the unit vector tangent to the trajectory, $e_i = u_i/\sqrt{2K}$. It is interesting to remark that the rotational part of the diffusion tensor induces an asymmetry of the projector between positive and negative power exchange (recall that $P = \sqrt{2K}a_T$). Indeed for $P \geq 0$, $\mathcal{P}_j = e_j$ while for $P < 0$ one has $\mathcal{P}_j = (1-2p^2)e_j - 2p\sqrt{1-p^2}b_j$ with $p = P/\sqrt{2Ka^2}$. In both cases, as it can be readily checked, $\mathcal{P}$ is a unit vector.
Substituting the expressions (2.71) and (2.72) for Π and Σ in Eq. (2.70) we have

$$a_i M_i = a^2\left(\frac{\alpha}{2\langle K\rangle}P - \frac{\gamma}{2\tau_\varepsilon}(\ln\frac{\varepsilon}{\langle\varepsilon\rangle} + \frac{1}{2}\sigma^2 - \frac{\sigma}{\Lambda}\hat{\Gamma}\tau_\varepsilon)\right) - a_T^2\frac{\gamma^2}{8}\frac{\sigma^2}{\Lambda^2\tau_c}\,. \tag{2.75}$$

According to Eq. (2.52), we can write:

$$\ln\left(\frac{\varepsilon}{\langle\varepsilon\rangle}\right) = \frac{1}{\gamma}\left(\ln\frac{a^2}{a_\eta^2} - \ln C - \alpha\frac{K}{\langle K\rangle}\right)\,, \tag{2.76}$$

which gives, once substituted into Eq. (2.75),

$$a_i M_i = a^2 \left[\frac{\alpha}{2\langle K\rangle}\left(P + \frac{K}{\tau_\varepsilon}\right) - \frac{1}{2\tau_\varepsilon}\left(\ln(\frac{a^2}{a_\eta^2}) \underbrace{- \ln C + \frac{\gamma}{2}\sigma^2 - \gamma\frac{\sigma}{\Lambda}\hat{\Gamma}\tau_\varepsilon}_{-\hat{\Gamma}_*} \right) \right] - \frac{a_T^2}{\tau_c}\underbrace{\frac{\gamma^2}{8}\frac{\sigma^2}{\Lambda^2}}_{\sigma_*^2} . \tag{2.77}$$

To simplify the notations, we have introduced $\hat{\Gamma}_* = \gamma\frac{\sigma}{\Lambda}\hat{\Gamma}\tau_\varepsilon + \ln C - \frac{\gamma}{2}\sigma^2$ and $\sigma_*^2 = \frac{\gamma^2}{8}\frac{\sigma^2}{\Lambda^2}$.
It is interesting to notice that in Eq. (2.77) the terms $P + \frac{K}{\tau_\varepsilon} = \frac{dK}{dt} + \frac{K}{\tau_\varepsilon}$ acts as a penalization leading the correlation of the kinetic energy to decay exponentially.
We then propose for M_i an expression compatible with Eq. (2.77). Proceeding by identification, we have the following relation:

$$\begin{aligned} M_i &= \frac{\alpha}{2\langle K\rangle}\left(\lambda a_i P + (1-\lambda)a^2 u_i + a_i\frac{K}{\tau_\varepsilon}\right) \\ &\quad - a_i\left(\ln(\frac{a^2}{a_\eta^2}) - \hat{\Gamma}_*\right)\frac{1}{2\tau_\varepsilon} \\ &\quad - \frac{\sigma_*^2}{\tau_c}\frac{a_T^2}{a^2}a_i + B_i\,, \end{aligned} \tag{2.78}$$

where we have introduced the vector B_i, such that $B_i a_i = 0$ as well as the factor λ that both account for the indeterminacy inherent to the inverse projection. By assuming again that there are only two vectors at our disposal, we can take $B_i = \frac{\alpha}{2\langle K\rangle}\lambda'\left(P a_i - a^2 u_i\right)$ by introducing the factor λ'. Note that from the point of view of the projection, the factors λ and λ' are arbitrary in the sense that the scalar product of a_i and Eq. (2.78) gives Eq. (2.77) whatever their values. We can nevertheless notice that the terms involving λ and λ' can be combined, and, by noting $c_u = \lambda + \lambda'$, we get:

$$\begin{aligned} M_i &= \frac{\alpha}{2\langle K\rangle}\left(a_i(c_u P + \frac{K}{\tau_\varepsilon}) - (c_u - 1)a^2 u_i\right) \\ &\quad - a_i\left(\ln(\frac{a^2}{a_\eta^2}) - \hat{\Gamma}_*\right)\frac{1}{2\tau_\varepsilon} \\ &\quad - \frac{\sigma_*^2}{\tau_c}\frac{a_T^2}{a^2}a_i\,. \end{aligned} \tag{2.79}$$

We can notice that the terms of the first line correspond to the coupling with the velocity, those of the second take into account the log-normal and non-Markovian character of the dissipation and the last term is due to the rotational part of the diffusion tensor. The diffusion term (2.67) becomes, by using expression (2.72),

$$D_{ij} = \sqrt{\frac{2\sigma_*^2}{\tau_c}}\left[\sqrt{a_T^2}\delta_{ij} + \sqrt{a_N^2}\epsilon_{ijk}b_k\right] . \tag{2.80}$$

We have thus specified our stochastic model for the dynamics of a fluid particle. It is given by Eqs. (2.56), (2.57), (2.79) and (2.80).

2.4.2 Parameters and numerical approach

From a dimensional point of view, to determine the physical parameters of the stochastic model, one must specify time and velocity scales as well as a Reynolds number. This amounts for example to imposing the average kinetic energy $\langle K \rangle$, the average dissipation rate $\langle \varepsilon \rangle$ and the viscosity ν. From these physical parameters, we calculate $a_\eta^2 = \langle \varepsilon \rangle^{3/2} \nu^{-1/2}$, $\tau_\eta = \langle \varepsilon \rangle^{-1/2} \nu^{1/2}$. We can also get the Reynolds number based on the Taylor scale $Re_\lambda = u' \lambda / \nu = 2\sqrt{15}/3 \, \langle K \rangle / \sqrt{\langle \varepsilon \rangle \nu}$ with $u' = \sqrt{2\langle K \rangle / 3}$ and $\lambda^2 = 15 \nu u'^2 / \langle \varepsilon \rangle$. We then deduce the Lagrangian integral times scale τ_L as $\tau_L = 0.08 Re_\lambda \tau_\eta$ from the DNS results reported by Refs. [101, 238].

The parameter σ^2 is estimated using the relation given by Ref. [271]: $\sigma^2 \approx 3/8 \ln Re_\lambda / R_c$ with $R_c \approx 10$ compatible with the prediction of Kolmogorov and Obhoukov [128, 192]. As mentioned in Refs. [128] and [178], the specific value of R_c is depending on the large-scales. Since the influence of the large-scales is neglected in our modeling (see Sec. 2.3.4), we choose in the following simply $\sigma^2 \approx 3/8 \ln Re_\lambda$. We set as well $\alpha = 1/3$ and $\gamma = 3/2 + \beta$ with $\beta = -1/\ln Re_\lambda$ in accordance with the results of the DNS presented above. The prefactor C is computed as $C = c_0 \, A \, B$ where $A = \left(1 - \frac{2}{3}\alpha\right)^{3/2} \approx 0.686$, $B = 17.1 - 54.7/\ln Re_\lambda$ as determined by DNS. The term c_0 is introduced so that the predicted acceleration variance follows Eq. (2.44), as one would expect from the construction of the stochastic model, despite the fact that we take $\sigma^2 = 3/8 \ln Re_\lambda$ instead of $\sigma^2 = 3/8 \ln Re_\lambda / R_c$. Consequently, we have $c_0 = (1/Re_c)^{9/64 + 3\beta/8(1+\beta/2)}$.

For simplicity we have used $\tau_c = \tau_\eta$ and $\tau_\varepsilon = \tau_L$. From τ_ε and τ_c we calculate the value of the normalizing constant Λ as explained after (2.23). Finally, for the parameter c_u, which is the only free parameter of the model, we have determined numerically that with $c_u = 5.22$ the ratio $K/\langle K \rangle$ is 1 on average for all values of the Reynolds number.

The sample paths of this model are obtained by numerical integration of the stochastic differential equation. Numerical integration is made with an explicit Euler scheme by taking a time-step $dt = \tau_{\eta,min}/100$ with $\tau_{\eta,min} = \sqrt{\nu/\varepsilon_{max}}$, an estimation of the minimum dissipative timescale likely to happen during the simulation. This is estimated from the log-normal distribution of the dissipation: $\tau_{\eta,min} = \tau_\eta \exp(-x\sigma/2 + \sigma^2/4)$, with $x = 6$ by considering that the probability that a random number following the normal distribution reaches a value of 6 standard deviation is sufficiently low (see Eq. (2.17)).

For the calculation of the convolution term $\hat{\Gamma}$ appearing in Eq. (2.79), we propose in appendix of [274] an efficient algorithm. Note also that a simple Python script presenting the algorithm used to integrate the proposed stochastic model is available in supplemental material of Ref. [274].

2.4.3 Results

We show in Fig. 2.11 a realization of this process for $Re_\lambda = 1100$. We see the temporal evolution of the components of acceleration and velocity. There is a very intermittent acceleration with an alternation of periods in which the acceleration of the fluid particle is almost zero with phases of very intense activity. This results in fluid-particle trajectories, obtained by integration of the velocity $x_i = \int u_i(t) dt$, in long quasiballistic periods with typical length of the order of the integral scale ($L \approx \langle K \rangle^{3/2} / \langle \varepsilon \rangle$) and short-term disruptions during which the trajectory rolls up on itself.

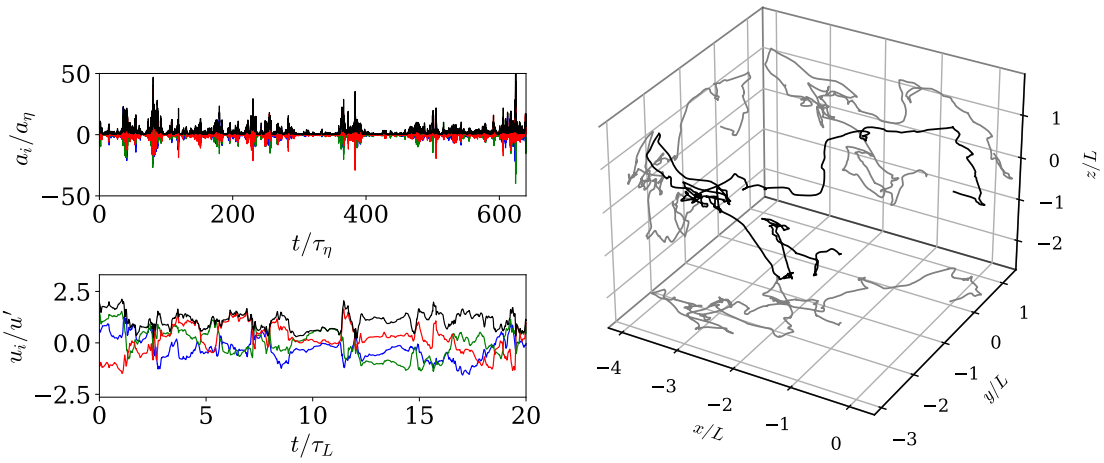

Figure 2.11: A realization of the stochastic process for $Re_\lambda = 1100$. Top left: evolution of the acceleration with time, a_x: red, a_y: green, a_z: blue, $|a|$: black. Bottom left: evolution of the velocity with time, u_x: red, u_y: green, u_z: blue, $|u|$: black. Right: 3D trajectory of a fluid particle for a duration of 100 τ_L.

We have simulated the stochastic model for 15 different Reynolds numbers between $Re_\lambda = 70$ and 9000. In each case, we have computed 26,000 realizations. The simulations are carried out over a period of $120\tau_L$, over which we exclude an initial transitional regime of $20\tau_L$ for the calculation of the statistics. In all cases, the initial value of the components of acceleration and velocity are sampled from the normal distribution having a standard deviation of $10^{-9}a_\eta$ for the acceleration and $10^{-9}\sqrt{2\langle K\rangle/3}$ for the velocity. We can indeed notice from Eqs. (2.79) and (2.80) that, if the acceleration is exactly zero, the stochastic model predicts that the acceleration would remain so. However, it should be noted that this event has a zero probability, and that for arbitrarily small, but nonzero, accelerations, the model presents evolution towards a nontrivial stationary state. This is illustrated in Fig. 2.12, which presents the temporal evolution of the variance of the velocity and of the acceleration for $Re_\lambda = 1100$, calculated from all the realizations.

Figure 2.13 shows the evolution with the Reynolds number of the mean kinetic energy in the stationary state. In this figure, we see that the average kinetic energy is equal, within the statistical convergence, to the value prescribed to the model. We note that the value of the average kinetic energy is directly related to the value of the parameter c_u in Eq. (2.79) as mentioned above.

Regarding the variance of the acceleration, we expect, by construction of the stochastic model, that the predicted value follows the log-normal relation (2.44). We observe in Fig. 2.10, that it is indeed the case, with only slight deviations for the largest Reynolds numbers which are attributed to numerical errors. We recall that the underestimation of the acceleration variance at small Reynolds numbers compared to the DNS or Eq. (2.45) stems from the fact that the model is based on the relation (2.47) in which the effect of low dissipative and large-scale structures are neglected (see the discussion in Sec. 2.3.3). This simplification enables us to obtain the analytical formulation of the model proposed here.

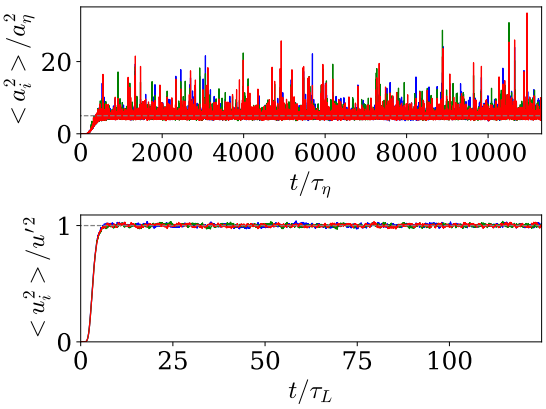

Figure 2.12: Evolution of the acceleration and velocity variance with time for the stochastic model at $Re_\lambda = 1100$ starting from an initial condition for the acceleration and velocity with very small magnitude. Comparison in dashed gray line with the expected values: Eq. (2.44) for the acceleration and the prescribe value of $u' = \sqrt{2\langle K \rangle / 3}$ for the velocity.

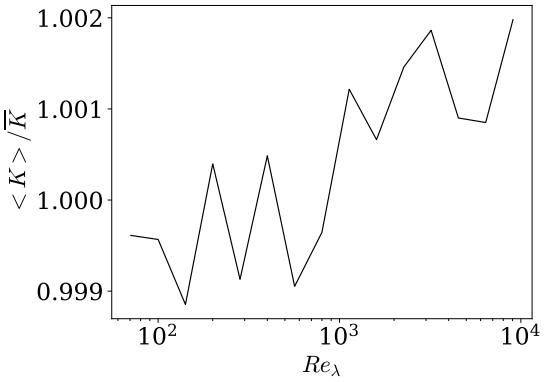

Figure 2.13: Evolution with the Reynolds number, in the stationary regime, of the kinetic energy obtained by the stochastic model normalized by the prescribed kinetic energy $\langle K \rangle$.

Figure 2.14 compares the autocorrelation of the components of the acceleration and of its norm calculated from the stochastic model for $Re_\lambda = 400$ with the calculations from the DNS of [140, 21]. It can be seen that the characteristic times of these two quantities are very different and that it is in good agreement with the DNS. It should be mentioned that the scale separation between the components and the norm results from the rotational part of the diffusion tensor. Indeed, no scale separation is found when c_R is set to zero in Eq. (2.66) (corresponding then to a diagonal diffusion tensor). We see in Eq. (2.67) that considering this rotational part, leads to the decomposition of the acceleration into its normal and tangential component. The former is associated with the intense rotation that rapidly changes the acceleration direction, whereas the second is associated with the variation of the kinetic energy of the particle.
Figure 2.14 also presents the evolution of the autocorrelation coefficient of the velocity components and of the power. It can be seen here also that the agreement with the DNS is relatively good. In Fig. 2.14, we also show the evolution of the characteristic correlation times for these four quantities with Reynolds numbers in the range $Re_\lambda = 70 - 9000$ as

predicted by the stochastic model. The characteristic correlation time for the velocity, the acceleration norm, the acceleration components and the power are $\tau_u = \int \rho_{u_i}(\tau)d\tau$, $\tau_{|a|} = \int \rho_{|a|}(\tau)d\tau$, $\tau_{a_i} = \int |\rho_{a_i}|(\tau)d\tau$ and $\tau_P = \int |\rho_P|(\tau)d\tau$. It can be seen in Fig. 2.14 that the scales for the norm of the acceleration and for the velocity normalized by τ_L remains quasiconstant with the Reynolds number and that the ratio between the correlation scale for the velocity and τ_L is of order 1. Note that the characteristic time entering the model formulation is τ_ε (the correlation time of the dissipation rate following the path of a fluid particle). For the calculation of the model, we simply set $\tau_\varepsilon = \tau_L$ arguing that the two quantities should be closed. It is therefore interesting to remark that the integral time of the velocity is very close to the prescribe one $\tau_u \approx \tau_L$. Regarding the correlation scales for a component of acceleration and for the power normalized by τ_L, they both present a variation close to $1/Re_\lambda$, as expected.

We also show in Fig. 2.14 autocorrelation coefficient of a_i, $(a^2)^{1/2}$, $P = a_i u_i$ and u_i for Reynolds numbers in the range $Re_\lambda = 70 - 9000$ obtained from the model. It is seen that, when the time shift is normalized by the corresponding integral timescale, the correlation coefficients of the power and of the acceleration component remains nearly unchanged with the Reynolds number. We observe as well that the shape of the autocorrelation obtained from DNS is well reproduced, although the decay predicted by the model is too fast at very short time lag. This is attributed to the fact that the dissipative region is only taken into account in the model via the cutoff $\tau_c = \tau_\eta$ of the kernel $\hat{\Gamma}$. We observe that the correlation for the acceleration norm presents a logarithmic decrease, reflecting the absence of characteristic time for its evolution. As expected, the correlation norm exhibits a lower slope as the Reynolds number increases. This is directly attributed to the use of the non-Markovian process of Ref. [54] for the dissipation rate, which proposes a logarithmic evolution of the autocorrelation in agreement with the underlying model of the turbulent energy cascade as discussed in section 2.1 (see figure 2.3).

The shape of the velocity correlation from the model is overall close to the DNS. At small τ, it presents some dependence on the Reynolds number, while at large time shift (*i.e.* τ of the order of τ_L) the correlation decreases exponentially, as it can be seen in the inset of Fig. 2.14(f), in agreement with DNS and experiments. The exponential relaxation results from the terms $P + K/\tau_\varepsilon = dK/dt + K/\tau_\varepsilon$ appearing in the drift part of the stochastic model (2.78). It is interesting to remark that the presence of this term in the model is a direct consequence of the exponential dependence of the conditional acceleration variance on the kinetic energy (2.47). This term leads to the Reynolds number dependence on the velocity correlation observed at small τ, which is connected to the logarithmic decorrelation of the acceleration norm, to vanish at large τ at which it relaxes exponentially. This suggests therefore anomalous scaling at intermediate time lag.

We show in Fig. 2.15 the velocity spectrum for Re_λ between 400 and 9000, which we compare with the DNS of Ref. [21] for $Re_\lambda = 400$. We see a good agreement between the DNS and the stochastic model. For higher Reynolds numbers, we clearly see that a power-law behavior develops at intermediate scales. We see that the slope of the power-law deviates from the Hinze spectra [256] predicted by dimensional arguments similar to those presented by Kolmogorov, with spectra less stiff than ω^{-2}. This shows that the proposed stochastic model leads to an anomalous scaling that reflects the persistent influence of the Reynolds number in the inertial-scales. We further notice that the slope that develops at intermediate scales are close to $-2 + 0.14$, where 0.14 is the exponent of the asymptotic power-law of the acceleration variance with the Reynolds number determined in Eq. (2.46)

(see also Fig. 2.10). We see here a confirmation of the relation between the acceleration scaling and the anomalous scaling of the velocity spectra proposed by Ref. [75].
We present in Fig. 2.16 the PDFs of the velocity and of the acceleration for $Re_\lambda = 400 \sim 9000$, as well as the comparison with the DNS of Ref. [21]. First, we find that the velocity distribution is very close to a Gaussian distribution for all Reynolds numbers, while the acceleration presents a much more stretched distribution. For $Re_\lambda = 400$ the acceleration PDF is in very good agreement with the DNS, and, the model predicts an increase of the stretching of the tails with increasing the Reynolds number. We also show in this figure the PDF of the velocity increments for different time shifts $\delta_\tau u_i = u_i(t+\tau) - u_i(t)$ at $Re_\lambda = 400$. We observe that the distribution gradually returns to a Gaussian distribution as the time shift increases, and that at each time shift the agreement with the DNS of Ref. [21] is very good. This is confirmed by the presentation of the flatness of the velocity increments for $Re_\lambda = 400 \sim 9000$, which reflects the strongly non-Gaussian behavior on small-scales which decreases to 3 for the larger-scales. Here also we notice a good agreement with the DNS of [21] for $Re_\lambda = 400$. We also show in the inset, a quasi-linear increase of the flatness of the acceleration with the Reynolds number.
Finally, in Fig. 2.17 we show the second and third moments of the power $P = a_i u_i$. It is observed that the increases of both moments with the Reynolds number are in close agreement with the power-law supported by the DNS results of Ref. [268], $\langle P^2 \rangle / \langle \varepsilon \rangle^2 \sim Re_\lambda^{4/3}$ and $-\langle P^3 \rangle / \langle \varepsilon \rangle^3 \sim Re_\lambda^2$. Clearly, the third order moment is negative, meaning that the time irreversibility of the dynamics of a fluid particle in a turbulent flow is correctly reproduced by the proposed stochastic model. The skewness of the power, $S = \langle P^3 \rangle / \langle P^2 \rangle^{3/2}$, seems to converge to -0.5 as the Reynolds number increases, as reported in Ref. [268].

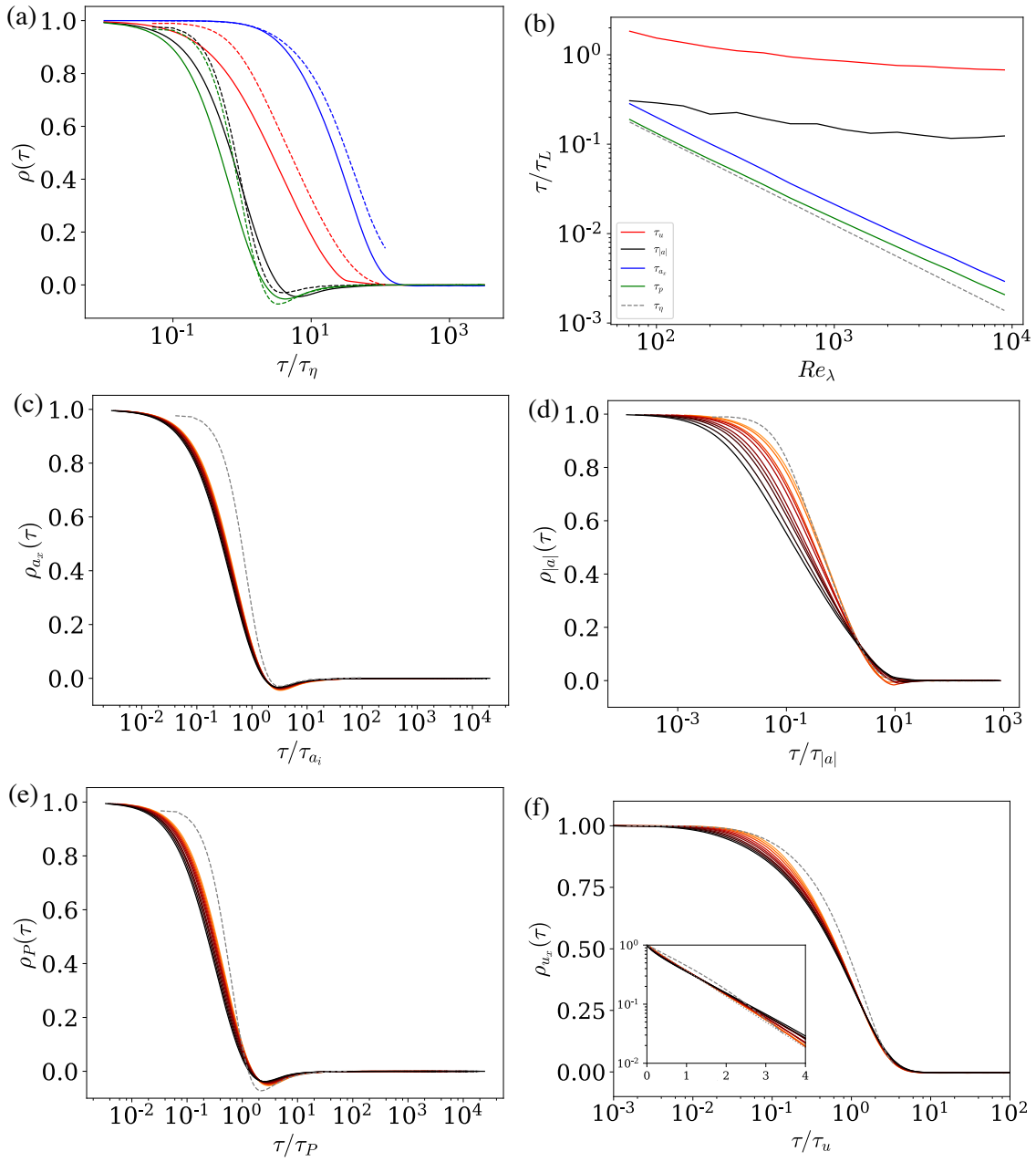

Figure 2.14: (a) Evolution of the autocorrelation of a_i (black), $(a^2)^{1/2}$ (red), u_i (blue) and $P = a_i u_i$ (green) from the stochastic model for $Re_\lambda = 400$ and comparison with the DNS data from Ref. [21] in dashed lines. (b) Evolution of the integral timescale of a_i (black), $(a^2)^{1/2}$ (red), u_i (blue) and $P = a_i u_i$ (green) normalized by τ_L with the Reynolds number. (c,d,e,f) Evolution of the autocorrelation of a_i, $(a^2)^{1/2}$, $P = a_i u_i$ and u_i respectively, for $Re_\lambda = 400$, 567, 800, 1130, 1600, 2263, 3200, 4526, 6400 and 9051 from orange to black and comparison with the DNS data from Ref. [21] in dashed lines. In these plots the time lag is normalized by the corresponding integral timescale. For panel f, inset: logarithmic scaling of the y-axis and comparison with $\exp(-\tau/\tau_u)$ in dotted line.

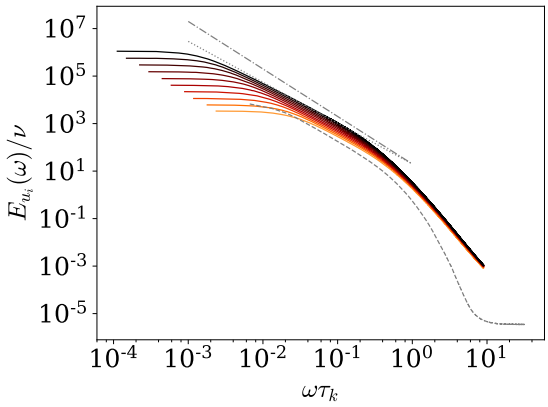

Figure 2.15: Velocity spectra from the stochastic model for $Re_\lambda = 400$ to $Re_\lambda = 9000$ from orange to black and comparison with the DNS data from [21] at $Re_\lambda = 400$ (gray dashed line), with the Hinze spectra ω^{-2} (gray dot-dashed line), and with the power-law with anomalous exponent $\omega^{-2+9/64}$ (gray dotted lines).

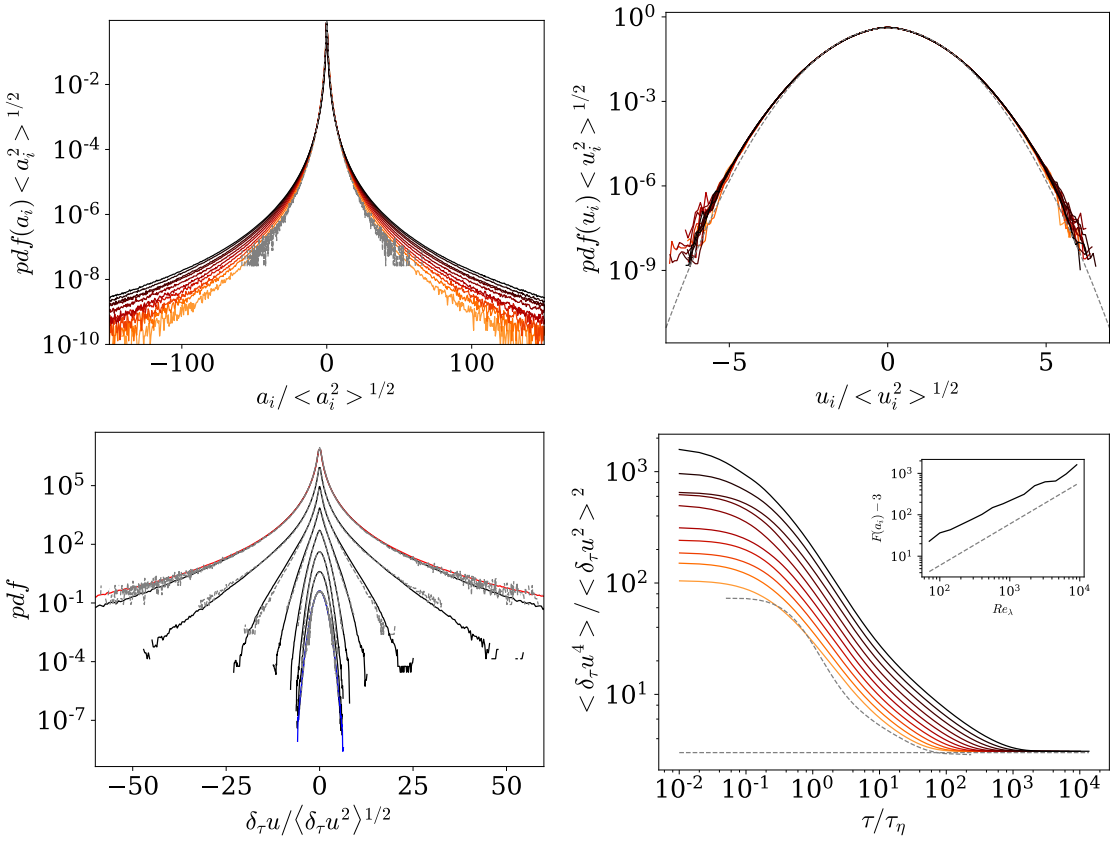

Figure 2.16: PDF of a_i(top left) and comparison with the DNS data from Ref. [21], and PDF of u_i (top right) and comparison with the normal distribution, for $Re_\lambda = 400$ to 9000 from orange to black. (Bottom left) PDF of the velocity increments for various times shift: $\tau/\tau_\eta = 610$, 200, 70, 22, 7.3, 2.4, 0.8 and 0.25 each time lag is shifted upward by one decade for $Re_\lambda = 400$ comparison with the PDF of the acceleration from the model (red) and from the DNS of Ref. [21] (gray) and the PDF velocity (blue). (Bottom right) Evolution of the Flatness of the velocity increments versus the time shift for $Re_\lambda = 70$ to 9000 from orange to black and evolution of the flatness of the acceleration with the Reynolds number and comparison with the linear law in the inset.

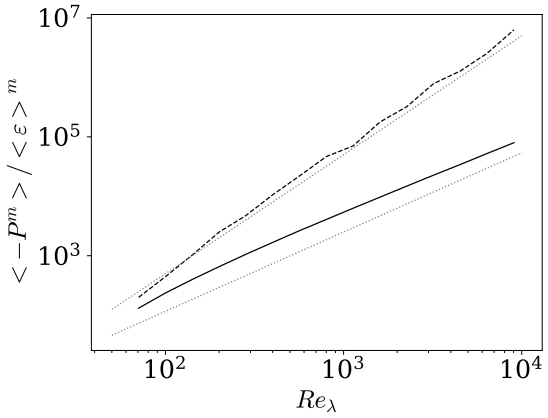

Figure 2.17: Evolution of $\langle P^2 \rangle / \langle \varepsilon \rangle^2$ (continuous black line) and $-\langle P^3 \rangle / \langle \varepsilon \rangle^3$ (dashed black line) with the Reynolds number, and comparison with the power-laws $Re_\lambda^{4/3}$ and Re_λ^2.

2.5 Discussion and perspectives

We have analyzed the behavior of the acceleration statistics conditioned on both local dissipation rate and local kinetic energy, which to our knowledge have not been considered before. We have reported that the doubly conditional variance is proportional to the acceleration variance conditional on the dissipation rate solely, with the proportionality factor depending exponentially on the kinetic energy: $\langle a^2|\varepsilon, K\rangle = A\exp(\alpha K/\langle K\rangle)\,\langle a^2|\varepsilon\rangle$. For large enough Reynolds number, we show that $A = (1-2\alpha/3)^{3/2}$ and we proposed that the α coefficient is independent of the Reynolds number and its value $\alpha = 1/3$ was obtained from the DNS.

This expression shows a direct effect of the kinetic energy, a large-scale quantity, on the Lagrangian acceleration. Furthermore since the argument of the exponential depends on $K/\langle K\rangle$, not on a local Reynolds number, it suggests a kinematic effect for the acceleration which may be due to the nonlocality of the pressure. More specifically, these effects can be due to the interaction of vorticity and strain [65]. In case of persistent large-scale strain, intense vorticity tube would be generated and align with the principal direction of the strain [175]. It was shown that such vortical structure can produce significant acceleration in the direction of the vorticity [17, 145]. Anyway, although the proper physical mechanism leading to the exponential dependence of the acceleration on the kinetic energy deserves further studies, it is an additional effect to the influence of the large-scales on the acceleration through the intermittency of the dissipation rate. To study this later effect, we subsequently have proposed to account for the Reynolds number dependence of the acceleration variance conditional on the dissipation rate within the intermediate asymptotic framework [13] leading to: $\langle a^2|\varepsilon\rangle = a_\eta^2 B(\varepsilon/\langle\varepsilon\rangle)^{3/2+\beta}$ for $\varepsilon \gg \langle\varepsilon\rangle$ with B and β depending logarithmically on the Reynolds number as the signature of the intermittency and the persistence of viscous effects. Further, we advance an expression for the conditional acceleration variance valid for the whole range of fluctuations of ε by accounting for the dominant effect of the large-scale structures in low dissipative regions (2.41). From this finding we determine the evolution of the unconditional acceleration variance with the Reynolds number (2.45) and show that it is in good agreement with DNS, which gives another empirical validation of the incomplete similarities assumption used to obtain these results.

Eventually, for large Reynolds numbers, we propose to express the doubly conditional variance as $\langle a^2|\varepsilon, K\rangle = C a_\eta^2 \exp(\alpha K/\langle K\rangle + \gamma \ln \varepsilon\langle\varepsilon\rangle)$, $\gamma = 3/2 + \beta$, which can be viewed as the results of a multiplicative process for the acceleration. Such a process can be interpreted as a momentum fluctuation cascade that includes kinematic effects by eddies all along the turbulence spectrum.

Based on these results we propose a 3D stochastic model for the dynamics of a fluid particle that reproduce the essential features of the Lagrangian dynamics observed from DNS and experiments. To obtain such a model, (i) we have assumed, inline with the Kolmogorov universality hypothesis, that the dynamics can be described as a set of stochastic differential equation $da_i = M_i dt + D_{ij} dW_j$; $du_i = a_i dt$, with M_i and D_{ij} depending on the velocity and acceleration along with Reynolds number dependent parameters. (ii) We used the doubly conditional acceleration variance presented first, to model the instantaneous relation of the dynamics between acceleration (or force), kinetic energy, and energy dissipation. This amounts to consider that the remaining degree of freedom can be discarded in procedure similar to an adiabatic elimination [84] as discussed by Ref. [49]. (iii) We

introduce a nondiagonal diffusion tensor along with a maximum winding hypothesis to ensure its physical realizability. (iv) We consider that the dissipation rate along the trajectory is given by the non-Markovian log-normal process proposed recently by Ref. [54], giving logarithmic correlation consistently with the turbulent cascade picture. The model is closed by using the relation $DK/Dt = P = a_i u_i$. For the model, it implies dependence of K on ε through the dependence of a^2 on ε. This can be interpreted as feedback of the small scales on the large scales. On the other hand, the influence of the large-scales on the small-scales is accounted for in the model through the intermittent cascade model for the dissipation rate. With these four hypotheses, we obtain the model given by Eqs. (2.56), (2.57), (2.79), and (2.80) which reads:

$$\begin{aligned} da_i &= \left[\frac{\alpha}{2\langle K\rangle}\left(a_i(c_u P + \frac{K}{\tau_\varepsilon}) - (c_u - 1)a^2 u_i\right) - a_i\left(\ln(\frac{a^2}{a_\eta^2}) + \hat{\Gamma}_*\right)\frac{1}{2\tau_\varepsilon} - \frac{\sigma_*^2}{\tau_c}\frac{a_T^2}{a^2}a_i\right]dt \\ &\quad + \sqrt{\frac{\sigma_*^2}{\tau_c}}\left[\sqrt{a_T^2}\delta_{ij} + \sqrt{a_N^2}\epsilon_{ijk}b_k\right]dW_j \ . \end{aligned} \tag{2.81}$$

We show that the proposed model predicts Lagrangian dynamics presenting non-Gausssianity, long-range correlations, anomalous scaling and time irreversibility. Moreover statistics obtained from the stochastic model are in good agreement with the DNS.

In Eq. (2.81) the term proportional to α, which follows directly from the exponential dependence of the conditional acceleration on the kinetic energy, involves the coupling between velocity and acceleration and leads to the exponential relaxation of the velocity correlation for large time lag along with one-time Gaussian distribution for the velocity. Introducing a rotational part in the diffusion tensor naturally leads to decomposition of the acceleration vector into its tangential part and its normal components. Since the normal part is associated with the curvature of the trajectory, the rotational part of the diffusion leads to the emergence of a time-scale separation between the correlation of the norm and the components of the acceleration. The term associated with the non-Markovianity of the dissipation along with the rotational part produce irreversible dynamics, as seen by the skewness of the exchanged power and ensures a scale separation between velocity and acceleration. These three points can be easily checked, by taking $\alpha = 0$ or $c_R = 0$ in Eq. (2.66) or by using for Π the Markovian log-normal dissipation model proposed by Ref. [203] rather than the non-Markovian one of Ref. [54].

It is worth noting that from the conditional acceleration statistics obtained from DNS of the Navier-Stokes equation, it is possible to establish, in a fairly natural way, that is to say without using any other hypothesis than the cascade picture, a link between the refined Kolmogorov assumption and the dynamics of fluid particles. It would be interesting to analyze further the stochastic equation to demonstrate the irreversibility of the dynamics, the emergence of anomalous scaling or to study the geometry of the particle trajectory e.g. its curvature and torsion, as well as to further test the conditional statistics between the acceleration and the velocity. Also interesting could be the improvement of the modeling of the high frequency part of the spectrum. Indeed, the dissipative part of the spectrum is not well reproduced by the model of Ref. [54] which intends to model the dissipation rate in the inertial range.

To simplify the construction of the model, we have not taken into account the nonlocal effects of the largest structures of the flow, arguing that their effect vanish as the Reynolds number increases (term with a_0^2 in eq. (2.41)). Based on the relation (2.41) it is possible

to account for the large-scale in the stochastic modeling. However, since this term is dependent on the Reynolds number, it is likely that it also depends on the flow configuration and boundary conditions. The proposed stochastic model could be further generalized to address shear flows [17] and improve Reynolds-averaged simulations [200, 109]. This model could be used among other things to improve the calculation of the dynamics of a dispersed phase with the large eddy simulation (LES) approach [279, 92, 280]. Finally, let us mention that an interesting extension could be the coupling of the proposed model with stochastic model for the evolution of the velocity gradients as proposed in Refs. [89, 168, 114, 195].

3 Particles and turbulence

Contents

In this section, I present some works on the modeling of turbulent flows with dispersed phases. Several problems are addressed: the a priori estimation of the statistics of the forces experienced by a particle in turbulent flows, the stochastic modeling of the instantaneous value of the forces and its application to the large eddy simulations (LES), and the turbulence induced by the rising of a cloud of bubbles.
One speaks of a dispersed phase when the evolution of each of these components, typically a bubble, a drop or a solid particle, can be obtained from the Newton's equation, by applying the sum of the forces to the center of mass of the object

$$\frac{d\boldsymbol{x}_p(t)}{dt} = \boldsymbol{v}_p \quad ; \quad m_p \boldsymbol{a}_p = m_p \frac{d\boldsymbol{v}_p(t)}{dt} = \boldsymbol{F}_p \ . \tag{3.1}$$

We can decompose this resulting force by separating the hydrodynamic forces $\boldsymbol{F}_{\text{fluid}}$ resulting from the exchange of momentum between the continuous phase (the carrier phase) and the particle, from the external forces $\boldsymbol{F}_{\text{ext}}$, typically the weight: $\boldsymbol{F}_p = \boldsymbol{F}_{\text{fluid}} + \boldsymbol{F}_{\text{ext}}$[1]. From a formal point of view, the hydrodynamic force on a particle is determined by integrating the fluid stresses Σ (normal stress and shear) on the surface of the particle $\boldsymbol{F}_{\text{fluid}} = \int_{S_p} \Sigma \cdot \boldsymbol{n}_p ds$.

[1] There is also the force $\boldsymbol{F}_I$ which translates the direct interactions between objects of the dispersed phase, typically the collisions, but it can also be an electromagnetic force if the particles are charged or if the medium conducts electricity ...

3.1 The Euler-Lagrange approach

In the Euler-Lagrange approach, the fluid is described in an Eulerian way and each object of the dispersed phase in a Lagrangian way, based directly on Newton's equation. One of the limitations of this approach is that it requires the resolution of a differential equation for each object of the dispersed phase, which is impossible if they are too many. The alternative, logically called Euler-Euler approaches, is to give a continuous description of the dispersed phase, by proposing statistical closures [33, 142, 245, 260, 77, 71, 78, 170, 211]. However, the main difficulty remains, that of estimating the resulting force on each particle. Indeed, the calculation of the stress that the fluid exerts on a particle requires to know precisely (*i.e.* at a scale smaller than the particle) the velocity and pressure field. When the particles are small, or when the boundary layers developing around them are small, in comparison of the other characteristic scales of the flow, it becomes impractical. The Euler-Lagrange approach is based on an effective description of the fluid at a scale ℓ larger than that of the particle. That is to say that the details of the velocity field are removed: $\boldsymbol{u}_f \to \overline{\boldsymbol{u}}_f$, and with respect to this filtered velocity field, the particle is pointwise. The resultant of the hydrodynamic forces is then estimated by a model which depends on the filtered velocity field, without requiring to have the full details of the velocity field.
Formally, we can introduce a functional $\mathcal{F}$ giving the force on a particle from the (filtered) velocity field of the fluid, the velocity of the particles $\boldsymbol{u}_p(t)$, their positions $\boldsymbol{x}_p(t)$, as well as their orientation $\theta_p(t)$ and rotation speed $\Omega_p(t)$ ...:

$$\boldsymbol{F}_{\text{fluid}} = \mathcal{F}\left[\overline{\boldsymbol{u}}_f(\boldsymbol{x},t); \boldsymbol{u}_p(t), \boldsymbol{x}_p(t), \Omega_p(t), \theta_p(t) \ldots\right] \ . \tag{3.2}$$

In general, the expression of such a functional is unknown. As an example, in the case of a fixed object in a uniform and stationary flow, we can make ℓ go to infinity, and obtain the force (or at least its average value in time) from the value of the velocity far upstream and its orientation relative to the object by relying on relations (most often empirical) for the drag and lift coefficients.
For a turbulent flow which is obviously neither stationary nor uniform, the use of the upstream velocity does not make sense. The method generally adopted is rather to use the value of the velocity field at the position of the particle. Indeed, the field $\overline{\boldsymbol{u}}_f$ is defined everywhere, including at the particle position. This is fully justified if we restrict ourselves to particles with a diameter d much smaller than the smallest scale of the turbulence (the dissipative scale of the turbulence η) $d \ll \eta$. In this limit, one can consider that at an intermediate scale ℓ, $\eta \gg \ell \gg d$, the velocity field $\overline{\boldsymbol{u}}_f(\boldsymbol{x},t)$ is quasi-uniform[2] at scale ℓ. With this scale separation, the expression of the fluid force must depend only on the local value of the fluid velocity field and its derivatives described at scale ℓ.
In this way, we can write that the hydrodynamic force must be a functional of the value of the velocity and its derivatives at the position of the particle (and not of the whole field as in (3.2)):

$$\boldsymbol{F}_{\text{fluid}} = f[\overline{\boldsymbol{u}}_{f(\boldsymbol{x}=\boldsymbol{x}_p(t),t)} - \boldsymbol{u}_p(t), \nabla\overline{\boldsymbol{u}}_f|_{\boldsymbol{x}_p}, D_t\overline{\boldsymbol{u}}_f|_{\boldsymbol{x}_p}, d_t\boldsymbol{u}_p(t)] \ . \tag{3.3}$$

Since the force must be Galilean invariant, only the relative velocity of the fluid and the particle can be used to determine the force. For the same reason, it is the material

[2] This uniformity assumption also implies that we consider an isolated particle, or in practice sufficiently diluted suspension.

derivative of the velocity of the fluid that must intervene. Note that for simplicity, we have omitted the terms involving the orientation and rotation of the particle.
The functional (3.3), and thus the expression of the hydrodynamic force, is only well known for spherical objects moving in a quasi-uniform flow with a very small relative velocity, so that their Reynolds number is small: $Re_p = |\overline{\boldsymbol{u}}_f - \boldsymbol{u}_p|d/\nu \ll 1$. In this case we can decompose the hydrodynamic force into drag force, history force (unsteady effect of the drag)[3], added-mass force and inertia force [86, 164, 152, 74]. When Re_p is larger, it is generally assumed that this decomposition remains valid if one corrects certain force expressions (e.g. inertia effect on the drag force) and adds other forces such as lift forces (note that several effects are grouped under the name of lift force). At high Reynolds numbers Re_p, the validity of the previous equation is more empirical than really rigorously shown, see for example [171] which considers the case of a fixed particle in a turbulent flow.
In practice the scale ℓ can be taken as the resolution scale of the numerical simulation $\ell \approx \Delta x$ and $\overline{\boldsymbol{u}}_f$ corresponds then to the velocity resolved by the simulation. If, in addition, the mesh is fine enough to resolve the turbulent fluctuations, we have $\eta \gg \ell \gg d$. This setting is sometimes described as quasi-DNS although the dynamics of the small particles are obtained from a model for the hydrodynamic force. In Sec. 3.2, we discuss the statistics of acceleration and particle forces in a turbulent flow obtained assuming such scale separation.
In the case where $\ell \gg \eta$, the mesh cannot capture all the turbulent scales of the flow, we then speak about Large Eddy Simulations. In this case the model for the hydrodynamic force must take into account the fluctuations that are not resolved by the mesh. In Sec. 3.3 we discuss the stochastic model formulation for such an approach for small particles $\ell \gg \eta \gg d$ as well as for large particles $\ell \gg d \gg \eta$.
Finally, we consider the case where the particle size is not negligible compared to the size of the mesh (the scale separation $\ell \gg d$ is not verified anymore). In this case, due to the presence of the particle, the velocity of the fluid $\overline{\boldsymbol{u}}_f$ close to the particle can be altered considerably [231, 86, 164]. Therefore the fluid velocity $\overline{\boldsymbol{u}}_f$ at the particle position must be corrected to reliably calculate the hydrodynamic force. This case can be encountered when studying the effect of the particles on the carrier phase (this is called "Two-Way coupling"), at least when one is interested in the effect of each particle more than in a global effect resulting from a large mass or volume loading. We will discuss in Sec. 3.4 the simulation of the turbulence induced by the rising of a cloud of bubbles and the correction that we have proposed for the calculation of the force for bubbles generating a significant wake.

3.2 Force and acceleration statistics for particles in turbulence

We present models for the variance of the acceleration of spherical particles in a homogeneous and isotropic turbulent flow. In this section, we consider that the particles are isolated (negligible volume fraction) and that we can neglect the modifications they cause on the flow of the carrier phase. We are interested in particles that can be heavy or

[3]Note that if history effects are neglected, the hydrodynamic force is given by the instantaneous value of the velocity and its derivatives at the position of the particle so (3.3) can be understood as a function (and not a functional).

light with respect to the carrier phase and smaller or larger than the Kolmogorov scale. Three dimensionless numbers are involved in the description of this problem: the ratio of the particle size to the dissipative scale of the flow d/η, the density ratio ρ_p/ρ_f and the Reynolds number of the flow, for example the Taylor scale Reynolds number Re_λ.

3.2.1 Small particles

We first consider the case of small particles in the sense that both $d < \eta$ and $Re_p < 1$. In this limit, it is reasonable to neglect lift and history force [153, 86, 164].
We can thus express the acceleration on these small particles as:

$$\frac{d\boldsymbol{u}_p}{dt} = -\frac{\boldsymbol{u}_p - \boldsymbol{u}_f}{\tau_p} + \beta\frac{D\boldsymbol{u}_f}{Dt} \ . \tag{3.4}$$

The coefficient β depends on the density ratio of the particle:

$$\beta = \frac{1 + C_M}{\rho_p/\rho_f + C_M} \tag{3.5}$$

with C_M the added-mass coefficient which is $C_M = 1/2$ for a sphere in an infinite medium [153, 19]. For a particle of high density $\rho_p/\rho_f \gg 1$ we have $\beta \to 0$ and for an extremely light particle $\rho_p/\rho_f = 0$ (typically the case of a bubble) we have $\beta = 3$. The relaxation time of the particle τ_p is:

$$\tau_p = (\rho_p/\rho_f + C_M)\,\frac{d^2}{18\nu} \ . \tag{3.6}$$

The expression is given here for the case where there is no slip of the fluid at the interface of the object. In the case where there is free shear at the interface, it is appropriate to replace the factor 18 by 12 as in Ref. [280]. This last condition corresponds in some cases to a bubble with an uncontaminated interface, but we draw attention to the fact that the interfacial dynamic is very rich is that a bubble is much more complicated than a light particle with a slip condition [149, 207].
To describe the dynamics of such a small particle, we prefer to use the following dimensionless numbers:

$$St = \tau_p/\tau_\eta \ ; \ \beta \tag{3.7}$$

with $\tau_\eta = \eta^2/\nu$ the dissipative timescale of the flow structure. Note that in Eq. (3.4) buoyancy has been neglected, which is valid for sufficiently intense turbulence and low gravity, *i.e.* if $Fr/St \gg 1$ [162], where $Fr = a_\eta/g$ [110, 22].

Small heavy particles

We consider first the case of small and heavy particles so that in the limit $\beta \to 0$ only drag force is important. In this case, the equation of motion of the particle simply becomes:

$$\frac{d\boldsymbol{u}_p}{dt} = -\frac{\boldsymbol{u}_p - \boldsymbol{u}_f}{\tau_p} \ . \tag{3.8}$$

This regime has attracted considerable attention for several decades, most certainly because of its interest in the understanding of many problems both industrial and natural, but probably also because of the simplicity of the model.

Among the remarkable aspects that have been highlighted is the formation of areas of very high particle density (clusters) [12, 45, 246, 69]. Due to their inertia, the particles tend to be ejected from areas of high rotation and accumulate in regions of high shear [163]. This cluster formation is maximum for St numbers around unity. For larger Stokes numbers, particles are expected to respond to structures with longer lifetimes, which are less intense [94].
It is important to note that Eq. (3.8) shows that the inertia of the particle acts as a first-order filter: high-frequency fluctuations in the fluid velocity along the particle trajectory are filtered out.
As shown in Ref. [20] for weakly inertial particles ($St < 1$), the inertia does not have a very large impact on the statistics of the particle acceleration which remain very close to the rate of variation of the fluid velocity along the trajectory. However the acceleration is sufficiently different from the acceleration of a fluid particle that would occupy the same place, to deviate the trajectory of the inertial particle from that of fluid particles and leads to cluster formation.
For larger inertia ($St > 1$) the fluctuations of the fluid along the trajectory of a particle are effectively filtered out and the particle only responds to low frequencies. This results in a much reduced variance of the particle acceleration compared to that of a fluid particle occupying the same position, and the trajectories become much straighter, thus reducing the phenomenon of preferential concentration. Particles with high inertia can pass through the high rotation zones without being significantly affected.
As proposed in Ref. [92] this results in the following relations for the variance of the acceleration of a particle. For $St \ll 1$, the variance of the acceleration remains very close to that of a fluid particle, so neglecting the preferential concentration, and the effect of intermittency (which was discussed at length in the first chapter, but which we leave aside for now) we have:

$$\langle \boldsymbol{a}_p^2 \rangle / a_\eta^2 = O(1) \ , \tag{3.9}$$

where $a_\eta^2 = \langle \varepsilon \rangle / \tau_\eta$. For very large inertia, $St \gg \tau_L/\tau_\eta$ where τ_L is the Lagrangian integral scale of the flow, we can consider that the velocity fluctuations of the particle appear decorrelated from the fluid ones, leading to a "thermalization" of the particle with the flow. And because of the particle inertia the variance of the relative velocity will be equal to that of the fluid: $\langle (\boldsymbol{u}_p - \boldsymbol{u}_f)^2 \rangle \approx \langle \boldsymbol{u}_f^2 \rangle$. This gives the following estimate for the variance of the particle acceleration:

$$\langle \boldsymbol{a}_p^2 \rangle / a_\eta^2 \sim Re_\lambda St^{-2} \ . \tag{3.10}$$

To obtain this relation we used that $\tau_L \sim \langle \boldsymbol{u}_f^2 \rangle / \langle \varepsilon \rangle$ and that $\tau_L/\tau_\eta \sim Re_\lambda$.
For intermediate inertia $1 \ll St \ll \tau_L/\tau_\eta$ one can make the assumption, similar to Kolmogorov, that the variance of the particle acceleration depends only on the average dissipation rate $\langle \varepsilon \rangle$ and on the response time of the particle and obtain:

$$\langle \boldsymbol{a}_p^2 \rangle / a_\eta^2 \sim St^{-1} \ . \tag{3.11}$$

A comparison is made with results computed from the DNS database [21, 141] obtained with the inertial particle model (3.8). We observe that the agreement is only partial and that the three scaling laws seem to give rather the envelope of the evolution of the variance with St. This comes from the fact that the Lagrangian inertial zone is very small even at large Reynolds (at least large for the current capabilities of DNS). Indeed from DNS we can see that $\tau_L/\tau_\eta = 0.08 Re_\lambda$ [238, 101]. Thus for $Re_\lambda = 400$ we have only

$\tau_L/\tau_\eta = 32$ which strongly limits the inertial zone where $1 \ll St \ll \tau_L/\tau_\eta$. Thus, without invalidating the proposed scaling laws, it shows that the way of matching these laws has a great importance to obtain an accurate estimate of the variance of the acceleration.

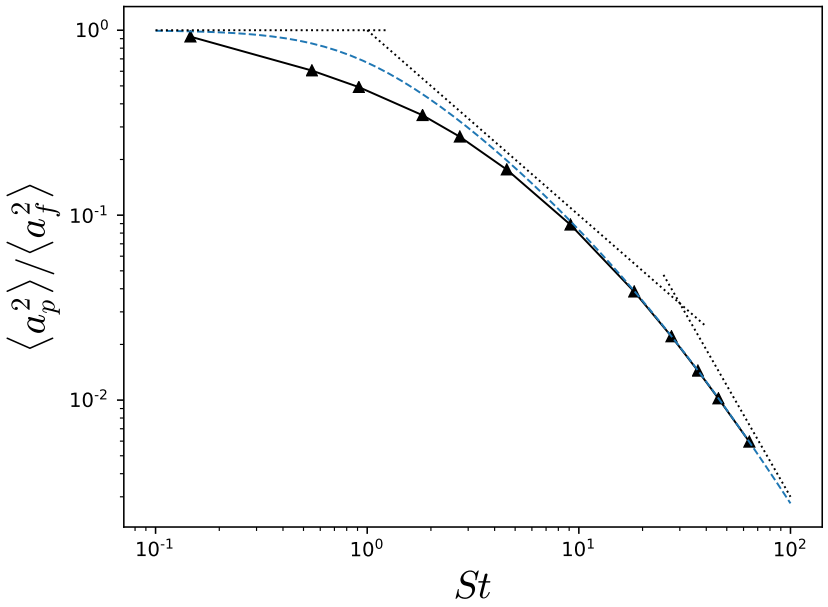

Figure 3.1: Variance of the acceleration of an inertial particle normalized by the variance of the acceleration of a fluid particle as a function of the Stokes number, obtained from the DNS database of Refs. [21, 140] at $Re_\lambda = 400$. Comparison with (3.9), (3.10) and (3.11) relations in doted line, as well as with (3.14) in dashed lines.

A more systematic approach taking advantage of the linearity of (3.8) proposes to calculate the associated transfer function [253, 104, 273, 279]. By taking the Fourier transform of (3.8) we obtain a relation between the spectrum of the particle velocity and that of the fluid velocity along the trajectory:

$$E_p(\omega) = \frac{1}{1+\omega^2\tau_p^2} E_f(\omega) \tag{3.12}$$

with $E_p(\omega) = \hat{\boldsymbol{u}}_p \hat{\boldsymbol{u}}_p^\star$ and $E_f(\omega) = \hat{\boldsymbol{u}}_f \hat{\boldsymbol{u}}_f^\star$ the spectral density of velocity of the particle and of the fluid. The evolution of the spectrum of the fluid velocity along the trajectory of the particle with St from DNS is shown in figure 3.2. Without going into details, we can see that, on the one hand, for very weakly inertial particles, the spectrum of the velocity seen by the particle is relatively well described by the Hinze spectrum [256, 184]:

$$E_f(\omega) \approx \frac{k_0 \langle \varepsilon \rangle \tau_L^2}{1+\tau_L^2\omega^2}\,, \tag{3.13}$$

at least for $\omega \ll \omega_\eta = 2\pi/\tau_\eta$. Note that this spectrum simply corresponds to an exponential decay of the Lagrangian autocorrelation of the velocity.
Moreover, we note that at frequencies lower than $\omega < 2\pi/\tau_p$ we can consider that the spectra of the fluid velocity are invariant with St. Specifically, the value of k_0 seems constant.

Using the normalization condition $\langle u_f^2 \rangle = 2 \int E_f(\omega) d\omega$ we find that $k_0 = \frac{1}{\pi} \frac{\langle u_f^2 \rangle / \langle \varepsilon \rangle}{\tau_L}$ where $\langle u_f^2 \rangle$ represents the variance of the velocity of the particle along the trajectory. We measured from DNS $k_0 = 1.04$. The dependence on St at higher frequency reflects, on the one hand, the effect of the preferential concentration (moderate St) and, on the other hand, the fact that the trajectory becomes more ballistic and thus cuts the turbulent structures developing a more energetic spectrum at high frequency in agreement with the sweeping mechanism proposed by Ref. [255].

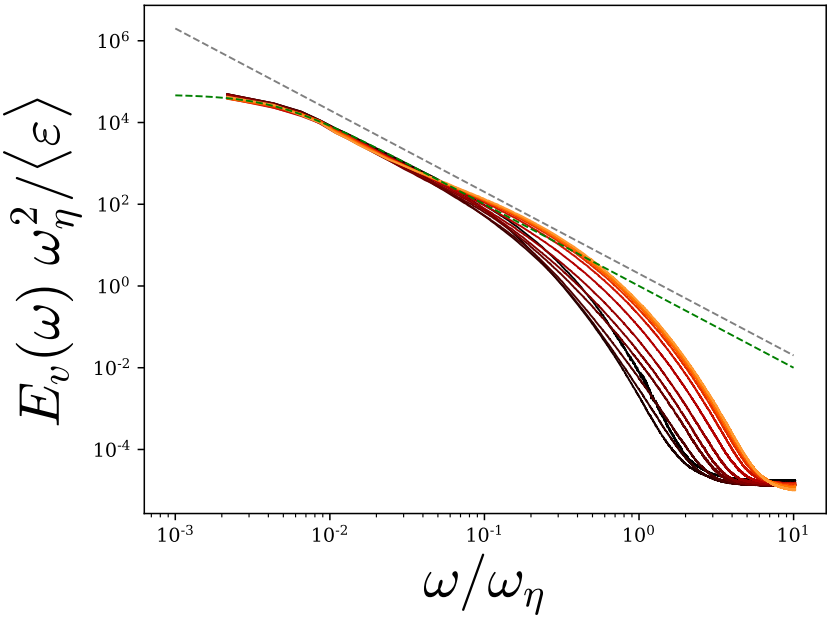

Figure 3.2: Spectrum of the fluid velocity along the trajectory of an inertial particle for $St = 0.24$, 0.9, 1.5, 3., 4.5, 7. 5, 15, 30, 45, 60, 75 (from black to orange), obtained from the DNS database of Refs. [21, 140] at $Re_\lambda = 420$. Comparison with the relation $\langle \varepsilon \rangle \omega^{-2}$ and the relation (3.13).

The spectrum of the particle acceleration is simply obtained by multiplying that of its velocity by ω^2. We obtain an estimate of the variance of the acceleration by integration:

$$\begin{aligned} \langle \boldsymbol{a}_p^2 \rangle &= 2 \int_0^\infty \omega^2 E_p(\omega) d\omega \\ &\approx \frac{c_0 a_\eta^2}{1 - St_L^2} \left[\frac{\tan^{-1}(c_1 St)}{c_1 St} - \frac{\tan^{-1}(c_1 \tau_L / \tau_\eta)}{c_1 \tau_L / \tau_\eta} \right] . \end{aligned} \tag{3.14}$$

The constant $c_1 = 2.8$ appears, because the previous integral is truncated for $\omega > c_1/\tau_\eta$ and we introduce $c_0 = 2 c_1 k_0$ to simplify the notations. We also introduced $St_L = \tau_p/\tau_L = St/0.08 Re_\lambda$. The relation (3.14) is compared with the DNS in the figure 3.1. In this figure the variance of the acceleration is normalized by the variance of the acceleration of a fluid particle, which is estimated from (3.14) with $St = 0$. We can see a fairly good agreement with the DNS, although around $St \approx 1$ the variance of the acceleration is underestimated, because the effect of the preferential concentration on the spectrum of the fluid velocity has been neglected. One can check that the expression (3.14) is in agreement with the

relations (3.9), (3.10) and (3.11). For example, in the case of large Reynolds numbers, $\tau_L/\tau_\eta = Re_\lambda/0.08 \gg 1$ and $\tau_L/\tau_\eta \gg St$, the relation (3.14) simplifies into

$$\langle \boldsymbol{a}_p^2 \rangle \approx c_0 a_\eta^2 \frac{\tan^{-1}(c_1 St)}{c_1 St} \ . \tag{3.15}$$

This relation behaves indeed as St^{-1} for $St \gg 1$ and tends to a constant for $St \ll 1$. In the limit where the Stokes number is large $St \gg 1$ (and also $\tau_L/\tau_\eta \gg 1$) we find:

$$\langle \boldsymbol{a}_p^2 \rangle \approx a_\eta^2 \frac{k_0 \pi/2}{St(1+St_L)} \ . \tag{3.16}$$

This corresponds to (3.10) and (3.11). We can notice that in the previous relation the constant c_1 is eliminated meaning that for large Stokes numbers the dissipative zone has no more direct effect, because it appears anyway filtered by the inertia of the particle.
Moreover, it should be noted that k_0 presents dependence with the Reynolds number in order to account for the intermittency of the flow (as discussed in the first chapter, see the relation (2.43)) reflecting that for very high Reynolds numbers even at high Stokes numbers, one should expect that the large fluctuations at small scales might influence the dynamics of the particle.

Small, heavy or light particles

We are now interested in particles with arbitrary density, small or large, but whose size remains small ($d/\eta \ll 1$ and $Re_p \ll 1$). We mention that bubbles can be assimilated to very light particles [4]. It is therefore a priori necessary to take into account the effect of the inertia of the fluid, which includes the added-mass force and the Tchen force. The dynamics of the particle is therefore given by (3.4). We note

$$\boldsymbol{F}_I = \beta D_t \boldsymbol{u}_f \ , \tag{3.17}$$

the inertia force per unit of displaced mass, and

$$\boldsymbol{F}_D = -(\boldsymbol{u}_p - \boldsymbol{u}_f)/\tau_p \ . \tag{3.18}$$

The drag force also per unit of displaced mass, with the relaxation time always defined by (3.6).
The first question concerns the importance of the inertia force of the fluid compared to the drag force. In the case of very small inertia $St \to 0$, the particle behaves like a tracer. Therefore in this limit, its acceleration will be identical to the acceleration of a fluid particle $\boldsymbol{a}_p = \boldsymbol{a}_f = D_t \boldsymbol{u}_f$. Then from (3.4), and using (3.17), we have $\boldsymbol{F}_D = (1-\beta)\boldsymbol{a}_f$. It implies that for $\beta > 0$

$$\boldsymbol{F}_D = \frac{1-\beta}{\beta} \boldsymbol{F}_I \ . \tag{3.19}$$

For example, for very light particles ($\beta = 3$), we expect that the two forces are of the same order of magnitude, but of opposite directions.

[4] There are however some precautions to take, such as contamination of the interface by surfactants which change the dynamics condition on the interface (free slip or no-slip), the deformation of the bubble, characterized for example by the Weber number ...

As the inertia of the particle increases, the drag force (per unit mass) is expected to decrease, as seen earlier. This suggests that for inertial particles with $St \gg 1$, the fluid inertia force can be important even if the density ratio is not very low. Moreover, for light particles we expect the variance of the particle acceleration to increase with St, since $\boldsymbol{F}_I$ and $\boldsymbol{F}_D$ are opposite.
These behaviors are confirmed in figure 3.3 showing the evolution of the variance of the particle acceleration for different values of β. The reported values were obtained by Zhentong Zhang from DNS [279] for $\beta = 3$, for $\beta = 2.5$ and 0.14 by those of Ref. [46], and for $\beta = 0$ by Ref. [21]. We see that for $\beta > 0$, the variance of the acceleration tends to a constant value when St becomes large, and that the asymptotic value depends on β. This reflects the fact that the drag force becomes negligible at large St. For particles with density less than the fluid ($\beta > 1$) we also see that the variance becomes larger than for a fluid particle. In fact, we will show below that this asymptotic value is β^2.
A remark is necessary: the model (3.4) is based on the hypothesis that $d/\eta < 1$ and $Re_p < 1$ but this imposes limits for the value of St and β as we can see with the relation:

$$\left(\frac{d}{\eta}\right)^2 = \frac{18\beta St}{(1 + C_M)} \ . \tag{3.20}$$

For $\beta = 3$, the Stokes number must be less than 5 to guarantee that the diameter remains small enough for neglecting the finite size of the particles (corresponding roughly to $d/\eta < 10$). Indeed on the figure 3.3, we see that for β close to 3, the experimental results show a decrease of the variance when St increases, this is attributed to finite size effects of the particle. These effects are discussed in paragraph 3.2.2. We come back to the condition $Re_p \ll 1$ a little later.
The approach of Tchen can be generalized [104, 166, 3, 279] to account for the fluid inertia force in order to propose an estimate of the variance of the acceleration of a small, heavy or light particle as a function of St, β, and $\tau_L/\tau_\eta \approx 0.08 Re_\lambda$:

$$\frac{\langle \boldsymbol{a}_p^2 \rangle}{a_\eta^2} \approx c_0 \left[\beta^2 + \frac{1-\beta^2}{1 - St_L^2} \frac{\tan^{-1}(c_1 St)}{c_1 St} - \frac{1-\beta^2 St_L^2}{1 - St_L^2} \frac{\tan^{-1}(c_1 \tau_L/\tau_\eta)}{c_1 \tau_L/\tau_\eta} \right] = \Gamma_a(St, \beta, \tau_L/\tau_\eta) \ . \tag{3.21}$$

Again with $St_L = \tau_p/\tau_L = St\tau_\eta/\tau_L$ and $c_1 = 2.8$. This estimate is compared to the results of DNS in figure 3.3. We see that the agreement is relatively good, at least as long as the finite size effects are negligible. We can notice that for $\beta = 0$, the relation (3.21) is indeed identical to (3.14). For $Re_\lambda \gg 1$ and $St_L \ll 1$ we can simplify the relation:

$$\frac{\langle \boldsymbol{a}_p^2 \rangle}{a_\eta^2} \approx c_0 \left[\beta^2 + (1-\beta^2) \frac{\tan^{-1}(c_1 St)}{c_1 St} \right] \ . \tag{3.22}$$

We notice that for $St \ll 1$ and $Re_\lambda \gg 1$ the variance of the acceleration tends to a constant value $\langle \boldsymbol{a}_p^2 \rangle \approx c_0 a_\eta^2 \beta^2$.
The equation (3.21) is obtained from the following transfer function

$$E_p(\omega) = H_u^2(\omega) E_f(\omega) \qquad ; \qquad H_u^2(\omega) = \frac{1 + \beta^2 \omega^2 \tau_p^2}{1 + \omega^2 \tau_p^2} \ , \tag{3.23}$$

and by estimating, as before, that the spectrum of the fluid velocity at the particle position is given by (3.13). This transfer function is obtained at the cost of an approximation on

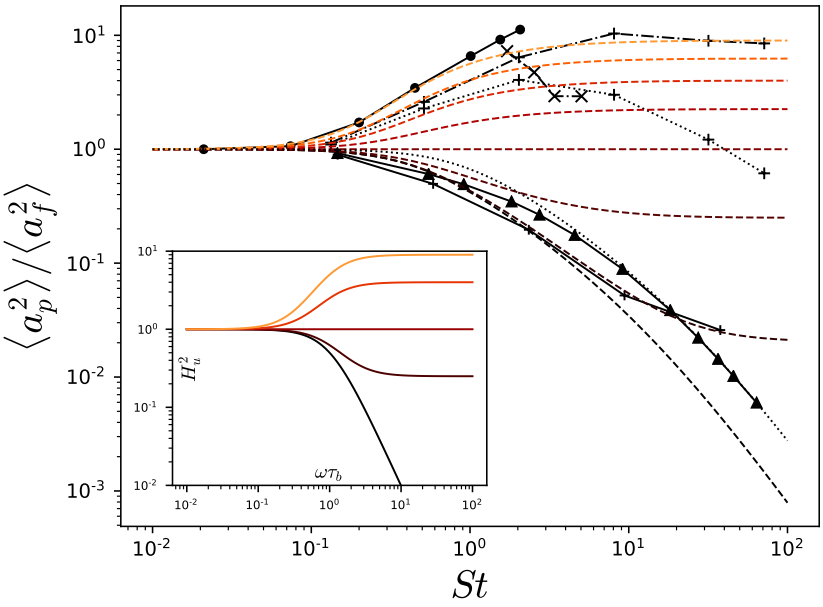

Figure 3.3: Variance of acceleration normalized by the acceleration of a fluid particle from the DNS of [279] for a bubble $\beta = 3$, $Re_\lambda = 215$ (• and continuous line), the DNS of [21, 140] for dense particles $\beta = 0$, $Re_\lambda = 400$ (▲ and continuous line), the DNS of [46] for $\beta = 2.5$ and $Re_\lambda = 180$, with or without finite size correction (+ with dash-dotted and dotted lines respectively), and $\beta = 0.14$ (+ and continuous line), experimental measurements of [205] for $Re_\lambda = 145 - 230$ and $\beta \approx 3$ (× and dashed lines). Comparison with the equation (3.21): $\langle \boldsymbol{a}_b^2 \rangle_{(St,\beta,\tau_L/\tau_\eta)} / \langle \boldsymbol{a}_b^2 \rangle_{(0,1,\tau_L/\tau_\eta)}$ with $c_1 = 2.8$ and $Re_\lambda = 200$ for $\beta = 0$, 0.14, 0.5, 1, 1.5, 2, 2.5 and 3 from black to orange, in dash line, and with $c_1 = 2.8$ and $Re_\lambda = 400$, $\beta = 0$ in black doted line. Inset: the transfer function (3.23) as a function of $\omega\tau_b$ for $\beta = 0$, 0.5, 1, 2 and 3 from black to orange.

the total acceleration of the fluid at the particle position. We have indeed replaced the total acceleration of the fluid at the position of the particle $D\boldsymbol{u}_f/Dt$ by the Lagrangian derivative along the trajectory of the particle $d\boldsymbol{u}_f/dt = \partial_t \boldsymbol{u}_f + \boldsymbol{u}_p.\nabla \boldsymbol{u}_f$. This allows the use of the linear response approach, since it is equivalent to considering that the velocity of the particle responds only to the fluctuations of the fluid velocity along the trajectory and its time derivative. This assumption can be evaluated by writing the material derivative of the fluid in the following form

$$D_t \boldsymbol{u}_f = \partial_t \boldsymbol{u}_f + \boldsymbol{u}_f \nabla \boldsymbol{u}_f = d_t \boldsymbol{u}_f - (\boldsymbol{u_p} - \boldsymbol{u}_f).\nabla \boldsymbol{u}_f \ . \tag{3.24}$$

We thus see that our approximation is a priori valid for Stokes numbers small enough for the relative velocity to be small (as discussed in the previous paragraph about the drag force). Figure 3.4 compares the variance of $D_t \boldsymbol{u}_f$ and $d_t \boldsymbol{u}_f$, as well as the variance of their difference, for the extreme cases $\beta = 0$ and $\beta = 3$. We notice that $\langle (D_t \boldsymbol{u}_f)^2 \rangle$ evolves only slightly with St, although it presents a slightly lower value around $St = 1$ for both $\beta = 0$ and $\beta = 3$. On the other hand, the Lagrangian derivative of the velocity along the trajectory shows a clear increase with St. However, it should be noted that our estimate is not so bad, because we have also neglected the phenomenon of preferential concentration

(in fact the effect of St in the velocity spectrum seen by the particle E_f), and thus the variance of the inertial term predicted by the approach does not depend on St which is finally in relatively good agreement with the DNS. This is the result of two errors which, by chance, compensate each other.

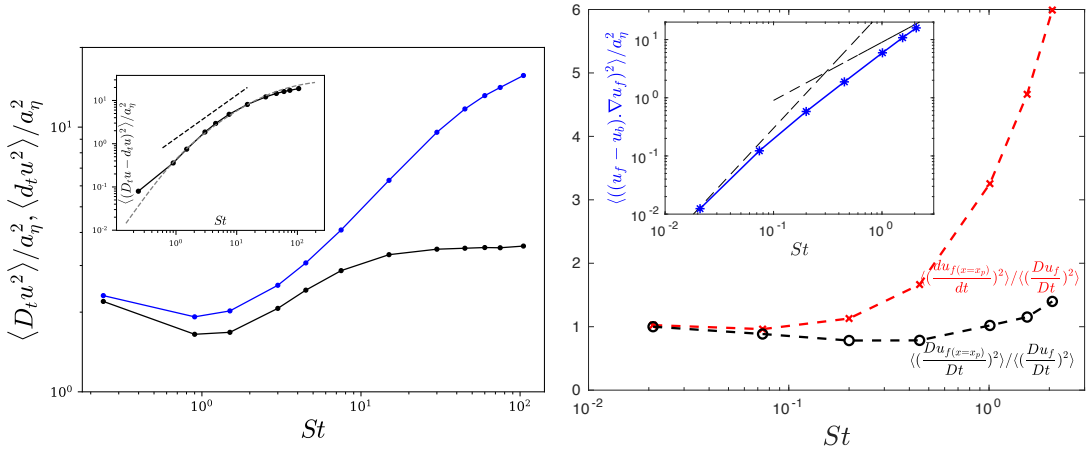

Figure 3.4: Evolution with St of the variance of the material derivative of fluid velocity at the particle position $D_t\boldsymbol{u}_f$ (black) and of its Lagrangian derivative along the particle trajectory $d_t\boldsymbol{u}_f$ (blue/red), for inertial particles $\beta = 0$ at $Re_\lambda = 400$ (left) and light particles $\beta = 3$ at $Re_\lambda = 200$ (right). The quantities are normalized by the variance of the acceleration of a fluid particle computed on the whole domain. Inset: variance of $D_t\boldsymbol{u}_f$ - $d_t\boldsymbol{u}_f$.

We just mention that in Ref. [279] we have also studied by DNS, the PDFs of the particle acceleration for $St = 3$. We observe that for $St = O(1)$, the flatness of the PDFs is much larger than that for fluid particles. This is because the two forces $\boldsymbol{F}_D$ and $\boldsymbol{F}_I$ are of the same order of magnitude and mostly anti-aligned, as the drag force responds quickly to the solicitation imposed by the inertial force, leading to a relatively low acceleration. However, when the two forces are aligned, this leads to very high accelerations.
Using the response function approach, we can estimate the variance of the drag force $\boldsymbol{F}_D$ as well as of the fluid inertia force $\boldsymbol{F}_I$:

$$\frac{\langle \boldsymbol{F}_D^2\rangle}{a_\eta^2} \approx c_0 \frac{(1-\beta)^2}{1-St_L^2}\left[\frac{\tan^{-1}(c_1 St)}{c_1 St} - \frac{\tan^{-1}(c_1\tau_L/\tau_\eta)}{c_1\tau_L/\tau_\eta}\right] = \Gamma_D(St,\beta,\tau_L/\tau_\eta)\ , \tag{3.25}$$

$$\frac{\langle \boldsymbol{F}_I^2\rangle}{a_\eta^2} \approx c_0\beta^2\left[1 - \frac{\tan^{-1}(c_1\tau_L/\tau_\eta)}{c_1\tau_L/\tau_\eta}\right] = \Gamma_I(St,\beta,\tau_L/\tau_\eta)\ . \tag{3.26}$$

We see that indeed the estimate of the predicted inertia force is independent of St, as mentioned above.
The previous relations were obtained by assuming a Stokes regime for the flow around the particle. This results in a Reynolds number of the particles that must necessarily be very small in front of 1. Using the relation of the variance of the drag force (3.25), one can estimate the evolution of the Reynolds number or more exactly of its second order moment with St:

$$\langle Re_p^2 \rangle = \langle \boldsymbol{F}_d^2 \rangle \tau_p^2 d^2/\nu^2 = \frac{18\beta}{1+C_M} St^3 \Gamma_D(St, \beta, \tau_L/\tau_\eta) \ . \tag{3.27}$$

Effect of the finite Reynolds number of the particles

The relative velocity between the particle and the fluid increases with the inertia of the particle. The inertial effects of the flow around the particle are characterized by the Reynolds number of the particle Re_p. These are generally considered to be present from $Re_p = 0(1)$, although the drag force remains dominated by viscous effects until $Re_p = 0(100)$. Such inertial effects are not taken into account in (3.4) which assumes a Stokes regime for the flow around the particle giving a drag force proportional to the relative velocity. One can introduce a correction $\phi(Re)$ to the drag force to take into account finite Reynolds number effects:

$$\boldsymbol{F}_D = -\phi(Re_p) \frac{\boldsymbol{u}_p - \boldsymbol{u}_f}{\tau_p} \ . \tag{3.28}$$

We choose[5] by definition that for a solid particle with $Re_p \ll 1$ we have

$$\phi(Re) = 1 \ . \tag{3.29}$$

For a solid particle, we obtain the correction from the expression of the drag coefficient proposed by Ref. [242], valid for $Re_p < 800$:

$$\phi(Re_p) = 1 + 0.15 Re_p^{0.687} \ . \tag{3.30}$$

This empirical relation is based on experimental data for the mean drag and tends towards the Stokes solution in the limit $Re_p \to 0$. The ϕ correction can also integrate other effects such as the mobility of the interface or its contamination, the viscosity of the fluid in the case of drops or even the shape of the particle. For example, we can also consider the case of clean spherical bubbles (spheres with a free shear condition at the interface), with the Mei drag law valid for all Re_p:

$$\phi(Re_p) = \frac{2}{3} + \frac{2}{3}\left(\frac{8}{Re_p} + \frac{1}{2}\left(1 + \frac{3.315}{Re_p^{1/2}}\right)\right)^{-1} \ . \tag{3.31}$$

This relation is based on DNS and has been constructed so as to find in the limit $Re_p \to 0$ the viscous solution and the Oseen development [102, 227, 252]. At high Reynolds numbers the relation (3.31) gives $\phi(Re_p) = 2$ and $\phi(Re_p) = 2(1 - 2.211 Re_p^{-1/2})$ corresponding respectively to the Levich viscous potential solution [147] and the Moore correction [179] taking into account the development of a boundary layer.
The ϕ correction coefficient is related to the drag coefficient by

$$\phi(Re) = \frac{C_D}{C_{D,0}} \ , \tag{3.32}$$

with $C_{D,0} = 48/Re_p$ the drag coefficient of a solid particle in the Stokes regime as a reference. The evolution of ϕ with Re_p corresponding to (3.29), (3.30) and (3.31) is shown

[5] This choice is different in [280] where we had chosen as reference the case of a clean spherical bubble, *i.e.* with a free slip condition at the interface.

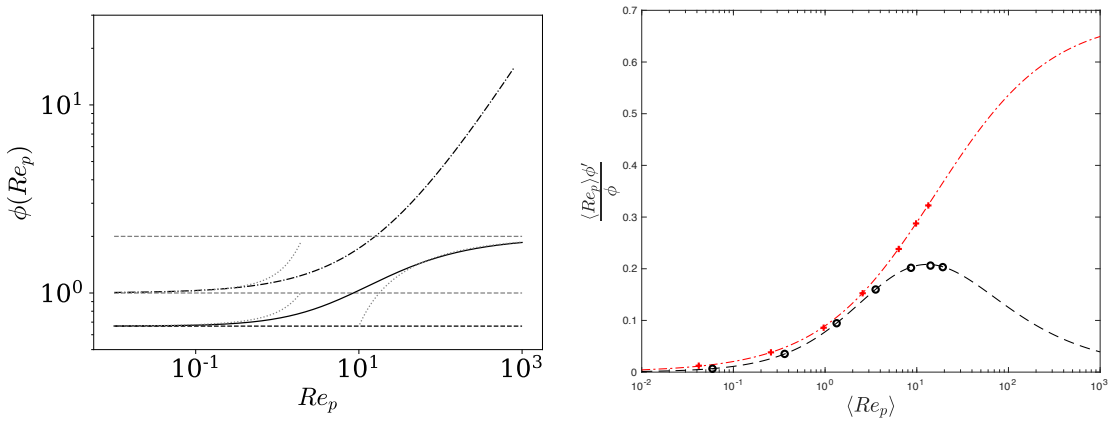

Figure 3.5: On the left: $\phi(Re_p)$ as a function of Re_p. The case of a solid particle: (gray dotted lines) Stokes solution $\phi = 1$ (relation (3.29)); (thin gray dotted lines) the Oseen solution $\phi = 1 + 3Re/8$; (black dotted lines) the Schiller and Naumann relation (3.30). For a spherical bubble: (black line) relation (3.31); (black dotted lines) Stokes regime $\phi = 2/3$; (thin gray dotted lines) the Taylor and Acrivos solution $\phi = 2/3(1+Re/8)$; (thin gray dotted lines) the Moore relation $\phi(Re_p) = 2\left[1 - 2.211Re_p^{-1/2}\right]$; (gray dotted lines) Levich's solution $\phi(Re_p) = 2$.
Right : Evolution of $\langle Re_p\rangle\phi'(\langle Re_p\rangle)/\phi(\langle Re_p\rangle)$ as a function of $\langle Re_p\rangle$. The symbols correspond to the results of the DNS: ($\circ$) for the law (3.31) and ($\times$) for (3.30). The lines are the analytical results.

in Figure 3.5. The expressions for ϕ are based on the implicit assumption, generally accepted, that the expression for the mean drag force is applicable to the instantaneous drag force and that the decomposition of the force balance on the particle remains unchanged. Such an assumption is certainly valid if the fluctuations of the Reynolds number are small compared to its mean value and the transient effects (related to the history force) are very brief.
In Ref. [280] we considered simulations for the three drag laws (3.29), (3.30) and (3.31), with $\beta = 3$. We found that the instantaneous Reynolds number of the particles in these three cases presents a distribution close to a log-normal with a mean of the same order of magnitude as its standard deviation:

$$\langle Re_p\rangle \approx \sqrt{\langle Re_p^2\rangle/2}\ . \tag{3.33}$$

To propose an estimate of the variance of the acceleration and forces, taking into account the inertial effects in the response of the particle, we can decompose the Reynolds number of the particle into an average part and a fluctuating part $Re_p = \langle Re_p\rangle + Re_p'$ and approach the drag force (3.28) thanks to a Taylor development of the function ϕ around $\phi(\langle Re_p\rangle)$:

$$\boldsymbol{F}_D = -\phi(\langle Re_p\rangle)\frac{\boldsymbol{u}_p - \boldsymbol{u}_f}{\tau_p} - Re_p'\phi'(\langle Re_p\rangle)\frac{\boldsymbol{u}_p - \boldsymbol{u}_f}{\tau_p} + \ldots \tag{3.34}$$

with ϕ' the derivative of ϕ with respect to Re_p. Although the Reynolds number of the particle presents important fluctuations, we show in figure 3.5 by plotting the ratio $\langle Re_p\rangle\phi'(\langle Re_p\rangle)/\phi(\langle Re_p\rangle)$, that we can retain only the first term of the Taylor expansion,

at least as long as we are interested in basic statistics (typically mean or variance). When the Stokes number becomes very large, the second order is no longer negligible, but the first term remains dominant.
The relation (3.34) allows introducing an effective relaxation time τ_p^*, as proposed for example in Refs. [77, 26, 280], which allows to take into account the effect of the finite Reynolds number of the particles:

$$\tau_p^* = \tau_p / \phi(\langle Re_p \rangle) \ , \tag{3.35}$$

and an effective Stokes number

$$St_* = St / \phi(\langle Re_p \rangle) \ . \tag{3.36}$$

To illustrate the relevance of introducing St_*, we present on figure 3.6 the evolution of the variance of the drag force and of the acceleration of the particles as a function of St and St_* for the DNS performed with the drag laws (3.29), (3.30) and (3.31) and $\beta = 3$. It can be seen that the evolution with the Stokes number differs quite markedly when the drag law is modified. When these evolutions are plotted as a function of St_* we notice that the different curves almost merge. This means that the effects of finite Re_p can be taken into account, at first order, thanks to the effective Stokes number.
Moreover, we have shown in the previous paragraph that for $\phi(Re_p) = 1$ we can estimate the evolution of the variance of the forces and the acceleration as a function of St and β thanks to the relations (3.21), (3.25), (3.26). Thus, the (approximate) self-similarity of the variances as a function of St_* in figure (3.6) indicates that we can estimate the variance of the particle forces and acceleration taking into account inertial effects ($Re_p > 1$) with the formulas (3.21), (3.25), (3.26) evaluated with St_* instead of St:

$$\frac{\langle \boldsymbol{a}_p^2 \rangle}{a_\eta^2} \approx \Gamma_a(St_*, \beta, \tau_L/\tau_\eta) \tag{3.37}$$

$$\frac{\langle \boldsymbol{F}_D^2 \rangle}{a_\eta^2} \approx \Gamma_D(St_*, \beta, \tau_L/\tau_\eta) \tag{3.38}$$

$$\frac{\langle \boldsymbol{F}_I^2 \rangle}{a_\eta^2} \approx \Gamma_I(St_*, \beta, \tau_L/\tau_\eta) \tag{3.39}$$

To use these relations one needs to estimate St_*, which requires to know the mean value of the particle Reynolds number. By using (3.33), (3.34), (3.38) and the definition of Re_p, we can obtain an implicit relation allowing estimating, to the first order, the average Reynolds number

$$\langle Re_p \rangle \approx \frac{St}{\phi(\langle Re_p \rangle)} \frac{d}{\eta} \left(\frac{1}{2} \Gamma_D(St/\phi(\langle Re_p \rangle), \beta, \tau_L/\tau_\eta) \right)^{1/2} \tag{3.40}$$

This relation can be solved iteratively by taking for example as initial value $\langle Re_p \rangle = 0$. A validation of (3.40) can be found in Ref. [280] based on comparisons with the DNS for different drag laws.
Fluid inertia forces have a dominant role in the dynamics of light particles ($\rho_p/\rho_f \ll 1$), in contrast, it is generally considered that for very dense particles ($\rho_p/\rho_f \gg 1$), the fluid inertial force is irrelevant. This suggests that one can conclude about the relevance of the

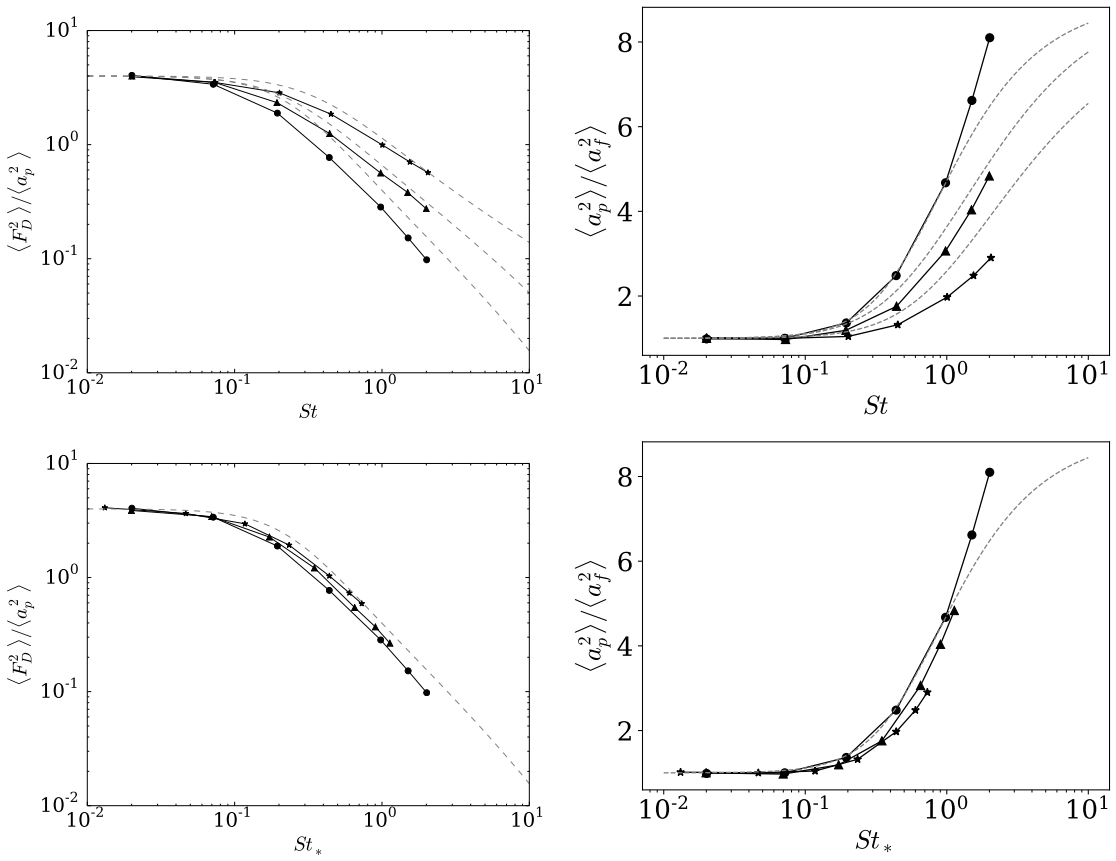

Figure 3.6: Left: Variance of the drag force normalized by the variance of the particle acceleration. Right: Variance of the particle acceleration normalized by the variance of the fluid particles. Top : Evolution as a function of St; bottom : Evolution as a function of $St_* = St/\phi(\langle Re_p \rangle)$. With $\phi(Re_p)$ given by (3.29) ($\circ$), (3.30) ($*$) and (3.31) (Δ). The dotted lines correspond to estimates by (3.38) and (3.37).

inertial force based only on the density. Using the estimates (3.38) and (3.39) for the drag force and inertia force, we show in what follows that this is more subtle and also depends on the particle size.

Figure 3.7 shows the evolution of the ratio $\langle F_I^2 \rangle / \langle F_D^2 \rangle$ estimated from (3.38) and (3.39) for a range of density and particle size. For this figure we chose the Re_p-correction (3.30) corresponding to the drag force of a solid sphere given by the Schiller and Naumann relation. The figure 3.7(a) presents 3 levels of the force ratio $\langle F_I^2 \rangle / \langle F_D^2 \rangle = 1\%$, 10% and 100% as a function of ρ_p/ρ_f and St. The shaded area indicates the region of parameter space in which the fluid inertia force is not negligible (arbitrarily set to $\langle F_I^2 \rangle / \langle F_D^2 \rangle = 10\%$). As expected, we observe that for light particles ($\rho_p/\rho_f < 1$), the inertia force of the fluid is dominant, whereas for very heavy particles, $\rho_p/\rho_f \gg 1$, we observe that the inertia force of the fluid can be neglected. However, we observe that when the Stokes number of the particle increases, the density threshold from which the inertia force is negligible increases. Typically for $St < 1$, this force is negligible if $\rho_p/\rho_f > 10$, while for $St = 100$ it requires $\rho_p/\rho_f > 100$. The non-negligible role of the fluid inertia force for very heavy particles and of inertia (or size, both are related, see (3.20)) is simply explained by the observation that at first order the fluid inertia force (per unit of displaced mass) is independent of particle size, as long as finite size effects can be ignored, while the magnitude of the drag force (again per unit of displaced mass) decreases with particle size, as shown in figures 3.1 and 3.6.

Moreover, considering the evolution of the force ratio as a function of ρ_p/ρ_f and d/η given in figure 3.7(b), we can notice that for particles of size $d/\eta \approx 3$ the inertial force remains important even for very large density ratios. This observation depends on the Reynolds number of the flow. Indeed, for $Re_\lambda = 400$, the inertia force of the fluid should not be neglected for particles larger than $d/\eta \approx 7$. Since it has been proposed by Ref. [46] that the finite size effect can be ignored for particles smaller than $d/\eta \approx 10$, the results presented in this section indicate that the added-mass force may turn out to be of the order of magnitude of the drag force, when the inertia of the particles becomes large, even for high density ratio. For higher Reynolds numbers, one has to keep in mind that intermittency is not taken into account, and since the fluctuations of the fluid acceleration can be much larger than its standard deviation, this contributes a priori to reinforce the effect of the fluid inertia force.

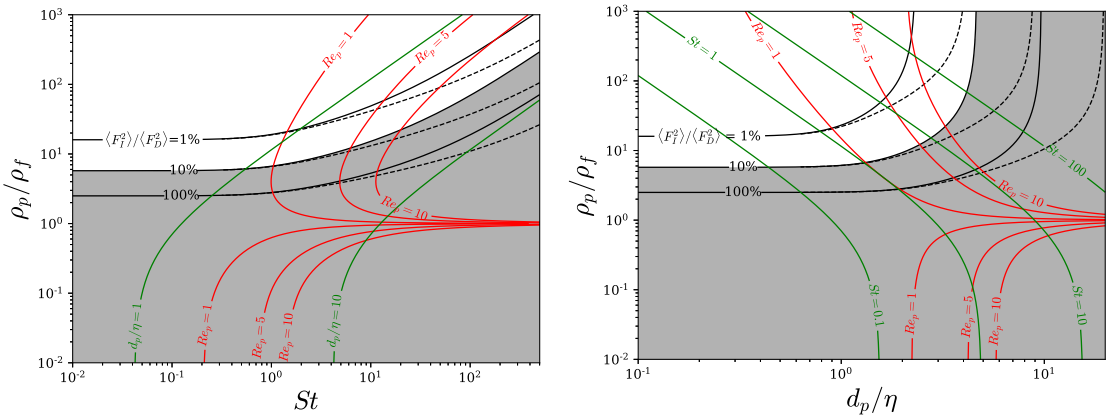

Figure 3.7: Contours level $\langle F_I^2\rangle/\langle F_D^2\rangle = 0.01$, 0.1 and 1, estimated from (3.38) and (3.39) for $Re_\lambda = 100$ (continuous black lines) and $Re_\lambda = 400$ (dashed lines) as a function of ρ_p/ρ_f and St (a) and of ρ_p/ρ_f and d/η (b). The red lines give the iso values of the Reynolds number obtained from (3.40) for $Re_\lambda = 100$. The green lines give the iso values of d/η (a) and St (b). The shaded region corresponds to $\langle F_I^2\rangle/\langle F_D^2\rangle > 0.1$.

3.2.2 Large particles

We are considering the statistics of the acceleration of finite size particles, *i.e.* whose diameter is not negligible in comparison with the Kolmogorov scale. Experimental works of Refs. [264, 210, 209, 263, 38, 40, 267] have shown that for particles with $d > \eta$ and having a density ratio close to 1 the variance of their acceleration varies as $\langle \boldsymbol{a}_p^2\rangle \sim \langle \varepsilon^{4/3}\rangle d^{-2/3}$. The experiments of Refs. [209, 38] have studied in detail the effect of size and density for size ratios between $d/\eta = 10$ and 26 and density between 1 and 100. They showed a complicated evolution of the variance of the acceleration with size and density. It also appears that the tails of the PDFs of particle acceleration tend to shrink with increasing size [263]. It should be noted, however, that this behavior is not observed in the results of [209] which has PDFs that appear to be nearly invariant with size, this may be due to the resolution limitations of the measurements.

On the other hand, in numerical simulations of Refs. [105, 57], at moderate Reynolds numbers, it was observed that the variance varies as $d^{-4/3}$. This would result from the fact that the particle dynamics is dominated by large flow structures leading to $\langle \boldsymbol{a}_p^2\rangle \sim \varepsilon^{2/3} d^{-4/3}\langle(\boldsymbol{u}_f - \boldsymbol{u}_p)^2\rangle$. It should be noted that studies on finite size particles are still mainly experimental and that DNS at high Reynolds numbers are not yet available.

To model these different aspects, we can assume first that the decomposition of the hydrodynamic force (drag, mass added inertia force ...) remains relevant for particles much larger than the Kolmogorov scale. This remains, of course, hypothetical, because there is no rigorous derivation of the hydrodynamic force for such particles (except for the added-mass force). Many works are currently looking for empirical expressions of such forces [150]. The main difficulty in this path being to define the fluid velocity seen by the particle that appears in the expression of the forces. We return to this point in the paragraph 3.4. In this hypothesis, we consider that the hydrodynamic force on the particle can generally be given by the drag force and the inertia force, as in the previous part.

We discuss here, how the expressions of these two forces can be adapted to take into

account the finite size effect.
To determine the drag force it is necessary to take into account that the flow is non-homogeneous at the scale of the particle, thus leading to exchanges of momentum between the fluid and the particle, and which can be related to an additional drag. In Ref. [92] it has been proposed to model this aspect by introducing an effective viscosity to account for inertial effects in the drag calculation. The effective viscosity takes into account the momentum flux induced by fluctuations at the particle scale. Using the Prandtl mixing length model, it is estimated as:

$$\nu_{eff} = \nu + u'd = \nu + c\varepsilon_d^{1/3} d^{4/3} \tag{3.41}$$

where u' is the characteristic velocity at the scale of the particle that we estimated from the Kolmogorov scaling law. Thus, ε_d must be understood as the dissipation rate averaged at the particle scale. Putting aside for the moment the aspects related to ν_{eff} fluctuations and intermittency, we write that $\nu_{eff}/\nu = 1+(d/d_c)^{4/3}$ where we have introduced $d_c \approx 10\eta$ the diameter of the particle from which the effects of finite size are felt. From this turbulent viscosity, we can construct a turbulent response time for the particle:

$$\tau_p^* \to \tau_{p,eff} = \tau_p^* \frac{\nu}{\nu_{eff}} \ . \tag{3.42}$$

We have used here $\tau_p^* = \tau_p/\phi(\langle Re_p \rangle)$ introduced in the previous paragraph (3.35) in order to take into account also the finite Reynolds number effects (which are also inertial effects). The idea is then to estimate the drag force, per unit mass, from the velocity field filtered at the scale of the particle $\eta \ll d \ll L$, as $(\boldsymbol{u}_f - \boldsymbol{u}_p)/\tau_{p,eff}$.
The inertia forces of the fluid, which is directly proportional to the acceleration of the fluid, can be seen as a multiplicative cascade (as discussed in Part 1). Thus this term will be directly influenced by the filtering effect operated by the particle size. This is equivalent to considering that from the point of view of the particle the turbulent cascade stops at a scale $d > \eta$. Using a dimensional argument, we can write that the acceleration of the fluid at scale d thus varies as $a_d \sim \varepsilon_d^{2/3} d^{-1/3}$. This view is consistent with the Faxen formulation used in [45] also see [135, 254, 148]. Thus the proposal is to replace the material derivative of the fluid entering the expression of the fluid inertia term by a filtered acceleration:

$$D_t \boldsymbol{u}_f \to \overline{D_t \boldsymbol{u_f}} \sim D_t \boldsymbol{u_f} \, (d/d_c)^{-1/3} \, . \tag{3.43}$$

In this relation we used again $d_c \approx 10\eta$ as introduced previously.
With the two previous ingredients, we propose to model the motion of large particles by the following equation:

$$d_t \boldsymbol{u}_p = -\frac{\boldsymbol{u}_p - \boldsymbol{u}_f}{\tau_{p,eff}} + \beta_{eff} D_t \boldsymbol{u}_f \tag{3.44}$$

with $\beta_{eff} = \beta(d/d_c)^{-1/3}$.
This amounts to introducing two dimensionless numbers $St_{eff} = St_* \dfrac{\nu}{\nu_{eff}}$ and β_{eff} instead of St_* and β which are the relevant dimensionless numbers for the case of small particles. One can notice that for $d/\eta \gg 1$, $St_{eff} \sim (d/\eta)^{2/3}$. Thus when the inertia force of the fluid is negligible we expect to find (from what we saw with the equation (3.11)) that the variance of the acceleration behaves as $\langle \boldsymbol{a}_p^2 \rangle \approx a_\eta^2 / St_{eff}^{-1} \sim a_\eta^2 (d/\eta)^{-2/3}$. On the other hand,

when the inertia force dominates we saw with (3.22) that the variance of the acceleration was given by $\langle \boldsymbol{a}_p^2 \rangle \approx a_\eta^2 \beta_{eff}^2$, which again gives the scaling law in $(d/\eta)^{-2/3}$.
In fact, one can argue that for large particles $\eta \ll d \ll L$ the various forces are dominated by inertia and thus must exhibit a scaling law as $\varepsilon_d^{2/3} d^{-1/3}$. This can be formalized by considering the momentum exchanged between the particle and the fluid per unit time dP/dt . Placing ourselves in the reference frame of the particle, we write that dP is the mass of fluid swept by the particle ($\rho_f u' \pi d^2 dt/4$) multiplied by u'. Thus, with $u' \sim (\varepsilon_d d)^{1/3}$, we find that the acceleration of the particle, *i.e.* the momentum exchanged per unit of time and displaced mass ($(\rho_p + C_M \rho_f)\pi d^3/6$) varies as:

$$a_p^2 \sim (\rho_p/\rho_f + C_M)^{-2} \varepsilon^{4/3} d^{-2/3}. \tag{3.45}$$

Finally, assuming that the relation (3.21) giving the variance as a function of St and β proposed previously remains valid, providing we substitute β by β_{eff} and St by St_{eff}, one can thus obtain an estimate of the variance of the acceleration of large particles, given here in the limit of large Reynolds numbers:

$$\begin{aligned} \frac{\langle \boldsymbol{a}_p^2 \rangle}{a_\eta^2} &= \Gamma_a(St_{eff}, \beta_{eff}, \tau_L/\tau_d) \\ &\approx \beta_{eff}^2 + \left(1 - \beta_{eff}^2\right) \frac{\tan^{-1}(St_{eff})}{St_{eff}}\,. \end{aligned} \tag{3.46}$$

The evolution of the estimate for the variance of the acceleration as a function of d/η and ρ_p/ρ_f is shown in figure 3.8. This estimate is compared with the experimental results of Refs. [205, 263, 209]. It can be seen that the agreement is reasonable over the range of diameters and density considered experimentally. For $d/\eta \gg 1$, we find that (3.46) behaves like the asymptotic expression (3.45). The expression (3.46) is a priori valid only for large enough d/η as β_{eff} diverges for $d/\eta \to 0$. However, we can note that (3.46) behaves as (3.22) in the limit $d/\eta \to 0$. This can be shown with the series expansion of $\tan^{-1}(x)/x$ around 0. This can also be observed in figure 3.8. Nevertheless, the behavior in the transition zone between small particles ($d < d_c$) and large ones ($d > d_c$) is undoubtedly much more complex as can be seen in figure 5 of Ref. [209]. It is quite likely that in addition to preferential concentration effects, there is also the effect of lift forces.

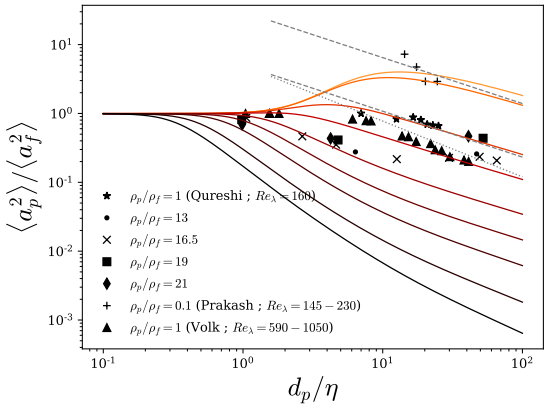

Figure 3.8: Variance of the acceleration of finite-size particles. Comparison with the experiments of Refs. [205, 263, 209] and the model (3.46) for $\rho_p/\rho_f = 0$, 0.1, 1, 2, 5, 10, 20, 50 and 100 (from orange to black). The gray dashed lines correspond to the power law $d/\eta^{-2/3}$, and the gray dotted line to the power law $d/\eta^{-0.81}$.

3.3 Stochastic modeling of the dynamics of a particle and application to LES

In this section, we are interested in taking into account the fluctuations at subgrid scale in the dynamics of particles.

3.3.1 The large eddy simulation approach

To compute a turbulent flow by the direct numerical simulation (DNS) method from the Naviers-Stokes equations, all scales of the flow must be solved. The smallest scale of the turbulence, the Kolmogorov scale η, imposes the resolution of the mesh, while the size of the integration domain must include the largest structures. It is then usually considered that the necessary number of meshes points N varies as $N \sim (L/\eta)^3 \sim Re^{9/4}$. The strong dependence of the number of operations to be performed with the Reynolds number, makes that the computational power remains the limiting factor to simulate flows at high Reynolds numbers, despite an exponential increase in the computational power. This is illustrated in figure 3.9 showing the time evolution of the largest number of mesh points and the maximum Reynolds number, based on the Taylor scale, Re_λ for DNS of incompressible and isotropic turbulent flow. We can see in this figure the counterpart of Moore's law for fluid mechanics: since the 70s, the number of mesh points has doubled every 2 years and the maximum Reynolds number Re_λ has doubled about every 8 years[6]. Nevertheless, we can note that lately, although the mesh number follows an exponential growth, this does not seem to be the case for the Reynolds number reached by these simulations. Indeed Refs. [68, 272] draw attention to the fact that the number of mesh points required for a uniform mesh is certainly underestimated by the previous relation, because of the occurrence of extreme events in the dissipation leading to fluctuations at scale well below η. Thus, at this rate, even if the power of computers continues to grow exponentially, the DNS at Reynolds numbers relevant to the applications will remain

[6]The Reynolds number based on the large scales $Re \sim Re_\lambda^2$ doubles every 4 years

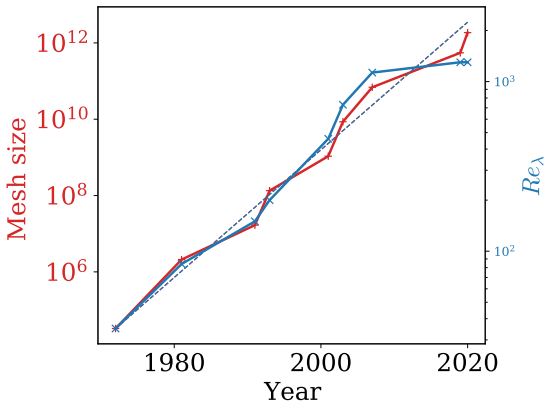

Figure 3.9: Evolution of the mesh size and Reynolds number of the largest DNS over the years. From [193, 226, 64, 262, 234, 243, 95, 119, 113, 41]. Update from Ref. [52]. Comparison with exponential growth at a rate $\ln(2)/8$ for Re_λ vs. years.

inaccessible for a long time.
The alternative proposed by the large eddy simulation (LES) approach is to decouple the required mesh size from the Reynolds number of the flow, by not resolving the smallest structures. This approach is justified because the largest structures (those that are resolved) contain most of the kinetic energy, are the most efficient in the transport phenomena while being very dependent on the flow configuration (its forcing and boundary conditions). The small (unresolved) structures are considered universal, at least when the turbulence can be assumed to be locally homogeneous and isotropic (e.g. far from the walls). Nevertheless, a model must be used for the effective action of small scales on large-scale dynamics.
The equation for the filtered velocity field $\overline{\boldsymbol{u}}$ is obtained in two steps, similar to those used to study critical phenomena with the renormalization group technique [117]. The first step of "decimation" consists in eliminating the small scales: $u_i(\boldsymbol{x},t) \rightarrow \overline{u}_i(\boldsymbol{x},t) = \int H_\Delta(\boldsymbol{x}')u_i(\boldsymbol{x}-\boldsymbol{x}',t)$. where H_Δ represents the kernel of the filter at the Δ scale, typically the mesh scale. The second step of "renormalization" consists of modifying the interaction between the remaining degrees of freedom to leave unchanged the kinetic energy of the large scales and its rate of change (transfer rate). Classically, this is obtained by introducing an effective viscosity. We thus obtain the LES equation:

$$\frac{\partial \overline{u}_i}{\partial t} + \overline{u}_j \frac{\partial \overline{u}_i}{\partial x_j} = -\frac{1}{\rho}\frac{\partial \overline{p}}{\partial x_i} + \frac{\partial}{\partial x_j} 2\nu_\Delta \overline{S}_{ij}, \tag{3.47}$$

with $S_{ij} = 1/2(\partial_j u_i + \partial_i u_j)$ the rate of strain of the flow. The effective viscosity ν_Δ models the effect of unresolved scales on the resolved scales. It can be obtained from the mixing length model [7]: $\nu_\Delta = \nu + (c_s\Delta)^2|S_{ij}|$ with $c_s \approx 0.2$ for HIT flows [87, 58].
When $\Delta \gg \eta$ the computation cost is thus much less than for DNS. But this has a price! At high Reynolds number, the dissipation is very intermittent. These very intense fluctuations of the velocity gradients over very short distances (and whose statistics depend on the Reynolds number) are not reproduced by the LES. The LES has a much lower effective Reynolds number $Re_{eff} = Re\,\nu/\nu_\Delta$. Is this problematic? Yes, if one is interested

[7] This is the Smagorinski model, there are many other models for inhomogeneous flows [201, 232]

in the coupling of the flow with other phenomena that depends on the small scales of the flow.

3.3.2 Large eddy simulations for two-phase flows

The interactions between particles and turbulence depend a priori on all scales of the flow. In order to calculate the hydrodynamic forces on the particles, it is necessary to have access to the turbulent fluctuations of the velocity field at the particle scale. But with a LES simulation the velocity field is filtered at the scale of the mesh Δ, so that the fluctuations of the field between Δ and d are not available. The naive approach then consists of simply ignoring the problem and calculating the evolution of the particles directly from $\overline{\boldsymbol{u}}$. For example, in the case of a small particle ($d < \eta$ and $Re_p < 1$) discussed earlier:

$$\begin{aligned} \boldsymbol{a}_p = \frac{d\boldsymbol{u}_p}{dt} &= \overline{\frac{d\boldsymbol{u}_p}{dt}} \\ &= -\frac{\boldsymbol{u}_p - \overline{\boldsymbol{u}}_f}{\tau_p} + \beta\overline{\frac{D\boldsymbol{u}_f}{Dt}} \end{aligned} \tag{3.48}$$

With such an approach one expects that the highest frequencies are eliminated. In order to illustrate the problems of this approach, we compare in figures 3.10 and 3.11 the variance and the PDF of the particle acceleration obtained by LES with the integration of (3.48) with the one obtained with a finely resolved velocity field (DNS). This test is performed for small, heavy $\beta = 0$ and light $\beta = 3$ particles, for different Stokes numbers and different LES resolutions. We find that the acceleration of the particles is largely underestimated with the LES approach and that the LES resolution has a strong effect on the acceleration statistics. Moreover, we see that the PDF of the acceleration tends to a Gaussian shape when the small scales are not taken into account in the calculation of the forces. This reflects that the dynamics of the particles is clearly influenced by the small scales of the flow, and shows that it is necessary to introduce the effect of the small scales not resolved by the LES.

Different approaches have been considered to account for unresolved scales in the calculation of the drag force on small inertial particles. Many of them stochastically reconstruct the subgrid scales of the fluid velocity carrying the particles [27, 204, 39, 76, 172, 115, 237, 236, 194]. Most of these models are energetic in nature and aimed primarily at reconstructing a realistic spectrum of the velocity seen by the particles but do not exhibit an explicit dependence on the Reynolds number. Therefore, the effect of the intermittency of the flow in the dynamics of the particles cannot be reproduced. Moreover, none of the cited approaches has addressed the issue of the fluid inertia force, which is essential in the dynamics of light particles.

On the other hand, approaches have been proposed to reconstruct an Eulerian field which will then be interpolated to move the dispersed phase [43, 44, 123, 88]. Among these approaches, Ref. [229] introduced the decomposition of the instantaneous fluid acceleration field into a filtered contribution and a random contribution to account for intermittency at small unresolved scales (see also Refs. [230, 276, 228]).

In Refs. [92, 279] it was proposed to consider a similar decomposition for the instantaneous

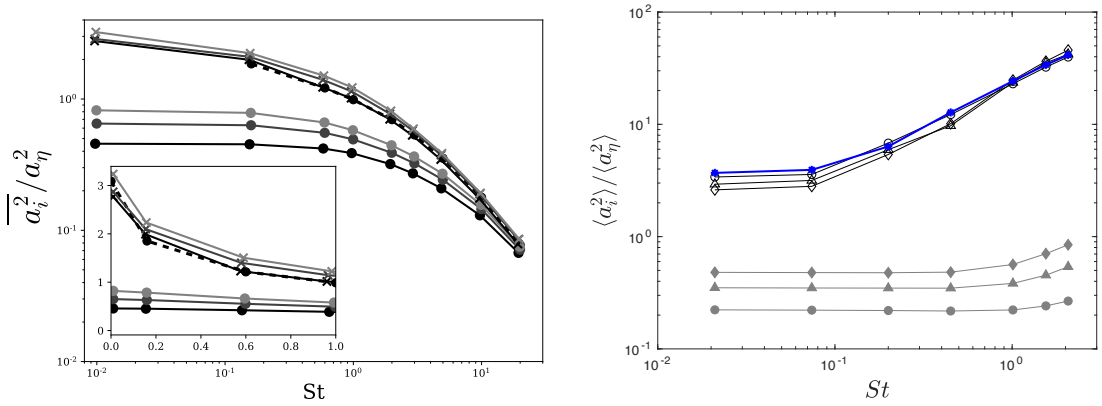

Figure 3.10: Variance of the acceleration of small particles as a function of the Stokes number . Left: for heavy particles ($\beta = 0$) in THI for $Re_\lambda = 420$, dashed lines: DNS (with $N = 2048^3$ mesh), circles: LES without model, and cross: LES with stochastic model, for $N = 64^3$, 96^3 and 128^3 from black to gray. Right: for light particles ($\beta = 3$) in THI for $Re_\lambda = 200$, blue stars: DNS (with $N = 1024^3$ meshes), solid symbols: LES without model, open symbols: LES with stochastic model, with $N = 64^3$ (diamonds), 48^3(triangles), 32^3 (circles)

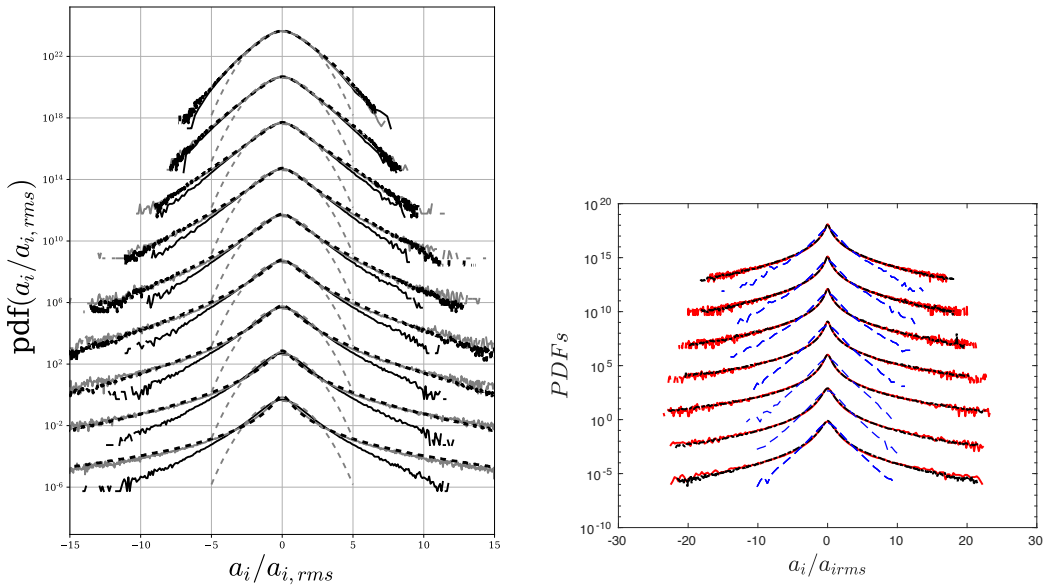

Figure 3.11: Normalized PDFs of small particle acceleration for DNS, LES without model and LES with model. Left: for heavy particles ($\beta = 0$) in THI for $Re_\lambda = 420$ for $St = 0.016$, 0.16, 0.6, 1, 2, 3, 5, 10, 20 (respectively, shifted up by one decade relative to each other for clarity), black dashed lines: DNS (with $N = 2048^3$ meshes), continuous black lines: LES without model, and continuous gray lines: LES with stochastic model, for $N = 64^3$. Right: for light particles ($\beta = 3$) in THI for $Re_\lambda = 200$ for $St = 0.02$, 0.074, 0.20, 0.45, 1.01, 1.55 and 2.07. Continuous black line: DNS (with $N = 1024^3$ meshes), blue dotted lines: LES without model, continuous red lines: LES with stochastic model, for $N = 64^3$.

acceleration of particles:

$$\boldsymbol{a}_p = \underbrace{\overline{\frac{d\boldsymbol{u}_p}{dt}}}_{\substack{\text{Filtered} \\ \text{acceleration}}} + \underbrace{\boldsymbol{a}_*}_{\substack{\text{Stochastic} \\ \text{acceleration}}} \quad . \tag{3.49}$$

The first term represents the response of the particles at large scales governed by the fluid velocity field resolved by the LES. The second, the residual acceleration, reproduces the effect of fluctuations at unresolved scales in the particle momentum balance. According to the Kolmogorov 62 hypothesis, fluctuations at unresolved scales are mainly attributed to fluctuations in the rate of energy transfer to smaller scales.
Based on the separation of timescales for the evolution of the norm of the acceleration and its orientation [199, 184], we consider here that the residual acceleration of the particles is given by the product of two independent stochastic processes, one for the norm, the other for the orientation.

$$\boldsymbol{a}_* = a_* \boldsymbol{e}_* \tag{3.50}$$

The norm of the residual acceleration is obtained from the local value of the energy transfer rate "seen" by the particle along its trajectory. This transfer rate at the particle scale is not accessible from the velocity field computed by LES and will be obtained by a stochastic log-normal model, from the energy transfer rate resolved by the LES. The stochastic process for the norm should present a correlation over a time of the order of the integral scale. The process for the orientation is obtained from a random walk on a sphere and presents a fast decorrelation on the order of the dissipative time.

Model for the norm

More specifically for the stochastic process for the norm we consider, according to the local similarity hypothesis (K62), that the main source of fluctuations comes from the fluctuations of the dissipation rate [128, 49] and that the statistics of the acceleration of the particle conditioned to the value of the dissipation seen by the particles are universal and depend only on the characteristics of the particle (size, density)

$$\langle \boldsymbol{a}_p^2 \rangle = \int \langle \boldsymbol{a}_p^2 | \varepsilon_p \rangle P(\varepsilon_p) d\varepsilon_p \ . \tag{3.51}$$

In this relation ε_p represents the dissipation rate filtered on the particle timescale. It has been shown that for particles and bubbles [92, 279] the acceleration conditioned by ε_p evolves as a power law for $\varepsilon_p / \langle \varepsilon \rangle \gg 1$:

$$\langle \boldsymbol{a}_p^2 | \varepsilon_p \rangle / \langle \boldsymbol{a}_p^2 \rangle \approx \left(\varepsilon_p / \langle \varepsilon \rangle \right)^{3/2} \ . \tag{3.52}$$

This relation is consistent with the case of fluid particles at large Reynolds number shown in the first part (see figure 2.8). We then propose to write the norm of the subgrid acceleration as

$$\begin{aligned} a_* &= \langle \boldsymbol{a}_p^2 | \varepsilon_* \rangle^{1/2} \\ &= a_\eta \Gamma_a^{1/2} (St, \beta, Re_\Delta)^{1/2} \frac{\varepsilon_*^{3/4}}{\langle \varepsilon \rangle^{3/4}} \ . \end{aligned} \tag{3.53}$$

To obtain the second line in the previous equation we used the estimate of the acceleration variance $\Gamma_a(St, \beta, Re_\Delta)$ introduced previously (3.21) (or (3.37) to take into account the finite Reynolds number effects). In order to take into account only the non-resolved part of the fluctuations, the function Γ_a is here evaluated with the Reynolds number of the subgrid scale of the flow $(\tau_L/\tau_\eta) \to \tau_\Delta/\tau_\eta = (\Delta/\eta)^{2/3} = Re_\Delta^{1/2}$, where we introduced the characteristic time of the largest unresolved scales $\tau_\Delta = \Delta^2/\nu_\Delta$.
The dissipation rate along the trajectory of the particle ε_* is considered as a stochastic variable. Its evolution is obtained here with the stochastic log-normal model of Pope [203] (also discussed in the first part (2.18)). From the Ito transformation, we obtain the stochastic process for $\varepsilon_*^{3/4}$ which depends on the local value of the transfer rate $\varepsilon_\Delta(t) = \nu_\Delta(\nabla \overline{\boldsymbol{u}})^2$ computed at the scale of the LES mesh and interpolated to the particle position.

$$\frac{d\varepsilon_*^{3/4}}{\varepsilon_*^{3/4}} = \frac{d\varepsilon_\Delta^{3/4}}{\varepsilon_\Delta^{3/4}} - \left(\ln\left(\frac{\varepsilon_*^{3/4}}{\varepsilon_\Delta^{3/4}}\right) - \frac{3}{16}\sigma^2 \right) \frac{dt}{\tau_\Delta} + \sqrt{\frac{9}{8}\frac{\sigma^2}{\tau_\Delta}} dW \,. \tag{3.54}$$

In this equation dW is the increment of the Wiener process and $d\varepsilon_\Delta^{3/4}$ is the increment of $\varepsilon_\Delta^{3/4}$ along the particle trajectory. This stochastic process ensures that $\langle \varepsilon_* \rangle = \langle \varepsilon_\Delta \rangle$ (see [92]). The parameter $\sigma^2 = 1/2 \ln \frac{\tau_\Delta}{\tau_p + \tau_\eta}$ gives the depth of the cascade. The value of the coefficient in front of the logarithm is set to reproduce the Reynolds number dependence reported by [271]. The timescale τ_Δ imposes the temporal correlation of ε_*. As discussed previously this model does not reproduce satisfactorily all the constraints of the energy cascade, but it is used here for simplicity and also because the work presented in the first part, which is an improvement of this process, was done afterwards.
To illustrate the process (3.54) we compare in figure 3.12 a realization of the dissipation rate ε along the trajectory of a solid particle at $St = 1$ and $Re_\lambda = 420$ obtained the DNS of [140] with the evolution of ε_Δ obtained by LES under the same conditions with $N = 64^3$ and the realization of ε_* obtained from stochastic process (3.54) and ε_Δ. We observe that ε_Δ (LES) shows much smaller fluctuations than ε (DNS), but that the stochastic model is able to reproduce well the intermittency of the dissipation rate for ε_* while ensuring some correlation with ε_Δ.

Model for the orientation

With the stochastic model for orientation, we first want to impose the temporal correlation of the components of the acceleration vector. In the case of weakly inertial particles, this one persists over a time of the order of the Kolmogorov scale, much shorter than the correlation scale for the norm. Thus the correlation of the components of the acceleration will be given by that of its orientation. We thus propose to model the orientation of the subgrid scale force by a random walk on a sphere with a unit radius:

$$d\boldsymbol{e}_* = \boldsymbol{e}_* \times \boldsymbol{\alpha} dt \tag{3.55}$$

In this model the position $\boldsymbol{e}_*$ is modified by a random angular displacement $\boldsymbol{\alpha} dt$. In the simplest case, when the inertia force is neglected ($\beta = 0$), the angular velocity α follows a diffusive process including restoring, damping and diffusion terms:

$$d\boldsymbol{\alpha} = -\boldsymbol{e}_* \times \frac{\overline{d\boldsymbol{u}_p/dt}}{\Delta} - \boldsymbol{\alpha}\frac{dt}{\tau_e} + \sqrt{\frac{\sigma_e^2}{\tau_e}} d\boldsymbol{W} \tag{3.56}$$

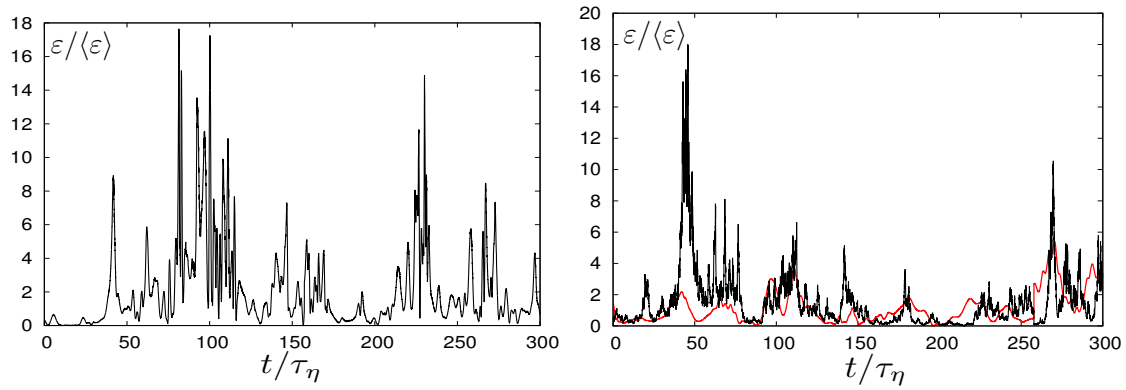

Figure 3.12: (Left) A realization of the evolution of ε along a particle trajectory at $St = 1$ and $Re_\lambda = 420$, from the DNS of [141]. (right) In red, a realization of the evolution of ε_Δ along a particle trajectory at $St = 1$ and $Re_\lambda = 420$, from a LES with a mesh size of $N = 64^3$; in black, a realization of the stochastic process for ε_*.

The diffusion term, in which $d\boldsymbol{W}$ is a 3D Wiener process, ensures the tendency to return to a statistically isotropic orientation by allowing the vector $\boldsymbol{e}_*$ to take all possible orientations (*i.e.* to visit the whole sphere). The time to return to isotropy corresponds to the characteristic time for the "walker" to invade the whole sphere and is therefore related to its characteristic (angular) velocity σ_e. The damping term is necessary to control the rate of return to isotropy at short times and thus guarantee that the orientation remains correlated over a time of the order of τ_e. We chose $\tau_e = \frac{1}{2}(\tau_p + \tau_\eta)) = 1/\sigma_e$ so that in the case of fluid particles ($\tau_p = 0$) the orientation correlation time is of the order of the Kolmogorov time, and that for very inertial particles ($\tau_p \gg \tau_\eta$) the orientation of the particle remains correlated over a time of the order of τ_p reflecting the more and more ballistic character of its trajectory. Finally, the restoring term tends to align $\boldsymbol{e}_*$ with the orientation of the resolved contribution $\overline{d_t \boldsymbol{u}_p}/|\overline{d_t \boldsymbol{u}_p}|$, and thus counteracts the diffusive tendency. Since the return to small-scale isotropy results from the cascade, the alignment between the resolved acceleration and the subgrid acceleration depends on the ratio between the resolved scale and the Kolmogorov scale. We assume that the strength of the restoring force is estimated as $|\overline{d_t \boldsymbol{u}_p}|/\Delta$. For $\tau_e \ll (|\overline{d_t \boldsymbol{u}_p}|/\Delta)^{1/2}$ the orientation becomes independent of the large-scale orientation, which is consistent with the assumption of local isotropy on small scales at large Reynolds number. On the other hand, for $\tau_e \gg (|\overline{d_t \boldsymbol{u}_p}|/\Delta)^{1/2}$ the orientation is imposed by the resolved scales.

An illustration of this diffusive process on the sphere is shown in figure 3.13.

In the case where the inertial force is not neglected ($\beta > 0$), we wish to take into account the correlation between the inertia and drag forces. Indeed, in Ref. [279], we showed that the strong increase in the flatness of the particle acceleration around $St = 1$ for light particles ($\beta = 3$) should be attributed to the correlation between these forces and their relative orientation rather than to preferential concentration effects. For $St \approx 1$ the two forces F_D and F_I are typically of the same order of magnitude and generally anti-aligned, leading to a relatively small acceleration, whereas when these forces tend to align a high acceleration will result. To reproduce this geometric effect we introduced the orientation

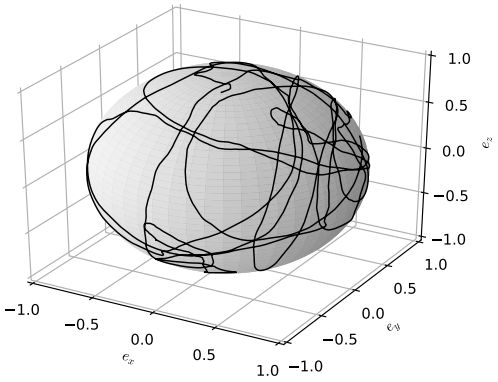

Figure 3.13: A realization of the stochastic process (3.55) and (3.56) on the sphere.

of these two forces, respectively $\boldsymbol{e_I^*}$ and $\boldsymbol{e_D^*}$:

$$\boldsymbol{a}_* = |F_D|\boldsymbol{e}_D^* + |F_I|\boldsymbol{e}_I^* \tag{3.57}$$

where $|F_D|$ and $|F_I|$ represent the norm of the subgrid contribution of the drag and inertia forces. We then write:

$$\boldsymbol{a}_* = a_\eta \frac{\varepsilon_*^{3/4}}{\langle\varepsilon\rangle^{3/4}} \left(\Gamma_D^{1/2}\boldsymbol{e}_D^* + \Gamma_I^{1/2}\boldsymbol{e}_I^*\right) \tag{3.58}$$

where the intensity of the drag and inertia forces are estimated by (3.25), and (3.26) and considering that their conditional variance both vary as $\varepsilon_*^{3/4}$. By identifying (3.58) with (3.50) and (3.53) we can write the vector $\boldsymbol{e}^*$ as $\boldsymbol{e}^* = \left(\Gamma_D^{1/2}\boldsymbol{e}_D^* + \Gamma_I^{1/2}\boldsymbol{e}_I^*\right)/\Gamma_a^{1/2}$. It should be noted, however, that in this case the vector $\boldsymbol{e}^*$ is no longer an orientation vector because it does not necessarily have a unit norm. It depends on the orientation between the two forces and their correlation:

$$\boldsymbol{e}_*^2 = \left(\Gamma_D + \Gamma_I + 2\Gamma_D^{1/2}\Gamma_I^{1/2}\boldsymbol{e}_D^*.\boldsymbol{e}_I^*\right)/\Gamma_a = 1 + \frac{2\Gamma_D^{1/2}\Gamma_I^{1/2}}{\Gamma_a}\left(\boldsymbol{e}_D^*.\boldsymbol{e}_I^* - \langle\boldsymbol{e_I}.\boldsymbol{e_D}\rangle\right) \tag{3.59}$$

To obtain the second equality, we assumed the separation of the timescales of orientations and norms which allows us to deduce that the average orientation between $\boldsymbol{e_I}$ and $\boldsymbol{e_D}$ is given by:

$$\langle\boldsymbol{e_I}.\boldsymbol{e_D}\rangle = \frac{\langle\boldsymbol{F}_D.\boldsymbol{F}_I\rangle}{(\langle F_D^2\rangle\langle F_I^2\rangle)^{1/2}} = \frac{1}{2}\frac{\Gamma_a - \Gamma_D - \Gamma_I}{(\Gamma_D\Gamma_I)^{1/2}} \ . \tag{3.60}$$

This assumption was verified in Ref. [279].
To respect the constraint (3.60) in the modeling of $\boldsymbol{e}_*$, we have introduced two, coupled, stochastic processes for $\boldsymbol{e}_I^*$ and $\boldsymbol{e}_D^*$. The evolution of the two orientation vectors $\boldsymbol{e}_I^*$ and $\boldsymbol{e}_D^*$ is given by a model analogous to (3.55)-(3.56), but the restoring term of $\boldsymbol{e}_D^*$ imposes an equilibrium configuration where $\boldsymbol{e}_I^*$ and $\boldsymbol{e}_D^*$ are anti-aligned. The details are given in Ref. [279]. This model recovers the very strong increase in flatness observed by DNS around $St = 1$. It is interesting to note that such a mechanism has already been proposed concerning the antialigment between $\partial_t\boldsymbol{u}$ and $\boldsymbol{u}\nabla\boldsymbol{u}$ for a fluid particle [259]. Note that in the limit $\beta \to 0$ this model degenerates to the orientation model detailed above.

Contribution of the resolved scales

The first term of the equation (3.49) represents the contribution of large scales to the acceleration. It corresponds to the acceleration of the particles calculated from the LES field filtered spatially and temporally: In the case where the particles are small we write :

$$\overline{\frac{d\boldsymbol{u}_p}{dt}} = G_{\Delta,\tau_\Delta} * \frac{d\boldsymbol{u}_p}{dt} = \frac{\overline{\boldsymbol{u}}_f - \boldsymbol{u}_p}{\max(\tau_\Delta, \tau_p)} + \beta \frac{D\overline{u}_f}{Dt} \tag{3.61}$$

where G_{Δ,τ_Δ} represents the convolution by a space-time filter eliminating the wave numbers higher than Δ and the frequencies higher than $\tau_\Delta = \Delta^2/\nu_\Delta$. In the context of the LES, we can consider that the spatial filtering is implicit because of the mesh resolution with scale Δ. On the other hand, the time step of the simulation, which is fixed by the CFL criterion, can be much smaller than τ_Δ ($\tau_\Delta/dt \sim Re_{eff}^{1/4}$). Thus to avoid that the resolved term develops high frequencies in response to the stochastic forcing $\boldsymbol{a}_*$, we explicitly filter the high frequencies of this term. This is simply done by replacing the response time of the drag term by the characteristic time of the smallest resolved scales τ_Δ, if $\tau_p < \tau_\Delta$. Note that in the absence of stochastic forcing this time filter does not modify the dynamics of the particle since the particle inertia effectively filters the flow fluctuations.

Results for small particles

Figures 3.10 and 3.11 present the variance and PDFs of particle acceleration obtained by LES with the stochastic model compared to those obtained by DNS and by LES without the subgrid model. We consider in these two figures the case of heavy ($\beta = 0$) and light ($\beta = 3$) particles and a range of Stokes numbers. We can see that with the stochastic model the LES reproduces these statistics in very good agreement with the DNS, contrary to the LES without submesh model, as already discussed at the beginning of the paragraph. Moreover, we find that the agreement with the DNS remains good even when the resolution of the LES is strongly reduced. In the case of inertial particles, we can see on figures 3.10 and 3.11 (left) that the LES without model approaches the DNS when St increases, meaning that particles with high inertia filter out high frequencies of the flow.

Other interesting results have been obtained. It is shown in Ref. [279] that the variance of the particle velocity increments (equivalent to the Lagrangian velocity spectra) obtained by the LES with the stochastic model becomes very close to the DNS while without the model the LES gives a strong underestimation.

We have studied the variance of the particle acceleration conditioned on the instantaneous value of the dissipation rate ε_* estimated from the stochastic model. It was observed in Ref. [279] that, similarly to the DNS results, the particle acceleration from the LES with the model increases as $\varepsilon_*^{3/2}$ for large values of the dissipation rate, and is independent of ε_* for small values of the latter. This behavior shows that the acceleration of particles in weakly dissipative regions is given by the resolved contribution $\overline{d_t \boldsymbol{u}_p}$, while larger fluctuations in the acceleration are correctly reproduced with the stochastic model.

We are also interested in the power exchanged between the particles and the fluid $\mathcal{P} = \boldsymbol{a}_p.\boldsymbol{u}_p$. This quantity presents very strong fluctuations, much larger than $\langle\varepsilon\rangle$. With the stochastic model the LES is able to reproduce these large fluctuations, both the variance and the shape of the PDFs as can be seen on figure 3.14, whereas the LES clearly underestimates this quantity when the Stokes number is small. Nevertheless, we can notice

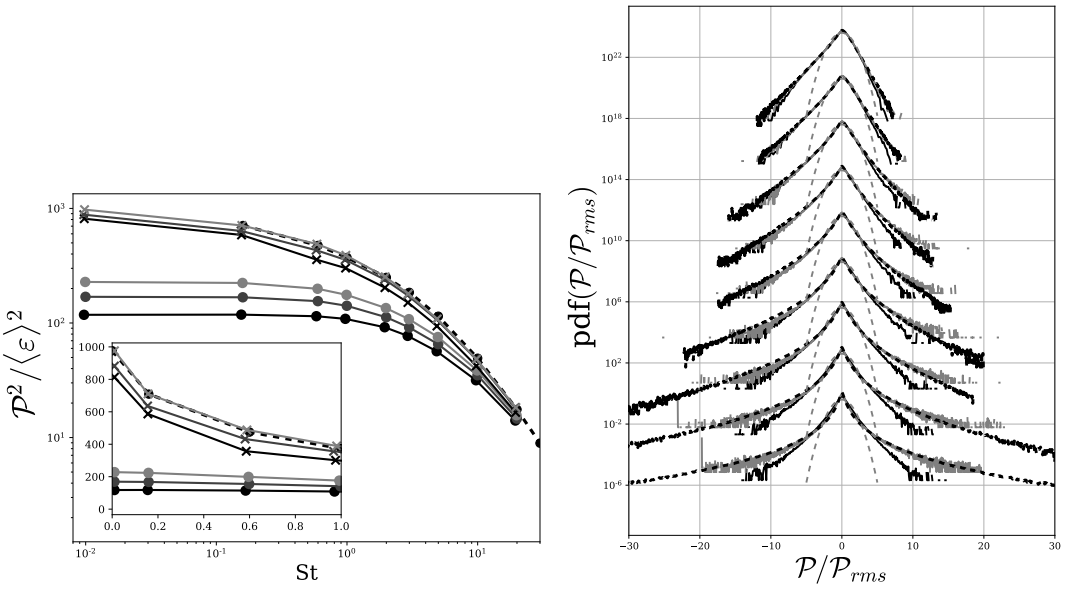

Figure 3.14: (Left) Variance of the power exchange with the fluid per unit mass of a particle normalized by the mean dissipation rate in logarithm scale. Crosses: LES with the proposed model; circles: LES without the model; for the three meshes: 64^3 (black), 96^3 (dark gray) and 128^3 (light gray). Comparison with the DNS of [21] in dashed lines. Inset zoom for small Stokes number in linear scale. (Right) PDF of the power exchange with the fluid normalized by its variance for $St = 0.016$, 0.16, 0.6, 1, 2, 3, 5, 10, 20 (respectively shifted upward by one decade from each other for clarity). gray: LES at 64^3 with the proposed model; black: LES at 64^3 without the model; black dashed line: DNS of [21] and Gaussian distribution in gray dashed line.

that the LES with the stochastic model does not succeed in reproducing the asymmetry of the PDF observed for small Stokes numbers, observed by DNS. This asymmetry is linked to the temporal irreversibility of the flow (the power $\mathcal{P}$ being the variation of the kinetic energy of the particles per unit of time). We have shown in the first part that for fluid particles this power asymmetry can be reproduced by a stochastic model and that it is linked to both the winding of the particles and the non-Markovian character of the dissipative model. This observation opens up new possibilities of improvement for the subgrid models by adapting the developments proposed in the first part to the case of inertial particles. On the other hand, it is interesting to note that when the Stokes number increases, the asymmetry of the PDF becomes much more marked and that the LES is able to reproduce it even without the addition of a stochastic model.

Results for large particles

For particles that are large compared to the Kolmogorov scale, we propose to start from (3.44) based on the effective relaxation time of the particle taking into account its finite size. In the case of the LES we write, assuming that the size of the particle remains much

smaller than the mesh size $\eta \ll d \ll \Delta$:

$$d_t \boldsymbol{u}_p = -\frac{\boldsymbol{u}_p - \overline{\boldsymbol{u}_f}}{\tau_{p,eff}} + \beta \overline{D_t \boldsymbol{u}_f} + a_* \boldsymbol{e}_* \tag{3.62}$$

In this equation we have kept β rather than β_{eff} introduced earlier, since the particle is smaller than the mesh it does not operate any additional filtering than the fluid acceleration already filtered at the mesh scale $\overline{D_t \boldsymbol{u}_f}$. The norm of the subgrid contribution is considered to be given by the relation (3.45):

$$a_* = \frac{3}{2} C_D \left(\frac{\rho_p}{\rho_f} + C_M \right)^{-1} \varepsilon_*^{2/3} d^{-1/3} \,. \tag{3.63}$$

In this equation, ε_* is the dissipation rate at the particle scale. To model this quantity we use a stochastic equation similar to (3.54) but whose exponent is adapted from $\varepsilon_*^{3/4}$ to $\varepsilon_*^{2/3}$. Another difference concerns the parameter σ^2. This one is always expressed as the logarithm of the ratio between the time of the largest non-resolved vortices (τ_Δ) and the characteristic time of the particle. In the case of large particles, we estimate the characteristic time from $\tau_{p,eff}$ introduced previously:

$$\sigma^2 = \frac{1}{2} \ln \frac{\tau_\Delta}{\langle \tau_{p,eff} \rangle} = \frac{1}{2} \ln \frac{18 \tau_\Delta \langle \varepsilon \rangle^{1/3}}{(\rho_p/\rho_f + C_M) d^{2/3}} \sim \frac{1}{3} \ln \Delta/d \,. \tag{3.64}$$

The model for orientation remains identical to (3.55)-(3.56) presented above.
Variances and PDFs for different particle sizes between 5 and 30 η and density of $\rho_p/\rho_f =$ 50, 100 and 1000 are presented in Figure 3.15. The LES results with the model are compared with the experimental results of Ref. [210, 263] and the standard LES approach, *i.e.* LES without model for unresolved fluctuations, and using either the linear drag law or the Schiller and Naumann drag law. The simulations are performed for a 64^3 mesh size. Note that we only consider relatively heavy particles $\rho_p/\rho_f > 50$, as the added-mass effects are not taken into account here. We see that both versions of the LES without model predict a strong reduction in the variance of the acceleration with increasing d/η. We also see that, as expected, in the linear drag case, the decrease is much more pronounced than with the case using the drag law proposed by Schiller and Naumann. On the other hand, with LES with the model, the decrease of the variance of the acceleration with d/η is much less important and presents a behavior close to $d^{-2/3}$.
We find that LES without model predicts a Gaussian distribution for the acceleration when Stokes drag is used. This deviates considerably from the experimental results, for which the tails of the PDF remain very broad even for a large value of d/η. With the nonlinear drag the LES without model predicts a wider distribution, which seems to be independent of the particle diameter. Nevertheless, the large fluctuations remain underestimated compared to the experiments. With the LES supplemented with the stochastic model, the PDF tails are in excellent agreement with the experiments of Ref. [263].
From (3.63), and considering that $C_D = 0(1)$, we estimate the variance of the acceleration of large particles:

$$\langle a_*^2 \rangle \sim \frac{\langle \varepsilon_*^{4/3} \rangle}{d^{2/3}} \tag{3.65}$$

From the log-normal model for ε_* we can compute $\langle \varepsilon_*^{4/3} \rangle$ as $\langle \varepsilon_*^{4/3} \rangle = \langle \varepsilon \rangle^{4/3} \exp 2\sigma^2/9$. Consequently, with the expression of σ^2 (3.64), we then estimate that $\langle a_*^2 \rangle \sim d^{-2/3-2/27} \sim$

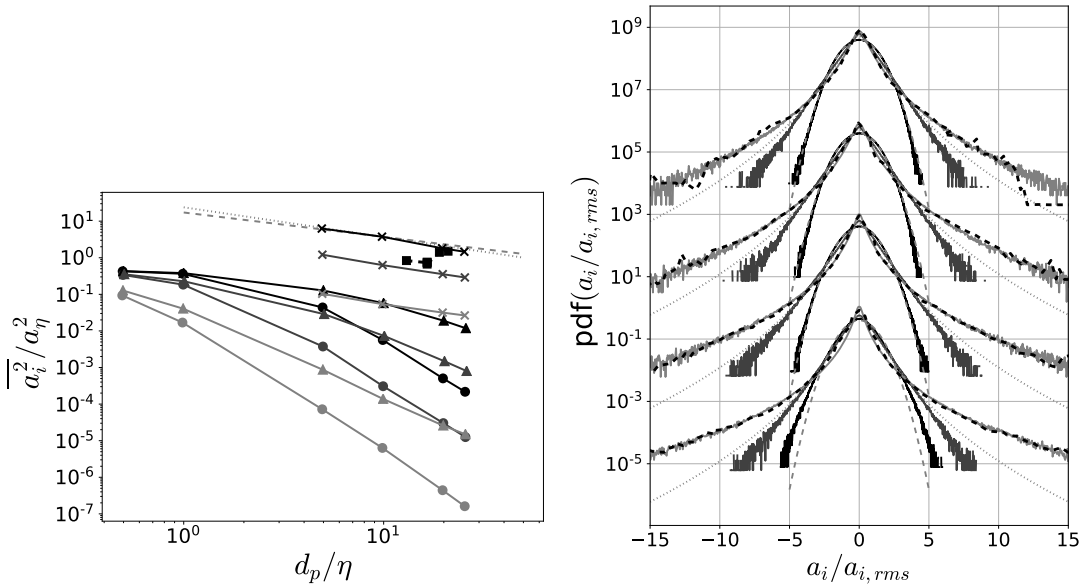

Figure 3.15: (Left) Variance of the large particle ($\Delta > d > \eta$) acceleration normalized by the Kolmogorov acceleration ($a_\eta^2 = \langle\varepsilon\rangle^{3/2}\nu^{-1/2}$) in logarithm scale. Crosses: LES with the proposed model; Circles: LES without the model with Stokes drag; Triangles: LES without the model and with the drag correction of Schiller and Naumann. For three density ratios: $\rho_p/\rho_f = 50$ (black), 100 (dark gray) and 1000 (light gray). For all cases the mesh size is 64^3. Comparison with the experiments of Ref. [209] with the particle density ratio around 50 in black squares and the power laws $< a_p^2 > \sim d^{-2/3}$ in gray dashed line and $< a_p^2 > \sim d^{-0.8}$ in gray dotted line. (Right) PDF of the large particle ($\Delta > d > \eta$) acceleration normalized by its variance for $d/\eta = 5$,10, 20 and 26 (respectively shifted upward by one decade from each other for clarity). light gray: LES with the proposed model; black: LES without the model with Stokes drag; dark gray: LES without the model and with the drag correction of Schiller and Naumann. In each case the density ratio is $\rho_p/\rho_f = 50$ and the mesh size 64^3. Comparison with the Gaussian distribution gray dashed line, with the experimental data of Ref. [263] (with $d/\eta = 1.6$, 8.2, 13.4 and 23.6) in black dashed line and with the fit from Ref. [209] in dotted line.

$d^{-0.74}$. It is interesting to note that this scaling law is relatively close to the $d^{-0.81}$ law which is shown in Ref. [263] to better describe the experimental measurements than the $d^{-2/3}$ law.
These comparisons between LES with the model and experiments show the interest of the proposed approach. Nevertheless it would be necessary to continue the comparison with experiments and particle-resolved DNS to refine the formulation of the models.

3.4 Turbulence induced by a swarm of rising bubbles

In this part, we are interested in the flow induced by the rise of a cloud of bubbles. In this system, the only source of momentum is the buoyancy acting on the bubbles, and without the bubbles the liquid would remain at rest. It is a complex system in which the movements of the bubbles and the liquid are coupled, leading to the emergence of collective

phenomena and original properties of the flow. We consider the case of a homogeneous swarm of large deformed bubbles, with a Reynolds number based on the bubble size and terminal velocity v_0 is of a few hundreds, so that each bubble generates an intense wake. A first manifestation of collective effects is the decrease in the average bubble rising speed as the gas volume fraction α increases [220]. On the other hand, the main cause of bubble velocity fluctuations is attributed to wake instabilities. Indeed, when the deformation of a bubble and its Reynolds number are large enough, the wake becomes unstable and the bubbles exhibit path oscillations [186, 278, 72] and this seems to remain the case even for high volume fractions, of the order of 30% [60]. These wake-induced fluctuations are probably the reason why bubbly flows can remain homogeneous, and be generated in laboratory bubble columns [265]. However, the stability of homogeneous bubble columns remains an open problem and is limited to reasonably small geometries (of the order of one meter) with well-controlled uniform bubble injection. In most industrial applications, the gas volume fraction is not homogeneous throughout the flow and large-scale buoyancy-induced motions develop [187].

Fluid fluctuations exhibit very specific properties that have been identified experimentally [137, 277, 85, 224, 213, 161, 220, 167, 206, 5]. Several contributions to the fluid fluctuations can be distinguished [223]. For a homogeneous swarm of bubbles, there are, on the one hand, the localized perturbations around the bubbles (due to both potential effects and their direct wake) and the turbulence induced by the bubbles. The latter is essentially driven by the interactions between the bubble wakes [220, 219, 6, 223]. The mean kinetic energy varies approximately as $K \sim \alpha v_0^2$. The velocity fluctuations are strongly anisotropic, with the variance of the vertical velocity being more intense than that of the horizontal velocity. Their PDFs are non-Gaussian, with exponential tails and a strong dissymmetry between the upward and downward directions.

The structure of this flow is also characteristic, and the velocity spectrum exhibits a rapid k^{-3} decay in a wavenumber range extending around the bubble diameters [137, 220, 5]. The origin of such a scaling law as well as its precise limits in the spectral domain remain poorly understood. From a dimensional point of view, we can write that the energy spectrum must be written as

$$E(k) = f^2 k^{-3} \tag{3.66}$$

where f is associated with the inverse of a timescale. Lance and Bataille [137] have proposed that the k^{-3} regime is associated with an equilibrium between production and dissipation and that this frequency results from the characteristic shear rate of the wakes. Other flows also present a k^{-3} spectrum. This is the case, for example, of two-dimensional turbulence at scales smaller than the energy injection scale. In this flow, the flow timescale is imposed by the conservation of the enstrophy [130, 18]. Decaying turbulence subjected to intense rotation also develops a k^{-3} spectrum with the timescale imposed by the rotation rate [24]. Another example concerns the turbulence under the wave surface and this time the timescale results from the frequency imposed by the swell [154, 257].

3.4.1 Simulation of the bubble swarm

Although the equations describing precisely this type of flow are relatively well known, their numerical simulation remains out of reach, due to the large spectrum of temporal and spatial scales involved. The smallest scales are a priori associated with the interfacial dynamics and the development of a very thin boundary layer around the bubbles, while

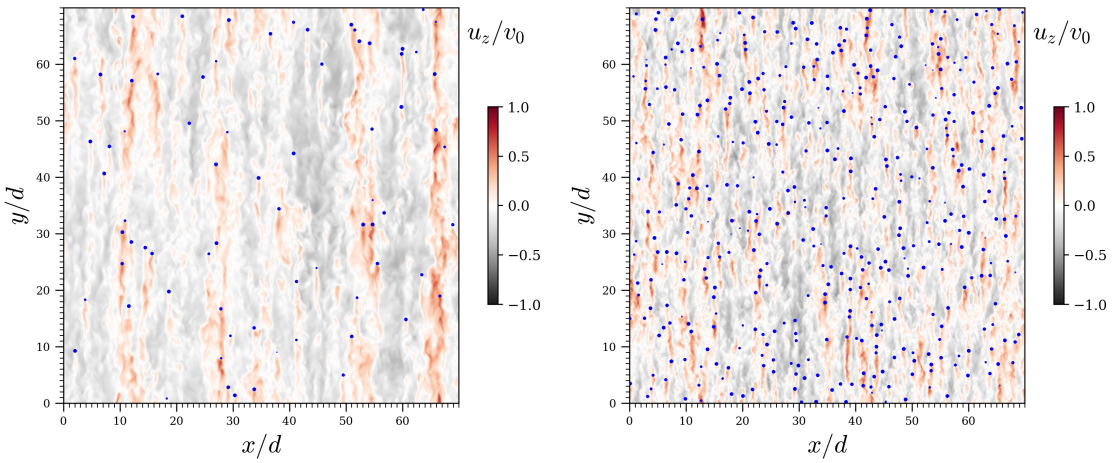

Figure 3.16: Cross-section of the vertical component of the liquid velocity field for $\alpha = 1\%$ and $\alpha = 7.5\%$. The blue points represent the position of the bubbles.

the largest scales are related to the length of the wakes and the evolution of the collective dynamics of the flow that takes place. In order to simulate these flows, and to study the structure of the fluctuations of the liquid velocity field and the stability of the bubble swarm we proposed in Ref. [144] to abandon the precise description of the flow around the bubbles as well as the capillary effects while keeping a realistic dynamic of the downstream part of each wake. This modeling, based on the Euler-Lagrange approach, allows us to simulate flows with a large number of bubbles and to focus on the interactions between wakes. As we will detail below, the main difficulty of this type of calculation comes from the self-interaction of a bubble with its own wake. We have proposed a method enabling taking into account this effect and to calculate precisely the trajectory of each bubble. This method allowed us to obtain numerical simulations of the turbulence induced by a swarm of bubbles in agreement with the experiment, as illustrated in figure 3.16.

Modeling

The use of the Euler-Lagrange approach amounts to considering a filtering of the field near the bubbles, as discussed at the beginning of the chapter. In this approach, the action of the dispersed phase on the flow is introduced as a volume source of momentum localized around the bubbles. The liquid velocity is given by the Navier-Stokes equations:

$$D_t \boldsymbol{u}_f = -\frac{1}{\rho_f}\nabla P_f + \nu \Delta \boldsymbol{u}_f + \frac{\boldsymbol{f}}{\rho_f} \quad ; \quad \nabla . \boldsymbol{u}_f = 0 \ . \tag{3.67}$$

where $\boldsymbol{u}_f$ represents a filtered velocity field around the bubbles. The volume forcing of the liquid phase is given by

$$\boldsymbol{f}(\boldsymbol{x}, t) = -\sum_{b=1}^{N_b} \boldsymbol{F}_{f\to b}(t) G_\sigma(\boldsymbol{x} - \boldsymbol{x}_b(t)) \tag{3.68}$$

where $\boldsymbol{F}_{f\to b}$ is the momentum exchange rate between the fluid and the bubble b, and N_b is the number of bubbles. G_σ is the Gaussian kernel of the projection and σ is its

characteristic size which is of the order of the diameter of the bubble. The latter is thus much larger than the mesh size: $\sigma \approx d > \Delta x$. Indeed, although the details close to the bubbles are filtered, the flow presents scales much smaller than the bubble size. These small-scale fluctuations result from the evolution of the turbulent wakes and their interactions.

The trajectory of the bubbles is obtained by solving Newton's equation (3.1) for each bubble. It involves the hydrodynamic force which depends on the velocity of the liquid (and its derivatives). This is called "two-way coupling" in the sense that the flow influences the bubbles and the bubbles influence the flow.

The use of such an approach raises some questions. (i) Which models should be adopted for the calculation of the hydrodynamic force on a bubble? (ii) Is such an approach able to reproduce the wakes? (iii) How to correct the self-induced force to obtain an adequate value of the hydrodynamic force on a bubble?

Hydrodynamic force on the bubbles As the flow is described on a smaller scale than the bubbles ($\ell \sim \Delta x < d$), the fluid motion directly induced by a bubble will be partly solved. However, the expression of the hydrodynamic forces already takes into account the fluid motion that the bubble induces in its vicinity (deviation of the streamlines, presence of a boundary layer and its possible detachment...). We assume that the usual expression of these hydrodynamic forces remains relevant, provided that their calculation is based on a fluid field in which the flow disturbance due to this bubble has been removed. We will note hereafter $\tilde{\boldsymbol{u}}_{f,b}$ such a field. We will see below that the definition of $\tilde{\boldsymbol{u}}_{f,b}$ is not trivial, and that its introduction remains an artifact for the calculation of hydrodynamic forces. Therefore rather than (3.3) giving the hydrodynamic force from the velocity described at a scale $\ell \gg d$ at the position of the bubble and its derivatives, we must consider:

$$\boldsymbol{F}_{\text{fluid},b} = f[\tilde{\boldsymbol{u}}_{f,b(\boldsymbol{x}=\boldsymbol{x}_p(t),t)} - \boldsymbol{u}_p(t), \nabla\tilde{\boldsymbol{u}}_{f,b}|_{\boldsymbol{x}_p}, D_t\tilde{\boldsymbol{u}}_{f,b}|_{\boldsymbol{x}_p}, d_t\boldsymbol{u}_p(t)] \ , \tag{3.69}$$

involving the field $\tilde{\boldsymbol{u}}_{f,b}$.

To illustrate the importance of this correction, let us specify that since the momentum exchanged with the bubble is injected over a volume of the order of $\sigma^3 \sim d^3$, the velocity of the liquid close to the bubble is of the order of the bubble velocity. Thus a naive calculation (*i.e.* without correction, $\tilde{\boldsymbol{u}}_{f,b} = \boldsymbol{u}_f$) would lead to a very low drag force. As this force does not oppose the buoyancy force, the bubble would present a non-physical acceleration which can be interpreted as a spurious self-induced force.

Let us return to the question (i). We have considered in Ref. [144] that the bubble is subject to the drag force, the added-mass force, the inertia force of the fluid, as well as the buoyancy. We have not retained the history force because it has a priori a negligible effect for large Reynolds numbers. On the other hand, when the velocity gradient is large at the scale of the bubble, the lift forces can certainly play a role. Similarly, the anisotropic effects of drag and added mass related to a non-spherical bubble are also important. We aim to reproduce the experiments performed at IMFT for millimetric air bubbles in water. Given the Reynolds number of the bubbles and the Morton number, the bubbles clearly adopt a non-spherical shape [165]. However, to simplify the modeling of the problem, we consider that the bubbles are spherical, assuming that in the case of the homogeneous cloud, the anisotropic aspects are not a priori essential. Consistently, we have as well not

retained the lift force[8]. Finally, considering that the density of the gas is very low we obtain for the dynamics of the bubble:

$$C_M \frac{d\boldsymbol{v}_b}{dt} = \frac{3C_D}{4d}(\boldsymbol{v}_b - \tilde{\boldsymbol{u}}_{f,b})|\boldsymbol{v}_b - \tilde{\boldsymbol{u}}_{f,b}| + (1 + C_M)\frac{D\tilde{\boldsymbol{u}}_{f,b}}{Dt} - \boldsymbol{g} + \boldsymbol{F}_{\mathrm{I},b} \tag{3.70}$$

The drag coefficient is chosen, in agreement with the experiment of an isolated bubble, at $C_D = 0.35$ and the added-mass coefficient at $C_M = 0.5$ in coherence with the spherical bubble hypothesis. In this equation the bubble force is calculated from the corrected liquid velocity $\tilde{\boldsymbol{u}}_{f,b}$.
Finally, the term $\boldsymbol{F}_{\mathrm{I},b}$ is a repulsive force between bubbles. It is introduced to prevent the bubbles from overlapping and to ensure that the distance between bubbles remains greater than the characteristic size σ of the momentum source.
The momentum exchanged between the bubble and the fluid via the volume force $\boldsymbol{f}$ in (3.68) is given by the sum of the drag force and the added-mass force, the contributions of the Tchen and Archimedes forces being already taken into account in the pressure term in a way consistent with the zero divergence of the flow [59, 144].

Correction of the self-induced force The fluid velocity, corrected for the influence of the bubble b, is defined by introducing the perturbation due to the bubble:

$$\tilde{\boldsymbol{u}}_{f,b}(x,t) = \boldsymbol{u}_f - \boldsymbol{u}^*_{f,b} \ . \tag{3.71}$$

Because of the non-linearity of the system, this immediately raises the question of the definition of the perturbation $\boldsymbol{u}^*_{f,b}$. It is indeed non-trivial to isolate the influence of a bubble among the fluctuations of the flow which include the effect of all the other bubbles. We propose here to define the perturbed field $\boldsymbol{u}^*_{f,b}$ as the flow generated by an isolated "imaginary" bubble, in a liquid at rest, which would have followed the same trajectory and exchanged as much momentum with the liquid phase as the actual bubble b. Accordingly, $\boldsymbol{u}^*_{f,b}$ is formally obtained by solving the following Navier-Stokes equation:

$$\nabla \cdot \boldsymbol{u}^*_{f,b} = 0 \ , \tag{3.72}$$

$$\partial_t \boldsymbol{u}^*_{f,b} + \boldsymbol{u}^*_{f,b} \cdot \nabla \boldsymbol{u}^*_{f,b} = -\nabla p^* + \nu \Delta \boldsymbol{u}^*_{f,b} + \frac{1}{\rho_f} \boldsymbol{F}_{f\to b(t)} G_{\sigma(\boldsymbol{x}-\boldsymbol{x}_b(t))} \ , \tag{3.73}$$

where the last term on the right-hand side is the forcing calculated by taking into account the actual position of the bubble and the momentum actually exchanged between the b-bubble and the liquid phase. This definition describes only the perturbation directly generated by the b-bubble, but ignores indirect perturbations resulting from the fact that the b-bubble may also have affected other bubbles and nonlinear interactions within the liquid flow. Consequently, other definitions of $\boldsymbol{u}^*_{f,b}$ can be proposed. For example, instead of isolating the trajectory of the b-bubble, one could define $\tilde{\boldsymbol{u}}_{f,b}(x,t)$ as the flow generated by the motion of all bubbles except the b-bubble. Insofar as the Reynolds number Re_b of the bubble and the volume fraction are finite, these two definitions of $\tilde{\boldsymbol{u}}_{f,b}(x,t)$ are not equivalent. We believe that there is no exact, or unambiguous, way to define $\tilde{\boldsymbol{u}}^*_{f,b}$, and this poses a fundamental problem for Euler-Lagrange approaches. At best the definition

[8] The value of the lift coefficient, and even its sign, being very dependent on the shape of the object, it would be very delicate to choose its value anyway

of the hydrodynamic force should be consistent with the expression of $\boldsymbol{u}^*_{f,b}$. But this raises the question of the experimental determination of the force, in order to establish a model of the force, in situations more complex than an isolated bubble in a well-controlled flow. In any case, computing $\boldsymbol{u}^*_{f,b}$ directly from (3.72)-(3.73) implies solving one additional Navier-Stokes equation per bubble, which is not actually practicable and we must therefore rely on approximate models.
We refer to Ref. [144] for a review of the different approaches proposed in the literature. In general, the approaches proposed previously consider particles subjected only to the viscous drag force and assume that their Reynolds number is small, in order to express the perturbation of the velocity from the Green function of the Stokes equation (Stokeslet) [231]. In Ref. [144] we propose an integral model to calculate $\boldsymbol{u}^*_{f,b}$ and its derivatives, which can be used to obtain the correct value of all the components of the hydrodynamic force and which is valid for the case of bubbles with large Reynolds number.
For the calculation of the hydrodynamic force, we only need to know $\boldsymbol{u}^*_{f,b}$ at the position of the bubble b and in its neighborhood (to calculate its derivatives). The main assumptions to obtain $\boldsymbol{u}^*_{f,b}$ are that in the vicinity of the bubble (i) given the importance of the Reynolds number, one can neglect the viscous term in (3.73) and (ii) one considers that the flow is quasi-parallel. The details of the derivation can be found in Ref. [144], but after a few steps we obtain the following integral expression for $\boldsymbol{u}^*_{f,b}$.

$$\boldsymbol{u}^*_{f,b}(\boldsymbol{x},t) = \frac{1}{\rho_f}\int_0^t \boldsymbol{F}_{f\to b}(s) G_\sigma(\boldsymbol{x}-\boldsymbol{x}_b(s)+\boldsymbol{\ell}_{adv}(t,s)) ds \ , \tag{3.74}$$

where $\boldsymbol{\ell}_{adv}(t,s) = \int_s^t \tilde{\boldsymbol{u}}_{f,b}(\boldsymbol{x}=\boldsymbol{x}_b(s'),s') ds'$. The velocity perturbation at a given position and time is obtained by integrating, over all previous instants, the momentum supplied by the bubble at the material point of the liquid at that specific position. The material point corresponding to the injection of momentum at an instant s can be advected by the undisturbed flow, and will be found at a distance $\boldsymbol{\ell}_{adv}(t,s)$ at the instant $t > s$. This $\boldsymbol{\ell}_{adv}$ term is essential to guarantee the Galilean invariance of the model. This is illustrated in figure 3.17 showing a space-time diagram of the evolution of the perturbation. By substituting (3.71) and (3.74) in the dynamics of the bubble (3.70) we notice that the expression of the hydrodynamic force on a bubble depends on the history of the whole velocity field. This amounts to say, as we wrote at the beginning of the chapter (see Eq. (3.2)), that the hydrodynamic force must in general be written as a functional of the velocity field of the fluid described at a scale ℓ (ℓ can be greater or smaller than d). In fact, with the simple model (3.74) taken for the perturbation, one can write that the force depends only on the history of the velocity field at the position of the particle, and on its derivatives, which corresponds to the functional (3.3).
We do not detail here the discretization of (3.74). The details of its numerical implementation can be found in Ref. [144]. We just mention that we have developed an algorithm similar to the one used in the first chapter to efficiently compute the history integral involved for non-markovian stochastic process, by optimizing the amount of information to be stored and the computation time. With this method, the extra cost of computing the correction term is negligible.

Wake of an isolated bubble To validate this approach of modeling of the perturbation, we considered the case of an isolated bubble rising in a liquid at rest. In this simple case,

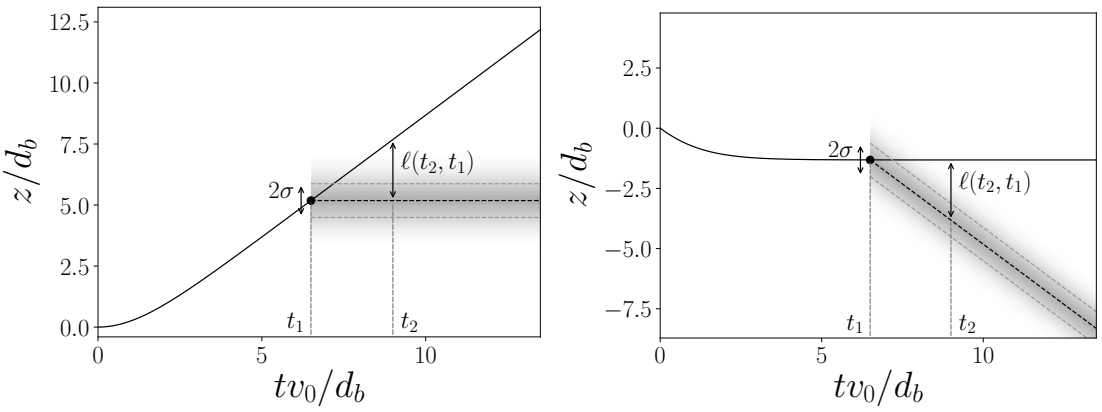

Figure 3.17: Spatio-temporal diagram of the evolution of the position of the bubble (continuous black line) and that of the material point where the momentum was injected at $t = t_1$ (dashed black lines). On the left: in the case of a zero carrier flow $\tilde{\boldsymbol{u}}_{f,b(\boldsymbol{x}=\boldsymbol{x}_b(t),t)} = 0$; on the right: in the case of uniform advection by a uniform carrier flow $\tilde{\boldsymbol{u}}_{f,b(\boldsymbol{x}=\boldsymbol{x}_b(t),t)} = -v_0\boldsymbol{e}_z$ with $\boldsymbol{e}_z$ the vertical direction. The Galilean invariance imposes the preservation of the length as shown in both cases by the distance $\ell(t_1, t_2)$. The shaded area represents the region of the flow influenced by the momentum deposited at time $t = t_1$.

we must have $\tilde{\boldsymbol{u}}_{f,b} = 0$. This allows us to compare the wake generated by the bubble with the experimental results and to determine the free parameters of the simulation (σ/d and a parameter c_0 involved in the discretization of (3.74)).
Without going into details (which can again be found in Ref. [144]), we have determined that for a range of resolution of the simulation $\Delta x/d < 1$ we have an optimal value for the ratio σ/d around $\sigma/d \approx 0.25$ allowing reproducing the wake accurately with nevertheless a clear underestimation of the velocity near the bubble. Larger values of σ further increase the filtering of the velocity near the bubble, while smaller values lead to a destabilization of the simulation due to a quantity of motion injected in a very concentrated area (the fluid velocity can thus become higher than that of the bubble).
We were able to verify that the model for the calculation of the perturbation works correctly by giving $\tilde{\boldsymbol{u}}_{f,b} = 0$ as well as for its material derivative $D_t\tilde{\boldsymbol{u}}_{f,b} = 0$. This allows us to calculate correctly the transient dynamics of the bubble and to obtain a correct rising speed and thus also to well predict the rate of momentum exchange with the liquid.
We could mention that the correction of the self-induced effect can be forgotten when $\ell \gg d$ whereas when $\ell < d$ this correction is essential. To be more precise we say that the correction is negligible if $|\tilde{\boldsymbol{u}}_{f,b} - \boldsymbol{v}_b| \gg |\boldsymbol{u}^*_{f,b}|$ and $|D_t\tilde{\boldsymbol{u}}_{f,b} - d_t\boldsymbol{v}_b| \gg |D_t\boldsymbol{u}^*_{f,b}|$. This can be tested a posteriori (once the simulation is done) by analyzing the trajectories. But we can also obtain a priori, in the simple case of the isolated rising bubble, that :

$$\frac{|\boldsymbol{u}^*_{f,b}|}{|\tilde{\boldsymbol{u}}_{f,b} - \boldsymbol{v}_b|} \sim C_D \frac{d^2}{\sigma^2} \,. \tag{3.75}$$

We conclude that it is essential to correct the fluid velocity for bubbles at high Reynolds number, since in this case $C_D = O(1)$ and $\sigma/d = O(1)$. Note that for particles moving at low Reynolds number, an estimate obtained by the Stokeslet gives $\dfrac{|\boldsymbol{u}^*_{f,b}|}{|\tilde{\boldsymbol{u}}_{f,b} - \boldsymbol{v}_b|} \sim O(d/\Delta x)$

[231, 32], which means that the correction can be forgotten for small enough objects and a sufficiently coarse description of the velocity field.
It is interesting to note that although the coupling between the two phases conserves momentum, it does not conserve its energy [269, 247]. Indeed, the power P_b of the hydrodynamic force working at the bubble velocity is a priori greater than the power P_f of the diffuse force working at the fluid velocity:

$$P_b = \sum_b \boldsymbol{F}_{f\to b} \cdot \boldsymbol{v}_b > P_f = \int dx^3 \boldsymbol{f} \cdot \boldsymbol{u}_f \ . \tag{3.76}$$

From a physical perspective, it is acceptable that energy is dissipated during the coupling. We consider a coarse description of the continuous phase, in which the strong velocity gradients in the close vicinity of the bubbles are not described. The dissipation of kinetic energy into heat that occurs in the region surrounding the bubble at scales smaller than σ cannot be calculated from the resolved velocity $\boldsymbol{u}_f$. In the case of the isolated bubble, we can estimate analytically that

$$\frac{P_f}{P_b} = \frac{C_D}{64}\left(\frac{d_b}{\sigma}\right)^2 . \tag{3.77}$$

Consequently an important part of the mechanical energy is dissipated around the bubbles, in the boundary layer and the near wake.

3.4.2 Analysis of the bubble swarm

Presentation of the simulations

With this method we simulated the flow of the rising bubble swarm. The parameters correspond to a 2.5 mm air bubble in water. The Reynolds number based on the terminal velocity of an isolated bubble is $Re_0 = v_0 d/\nu = 760$. A cubic domain of dimension $L/d = 70$ with tri-periodic boundary conditions is used. The characteristic size of the force projection kernel is $\sigma/d = 0.28$ and the resolution of the mesh is $\Delta x/d = 1/15$ which corresponds to 1024 points in each direction. We can notice that the number of mesh points per bubble can seem important for a method which does not try to solve precisely the dynamics around the bubbles. However, one must keep in mind that (i) the resolution with interface tracking methods (level-set or VOF type) for such a Reynolds number of bubbles, requires about 100 meshes per bubble (or even more) to capture the boundary layer which develops on the bubble [67] and (ii) the resolution is chosen here to capture the small scales which develop in the wakes, far from the bubbles, as we will see below.
We have simulated this flow for volume fractions of $\alpha = 1\%$, 2%, 5%, 7.5% and 10% corresponding to a number of bubbles ranging from 6500 to 65000. See the visualization of this flow for $\alpha = 1\%$ and 7.5% in the figure 3.16. In this figure, we can see the wakes generated by the passage of each bubble, and their interactions giving birth to the agitation induced by the rise of a bubble swarm.

Comparison with the experiment

We show in figure 3.18, the PDF of the horizontal and vertical components of the liquid velocity, obtained by simulations for the different α and by the experiments of Ref. [220]. It is found that for both components the PDF presents an exponential decay and that

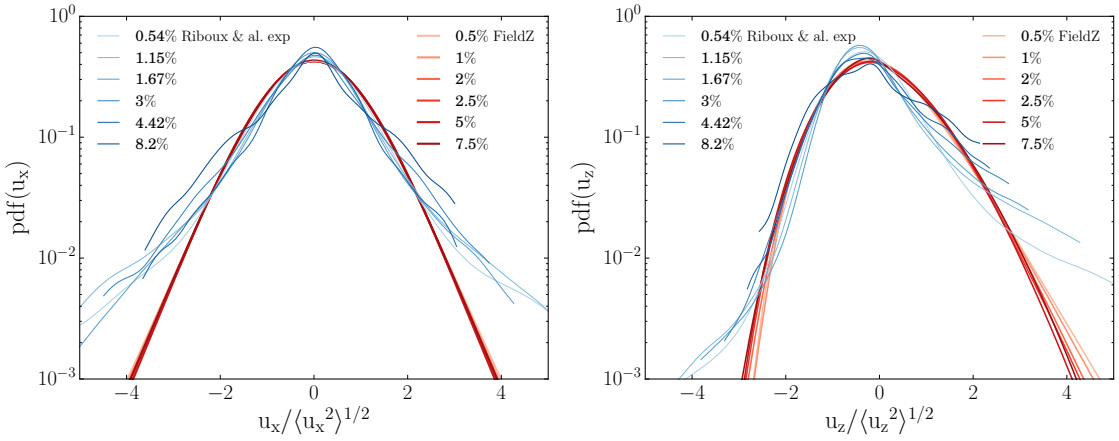

Figure 3.18: PDF liquid velocity for the horizontal velocity component (left) and the vertical velocity component (right) from the simulation for various α and comparison with the experiments of Ref. [220].

the PDF of the vertical component is clearly asymmetric. We further observe that the normalized PDFs are nearly invariant with α as the central part of the experimental PDFs. This behavior is the signature of the turbulence induced by the interactions between wakes. For large fluctuations, the experimental PDFs show a second region characterized by a less steep exponential decay. This behavior has been attributed to the large localized fluctuations very close to the bubbles, as well as to the self-sustained oscillations of the bubble trajectories [222]. As this region is not described in our modeling, we indeed find that the second exponential part of the PDFs is not reproduced by the simulations.

For the same reason, the mean velocity of the bubbles decreases only very slightly with α according to the simulations, whereas experimentally, it is observed to decrease as $\langle v \rangle / v_0 \approx 0.6\alpha^{-0.1}$ [220]. Also the kinetic energies of the liquid and the bubbles are underestimated compared to the experiment.

Figure 3.19 compares the longitudinal spectra[9] of the vertical and horizontal velocity $E_z(k_z)$ and $E_x(k_x)$ obtained experimentally and by simulations[10]. We can see that the spectra of the vertical and horizontal components are in fairly good agreement with the experiment. In particular, the simulations seem to reproduce a k^{-3} evolution of the spectra as experimentally observed on small scales (large wavenumbers) and a k^{-1} decay at large scales.

However, we note, on the one hand, an underestimation of the kinetic energy at small scales for the simulations. We attribute this underestimation to the lack of near-bubble resolution which leads to an underestimation of the power injected at the bubble scale (as discussed in the previous section). On the other hand, we also notice that the largest

[9] That is to say $E_x(k_x) = \int 1/2\phi_{xx}(\boldsymbol{k}')\delta(\boldsymbol{k}'.e_x - k_x)d^3\boldsymbol{k}'$ and $E_z(k_z) = \int 1/2\phi_{zz}(\boldsymbol{k}')\delta(\boldsymbol{k}'.e_z - k_z)d^3\boldsymbol{k}'$ with $\phi_{ij}(\boldsymbol{k}) = \sum_{\boldsymbol{k}'}\langle \hat{u}_i(\boldsymbol{k}')\hat{u}_i^*(\boldsymbol{k}')\rangle\delta(\boldsymbol{k} - (\boldsymbol{k}'))$ and $\hat{\boldsymbol{u}}$ the coefficients of the Fourier series of the velocity field $\boldsymbol{u}_f(\boldsymbol{x}) = \sum_{\boldsymbol{k}} e^{i\boldsymbol{k}.\boldsymbol{x}}\hat{\boldsymbol{u}}(\boldsymbol{k})$.

[10] With this approach, the spectra of the velocity field are very easy to obtain because the $\boldsymbol{u}_f$ field is smooth, whereas with a DNS type approach, or experimentally, the velocity of the liquid is not defined everywhere which poses some problems to make a spectral analysis. Here the approximations are made prior to the simulation, at the modeling phase, and there is no particular precaution to take for the calculation of the spectra.

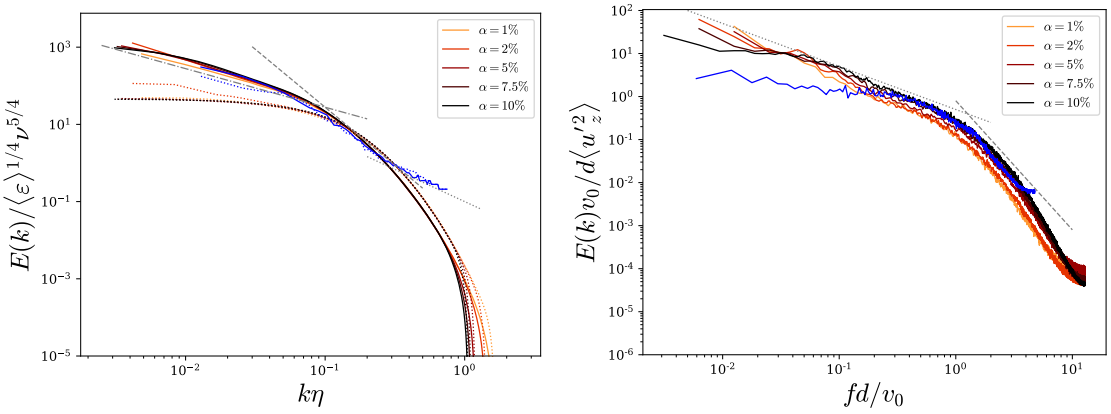

Figure 3.19: (Left) Longitudinal velocity spectra of the vertical component in the vertical direction ($E_z(k_z)$) (continuous lines) and of the horizontal component in the horizontal direction (dashed lines) from the simulations for various α ($E_x(k_x)$). Comparison, with the experiments of Ref. [220] for $\alpha = 2.5\%$ and $d = 2.5mm$ in blue, and with the power law k^{-1} (gray dot-dashed line), k^{-3} (gray dashed line) and $k^{-5/3}$ (gray doted line)
(Right) Frequency spectra of the liquid velocity at the bubble position from the numerical simulation and comparison with the experimental spectra of the liquid velocity of the flow past a random array of fixed spheres [6] in blue and with the ω^{-1} and ω^{-3} power laws.

scale of the horizontal component is also underestimated, due to the absence of bubble trajectory oscillations which limit the redistribution of the fluid energy between these vertical and horizontal components.

It has also been reported that experimentally the spectra are invariant with the volume fraction and the bubble diameter. When the spectra of the numerical simulations are normalized by the injected power and by the viscosity, we observe the same invariance of the spectra of the numerical simulation with α.

In figure 3.19 we also present the frequency spectra of the vertical liquid velocity measured at the position of the bubbles (the true velocity not the corrected velocity). These spectra is compared with the frequency spectrum of the velocity of the flow passing through an array of spheres held at a fixed position obtained in the experiments of Ref. [6] for a Reynolds number, based on the sphere diameter, of 600. Although these two flows are different, we can consider that this characterizes the fluctuations of the liquid in the reference frame of the bubble cloud. It can be seen that the simulations and the experiment also show a good agreement. For frequencies lower than d/v_0 the spectrum shows a ω^{-1} behavior while at high frequencies, the cutoff is much stronger with a slope close to ω^{-3}. It is interesting to note that this behavior seems invariant with α in the simulations and that from the experiments these temporal spectra had been reported as invariant with the Reynolds number, provided that $Re > 200$ [6].

In conclusion, we have a simulation approach which, although imperfect, allows obtaining the main characteristics of the turbulence induced by the bubble swarm as it accounts for the main ingredient: the interactions between wakes.

The spherically averaged spectra of the velocity[11] are shown in figure 3.20. Contrary to

[11] *i.e.*, $E(k) = \int 1/2\phi_{ii}(\boldsymbol{k}')\delta(|\boldsymbol{k}'| - k)d^3\boldsymbol{k}'$.

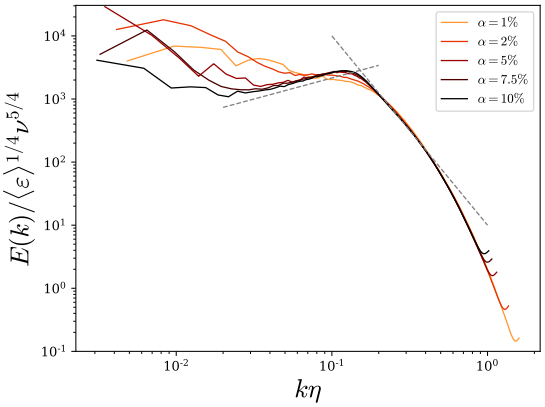

Figure 3.20: Sphericaly averaged spectra of the velocity field E from the numerical simulation at various α. Comparison with the power law k^{-3} in gray dashed line.

the longitudinal spectra presented in figure 3.19, the 3D spectra show a more complicated evolution with k as well as a rather clear dependence with α at large scales. Several regions can be distinguished. The local maximum, located around $k\eta \approx 2$ on the figure, coincides, as we will see, with the scale of the bubbles which gives the cut-off scale of the energy injection. We see that for larger wavenumbers, a region in k^{-3} clearly develops as α increases. The local minimum, located at large scales, corresponds to the wake scale. Between these two scales, the energy spectrum grows as $k^{2/3}$ for the 3 largest α and corresponds to the scales directly influenced by the wakes. The fact that the spherically averaged spectra E show such a qualitative difference at large scales with the spectra averaged over planes obviously indicates that the flow has a strong anisotropy at these scales. We will come back to the characterization of the anisotropy below.

Characteristic scales

The flow being dominated by the wakes of the bubbles and their interactions, an essential scale of the flow is the characteristic length of the wakes. To determine the latter, we consider the mean field conditioned on the position of a bubble (equivalent to a spatial phase average):

$$\langle \boldsymbol{u}_f \rangle_b(\boldsymbol{x}) = \frac{1}{T} \int dt \frac{1}{N_b} \sum_{b=1}^{N_b} \boldsymbol{u}_f(\boldsymbol{x} - \boldsymbol{x}_b(t), t) \ . \tag{3.78}$$

This mean field is illustrated in figure 3.21 for the case $\alpha = 5\%$. This figure also shows the evolution of the vertical velocity along the vertical axis passing through the bubble for the different volume fractions, as well as for an isolated bubble. The first observation is that the wakes are much shorter in the case of the bubble swarm than the wake of an isolated bubble. By plotting the logarithmic derivative of the wakes (also on the figure 3.21) we see that the wakes present a self-similar evolution for all α and that the velocity presents an exponential decrease with z. This remarkable feature is in agreement with the experimental results presented in Ref. [225]. This exponential decay of the wakes is likely due to the diffusion of the vorticity between the wakes, leading to the cancellation of the vorticity as proposed by Ref. [108].

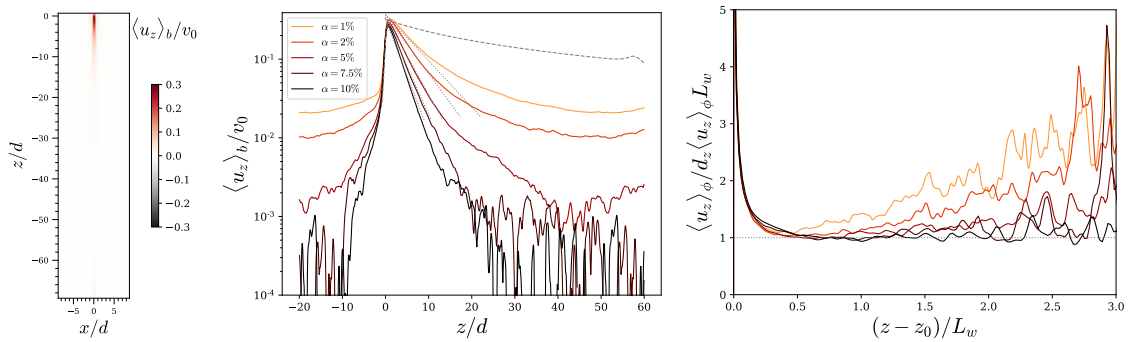

Figure 3.21: Left: cross-section of the vertical velocity conditionally averaged to the bubble position: $\langle u_{f,z} \rangle_b$ for $\alpha = 5\%$. Middle: evolution of the $\langle u_{f,z} \rangle_b$ along the vertical axis passing through the origin for the various α and for an isolated bubble (in gray dashed line) comparison with the exponential decay with a rate $L_w(\alpha)$ (in gray dotted line). Right: logarithmic derivative of the former quantity, $\langle u_{f,z} \rangle_b / d_z \langle u_{f,z} \rangle_b$, normalized by the characteristic wake length L_w.

We choose the relaxation length of the exponential as the characteristic scale of the wakes L_w. The evolution of the ratio L_w/d as a function of α is presented in figure 3.22. We can see that the length of the wakes shows evolution in $L_w \sim d\alpha^{-1/3}$. One can interpret this evolution as a simple geometrical relation, considering that the wakes tend to screen each other. It should be noted, however, that this is quite a notable difference compared to the experiments of Ref. [225] in which the characteristic length of the wakes is observed to be independent of α. This certainly reflects that there is additionally a dependence of L_w on C_D since in the experiments the average speed of the bubbles decreases with α.
From this characteristic length of the wakes, we define an inverse timescale $f = v_0/L_w$. This frequency f can be considered as imposing a shear-rate scale to small scales $k > 1/d$. This assumption allows us to estimate the average dissipation rate in the simulations as

$$\langle \varepsilon \rangle = \nu f^2. \tag{3.79}$$

Equivalently, we can interpret L_w as the Taylor length scale based on the velocity v_0, $\lambda = \sqrt{\nu v_0^2 / \langle \varepsilon \rangle}$. This is confirmed in figure 3.22 which shows that the evolution of λ/d varies as L_w/d in $\alpha^{-1/3}$.
The volume averaged power injected in the system corresponds to $\langle P_{tot} \rangle = n_b \langle P_b \rangle$ with n_b the average number of bubbles per unit of volume and $P_b = \boldsymbol{F}_{f \to b}.\boldsymbol{v}_b$ the power given by the bubble b. In the steady regime, this quantity is approximately given by $\langle P_{tot} \rangle = \alpha g v_0$ and as we have discussed above, it is larger than the power effectively received by the fluid in our simulations: $\langle P_{tot} \rangle > \langle P_f \rangle = \langle \varepsilon \rangle$. We will thus interpret $\langle P_f \rangle$ as the mechanical energy effectively injected in the wakes. Combining the previous relations, we find $\langle P_{tot} \rangle / \langle \varepsilon \rangle \sim \alpha Re_0 C_D (L_w/d)^2$ with $C_D = 4gd/3v_0^2$. Therefore at C_D and Re_0 constant, the proportion of energy injected in the wakes decreases as $\alpha^{-1/3}$.
From the estimate (3.79) of the mean dissipation rate, we compute the dissipative scale $\eta = \nu^{3/4} \langle \varepsilon \rangle^{-1/4} = \sqrt{\nu/f} \sim d\, Re_0^{-1/2} \alpha^{-1/6}$. It is this scale that is used to normalize the spectra presented in figures 3.19 and 3.20.
For $\alpha \geq 5\%$ we observe that the kinetic energy of the liquid is invariant with α and is commensurate with v_0^2. Consequently we estimate the integral scale $L_{int} = \langle K \rangle^{3/2} / \langle \varepsilon \rangle$

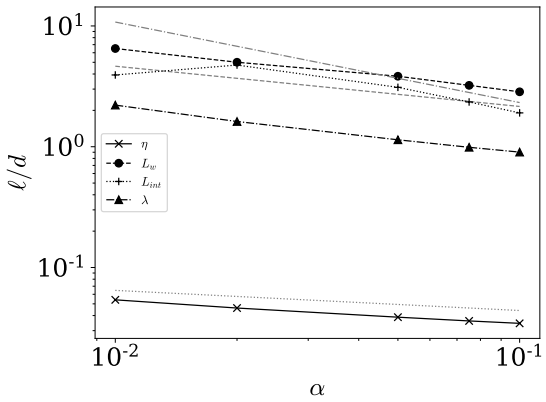

Figure 3.22: Evolution of the characteristic scales L_w, λ, η and L_{int} in the simulations of the bubble swarm with α. Comparison with the power law $\alpha^{-1/3}$ in dashed lines, $\alpha^{-1/6}$ in dotted lines and $\alpha^{-2/3}$ in dot-dashed lines.

to varies as $L_{int} \sim d\, Re_0 \alpha^{-2/3}$. This behavior is observed for $\alpha \geq 5\%$ in the figure 3.22. Note that in the experiments of Ref. [220] it is observed that the liquid kinetic energy varies roughly as αv_0^2. The discrepancy of the numerical simulations with the experiments is once again attributed to the absence of the fluctuations localized in the vicinity of the bubbles, which scales with α.

Spectral analysis of the bubble-induced turbulence

In order to identify the different regions of the spectra and to explain the observed scaling laws, we are interested in the spectral decomposition of the energy balance:

$$\frac{d}{dt}E(k) = T(k) - D(k) + P(k). \tag{3.80}$$

The terms of the right-hand side correspond respectively to the inter-scale energy transfer from a scale k (T), the kinetic energy dissipation at a scale k (D) and the energy injection (P). The expressions of these different terms are obtained from the Navier-Stokes equation (3.67). The transfer term T is the contribution of the non-linear terms[12], $D(k) = 2\nu \mathrm{k}^2 E(k)$ and $P(k)$ is the integral over the wave numbers $|\boldsymbol{k}| = k$ of the real part of $\hat{f}_i \hat{u}_i^*$. At steady state, the left-hand term of (3.80) is zero, so $T = D - P$. We present in figure 3.23 the terms $P(k)$ and $D(k)$ for the various α. We can see that the production term presents a cutoff for $k > 1/\sigma$ (we recall that $\sigma/d = 0.28$), and that on large scales it grows as k^2 for the largest α, while it is roughly constant for small α. Concerning the dissipation term, we notice that it also presents a peak around $k \sim 1/\sigma$. At large scales, the production dominates compared to the dissipation, which implies that $P(k) \approx -T(k)$. On the other hand, the dissipation dominates on small scales ($D(k) \approx T(k)$). From the absence of scale separation between the peaks of production and dissipation, we can conclude that this flow does not present an inertial zone. These budgets also show that there is no range of scales in which there is an equilibrium between P and D. This contradicts the hypothesis

[12] $T(k) = \int \sum_{k'} \left[-ik'_j (\widehat{u_i u_j} \widehat{u_i}^* + \widehat{P} \widehat{u_j}^*) \right] \delta(\boldsymbol{k'} - \boldsymbol{k}) \delta(|\boldsymbol{k}| - k) d^3\boldsymbol{k} + C.C.$, where $+C.C.$ denotes the complex conjugate terms

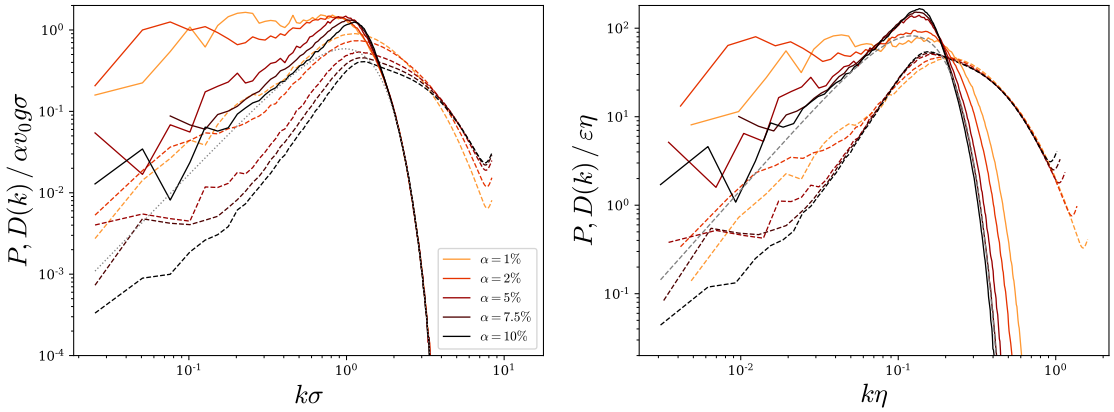

Figure 3.23: Evolution of P in continuous line and of $-D$ in dashed lines for the various α. Comparison with $\alpha g v_0 \sqrt{2/\pi}(k\sigma)^2 \exp(-k^2\sigma^2)$ in dotted line. Left: the power density and wavenumber are normalized by $\alpha g v_0 d$ and σ respectively. Right: the power density and wavenumber are normalized by the dissipative scales $\varepsilon\eta$ and η respectively.

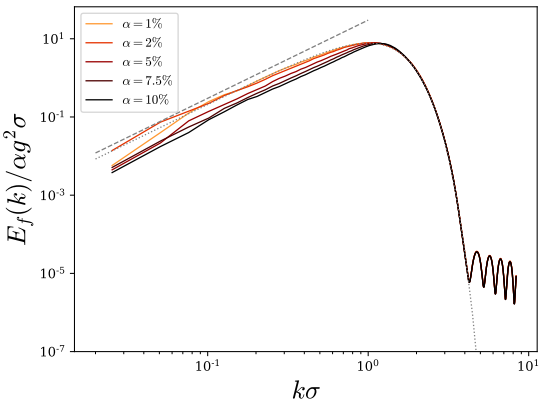

Figure 3.24: Spectra of the force E_f for the various α and comparisons with (3.81) in dotted line.

made in [137] to explain the presence of a k^{-3} zone in the velocity spectra. Furthermore, we notice that the k^{-1} region of D, which corresponds to the k^{-3} region of the velocity spectra, is observed in the crossover between the production dominated scales and the dissipation dominated scales.

To interpret the behavior of the production term P, we study the spectra of the force applied to the flow, $E_f(k)$, corresponding to the spherical averaged of $\hat{f}_i \hat{f}_i^*$. From the expression of the coupling force between the phases (3.68), we can obtain the following analytical expression for E_f:

$$E_f(k)/\alpha\sigma g^2 = \frac{1}{12\pi}(d/\sigma)^3 (k\sigma)^2 e^{-(k\sigma)^2}. \tag{3.81}$$

For this calculation we have assumed that (i) the positions of the bubbles are independent from each other and that (ii) the fluctuations of the rate of momentum exchanged between the bubble and the liquid are small: $\langle \boldsymbol{F}_{f\to b}^2 \rangle \approx \langle \boldsymbol{F}_{f\to b} \rangle^2 = (\rho g \pi d^3/6)^2$. The spectra of the

force is presented in figure 3.24. We note that for all volume fractions the agreement with the proposed expression is relatively good. We distinguish two regions: a region which grows as k^2 which reflects the equipartition of the fluctuations of the forces at large scales ($k < 1/\sigma$) and an exponential cut-off imposed by the Gaussian projection kernel for $k > 1/\sigma$. We notice that for high volume fractions, the positions of the bubbles are not really independent anymore, because they cannot overlap, which explains the discrepancy with (3.81).
Similarly, considering that the fluid velocity at the position of the bubbles is independent between the different bubbles and of the order of the bubble velocity we can estimate that P follows the same behavior as E_f. Namely, we can have :

$$P/\alpha g v_0 \sigma \sim (k\sigma)^2 e^{-(k\sigma)^2} \tag{3.82}$$

Indeed P presents an exponential damping for $k > 1/\sigma$, that overlaps for all α when normalized by $\alpha g v_0 \sigma$ as can be seen in the figure 3.23 (left). For $k < 1/\sigma$, P increase roughly as k^2 in agreement with the previous relation for $\alpha > 2\%$. The underestimation of P at large scales is attributed to the fact that the fluctuations of the velocity at the bubble position are important as can be seen on the frequency spectrum if figure 3.19 (right): $\langle \boldsymbol{u}_f(x = x_b)^2 \rangle > \langle \boldsymbol{u}_f(x = x_b) \rangle^2$. For small α, P no longer follows the proposed relation on large scales due to the presence of large structures in the flow leading to a significant correlation of the liquid velocity between distant bubbles.
For completeness, we present in figure 3.23 (right) the production and dissipation terms normalized by the dissipative scales $\langle \varepsilon \rangle$ and η for the various α. As noticed previously, with this normalization, we observed an overlap of the high wavenumber (typically $k > 1/2\eta$) part of D for all α. From the estimates of the characteristic scales of the previous section, we have $d/\eta = Re_0^{1/2} \alpha^{1/6}$, indicating that the gap between the production dominated scales and the dissipation dominated scales increases, slowly, with α. It seems that the k^{-1} subrange of D is observed in this gap of scales, provided that α is large enough.
In conclusion, we consider that for $k < 1/d$ the flow structure is driven by the interactions between wakes, while in the range $1/d < k < 1/\eta$ the strong damping of the wakes imposes a shear scale.
This assumption of constant shear rate f across scales allows us to explain the presence of a power law in k^{-3} for the flow, thanks to a matching argument similar to that proposed by Kolmogorov in 1941. It is assumed that at scales that are small compared to the length of the wakes ($k \gg 1/L_w$) the structure of the flow depends only on the diameter of the bubbles d, the viscosity, and the shear rate f :

$$E = E(k; d, \nu, f). \tag{3.83}$$

It is assumed that at scales larger than $\eta = \sqrt{\nu/f}$, one can neglect the effect of viscosity. Therefore, in this limit we can write:

$$E = E_I(k; d, f) = d^3 f^2 \Phi_I(kd) \tag{3.84}$$

where Φ_I is a dimensionless function. Conversely, at scales much smaller than the bubble size, we will suppose that this diameter does not play a role anymore, and we will make the hypothesis that

$$E = E_S(k; \nu, f) = \nu^{3/2} f^{1/2} \Phi_S(k\eta) \tag{3.85}$$

where Φ_S is another dimensionless function. Finally, if we assume that for a range of intermediate scales ($1/d \ll k \ll 1/\eta$), the two previous relations remain valid, we have $E_S(k) = E_I(k)$. Since kd and $k\eta$ can vary independently, the previous equality can hold only if the following expressions are constant:

$$(kd)^3\Phi_I(kd) = (k\eta)^3\Phi_S(k\eta) = c \tag{3.86}$$

This gives us for the velocity spectra:

$$E(k) = cf^2k^{-3} \tag{3.87}$$

in a range of scales where the shear rate can be considered constant.

The temporal spectra of the velocity seen by the bubbles (presented in figure 3.19 right) is influenced by the fact that the bubbles cut the wake of other bubbles. Thus the high frequencies of the temporal spectrum are dominated by the Doppler shift due to the high-speed crossing, of the order of v_0, of the dissipative structures of the flow. So using (3.87) and taking the argument of Ref. [255], with $\omega \sim v_0 k$, we can estimate the high frequency behavior of the frequency spectra:

$$E(\omega) = E(k)\frac{k}{\omega} = f^2 v_0^2 \omega^{-3} \, . \tag{3.88}$$

The temporal spectra from both the experiments and the simulations present a ω^{-3} zone at high frequency.

We have seen that at large scales ($k \ll 1/d$), where the flow is dominated by wake interactions, there is a balance between production and inertia. At these scales we notice that the 1D spectra of the velocity present a k^{-1} dependence. This means that each decade contains an equal amount of energy. This behavior can be explained by the intermittence of the wake passages, giving rise to an alternation between periods of activity and calm [158]. At these scales, the characteristic velocity no longer depends on a specific length scale and corresponds to the typical velocity of the bubbles v_0. These periods of activity (the wakes) are characterized by their self-similar character [11, 160] and present a variable intensity and duration, whereas the calm periods follow a Poissonian distribution reflecting the quasi-uniform distribution of the bubbles. The absence of a characteristic length leads directly to the absence of a characteristic time for the fluctuations. Hence the frequency spectrum of the velocity also shows a decay close to ω^{-1} at low frequency. As pointed out by Mandelbrot [155], these behaviors in ω^{-1} and k^{-1} must also be connected to the non-Gaussianity of the velocity distributions as well as to a long-range correlation of the velocity.

To extend the discussion on the large scales, we need to take into account the anisotropy of the flow. For the characterization of the anisotropy, it is necessary to distinguish the fact that the energy can be carried mainly by one component of the velocity vector (anisotropy between components) from the fact that the fluctuations in certain directions can carry more energy (directional anisotropy) [233]. To characterize the latter, we consider a spherical coordinate system of the wave vector space, as schematized in the figure 3.25. The angle θ characterizes the orientation of the wave vector with respect to the vertical direction: $\sin\theta = k_z/|k|$ ($\sin\theta = 0$ corresponds to fluctuations in the horizontal direction

and $\sin\theta = \pm 1$ to fluctuations in the vertical direction). We then consider the directional spectra $E(k,\theta)$ which allows decomposing the energy of the fluctuations according to the wavelength and the orientation with respect to the vertical direction[13].
We show in the figure 3.25 the directional spectra of the velocity for $\alpha = 10\%$. It can be seen that at large scales ($k < 1/\sigma$) the energy is concentrated in the horizontal direction. This concentration is characteristic of vertically aligned tubular structures [47], which can be seen on the flow visualization in figure 3.16. At smaller scales ($k \gg 1/\sigma$), one can see that the directional spectra become invariant with θ indicating that the directional anisotropy tends to vanish.
To characterize the anisotropy between components, we present as well in the figure 3.25 the directional spectrum for the vertical component of the velocity and for the horizontal component[14]. At large scales, we notice that the spectra of the vertical kinetic energy is very similar to that of the total kinetic energy, which indicates that at these scales the vertical component caries almost all the kinetic energy. This can be explained simply by the fact that the forcing due to the bubbles is essentially vertical. We can also note that the horizontal component of the velocity presents a very weak directional anisotropy. Finally, at small scales, we notice that the flow tends to become much more isotropic and presents both a decrease of the difference between the components and between the directions. This indicates that at scales where the energy injection is zero, there is a redistribution between the components that ensures a return to isotropy as k increases.
It should be noted that when considering the spectra with angular dependence for the horizontal and vertical components, no k^{-3} zone is distinguished. Thus, as noticed by Ref. [24] for the decaying turbulence under strong rotation, the k^{-3} region for the spherically averaged spectra results from an average between the different directions and the different components, raising the question of the universality of the k^{-3} power-law subrange.
If the structure of the flow becomes locally isotropic at scales much smaller than σ, one should expect the appearance of a $k^{-5/3}$ inertial range for the velocity spectra, if the local Reynolds is large enough, since at these scales there is no more energy injection. Such inertial range is not present in the numerical simulations reported here, but seems visible in the spectra obtained from the experiments of Ref. [220] (see figure 3.19 left). In case the velocity spectra first present evolution as $E(k) \sim f^2 k^{-3}$ followed by an inertial range $E(k) \sim \langle\varepsilon\rangle^{2/3} k^{-5/3}$, the characteristic length of the crossover between these two regimes would be given by $\ell_I = \sqrt{\langle\varepsilon\rangle/f^3}$. It is interesting to note that this length scale corresponds to the classical estimates of the scale from which a turbulent flow subject to mean shear can be considered as locally isotropic [53, 201]. Taking the usual Kolmogorov scale $\eta = \nu^{3/4}\langle\varepsilon\rangle^{3/4}$, the extension of the inertial regime is given by $\ell_I/\eta = (\langle\varepsilon\rangle/\nu f^2)^{3/4}$. In the simulations, as mentioned previously, no inertial range is present ($\ell_I = \eta$) and we have indeed $\langle\varepsilon\rangle = \nu f^2$. It is likely that a larger power injection in the simulations (e.g. increasing C_D) would allow to obtain a separation between the scales of return to isotropy and the dissipative scales and thus to obtain a $-5/3$ range in agreement with the experiments. Nevertheless, even in absence of the $k^{-5/3}$ regime, this indicates that the

[13] In a more formal way $E(k,\theta)$ is defined by integration on all "longitudes" for a fixed "latitude" and modulus of the wave vector: $E(k,\theta) = \int 1/2\phi_{ii}(\boldsymbol{k}')\delta(|\boldsymbol{k}'| - k)\delta(k_z'/|\boldsymbol{k}'| - \sin\theta)d^3\boldsymbol{k}'/2\pi\cos\theta = \int_0^{2\pi} 1/2\phi_{ii}(k,\theta,\phi)k^2\sin\theta d\phi/2\pi\cos\theta$. The normalization factor $2\pi\sin\theta$ is introduced to correct the geometrical effect due to the fact that a band near the poles covers a less important surface than a band near the equator.

[14] Because of the axisymmetry of the flow we have $E(k,\theta) = E_z(k,\theta) + 2E_x(k,\theta)$.

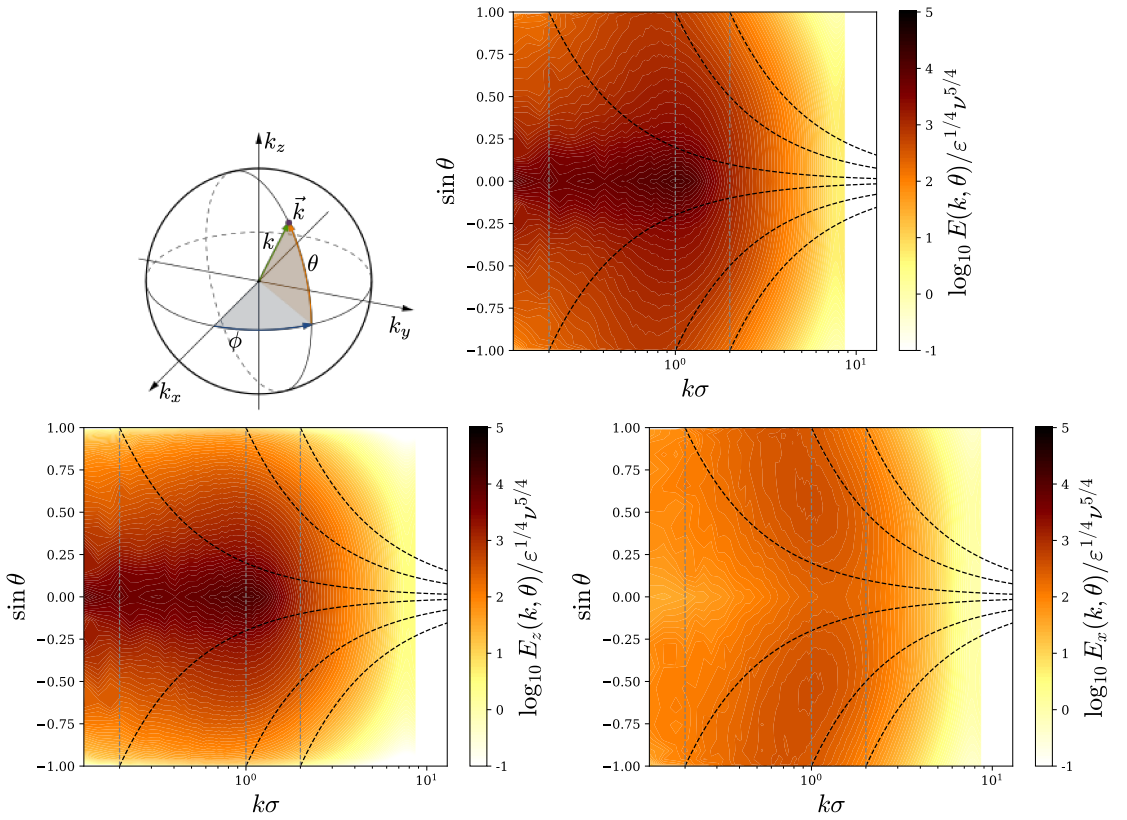

Figure 3.25: (a) Scheme of spherical coordinates in the Fourier space. (b) (c) and (d) Directional spectra of, respectively, the velocity vector, the vertical velocity component and a horizontal velocity component, for $\alpha = 10\%$. Note that the spherical spectra corresponds to an integral along a gray dashed line, while the longitudinal spectra in the vertical direction are obtained by integration along a black dashed line.

rate of shear imposed by the bubble wakes control the relaxation to small-scale isotropy.

3.4.3 Summary

We summarize the results presented in this section. Firstly, regarding the coarse-grained numerical approach, we have shown that it is possible to use the Euler-Lagrange framework for simulating the dynamics of large objects, that is to say much larger than the grid size. For this, it is mandatory to correct the spurious self-induced effect in the dynamics of the bubbles. For that purpose we proposed a model that allows determining the undisturbed fluid velocity for objects moving with quite a large Reynolds number, and then to obtain a relative velocity of the objects used for the computation of the hydrodynamic forces. Although this approach has some limitations, since the fine scales in the vicinity of the bubbles cannot be reproduced, it is nevertheless a nice tool to study the collective phenomena at play in the bubble column flow. We have shown that the interacting wakes lead to a screening mechanism of bubble wakes, as observed experimentally. We have also shown that the k^{-3} subrange of the energy spectra results from a rate of shear imposed by the bubble wakes. On larger scales the energy spectra evolves as k^{-1} indicating a Poissonian

spatial distribution of the wakes along with long-range correlation.

3.5 Perspectives

Concerning the statistical analysis of the dynamics of particles in turbulence, presented in §3.2, we can mention the following tracks for future works. Firstly, we would like to complete the panorama of the effect of the various forces by accounting for the effect of gravity and lift forces. We have done some preliminary work on the subject during the PhD of Zhentong Zhang, where we observed a significant anti-correlation between the fluid inertia force and the lift force for bubbles in a turbulent flow with Stokes numbers larger than one. To explain this observation we proposed to express the particle dynamics equation as $a_{p,i} = -R_{ij}(u_{p,j} - u_{f,j}) + B_j$, where the acceleration of the particle dynamics is given by a relaxation tensor R, with a diagonal part that accounts for the drag and a skew-symmetric part due to the lift force, and a forcing term B that accounts for fluid inertia effects and gravity. Qualitative explanation of these correlations were obtained by estimating the order of magnitude of the invariant of R. But a further analysis of this problem would be interesting as complex interplays between the various forces are present. It would also be useful to study the statistics of the particle acceleration and hydrodynamic force contributions conditional on the velocity of the particle, or of the fluid, similarly to the work presented in the first chapter for a fluid particles (see §2.3), and more specifically to analyze the effect of the Stokes number and density ratio on the correlation between velocity and acceleration.

Regarding the second part of this chapter dealing with the stochastic modeling for LES simulations (see §3.3), we would like to develop further stochastic model for the particles accounting for the, probable, dependence on the velocity, as discussed in the point just above. Based on the approach proposed in §2.4, we could propose an alternative framework to the decomposition between the norm/orientation presented in §3.3. Beside being simpler, we think that it can offer a more accurate and general description of the particle dynamics. A first step in this direction would be to consider the coupling of the model proposed in the first chapter for fluid particles with LES. Also of interest would be to consider the coupling with Lagrangian models for the velocity gradient tensor, as proposed for example in Refs. [89, 168, 114, 195]. With such an approach, we could obtain the evolution of the fluid velocity, acceleration and spatial derivatives along the path of particles. That opens the way to propose stochastic modeling of the particle dynamics accounting for further forces (e.g. lift forces), but also more complex sub-grid scale phenomena such as the fragmentation. Finally, let us mention that the goal of LES is to be able to predict flows in complex geometries, and in those conditions the local isotropy assumption at sub-grid scale may not hold, due for example to strong means shears. In that respect, it would be interesting to account for anisotropy and non-homogeneity of the flows, on the subgrid scale motion of the particles. Recently, Ref. [17] proposed stochastic modeling for the subgrid scale contribution with a preferred direction for the orientation imposed by the mean shear. Alternatively, we could extend the vectorial stochastic model proposed in the first chapter (2.4) to introduce dependence on the mean rate of shear tensor in the drift and diffusion terms.

Finally, let us mention some perspective concerning the simulations of the bubble swarm

presented in §3.4. First, regarding the approach, although we obtained a very good agreement for the energy spectra with the experimental measurements, the simulation will certainly be more accurate if one adopts a more detailed description of the bubble dynamics accounting for example for lift force, and non-spherical bubble shape (implying a tensorial drag and added-mass coefficients). It will also be interesting to consider the model for the large particles presented in §3.2.2 and 3.3.2. Although this model was derived for particles with size lying in the inertial range of locally isotropic turbulence, it could be an efficient way to account for fluid fluctuations at bubble scale in this flow. We could also improve the self-induced force correction. The model presented above can be seen as a first-order model, and one can consider a perturbative approach to account for correction terms at the higher orders. Since the bubble Reynolds number remains moderate, it is possible that only the second-order terms may be enough to account for the non-linear effect and reproduce, at least qualitatively, the wake induced instability of the bubble path. Note that, to our knowledge, no simulation in the Euler-Lagrnage framework has reproduced the zigzagging or spiraling motions of a rising bubble. Moreover, as discussed in §3.4.2 we think that the absence of this intrinsic instability is one of the main missing features of the simulations. Finally, we think that the model for the correction of the self-induced force can also present some interest outside the framework of Euler-Lagrange approach. As such model enables to define the fluid velocity at the particle position and thus the particle relative velocity, it can be of some help to propose a model for the hydrodynamic forces from measurements of the particles acceleration and total forces obtained from experiments and detailed DNS resolving the bubble interfaces.

We think that one of the interests of the kind of simulation presented in §3.4, is to provide a way of studying the stability condition of a bubble swarm. In the simulation presented above, the bubble cloud was observed to remain homogenous, but usually large-scale bubble columns tend to develop some instabilities that eventually lead to non-homogenous bubble distribution and large-scale recirculations. One way of studying the question could be to consider the simulations subject to various initial distribution of bubbles and boundary conditions to first analyze the sensitivity to injection conditions, and the presence of shear. We can also focus on setting with a large scale forcing of the flow, as considered for example in Ref. [5] or by Gabriel Ramirez (who his preparing his PhD at CEA). We could then study under which conditions in terms of length and energy scales the peculiar dynamics induced by a cloud of rising bubbles could be predominant, or how the turbulence will be modulated by the presence of the bubbles.

4 Magnetic fields, particles and turbulence

Contents

The coupling between electromagnetism and fluid mechanics, or MHD for magnetohydrodynamics, finds applications in very varied contexts ranging from liquid metal or ionized gas at a laboratory scale to conducting matter constituting the planets and the stars. In this chapter, we mainly discuss two projects, in which we have worked in collaboration with the CEA. The first one is about the magneto-thermoconvection of a liquid metal, in a context of prevention of nuclear power plant accidents. It has been the PhD subject of Sébastien Renaudière de Vaux and of Julien Guillou supervised with Wladimir Bergez and Philippe Tordjeman. The second one is related to bubble detection in a liquid metal, in the context of fast neutron reactors cooled by liquid sodium, and was studied during the PhD of Rafael Guichou, and Antoine Afflard and the PhD of Youssef Nasro Allah also supervised with Wladimir Bergez and Philippe Tordjeman. The common point of these two projects, and their main originality, is to involve flows subjected to an alternating magnetic field.

4.1 Convection of a liquid metal subject to alternating magnetic field

When an alternating electromagnetic field is applied to an electrically conductive fluid, typically a metallic liquid, electric currents are induced in it, they are called eddy currents or Foucault's currents. The induced currents generate both a heating of the fluid by Joule effect, and a volume force in the fluid resulting from their interactions with the applied magnetic field. These effects are used for induction heating or electromagnetic stirring applications. Additionally, when temperature heterogeneities are important, the buoyancy differences in the liquid can also lead to natural convection.

The objective of this project is to identify the different regimes that can be encountered when a metallic liquid is subjected to an alternating magnetic field and a different temperature on the boundary. In particular, we are interested in the influence of these regimes on the heat transfers. For this purpose, we consider the configuration of a liquid metal in a cylindrical container whose upper and lower walls are controlled in temperature (like in the Rayleigh-Benard convection, RBC) and surrounded by a coil through which an alternating current flows as depicted in figure 4.1. This device allows controlling the importance of the Laplace force and of the buoyancy force as well as the relative importance of the volume heating compared to the wall heating. During the thesis of Julien Guillou, we studied this flow by direct numerical simulations and experimentally, thanks to an experimental setup developed during the thesis. This study was motivated to simulate inductive heating experiments for studying severe accidents in the nuclear industry [116].

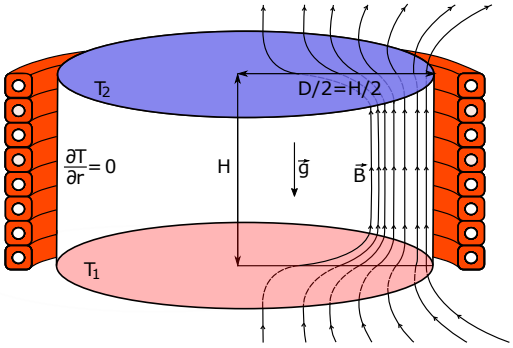

Figure 4.1: Diagram of the system studied with the cylinder containing the galinstan placed in the center of a coil. Several magnetic field lines are represented for a given frequency and allow, for this configuration, to visualize the skin effect.

The stirring effects of an isothermal liquid metal by an alternating magnetic field depend on three dimensionless numbers, the magnetic Reynolds number, $Re_m = \frac{UL}{\eta}$, the shielding parameter, $S_\omega = 2\frac{L^2}{\delta^2}$, and the Hartman number, $Ha = B_0 L\sqrt{\frac{\sigma}{\rho\nu}}$ where L is the characteristic size of the cell (say its diameter), B_0 is the magnitude of the magnetic field, σ and ρ are the electrical conductivity and mass density of the fluid, $\eta = 1/\mu_0\sigma$ is the magnetic diffusion coefficient, μ_0 being the permeability of vacuum, and δ is the skin depth. It has been shown that for a similar configuration and for $Re_m \ll 1$, the kinetic energy of the fluid presents a maximum value for $S_\omega \approx 20$ and decreases for higher S_ω [177, 248]. The Lorentz force, responsible for the flow forcing, is distributed in the skin depth, which is a function of the AC pulsation ω: $\delta = \sqrt{\frac{2\eta}{\omega}}$. The presence of this optimal forcing is due to the fact that the intensity of the Laplace force increases with the frequency as the intensity of the induced currents, while the volume in which the Laplace force is significant is of the order of $\delta \times L^2$ and thus decreases with the frequency.
On the other hand, the natural convection in RBC configuration is controlled by two dimensionless numbers, the Rayleigh number $Ra = \frac{g\beta\Delta T_0 L^3}{\kappa\nu}$, and the Prandtl number, $Pr = \frac{\nu}{\kappa}$, where ΔT_0 is the characteristic temperature difference, ν, κ and β are the liquid viscous and thermal diffusion coefficients and the liquid thermal expansion coefficient, and g is the gravitational acceleration. Grossmann and Lohse [96], have established the existence of turbulent flow regimes characterized by scaling laws of the Reynolds number

Re and the Nusselt number Nu, as functions of Ra and Pr, based on the kinetic and thermal dissipation rates in the bulk and in the boundary layer. Here Re and Nu are defined as $Re = \frac{UL}{\nu}$ and $Nu = \frac{hL}{\kappa}$ where U is the referenced velocity, h is the heat transfer coefficient and κ is the thermal conductivity of the fluid.
For steady magnetic fields (or magnetic varying with very low frequencies), it is known that the Lorentz force damps the flow as it is mainly opposite to the component of the velocity perpendicular to the direction of the magnetic field. By accounting for the Hartmann layer thickness, the scaling relation of Grossmann and Lohse for standard RBC has been extended to the magnetoconvection subject to steady vertical magnetic field [281]. The recent simulation of Ref. [2] of the RBC with a constant and uniform external magnetic field show that flow pattern becomes quasi-two-dimensional for large Hartmann number Ha. We show that beyond a certain frequency this situation changes radically. The induced currents force the flow resulting in a very significant increase in the heat flux as well as a qualitative change in the flow structure compared to the Rayleigh-Benard configuration.

4.1.1 Characteristic scales

We consider here the flow of liquid metal in a cylindrical cell under both the effects of an imposed temperature difference and an ac magnetic field. Two velocity scales can be defined, derived from the buoyancy force and the Lorentz force, $U_B = \sqrt{g\beta\Delta T H}$ and $U_L = B_0/\sqrt{\mu_0 \rho}$, respectively. In these expressions H is the height of the cell, ρ is the mass density of the fluid and μ_0 is the vacuum magnetic permeability.
As well, two scales of temperature can be introduced, one given by the temperature difference imposed at the bottom and top walls of the cylindrical cell, ΔT_0, and one corresponding to the characteristic temperature difference due to the Joule heating and obtained by an energy balance, $\Delta T_Q = \frac{<q_J>}{\rho c_p}\frac{H}{U}$. Here, $< q_J >$ is the time-volume average power density due to the Joule effect, c_p is the specific heat of the liquid metal and U is the characteristic liquid velocity, which is either U_L or U_B. Depending on the choice of U two definitions of ΔT_Q follow with different scalings at high and low frequencies:

- for $U = U_B$: $\Delta T_Q \sim S_\omega^2 Ha^2$ at $S_\omega < 1$, and $\Delta T_Q \sim S_\omega Ha^2$ at $S_\omega > 1$;
- for $U = U_L$: $\Delta T_Q \sim S_\omega^2 Ha$ at $S_\omega < 1$, and $\Delta T_Q \sim S_\omega Ha$ at $S_\omega > 1$.

Then one expects four main regimes depending on U_L/U_B and $\Delta T_Q/\Delta T_0$:

- $\Delta T_Q < \Delta T_0$ and $U_L < U_B$: Flow is driven by the buoyancy force corresponding to RBC;
- $\Delta T_Q > \Delta T_0$ and $U_L < U_B$: dynamics are controlled by the buoyancy force and the volume heating by Joule effect ;
- $\Delta T_Q < \Delta T_0$ and $U_L > U_B$: the Lorentz force governs the dynamics, and the heat flux is due to the imposed temperature difference ΔT_0;
- $\Delta T_Q > \Delta T_0$ and $U_L > U_B$: the Lorentz and the heating by Joule effect dominate.

4.1.2 Modeling

The magnetic induction in a liquid metal results from the time variation of $\boldsymbol{B}(\boldsymbol{r},t)$ and the velocity of the liquid. Owing to the linearity of the Maxwell equation, the magnetic field in the liquid can be expressed as the sum of the magnetic field in the absence of motion, $\boldsymbol{B}_0(\boldsymbol{r},t)$, and the perturbation due to the velocity field, $\boldsymbol{b}(\boldsymbol{r},t)$:

$$\boldsymbol{B} = \boldsymbol{B_0} + \boldsymbol{b} \ . \tag{4.1}$$

The induction equation for $\boldsymbol{b}$ is obtained from the Maxwell equations and the Ohm law assuming that the electrical conductivity is constant in the liquid and that the displacement currents are negligible:

$$\partial_t \boldsymbol{b} = \eta \nabla^2 \boldsymbol{b} + \nabla \times (\boldsymbol{u} \times \boldsymbol{b}) + \nabla \times (\boldsymbol{u} \times \boldsymbol{B}_0) \ . \tag{4.2}$$

The last two terms represent the induction of the magnetic field due to the motion of the liquid metal. The flow of the liquid metal is given by the Navier-Stokes equations, including the additional buoyancy force (expressed with the Boussniesq approximation) and the Lorentz force and is supplemented by the temperature equation with Joule heating:

$$\partial_t \boldsymbol{u} + \boldsymbol{u} \cdot \boldsymbol{\nabla} \boldsymbol{u} = -\frac{1}{\rho} \boldsymbol{\nabla} P + \nu \boldsymbol{\Delta} \boldsymbol{u} + \beta T \boldsymbol{g} + \frac{1}{\rho \mu_0} \boldsymbol{B} \cdot \boldsymbol{\nabla} \boldsymbol{B}, \tag{4.3a}$$

$$\frac{\partial T}{\partial t} + \boldsymbol{u} \cdot \nabla T = \kappa \Delta T + \frac{\boldsymbol{J}^2}{\rho c_p \sigma}, \tag{4.3b}$$

$$\boldsymbol{\nabla} \cdot \boldsymbol{u} = 0. \tag{4.3c}$$

In the momentum equation (4.3a), P is the total pressure including the magnetic pressure $\boldsymbol{\nabla} \boldsymbol{B}^2/2\mu_0$[1]. The boundary conditions are a no-slip condition on the walls for the velocity, a Dirichlet conditions on top and bottom walls for the temperature with a difference ΔT_0 on the two sides, and an adiabatic condition on the vertical wall. For the induction equation (4.2), the boundary conditions are integral relations ensuring the matching with the solution outside the metal $\nabla^2 \boldsymbol{b} = 0$, with continuity of $\boldsymbol{b}$ and its derivatives (in the absence of surface currents) at the boundary [112, 99].
The second term on the right-hand side of the induction equation (4.2), $\nabla \times (\boldsymbol{u} \times \boldsymbol{b})$, can be neglected when $Re_m \ll 1$. At small frequency, i.e. $S_\omega \ll 1$, and $Re_m \ll 1$, eq. (4.2) reduces to the quasi-static diffusion equation ($\eta \nabla^2 \boldsymbol{b} = -\nabla \times (\boldsymbol{u} \times \boldsymbol{B}_0)$). In the quasi-static approximation, the eddy currents are obtained from $\boldsymbol{B}_0$ explicitly, $\boldsymbol{J} = \sigma(\nabla \Phi + \boldsymbol{u} \times \boldsymbol{B_0})$, where the electrical potential is obtained by a Poisson equation ensuring that $\nabla \cdot \boldsymbol{J} = 0$.
At high frequency, i.e. $S_\omega \gg 1$, the quasi-static assumption is not valid. We can decompose the current density in the liquid as $\boldsymbol{J} = \boldsymbol{J}_0 + \boldsymbol{j}$, where $\boldsymbol{J}_0$ denotes the current density in absence of flow induced by the time variation of the magnetic flux and $\boldsymbol{j}$ is, according to the Ohm law, $\boldsymbol{j} = \sigma(\boldsymbol{e} + \boldsymbol{u} \times B_0 + \boldsymbol{u} \times \boldsymbol{b})$, with $\boldsymbol{e}$ the perturbation of the electrical field due to the flow. For large enough frequency and small magnetic Reynolds number, $\boldsymbol{j}$ can be neglected compared to $\boldsymbol{J}_0$, as we can estimate that $O(|\boldsymbol{J}_0|/|\boldsymbol{j}|) = \sqrt{S_\omega}/R_m$. Therefore for $Re_m \ll 1$ and $S_\omega \gg R_m^2$ it is possible to completely decouple the resolution of the flow from the resolution of the magnetic field. The magnetic field provides sources of

[1] The Lorentz force can be expressed as $\boldsymbol{F}_L = \boldsymbol{J} \times \boldsymbol{B} = 1/\mu_0 \boldsymbol{B}.\nabla \boldsymbol{B} - \boldsymbol{\nabla} \boldsymbol{B}^2/2\mu_0$, assuming the liquid metal is incompressible, the second term contributes only to the hydrostatic pressure.

momentum and heat for the liquid with no influence of the liquid motion on these sources. Therefore as in the quasi-static approximation it is not required to solve the induction equation (4.2).
The magnetic and electrical fields, $\boldsymbol{B}_0$ and $\boldsymbol{E}_0$, applied to the system, at rest, are solutions of the set of equations:

$$\nabla \cdot \boldsymbol{B}_0 = 0, \tag{4.4a}$$

$$\partial_t \boldsymbol{B}_0 = -\nabla \times \boldsymbol{E}_0, \tag{4.4b}$$

$$\nabla \times \boldsymbol{B}_0 = \mu_0(\boldsymbol{J}_0 + \boldsymbol{J}^e(t)), \tag{4.4c}$$

$$\boldsymbol{J}_0 = \sigma \boldsymbol{E}_0, \tag{4.4d}$$

where $\boldsymbol{J}_0$ and $\boldsymbol{J}^e(t)$ are respectively the current density in the liquid metal and in the coil. For the later we impose its amplitude J_e and pulsation ω which fix Ha and S_ω. The magnetic field $\boldsymbol{B}_0$ within the cell and outside is computed with Comsol for the various values of current intensity and frequency. The Maxwell equations (4.4) have been solved in 2D axisymmetric geometry for $H = D = 0.1\ m$ and a coil of rectangular section 5×5 mm^2 having 19 turns and 3 layers.
The equations (4.3a)-(4.3c) are solved with the finite volume code Jadim. The magnetic field computed with Comsol, with a resolution much finer than the DNS grid, is sampled at the vertices of the DNS grid. The Comsol simulations provide the magnitude and phase of the magnetic field inside the liquid. Consequently, the magnetic field and thus the momentum and heat sources can be computed at each instant in the DNS simulations. The details of the numerical simulations can be found in Refs. [100, 99].

4.1.3 Characterization of the magnetic forcing

In figure 4.2 we present the spatial distribution of the norm of $1/\mu_0 \boldsymbol{B}_0.\nabla \boldsymbol{B}_0$ for $S_\omega = 15$. This figure shows that the force is dominant close to the two edges, top and bottom, of the cylinder. The right part of Fig. 4.2 presents the amplitude of the Joule power density $q_J = \frac{\boldsymbol{J}_0^2}{\sigma} = \frac{\eta}{\mu_0}(\nabla \times \boldsymbol{B}_0)^2$ due to Joule effect also for $S_\omega = 15$. It is seen that the Joule heating is located in the skin depth close to the vertical wall.

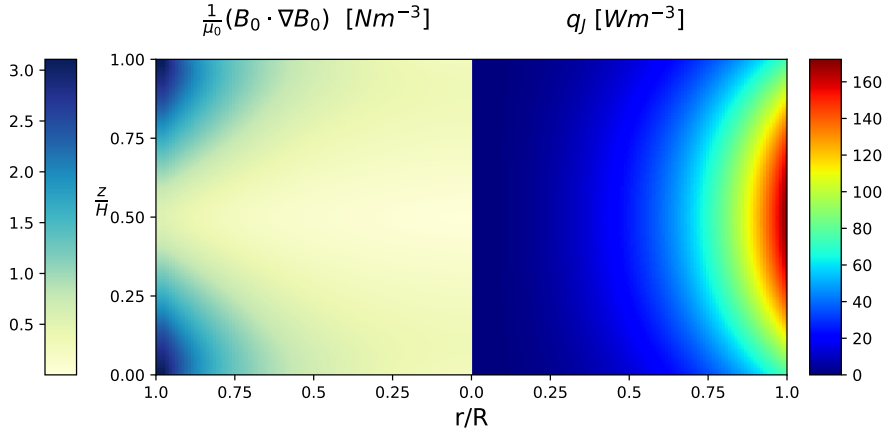

Figure 4.2: Distribution of $|\frac{1}{\mu_0}\boldsymbol{B}_0 \cdot \nabla \boldsymbol{B}_0|$ responsible for the fluid motion (left part of the cell cross-section) and q_J (right part) for $I_0 = 1$A and $S_\omega = 15$.

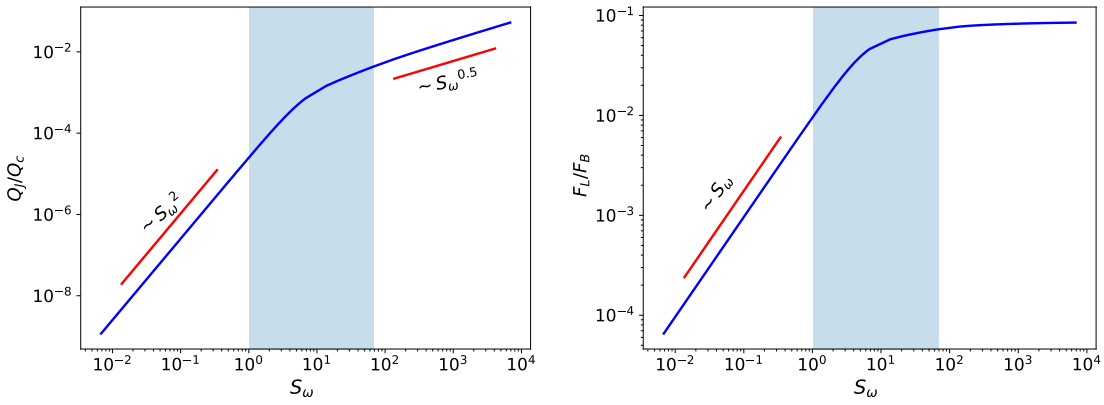

Figure 4.3: Left: Joule heating total power Q_J in the liquid metal volume normalized by Q_c versus the shielding parameter S_ω. Right: Volume-average Lorentz force normalized by F_B versus the shielding parameter S_ω. Each curve is computed at $I_0 = 1$ A; the power laws in S_ω are mentioned on each curve. The colored domain indicates the range of variation of S_ω for the DNS.

.

The total power deposited by Joule effect in the liquid metal, $Q_J = \int q_J \, dV$, normalized by the heat transferred by pure conduction, $Q_c = k\Delta T_0 \frac{\pi D^2}{4H}$, is plotted as a function of S_ω in figure 4.3. This curve shows that there are two asymptotic behaviors: the power scales as S_ω^2 for $S_\omega < 1$, and $\sqrt{S_\omega}$ for $S_\omega > 100$. Additionally, the spatially averaged amplitude of the Lorentz force, normalized by the buoyancy force, $F_B = \rho g \beta \Delta T_0 \frac{\pi}{4} D^2 H$, scales as S_ω, for $S_\omega < 1$, and is constant for $S_\omega > 100$. We find that these scaling relations are the same as in the case of an infinite cylinder. In this work, all the simulations are realized in the intermediate region, i.e. $1 < S_\omega < 100$.

4.1.4 Experimental setup

During the PhD of Julien Guillou, we develop an experimental setup that allows us to study the dynamics of a metal liquid in a Rayleigh-Bénard cell subjected to an ac magnetic field combined with a thermal gradient (see schematic representation in figure 4.4).
The convection cell is a cylinder with a unit aspect ratio and internal diameter $D = 10$cm. The top and bottom walls are two silicon carbide (SiC) disks and the lateral wall is made in polyether ether ketone (PEEK). Both these materials are good electrical insulators, and are therefore not affecting the magnetic field. SiC has a high thermal conductivity contrary to PEEK, so we can consider that the lateral wall is adiabatic whereas the top and bottom plates are at constant temperature. The two plate temperatures are set by circulation of water with different imposed temperatures.
A copper coil with an internal cooling (made by SEF) with a height of 10.2 cm and an external diameter of 17.4 cm, surrounds the convection cell. The coil is made of 57 turns with four insulated layers. The coil power supply is obtained by transforming the three-phase electrical power of the laboratory in continuous current and then to an alternating current with specified amplitude and frequency thanks to a H-bridge coupled with a Pulse With Modulated controller (made by Arcel). The coil with the cylinder fill with galinstan behaves as a low-pass filter with a cut-off frequency at about 11 Hz. To

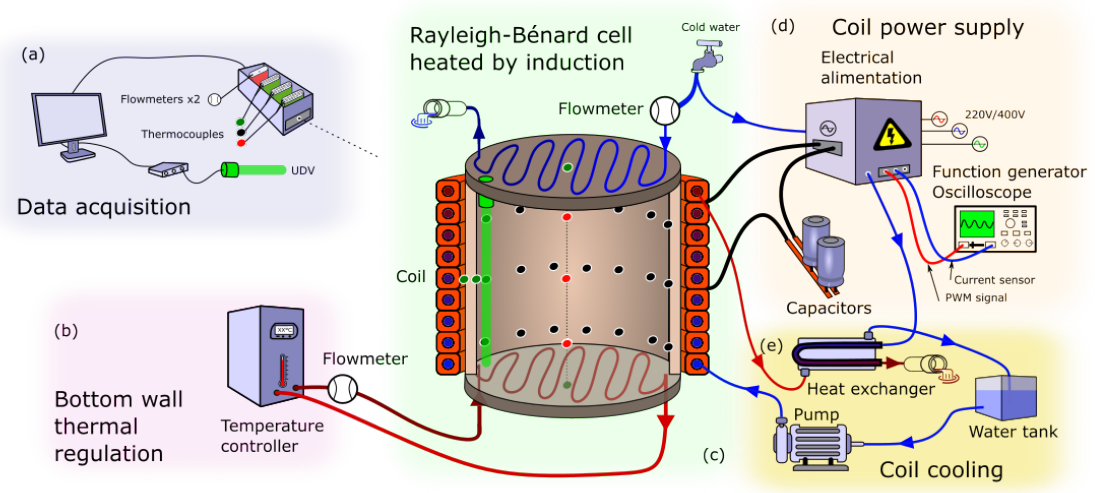

Figure 4.4: Diagram of the experimental device setup. (a) : Thermocouples, UDV transducer and flowmeter data acquisition system. (b) : Thermal regulation of the bottom side of the RBC cell. (c) : Rayleigh-Bénard cylinder heated by induction and position of thermocouples and the UDV transducer (green). A water circulation fixes the temperature difference between the top and bottom walls; flowmeters record the water flow rate in the disk. (d) : coil power supply, capacitors, oscilloscope and function generator. (e) : coil cooling device.

perform experiments at higher frequency, we connected a rack of capacitors in series with the coil. We have used up to three 70 μF capacitors mounted in parallel in the rack. The number of capacitors is variable to adapt the resonance close to the current frequency. We were then able to drive the intensity of the current I_0 between 2 and 67 A and the frequency f between 15 and 1000 Hz. Note that the experiment is designed to reach current intensity up to 500 A, but the capacitor used in the first experiments presented here does not allow too high currents.

The heat flux on both bottom and top plates are obtained by measuring the flow rate of the circulating water and its temperature difference between inlet and outlet. To measure the temperature distribution in the liquid, three rings of 11 type T thermocouples are placed in the cell close to the wall and at three different heights: $H/4$, $H/2$ and $3H/4$. 3 thermocouples are also positioned along the axis of the cylinder at the same heights. Finally, an acoustic transducer (UDV) with a diameter of 8 mm and placed at 1 cm from the wall, allows measuring the vertical distribution of the convection velocity close to the cylinder wall.

The details of the setup and the experimental protocol are presented in Ref. [99].

Experiments have been realized for $15 \leq f \leq 1000$ Hz, $2 \leq I_0 \leq 67$ A and $2 \leq \Delta T_0 \leq 11$ K. Under these conditions, we have $6 \leq Ha \leq 200$, $1 \leq S_\omega \leq 70$, $2.3 \times 10^5 \leq Ra \leq 3.1 \times 10^6$ for galinstan, and $3 \times 10^7 \leq Ra \leq 2 \times 10^8$ for water.

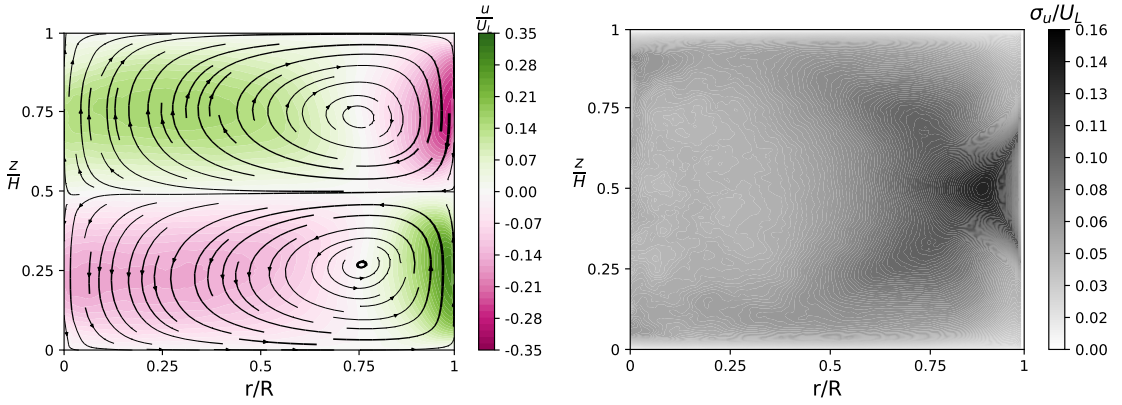

Figure 4.5: Left: Streamlines in vertical cross section of the time and azimuth averaged velocity for $I_0 = 100A$ and $S_\omega = 34$ computed by DNS. Right: standard deviation of the vertical velocity in vertical cross-section for I_0 =50A and $S_\omega = 10$, obtained from time and azimuthal averaging.

4.1.5 Flow structures and heat flux

We focus on the regime dominated by the Lorentz force ($U_L > U_B$), and heat transfer controlled by the wall temperature difference $\Delta T_0 > \Delta T_Q$. Hence we study the dynamics of the liquid metal under forced convection by Lorentz force, perturbed by Joule heating and buoyancy force.

When imposing an alternating magnetic field, the global flow patterns are drastically modified compared to the RBC flow. From the numerical simulation, we show that in the Laplace force forced convection regime, the flow is organized in two toroidal recirculation cells in agreement with the literature [185, 63]. This is illustrated in the figure 4.5, showing the average vertical velocity for $Ha = 301$ and $S_\omega = 34$ in a vertical plane of the vessel. It is seen that both cells have an opposite azimuthal vorticity. For $z < H/2$ the liquid metal goes upward close to the wall and goes downward in the bulk, and conversely, for $z > H/2$. This double-torus flow structure appears very robust for all intensity and frequency. Only, for the lowest intensity consider in our DNS (10A), the torus appears and disappears alternatively, showing that the flow is characterized by a mixture between free convection and forced convection.

The toroidal cells are separated by a mixing zone located at mid-height plane. In this region, the flow presents on average the structure of a plane jet pointed radially inward, and subject to mean vertical temperature gradient. As the mean vertical velocity is zero in this region, the momentum and heat transfer between both half of the vessel, are controlled by excursion or bursting of the recirculation cells across the midplane, as seen in figure 4.5 showing the standard deviation of the vertical velocity for $Ha = 150$ and $S_\omega = 10$. This figure points out that the velocity fluctuations are maximum in the mid plane and close to the wall, where the Joule heating is the largest. In this region, the characteristic value of the RMS is of the order of $U_L/10$. We mentioned that the normalized variance map remains similar whatever the Ha value, at high frequency ($S_\omega \geq 10$).

We present in Fig. 4.6 the average temperature of the three rings of thermocouples at various Ha and S_ω as well as the profile of the temperature averaged over the horizontal plane from the DNS. We observe that DNS and experiments present the same trends in

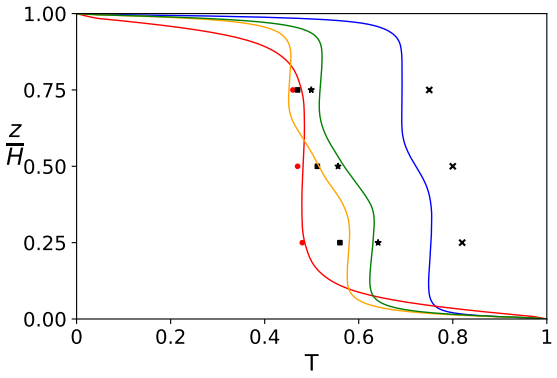

Figure 4.6: Vertical profile of the average temperature. The solid lines represent the average of the dimensionless liquid temperature from the DNS for different values of Ha and S_ω: $Ha = 150$ and $S_\omega = 10$ (orange), $Ha = 150$ and $S_\omega = 51$ (green), $Ha = 301$ and $S_\omega = 68$ (blue) and RBC (red). The points represent the measurements of the experimental average dimensionless temperature of the three rings of thermocouples for $Ha = 56.4$ and $S_\omega = 34.1$ (square), $Ha = 65.3$ and $S_\omega = 68$ (star), $Ha = 113$ and $S_\omega = 50.9$ (cross) and RBC (red dots).

Ha and S_ω in presence of the Lorentz force, the average temperature display a two-plateau profile. Each toroidal recirculation cells present different average temperatures, showing that within a recirculation cell the temperature is rapidly homogenized whereas the heat transfers between the two cells is not as efficient. When the Joule heating becomes significant, the average temperatures of the two cells shift to higher values and the difference between the two plateau temperatures decreases.
We consider the evolution of the average heat flux at the bottom and top walls obtained from DNS and the experiments. Based on the standard definition, Nu is equal to the ratio of these fluxes to the flux in absence of fluid motion and Joule heating, $Q_c = k\Delta T_0 \frac{\pi D^2}{4H}$. From the mean thermal budget, the difference between the bottom and top Nusselt numbers is given by:

$$Nu^+ - Nu^- = Q_J/Q_c \ , \tag{4.5}$$

where the evolution of Q_J/Q_c with S_ω is given in the left panel of figure 4.3, Note that Q_J/Q_c also varies as Ha^2.
We observed that the heat flux increases significantly with respect to RBC when the Lorentz force is applied. This is visible even for small frequency and intensity. For example, at $I_0 = 10$A and $S_\omega = 1$, the Nu is increased by a factor ≈ 1.5.
To characterize the forced convection we introduced a Péclet number defined with a characteristic velocity $U_\omega = U_L f(S_\omega)$, $Pe_\omega = U_\omega H/\kappa$. The function $f(S_\omega)$ characterizes the influence of the frequency on the Lorentz force. It behaves as $f(S_\omega) \sim S_\omega$ for $S_\omega \ll 1$ and for $S_\omega \gg 1$ it tends to a constant. The evolution of the function $f(S_\omega)$ is obtained by solving the Maxwell equations and is shown in the right panel of figure 4.3.
Figure 4.7 displays the Nu variations with Pe at the top wall for the experimental and numerical data. We first observe that all the results merge in a unique curve which presents two regimes: for $S_\omega < 10$ and $Ha < 30$, which corresponds to $Q_J/Q_c < 1$, Nu is constant. This result can be understood by considering that $U_L \lesssim U_B$ and the heat transfer is mainly driven by ΔT_0. For $S_\omega \geq 10$ and $Ha \geq 30$, which corresponds to $Q_J/Q_c \geq 1$, Nu scales

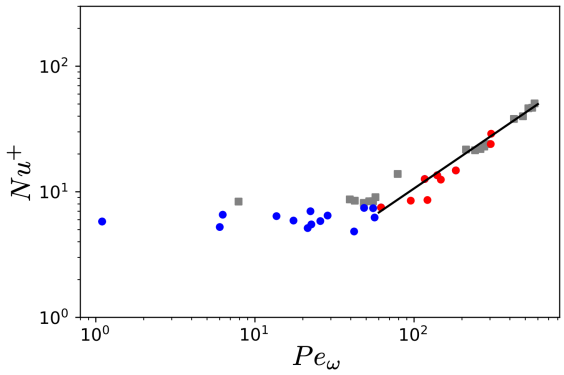

Figure 4.7: Evolution of Nu^+ vs. Pe_ω in Lorentz forced convection. The red points correspond to experimental data for $Q_J/Q_c > 1$. The blue points correspond to experimental data for $Q_J/Q_c < 1$. The square gray points correspond to DNS. For $Q_J/Q_c > 1$, $Nu \sim Pe^{2/3}$.

as $Pe^{2/3}$. Under this condition, $U_L > U_B$ and the Lorentz force controls the heat transfer by producing two toroidal recirculation cells. Note that the heat flux on the bottom wall can be obtained from (4.5). As long as the Joule effect can be neglected ($Q_J/Q_c \ll 1$), $Nu^+ \approx Nu^-$. When the Joule heating becomes significant, for high frequency and current intensity, the difference between the heat flux at the bottom and top rise and is directly given by eq. (4.5).

4.2 Perturbation of eddy-currents by inclusions in liquid metal

In this project we focus on the modifications of the magnetic field caused by the presence of a dispersed phase in a liquid metal. More specifically we are interested in electromagnetic measurements of the dispersed phase properties such as the void fraction, the characteristic size of particles or bubbles, and their velocity. Such measurements, even for a single inclusion, remain challenging because of the opacity of liquid metal. In this goal, various technics have been developed, based and acoustic method [70], X-ray imaging [4, 121, 122], or perturbation of electromagnetic fields [151]. Here we consider the use of an Eddy Current Flow Meter (ECFM) to detect and characterize the voids in a liquid metal. ECFM is currently used for measuring the flow rate of liquid metal flows in pipes [244]. In this device, an alternating magnetic field is generated in the flow by a primary coil. The fluid motion induces small eddy currents that perturb the magnetic field. These perturbations induced a variation of the magnetic flux that can be measured on the variation of electromotive force (emf) on a secondary coil.
More specifically, we consider the design depicted in figure 4.8, which consists of three external coils surrounded the pipe. A primary coil generates an alternating magnetic field in the flow, and the two secondary coils, located on each side of the primary coil, measure the difference of magnetic flux in two cross-sections of the flow. This configuration present the advantage of being easy to set up and not perturbing the flow. In the thesis of Mithlesh Kumar [132, 133] advised by Wladimir Bergez and Philippe Tordjman, it was shown that that the electrical potential difference between the two secondary coils of the ECFM, can be decomposed, at first order, as two independent contributions, one related to the global

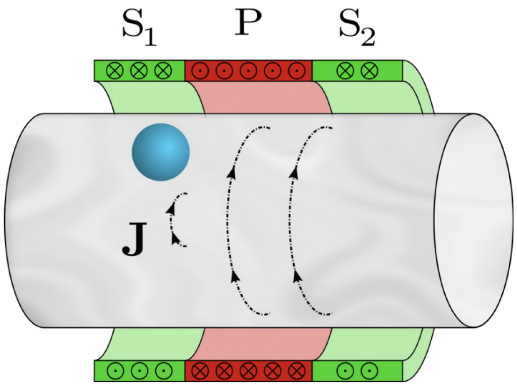

Figure 4.8: The ECFM is composed of three coils surrounding the pipe. P is the primary coil, S_1 and S_2 are the secondary coils; $\boldsymbol{J}$ is the eddy current field generated by P which is perturbed by the presence of the non-conducting inclusion (in blue).

velocity of the conductor, characterized by a magnetic Reynolds number Re_m, and the second due to the variation of the void fraction α. In the thesis of Rafaël Guichou [97, 98] the perturbation of the magnetic flux by the presence of an electrically non-conducting spherical particle in the liquid metal has been studied theoretically and experimentally. For low pulsations of current in the primary coil, it was shown the perturbation of the magnetic vector potential due to the inclusion satisfies a Poisson equation. Solving this equation, one can model the voltage in the secondary coil as a function of the particle diameter, its radial position in the pipe and the primary current frequency. This model is in good agreement with experimental results, for a small shielding parameter, $S_\omega \ll (R/R_b)^2$, where the shielding parameter is defined as $S_\omega = \omega R^2/\eta = 2(R/\delta)^2$, with R the radius of the pipe, $\delta = \sqrt{2\eta/\omega}$ the skin depth, and R_b it the particle radius. In the post-doctorate of Youssef Nasro Allah and the PhD of Antoine Afflard, we are developing this approach to account for inductive phenomena and extend the validity to higher frequency. We also performed numerical solutions and experiments to confirm the model. These results are presented below. We are also addressing the inverse problem of finding the size and position of the bubbles from the voltage signal of the secondary coils.

4.2.1 Model for the perturbation of the magnetic field due to an inclusion

We consider, a non-conducting particle of diameter d traveling along an infinite cylindrical pipe filled with a liquid metal and passing through an ECFM, as shown in figure 4.8. The effect of the traveling void inclusion is modeled with the vector and scalar potentials $\boldsymbol{A}$ and ϕ. Their equations in dimensionless form, satisfying the gauge condition $\nabla \cdot \boldsymbol{A} = 0$ reads:

$$\nabla^2 \boldsymbol{A} = nS_\omega \frac{\partial \boldsymbol{A}}{\partial t} - nRe_m \boldsymbol{u} \times \nabla \times \boldsymbol{A} + n\nabla\varphi - \boldsymbol{j}_e \ , \tag{4.6}$$

$$\nabla^2 \varphi = nRe_m \nabla \cdot (\boldsymbol{u} \times \nabla \times \boldsymbol{A}) \ , \tag{4.7}$$

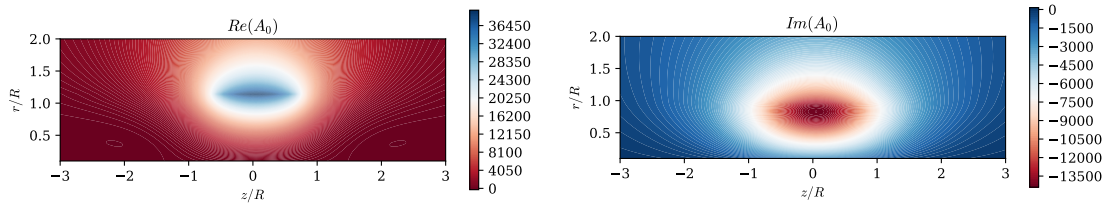

Figure 4.9: Distribution of $A_{0,\theta}(r,z)$. Right: real part. Left: imaginary part.

where n is equal to 1 in the liquid metal and 0 elsewhere, $\boldsymbol{u}$ is the velocity field in the liquid metal and $\boldsymbol{j}_e$ is the external electrical current density applied in the primary coil. Here the magnetic Reynolds number is defined as $Re_m = UR/\eta$, with U the average velocity of the liquid metal in the absence of a particle. At infinity we have the condition $|\boldsymbol{A}| = 0$. The source term $\boldsymbol{J}_e$ is modeled as a harmonic in time, unit azimuthal current density uniformly distributed in the volume corresponding to the primary coil. The advantage of considering the vector potential is that the emf on the secondary coils is directly obtained by computing the circulation of $\boldsymbol{A}$ on these coils. The emf (in dimensional form) induced by one turn of a coil is

$$\frac{emf}{\omega\mu_0 J_e R^3} = d_t \oint_c \boldsymbol{A}.d\boldsymbol{\ell} \tag{4.8}$$

where c is the contour of the turn of the coil.
The main hypothesis is to consider that the velocity and void position are quasi-static compared to the frequency of the current. We will further assume that Re_m and the void fraction α are small. With these approximations, we can obtain the linear response of the ECFM. For that we decompose the potential vector in $\boldsymbol{A} = \boldsymbol{A}_0 + \boldsymbol{A}_u + \boldsymbol{A}_\alpha + O(Re_m^2, \alpha^2, \alpha Re_m)$ where $\boldsymbol{A}_0$ is the vector potential in the absence of flow and particle, $\boldsymbol{A}_u$ is the perturbation of the vector potential due to the liquid metal flow without any particle, and $\boldsymbol{A}_\alpha$ is the perturbation due to the presence of the particle[2]. According to [132], we have $O(|\boldsymbol{A}_u|/|\boldsymbol{A}_0|) = Re_m$ and $O(|\boldsymbol{A}_\alpha|/|\boldsymbol{A}_0|) = \alpha \sim (R_b/R)^3$. With the previous approximations, the scalar potential is zero and the equations for the Fourier transform in time of $\boldsymbol{A}_0$, $\boldsymbol{A}_u$ and $\boldsymbol{A}_\alpha$ are

$$\nabla^2 \boldsymbol{A}_0 - in_0 S_\omega \boldsymbol{A}_0 = \boldsymbol{j}^e \ , \tag{4.9}$$

$$\nabla^2 \boldsymbol{A}_u - in_0 S_\omega \boldsymbol{A}_u = -n_0 Re_m \boldsymbol{u} \times \nabla \times \boldsymbol{A}_0 + O(Re_m^2) \ , \tag{4.10}$$

$$\nabla^2 \boldsymbol{A}_\alpha - in_0 S_\omega \boldsymbol{A}_\alpha = -in_b S_\omega \boldsymbol{A}_0 + O(Re_m^2, \alpha^2, \alpha Re_m) \ , \tag{4.11}$$

where $i^2 = -1$, n_0 equals 1 in the pipe (liquid metal without any particle) and 0 elsewhere, and n_b equals 1 in the particle and 0 elsewhere (note that $n + n_b = n_0$). According to the quasistatic hypothesis, when the particle moves, one has to consider that n and n_b are two slowly varying functions of time, i.e. time plays the role of a parameter in Eq. (4.11). Exact solution of (4.9) has been obtained for an infinite cylinder [98]. In this case $\boldsymbol{A}_0$ is azimuthal ($\boldsymbol{A}_0 = A_0(r,z)\boldsymbol{e}_\theta$), and an example of its real and imaginary part is shown in figure 4.9.

[2]In this decomposition their is no effect of liquid metal flow perturbation due to the particle motion. this could be introduced as higher order terms.

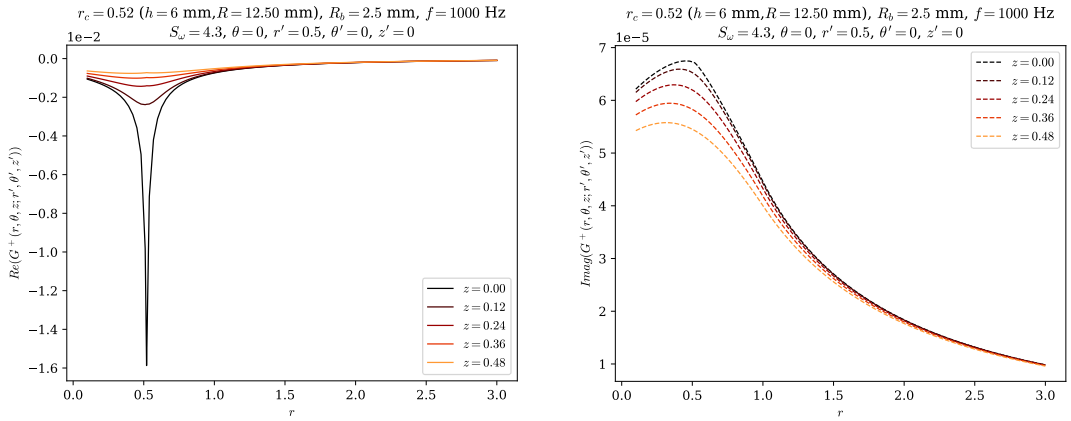

Figure 4.10: Real part (left) and imaginary part (right) of the green function for the perturbation of the vector potential $\boldsymbol{A}_\alpha$ as defined in (4.13) as a function of r for various values of z for a fixed value $\theta = \theta' = 0$, $r' = 1/2$ and $z' = 0$, corresponding here to the position of the source.

Equation (4.11) is a Helmholtz equation with a source term depending on $\boldsymbol{A}_0$. Accordingly the perturbation of the vector potential is given by

$$\boldsymbol{A}_\alpha(\boldsymbol{r}) = -iS_\omega \int n_b(\boldsymbol{r}')\ \boldsymbol{G}(\boldsymbol{r}, \boldsymbol{r}') \cdot \boldsymbol{A}_0(\boldsymbol{r}')\ dr'^3\ , \tag{4.12}$$

where $\boldsymbol{G}(\boldsymbol{r}, \boldsymbol{r}')$ is the tonsorial Green function solution of

$$\nabla^2 \boldsymbol{G}(\boldsymbol{r}, \boldsymbol{r}') - in_0 S_\omega \boldsymbol{G}(\boldsymbol{r}, \boldsymbol{r}') = -\delta(\boldsymbol{r} - \boldsymbol{r}') \cdot (\boldsymbol{e}_r \otimes \boldsymbol{e}_r + \boldsymbol{e}_\theta \otimes \boldsymbol{e}_\theta + \boldsymbol{e}_z \otimes \boldsymbol{e}_z)\ . \tag{4.13}$$

To obtain this Green function, we apply the Fourier transform in z and θ. The resulting Fourier coefficients are solutions of a Bessel equation, and can thus be expressed as a combination of Bessel functions. Finally, the Green function in physical space is obtained from an inverse Fourier transform performed numerically. An example of the resulting $\boldsymbol{G}(\boldsymbol{r}, \boldsymbol{r}')$ is shown in figure 4.10.
For a small particle volume, taking the pointwise limit for the source term, $n_b(\boldsymbol{r}')$ in (4.12) becomes $v_b \delta(\boldsymbol{r}_c - \boldsymbol{r}')$, where v_b is the particle volume normalized by the pipe radius and $\boldsymbol{r}_c$ the position of its center, also normalized by the pipe radius. This leads to an algebraic equation for the vector potential $\boldsymbol{A}_\alpha$:

$$\boldsymbol{A}_\alpha(\boldsymbol{r}) = -iv_b S_\omega \boldsymbol{G}(\boldsymbol{r}, \boldsymbol{r}_c) \cdot \boldsymbol{A}_0(\boldsymbol{r}_c)\ . \tag{4.14}$$

The condition of the validity of this solution ($v_b S_\omega \ll 1$) means that the particle must be small enough when the gradients of the eddy currents become large. Equation (4.14) shows that, in the linear approximation, the perturbation of the vector potential due to the presence of the particle, varies linearly with its volume as it has been already found for small particles at low frequencies [132, 98].
With this model, we can compute the time evolution of the amplitude of the tension difference between the two secondary coils ΔV_α generated by a traveling inclusion. In order to validate this approach, we compare the results of this model with numerical simulations, performed with Comsol, of (4.7) with $Re_m = 0$ and the quasi-static approximation. Such

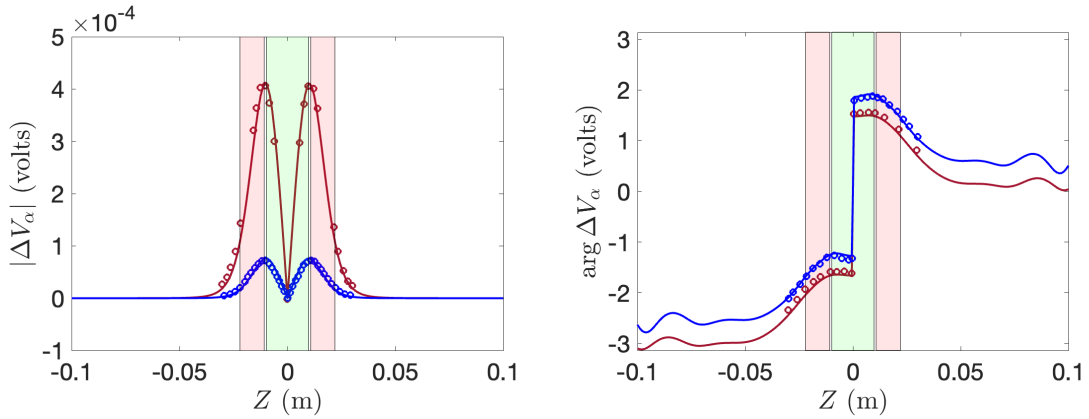

Figure 4.11: Theoretical ECFM response. Solid line: linear model; broken lines: numerical solution. Left: modulus of the complex amplitude of the ECFM response; right: its phase. Blue: $R_b = 1$ mm, $R_c = 9$ mm; brown: $R_b = 3$ mm, $R_c = 4$ mm; in both cases, frequency 1000 Hz. Abscissa Z corresponds to the axial position of the particle. The red and green areas show the positions inside the secondary and primary coils, respectively.

comparisons are shown in figure 4.11 for two non-conducting beads of different diameters, $R_b = 1$mm and $R_b = 3$mm, traveling in the pipe of radius $R = 13$mm with two constant radial positions $R_c = 9$mm and $R_c = 4$mm, respectively. In both cases the frequency of the current in the primary coil is 1000 Hz corresponding to $v_b S_\omega = 8.8 \times 10^{-3}$ and 0.24 respectively for the two bead sizes. In figure 4.11 we present the evolution of the modulus $|\Delta V_\alpha|$ of the generated signal as well as its phase $\arg \Delta V_\alpha = \phi_\alpha$ with respect to the current in the primary coil. We observed a very good agreement between the Comsol simulations and the model for both quantities. As seen in this figure, as the bead is traveling through the ECFM, the signal experience an oscillation. We note $\Delta V^* = \Delta V_\alpha(z_{max})$, where z_{max} is the position of the bead giving the maximum of $|\Delta V_\alpha|$.
Based on the inversion of the mapping $(R_b, R_c) \to (|\Delta V_\alpha^*|, \phi_\alpha^*)$ we proposed in ref. [1] a method to measure the size of an inclusion in a liquid metal.

4.2.2 Experimental setup

The capability of an ECFM to detect a particle and measure its size has been verified experimentally. Two experimental setups have been designed as depicted in figure 4.12. The first one enables us to validate the model for the detection of small beads of known diameter and position. In a second setup, we consider a bubble column in order to apply the method to a real fluid system.
For both setup, we have a tube filled with galinstan. The tube is in PVC with inner diameter 26 mm and thickness 3 mm. We applied an alternating electrical current of amplitude 0.2 A in the primary coil. We use a transconductance amplifier to impose a constant amplitude of the current independently of the variation of the impedance of the system caused by the traveling of the inclusions.
For the first setup, the particles are 3D printing PMMA beads of diameter 1, 2, 3 and 4 mm, whose positions are imposed by a thin fishing wire with diameter 0.08 mm. In the second experimental setup, we inject argon bubbles at the bottom of the tube.

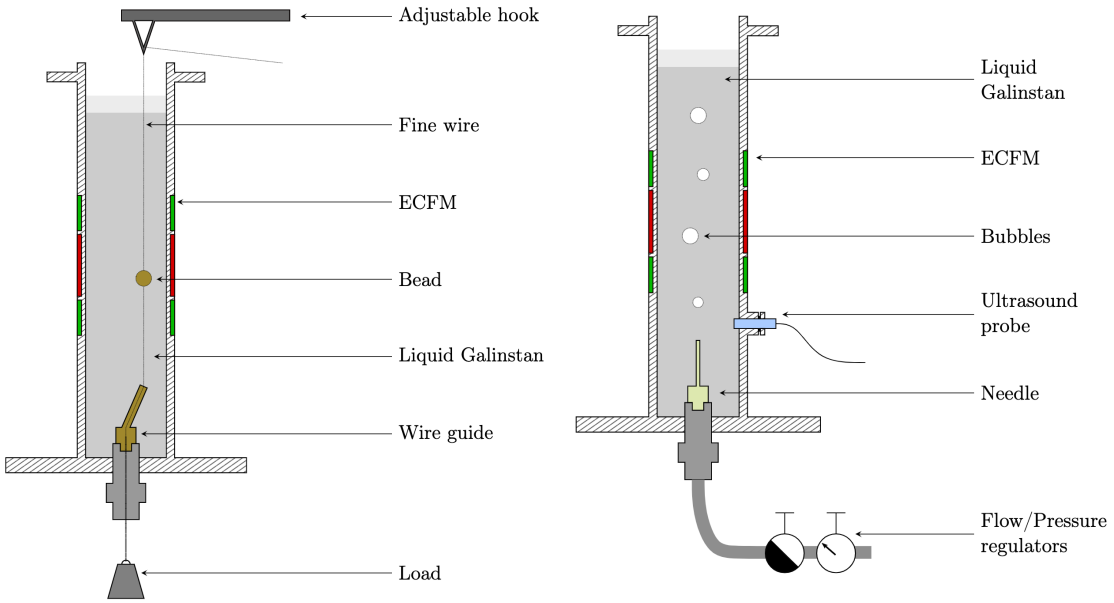

Figure 4.12: Experimental setups for detection and characterization of non-conducting inclusion by an ECFM. Left: beads of known diameters and position are traveling in a tube filled with galinstan. Right: Argon bubbles are rising in a tube filled with galinstan.

In figure 4.13 we compare the prediction from the model with the experimental response of the ECFM for the first setup. We present the evolution of the modulus and the phase of ΔV_α^* with the frequency of the current in the primary coil, for a bead size of $R_b = 3$mm and for 3 positions $R_c = 0$, 4.8 and 8.6 mm. The linear approximation also agrees with the experience for moderate frequencies (up to $3000Hz$), but present some deviation at larger frequencies which seems consistent with the limit of validity of the model $v_b S_\omega = 1$ that corresponds here to a frequency of 4200 Hz. At high frequency the skin depth becomes very small which implies strong variations of the vector potential over the size of the bead. Thus the approximation of integrals made to obtain (4.14) from (4.12) is not valid. Finally, the simple model (4.12) predict $\Delta V_\alpha^* = 0$ for a bead traveling along the axis of the cylinder, $R_c = 0$, since due to symmetry, $\boldsymbol{A}_0(r = 0) = 0$. In this case also one should consider finite volume effect of the bead though (4.14) instead of using the pointwise approximation of (4.12).

In figure 4.14, we present results of the bubble experiments. We show in this figure the time signal of $|\Delta V_\alpha|$ generating by the rising bubbles. From the detection of the peaks, we obtained $|\Delta V_\alpha^*|$ and ϕ_α^* corresponding to each event of a bubble passing through the ECFM, from which we can estimate the bubble size and radial position. Figure 4.14 presents histograms of the bubble size and bubble radial position. The total mass of bubbles injected in the galinstan is obtained by a time integration of the gas flow rate. The sum of the estimated volume of each bubble matches the measured mass of gas with an error of less than 2%. These preliminary results come as confirmation that the bubble size, and position, can be inferred from the measurement of the amplitude and phase of the signal of an ECFM.

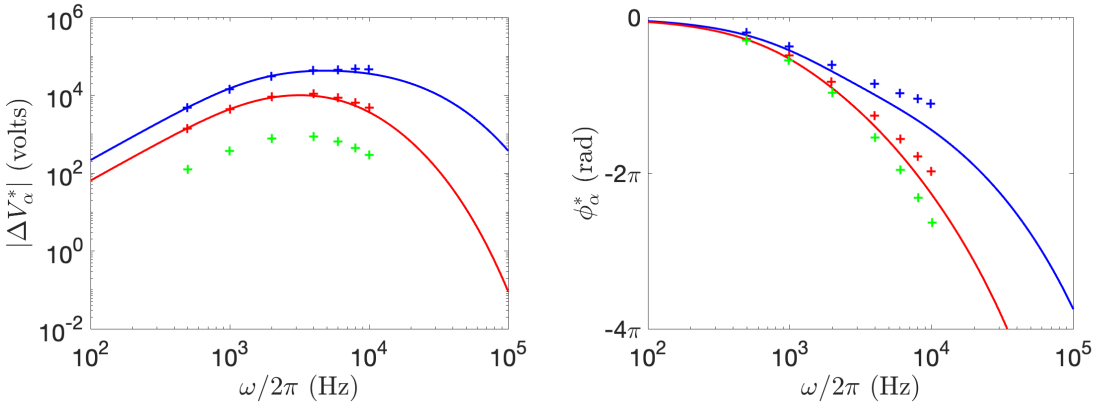

Figure 4.13: Effect of the frequency on the ECFM response for a particle of radius $R_b = 3$ mm and for three radial positions. Left : amplitude of the maximum $|\Delta V_\alpha^*|$; Right: the phase of the maximum ϕ_α^*. Blue: $R_c = 8.6$ mm; red: $R_c = 4.6$ mm; green: $R_c = 0$ mm. Continuous lines: linear model; crosses: experimental data.

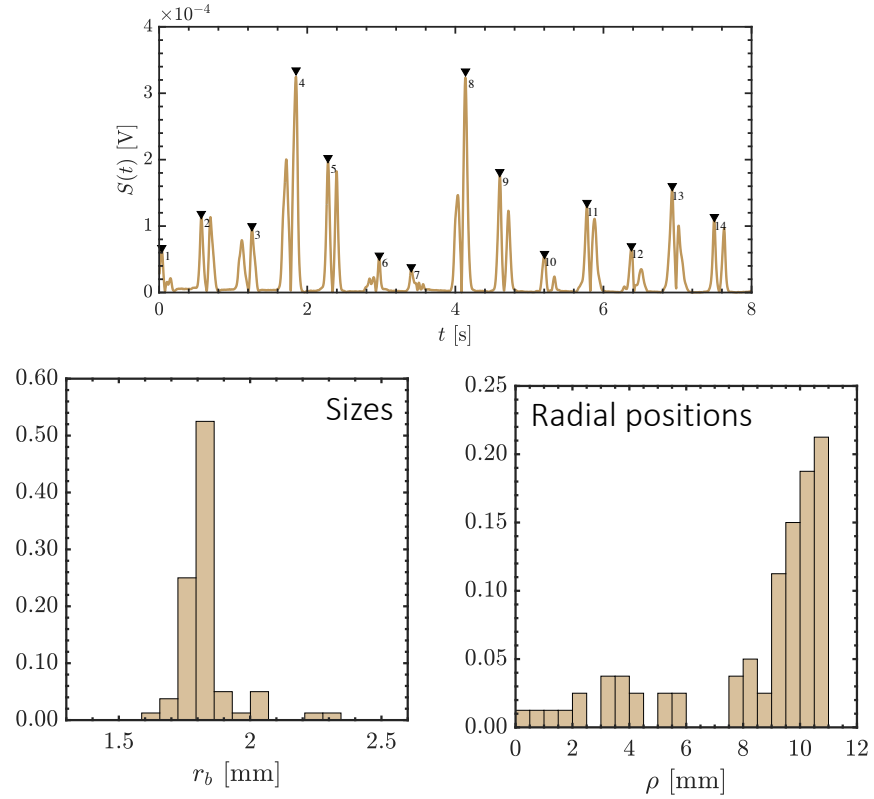

Figure 4.14: Top: time evolution $|\Delta V_\alpha|$ of the ECFM generating by rising bubbles in cylinder fill with galinstan. Right: Histogram of the estimated of the bubble size. Left: histogram of the estimated bubble radial position.

4.3 Perspectives

We present some perspectives envisaged extending these research activities around the MHD with variable fields.

Concerning the study of the single-phase flow presented in the paragraph 4.1, a direct extension is to further explore the parameter space of this original flow. We could firstly consider the situation in which the buoyancy force dominate the Lorentz force ($U_B > U_L$) for example by considering taller domain, as well as different aspect ratio of the vessel. It will also be interesting to study the flow when a more intense magnetic field is applied. In the work presented above, the technical limitations of our experimental setup and the capabilities of numerical simulations allowed us to study the effect of Hartman numbers up to $Ha \approx 300$, corresponding to intensities in the primary coil of the order of 100A. The installation of power capacitors on the experimental setup would allow us to reach currents up to 500A and thus to obtain Hartman numbers around $Ha = 1500$. For such Hartman numbers, we estimate that the flow velocity will be sufficient to obtain magnetic Reynolds numbers of the flow slightly higher than 1 and giving access to new regimes. In such a situation, one can expect magnetic induction mechanism to be important along with a strong influence of the imposed magnetic field similarly to Refs. [174, 173]. As a consequence the induced currents will depend on the local structures of the velocity field, and can be important, at least locally, compared to the currents induced by the temporal variation of the applied field. Consequently high velocity regions could then be prone to strong buoyancy forcing due to local Joule dissipation, leading to a feedback loop mechanism that tends to reinforce the largest velocity fluctuations. For the numerical study of this regime, it will be necessary to resolve the induction equation with its nonlocal boundary conditions to account for the $\nabla \cdot \boldsymbol{B} = 0$ condition outside the liquid metal. However, these simulations would remain challenging in terms of the size of the numerical grid, and may require to consider subgird scale modeling of the flow.

Regarding the study of the perturbation of magnetic fields by inclusions, we would like to pursue the approach to consider multi-bubble detection. For not too high volume fraction, we expect that (4.12) remains valid, it is then a priori possible the determine the ECFM response to a given distribution of voids. The challenge will be to propose an inverse procedure to obtain an estimate of the volume fraction as well as the distribution of the size and position of the inclusion. We would also consider the more realistic situation of gas bubbles in a turbulent pipe flows. We are planning to realize an experiment with a loop of flowing galinstan and bubble injection. We would try to use the ECFM to, on the one hand, measure velocity profile and characterize the velocity fluctuations in the liquid, and on the other hand, to confirm the capability of the ECFM to detects bubbles in the flow. It will also be interesting to consider higher order terms in the modeling of the ECFM response to measure the velocity perturbation induced by the passing of the bubbles.

We would also like to study a suspension of metallic particles subject to strong (in the sense of high Ha) alternating magnetic field. The electric currents induced in each particle generate Joule effect and interact with the applied field resulting in a Lorentz force (and possibly a torque). As a result, the phase is set in motion due to both the drag and the heating (buoyancy force) of the metallic suspension. Such a problem for a suspension of particles in a creeping flow has been studied both theoretically [176] and experimentally [34] but the heating effects causing local sources of buoyancy and its interactions with

turbulent fluctuations of the velocity field remains unexplored. On the other hand, there is an extensive literature on the preferential concentrations effects and formation of clusters of particles heavier than the carrier phase caused by turbulent flows. The question therefore is to analyze how the formation of inhomogeneity in such a suspension can appear due to hydrodynamic interactions between the two phases and due to the direct magnetic dipole-dipole interaction at short range. Since the flow would respond to such self-organization of the particles (due to the modification of the interphase heat transfer), we can expect to observe, as in Ref. [275], a clustering transition which generates strong fluctuations at all scales, in analogies with systems close to a critical point. Of particular interest is the question of the percolation of electrical conductivity. Indeed, once packing of particles is attained, one should expect a dramatic modification of the eddy currents and therefore significantly change the induced Joule dissipation and the Lorentz force. This flow could be studied numerically and experimentally. In order to focus on collective effects, we plan to use Lagrangian tracking and point-particle approximation for the modeling of the metallic dispersed phase. Within this framework, the dynamic equation of the particles needs to be supplemented in order to account for both the Lorenz force and torque as well as a heat source caused by the applied magnetic field. Such additional source terms can be obtained from dipole moment [176] assuming that the magnetic field remains homogenous at the scale of a particle. Preliminary work on the subject is presented in Ref. [212]. On the other hand, the screening of the magnetic field caused by the particles can be estimated by extending the two-way coupling between continuous and dispersed phase based on the magnetic field perturbation caused by a dipole as proposed in Refs. [120, 98].

5 Bibliography

[1] A. Afflard, R. Zamansky, W. Bergez, P. Tordjeman, and K. Paumel. Eddy-current flow meter response to spherical non-conductive inclusions travelling in a liquid metal. *Magnetohydrodynamics*, 58(4):501–508, 2022.

[2] R. Akhmedagaev, O. Zikanov, D. Krasnov, and J. Schumacher. Turbulent Rayleigh–Bénard convection in a strong vertical magnetic field. *J. Fluid Mech.*, 895:R4, 2020.

[3] V. M. Alipchenkov and L. I. Zaichik. Modeling of the motion of light-weight particles and bubbles in turbulent flows. *Fluid Dyn.*, 45(4):574–590, 2010.

[4] A. Aliseda and T. J. Heindel. X-ray flow visualization in multiphase flows. *Annu. Rev. Fluid Mech.*, 53(1):543–567, 2021.

[5] E. Alméras, V. Mathai, D. Lohse, and C. Sun. Experimental investigation of the turbulence induced by a bubble swarm rising within incident turbulence. *J. Fluid Mech.*, 825:1091–1112, 2017.

[6] Z. Amoura, C. Besnaci, F. Risso, and V. Roig. Velocity fluctuations generated by the flow through a random array of spheres: a model of bubble-induced agitation. *J. Fluid Mech.*, 823:592–616, 2017.

[7] F. Anselmet, Y. Gagne, E. J. Hopfinger, and R. A. Antonia. High-order velocity structure functions in turbulent shear flows. *J. Fluid Mech.*, 140:63–89, 1984.

[8] A. K. Aringazin and M. I. Mazhitov. Stochastic models of Lagrangian acceleration of fluid particle in developed turbulence. *Int. J. Mod. Phys. B*, 18:3095–3168, 2004.

[9] A. Arneodo, R. Benzi, J. Berg, L. Biferale, E. Bodenschatz, A. Busse, E. Calzavarini, B. Castaing, M. Cencini, L. Chevillard, R. T. Fisher, R. Grauer, H. Homann, D. Lamb, A. S. Lanotte, E. Lévêque, B. Luthi, J. Mann, N. Mordant, W.-C. Muller, S. Ott, N. T. Ouellette, J.-F. Pinton, S. B. Pope, S. G. Roux, F. Toschi, H. Xu, and P. K. Yeung. Universal intermittent properties of particle trajectories in highly turbulent flows. *Phys. Rev. Lett.*, 100:250504, 2008.

[10] E. Bacry, J. Delour, and J. F. Muzy. Multifractal random walk. *Phys. Rev. E*, 64(2):026103, 2001.

[11] P. Bak, C. Tang, and K. Wiesenfeld. Self-organized criticality: An explanation of the $1/f$ noise. *Phys. Rev. Lett.*, 59:381–384, 1987.

[12] S. Balachandar and J. K. Eaton. Turbulent Dispersed Multiphase Flow. *Annu. Rev. Fluid Mech.*, 42:111–133, 2010.

[13] G. Barenblatt and A. Chorin. A mathematical model for the scaling of turbulence. *Proc. Natl. Acad. Sci. U.S.A.*, 101:15023–15026, 2004.

[14] G. I. Barenblatt. *Scaling*. Cambridge University Press, Cambridge, U.K., 2002.

[15] G. I. Barenblatt and A. J. Chorin. New perspectives in turbulence: scaling laws, asymptotics, and intermittency. *SIAM Rev.*, 40(2):265–291, 1998.

[16] G. I. Barenblatt and N. Goldenfeld. Does fully developed turbulence exist? Reynolds number independence versus asymptotic covariance. *Phys. Fluids*, 7(12):3078–3082, 1995.

[17] A. Barge and M. A. Gorokhovski. Acceleration of small heavy particles in homogeneous shear flow: direct numerical simulation and stochastic modelling of underresolved intermittent turbulence. *J. Fluid Mech.*, 892:A28, 2020.

[18] G. K. Batchelor. Computation of the energy spectrum in homogeneous two-dimensional turbulence. *Phys. Fluids*, 12(12):II–233, 1969.

[19] G. K. Batchelor. *An Introduction to Fluid Dynamics*. Cambridge University Press, Cambridge UK, 2000.

[20] J. Bec, L. Biferale, G. Boffetta, A. Celani, M. Cencini, A. Lanotte, S. Musacchio, and F. Toschi. Acceleration statistics of heavy particles in turbulence. *J. Fluid Mech.*, 550:349–358, 2006.

[21] J. Bec, L. Biferale, M. Cencini, A. Lanotte, and F. Toschi. Intermittency in the velocity distribution of heavy particles in turbulence. *J. Fluid Mech.*, 646:527–536, 2010.

[22] J. Bec, H. Homann, and S. S. Ray. Gravity-driven enhancement of heavy particle clustering in turbulent flow. *Phys. Rev. Lett.*, 112:184501, 2014.

[23] C. Beck. Lagrangian acceleration statistics in turbulent flows. *Europhys. Lett.*, 64(2):151, 2003.

[24] F. Bellet, F. S. Godeferd, J. F. Scott, and C. Cambon. Wave turbulence in rapidly rotating flows. *J. Fluid Mech.*, 562:83–121, 2006.

[25] R. Benzi, G. Paladin, G. Parisi, and A. Vulpiani. On the multifractal nature of fully developed turbulence and chaotic systems. *J. Phys. A: Math. Gen.*, 17(18):3521–3531, 1984.

[26] L. Bergougnoux, G. Bouchet, D. Lopez, and É. Guazzelli. The motion of solid spherical particles falling in a cellular flow field at low stokes number. *Phys. Fluids*, 26(9):093302, 2014.

[27] A. S. Berrouk, D. Laurence, J. J. Riley, and D. E. Stock. Stochastic modelling of inertial particle dispersion by subgrid motion for les of high Reynolds number pipe flow. *J. Turbul.*, 8:N50, 2007.

[28] L. Biferale, E. Bodenschatz, M. Cencini, A. S. Lanotte, N. T. Ouellette, F. Toschi, and H. Xu. Lagrangian structure functions in turbulence: A quantitative comparison between experiment and direct numerical simulation. *Phys. Fluids*, 20(6):065103, 2008.

[29] L. Biferale, G. Boffetta, A. Celani, B. Devenish, A. Lanotte, and F. Toschi. Multifractal statistics of lagrangian velocity and acceleration in turbulence. *Phys. Rev. Lett.*, 93:064502, 2004.

[30] L. Biferale, G. Boffetta, A. Celani, A. Lanotte, and F. Toschi. Particle trapping in three-dimensional fully developed turbulence. *Phys. Fluids*, 17(2):021701, 2005.

[31] L. Biferale and F. Toschi. Joint statistics of acceleration and vorticity in fully developed turbulence. *J. Turbul.*, 6:N40, 2006.

[32] M. Boivin, O. Simonin, and K. D. Squires. Direct numerical simulation of turbulence modulation by particles in isotropic turbulence. *J. Fluid Mech.*, 375:235–263, 1998.

[33] M. Boivin, O. Simonin, and K. D. Squires. On the prediction of gas–solid flows with two-way coupling using large eddy simulation. *Phys. Fluids*, 12(8):2080–2090, 2000.

[34] R. Bolcato, J. Etay, Y. Fautrelle, and H. K. Moffatt. Electromagnetic billiards. *Phys. Fluids A*, 5(7):1852–1853, 1993.

[35] M. S. Borgas. The Multifractal Lagrangian Nature of Turbulence. *Philos. Trans. R. Soc. London, Ser. A*, 342(1665):379–411, 1993.

[36] M. S. Borgas and P. K. Yeung. Conditional fluid-particle accelerations in turbulence. *Theor. Comput. Fluid Dyn.*, 11(2):69–93, 1998.

[37] W. J. T. Bos and R. Zamansky. Power fluctuations in turbulence. *Phys. Rev. Lett.*, 122(12):124504, 2019.

[38] M. Bourgoin, N. M. N. M. Qureshi, C. Baudet, A. Cartellier, and Y. Gagne. Turbulent transport of finite sized material particles. *J. Phys. Conf. Ser.*, 318:012005, 2011.

[39] M. Breuer and F. Hoppe. Influence of a cost–efficient langevin subgrid-scale model on the dispersed phase of large–eddy simulations of turbulent bubble–laden and particle–laden flows. *Int. J. Multiphase Flow*, 89:23–44, 2017.

[40] R. D. Brown, Z. Warhaft, and G. A. Voth. Acceleration statistics of neutrally buoyant spherical particles in intense turbulence. *Phys. Rev. Lett.*, 103:194501, 2009.

[41] D. Buaria and K. R. Sreenivasan. Dissipation range of the energy spectrum in high Reynolds number turbulence. *Phys. Rev. Fluids*, 5(9), 2020.

[42] D. Buaria and K. R. Sreenivasan. Scaling of acceleration statistics in high Reynolds number turbulence. *Phys. Rev. Lett.*, 128(23), 2022.

[43] G. C. Burton and W. J. A. Dahm. Multifractal subgrid-scale modeling for large-eddy simulation. I. Model development and a priori testing. *Phys. Fluids*, 17:075111, 2005.

[44] G. C. Burton and W. J. A. Dahm. Multifractal subgrid-scale modeling for large-eddy simulation. II. Backscatter limiting and a posteriori evaluation. *Phys. Fluids*, 17:075112, 2005.

[45] E. Calzavarini, M. Kerscher, D. Lohse, and F. Toschi. Dimensionality and morphology of particle and bubble clusters in turbulent flow. *J. Fluid Mech.*, 607:13–24, 2008.

[46] E. Calzavarini, R. Volk, M. Bourgoin, E. Lévêque, J.-F. Pinton, and F. Toschi. Acceleration statistics of finite-sized particles in turbulent flow: the role of Faxén forces. *J. Fluid Mech.*, 630:179–189, 2009.

[47] C. Cambon and L. Jacquin. Spectral approach to non-isotropic turbulence subjected to rotation. *J. Fluid Mech.*, 202:295–317, 1989.

[48] B. Castaing. Scalar intermittency in the variational theory of turbulence. *Physica D*, 73(1-2):31–37, 1994.

[49] B. Castaing, Y. Gagne, and E. Hopfinger. Velocity probability density functions of high Reynolds number turbulence. *Physica D*, 46(2):177–200, 1990.

[50] B. Castaing, Y. Gagne, and E. J. Hopfinger. A new view of developed turbulence. In T. Dracos and A. Tsinober, editors, *New Approaches and Concepts in Turbulence*, pages 35–45, Basel, 1993. Birkhäuser Basel.

[51] B. Castaing, Y. Gagne, and M. Marchand. Log-similarity for turbulent flows? *Physica D*, 68(3-4):387–400, 1993.

[52] A. Celani. The frontiers of computing in turbulence: challenges and perspectives. *J. Turbul.*, 8:N34, 2007.

[53] F. H. Champagne, V. G. Harris, and S. Corrsin. Experiments on nearly homogeneous turbulent shear flow. *J. Fluid Mech.*, 41:81–139, 1970.

[54] L. Chevillard. Regularized fractional Ornstein-Uhlenbeck processes and their relevanceto the modeling of fluid turbulence. *Phys. Rev. E*, 96:033111, 2017.

[55] L. Chevillard, S. G. Roux, E. Levêque, N. Mordant, J.-F. Pinton, and A. Arneodo. Lagrangian velocity statistics in turbulent flows: Effects of dissipation. *Phys. Rev. Lett.*, 91(21), 2003.

[56] A. Chorin. *Vorticity and Turbulence*. Springer, Berlin, 1994.

[57] A. Chouippe and M. Uhlmann. Forcing homogeneous turbulence in direct numerical simulation of particulate flow with interface resolution and gravity. *Phys. Fluids*, 27(12), 2015.

[58] R. Clark, J. Ferziger, and W. Reynolds. Evaluation of subgrid-scale models using an accurately simulated turbulent flow. *J. Fluid Mech.*, 91(1):1–16, 1979.

[59] E. Climent and J. Magnaudet. Large-scale simulations of bubble-induced convection in a liquid layer. *Phys. Rev. Lett.*, 82:4827–4830, 1999.

[60] D. Colombet, D. Legendre, F. Risso, A. Cockx, and P. Guiraud. Dynamics and mass transfer of rising bubbles in a homogenous swarm at large gas volume fraction. *J. Fluid Mech.*, 763:254–285, 2015.

[61] P. Constantin and G. Iyer. A stochastic lagrangian representation of the three- dimensional incompressible navier–stokes equations. *Comm. Pure Appl. Math*, LXI:0330–0345, 2008.

[62] A. M. Crawford, N. Mordant, and E. Bodenschatz. Joint statistics of the lagrangian acceleration and velocity in fully developed turbulence. *Phys. Rev. Lett.*, 94(2):024501, 2005.

[63] P. Davidson. *An Introduction to Magnetohydrodynamics*. Cambridge University Press, 2001.

[64] J. A. Domaradzki, R. W. Metcalfe, R. S. Rogallo, and J. J. Riley. Analysis of subgrid-scale eddy viscosity with use of results from direct numerical simulations. *Phys. Rev. Lett.*, 58:547–550, 1987.

[65] S. Douady, Y. Couder, and M. E. Brachet. Direct observation of the intermittency of intense vorticity filaments in turbulence. *Phys. Rev. Lett.*, 67:983–986, 1991.

[66] T. D. Drivas. Turbulent cascade direction and lagrangian time-asymmetry. *Journal of Nonlinear Science*, 29(1):65–88, 2019.

[67] A. Du Cluzeau. *Modélisation physique de la dynamique des écoulements à bulles par remontée d'échelle à partir de simulations fines*. Theses, Université de Perpignan, 2019.

[68] B. Dubrulle. Beyond Kolmogorov cascades. *J. Fluid Mech.*, 867, 2019.

[69] J. K. Eaton and J. R. Fessler. Preferential concentration of particles by turbulence. *Int. J. Multiphase Flow*, 20:169–209, 1994.

[70] S. Eckert and G. Gerbeth. Velocity measurements in liquid sodium by means of ultrasound doppler velocimetry. *Exp. Fluids*, 32(5):542–546, 2002.

[71] O. Emre, R. O. Fox, M. Massot, S. De Chaisemartin, S. Jay, and F. Laurent. Towards eulerian modeling of a polydisperse evaporating spray under realistic internal-combustion-engine conditions. *Flow, Turbulence and Combustion*, 93(4):689–722, 2014.

[72] P. Ern, F. Risso, D. Fabre, and J. Magnaudet. Wake-induced oscillatory paths of bodies freely rising or falling in fluids. *Annu. Rev. Fluid Mech.*, 44(1):97–121, 2012.

[73] G. Eyink and N. Goldenfeld. Analogies between scaling in turbulence, field theory, and critical phenomena. *Phys. Rev. E*, 50:4679–4683, 1994.

[74] J. Fabre and D. Legendre. Ecoulement diphasique. cours de l'ENSEEIHT, 2011.

[75] G. Falkovich, H. Xu, A. Pumir, E. Bodenschatz, L. Biferale, G. Boffetta, A. S. Lanotte, and F. Toschi. On lagrangian single-particle statistics. *Phys. Fluids*, 24(5):055102, 2012.

[76] P. Fede and O. Simonin. Numerical study of the subgrid fluid turbulence effects on the statistics of heavy colliding particles. *Phys. Fluids*, 18(4):045103, 2006.

[77] P. Février, O. Simonin, and K. D. Squires. Partitioning of particle velocities in gas-solid turbulent flows into a continuous field and a spatially uncorrelated random distribution: theoretical formalism and numerical study. *J. Fluid Mech.*, 533:1–46, 2005.

[78] R. O. Fox. On multiphase turbulence models for collisional fluid-particle flows. *J. Fluid Mech.*, 742:368–424, 2014.

[79] U. Frisch. *Turbulence: The Legacy of A. N. Kolmogorov*. Cambridge university press, 1995.

[80] U. Frisch, P.-L. Sulem, and M. Nelkin. A simple dynamical model of intermittent fully developed turbulence. *J. Fluid Mech.*, 87(4):719–736, 1978.

[81] A. Fuchs, C. Herbert, J. Rolland, M. Wächter, F. Bouchet, and J. Peinke. Instantons and the path to intermittency in turbulent flows. *Phys. Rev. Lett.*, 129(3), 2022.

[82] Y. Gagne and B. Castaing. Une représentation universelle sans invariance globale d'échelle des spectres d'énergie en turbulence développée. *CR. Acad. Sci. Paris*, 312(série 2):441–445, 1991.

[83] Y. Gagne, M. Marchand, and B. Castaing. Conditional velocity pdf in 3-d turbulence. *J. Phys. II*, 4(1):1–8, 1994.

[84] C. W. Gardiner. *Handbook of Stochastic Methods for Physics, Chemistry and the Natural Sciences*. Springer, 1985.

[85] C. Garnier, M. Lance, and J. Marié. Measurement of local flow characteristics in buoyancy-driven bubbly flow at high void fraction. *Exp. Therm Fluid Sci.*, 26(6):811–815, 2002.

[86] R. Gatignol. The Faxén formulae for a rigid particle in an unsteady non-uniform Stokes flow. *Journal de Mécanique Théorique et Appliquée*, 1:143–160, 1983.

[87] T. B. Gatski, M. Y. Hussaini, and J. L. Lumley. *Simulation and Modelling of Turbulent Flows*. Oxford University Press, 1996.

[88] A. S. Ghate and S. K. Lele. Subfilter-scale enrichment of planetary boundary layer large eddy simulation using discrete fourier–gabor modes. *J. Fluid Mech.*, 819:494–539, 2017.

[89] S. S. Girimaji and S. B. Pope. A diffusion model for velocity gradients in turbulence. *Phys. Fluids A*, 2(2):242–256, 1990.

[90] N. Goldenfeld. *Lectures on Phase Transitions and the Renormalization Group*. Westview press, 1992.

[91] M. Gorokhovski and S. Oruganti. Stochastic models for the droplet motion and evaporation in under-resolved turbulent flows at a large Reynolds number. *J. Fluid Mech.*, 932:A18, 2022.

[92] M. Gorokhovski and R. Zamansky. Modeling the effects of small turbulent scales on the drag force for particles below and above the Kolmogorov scale. *Phys. Rev. Fluids*, 3(3):1–23, 2018.

[93] M. A. Gorokhovski and V. L. Saveliev. Statistical universalities in fragmentation under scaling symmetry with a constant frequency of fragmentation. *J. Phys. D: Appl. Phys.*, 41:085405, 2008.

[94] S. Goto and J. C. Vassilicos. Sweep-stick mechanism of heavy particle clustering in fluid turbulence. *Phys. Rev. Lett.*, 100:054503, 2008.

[95] T. Gotoh and D. Fukayama. Pressure spectrum in homogeneous turbulence. *Phys. Rev. Lett.*, 86(17):3775–3778, 2001.

[96] S. Grossmann and D. Lohse. Scaling in thermal convection: a unifying theory. *J. Fluid Mech.*, 407:27–56, 2000.

[97] R. Guichou. *Etude des perturbations du champ électromagnétique par un écoulement de métal liquide contenant une inclusion isolante.* PhD thesis, Toulouse, INPT, 2019.

[98] R. Guichou, H. Ayroles, R. Zamansky, W. Bergez, P. Tordjeman, and K. Paumel. Perturbation of eddy-currents by an inclusion in liquid metal flow. *J. Appl. Phys.*, 125:094504, 2019.

[99] J. Guillou. *Convection forcée d'un métal liquide sous champ magnétique alternatif : Simulation numérique et Expérimentation.* PhD thesis, Institut National Polytechnique de Toulouse, 2022.

[100] J. Guillou, W. Bergez, R. Zamansky, A. Boulin, and P. Tordjeman. Liquid metal convection induced by the lorentz force in a Rayleigh-Bénard cell. *Phys. Rev. Fluids*, 7(7), 2022.

[101] J. F. Hackl, P. K. Yeung, and B. L. Sawford. Multi-particle and tetrad statistics in numerical simulations of turbulent relative dispersion. *Phys. Fluids*, 23(6):065103, 2011.

[102] J. Hadamard. Mouvement permanent lent d'une sphere liquide et visqueuse dans un liquide visqueux. *C. R. Acad. Sci.*, 152:1735, 1911.

[103] R. J. Hill. Scaling of acceleration in locally isotropic turbulence. *J. Fluid Mech.*, 452:361–370, 2002.

[104] J. O. Hinze. *Turbulence.* McGraw-Hill, United States of America, 2nd edition, 1975.

[105] H. Homann and J. Bec. Finite-size effects in the dynamics of neutrally buoyant particles in turbulent flow. *J. Fluid Mech.*, 651:81–91, 2010.

[106] H. Homann, D. Schulz, and R. Grauer. Conditional Eulerian and Lagrangian velocity increment statistics of fully developed turbulent flow. *Phys. Fluids*, 23(5):055102, 2011.

[107] Y. Huang and F. G. Schmitt. Lagrangian cascade in three-dimensional homogeneous and isotropic turbulence. *J. Fluid Mech.*, 741, 2014.

[108] J. C. R. Hunt and I. Eames, I. The disappearance of laminar and turbulent wakes in complex flows. *J. Fluid Mech.*, 457:111–132, 2002.

[109] A. Innocenti, N. Mordant, N. Stelzenmuller, and S. Chibbaro. Lagrangian stochastic modelling of acceleration in turbulent wall-bounded flows. *J. Fluid Mech.*, 892:A38, 2020.

[110] P. J. Ireland, A. D. Bragg, and L. R. Collins. The effect of reynolds number on inertial particle dynamics in isotropic turbulence. part 2. simulations with gravitational effects. *J. Fluid Mech.*, 796:659–711, 2016.

[111] T. Ishihara, Y. Kaneda, M. Yokokawa, K. Itakura, and A. Uno. Small-scale statistics in high-resolution direct numerical simulation of turbulence: Reynolds number dependence of one-point velocity gradient statistics. *J. Fluid Mech.*, 592:335–366, 2007.

[112] A. Iskakov, S. Descombes, and E. Dormy. An integro-differential formulation for magnetic induction in bounded domains: boundary element–finite volume method. *J. Comput. Phys.*, 197(2):540–554, 2004.

[113] K. P. Iyer, K. R. Sreenivasan, and P. K. Yeung. Circulation in high Reynolds number isotropic turbulence is a bifractal. *Phys. Rev. X*, 9(4), 2019.

[114] P. L. Johnson and C. Meneveau. A closure for lagrangian velocity gradient evolution in turbulence using recent-deformation mapping of initially gaussian fields. *J. Fluid Mech.*, 804:387–419, 2016.

[115] P. L. Johnson and C. Meneveau. Restricted Euler dynamics along trajectories of small inertial particles in turbulence. *J. Fluid Mech.*, 816, 2017.

[116] C. Journeau, P. Piluso, J.-F. Haquet, E. Boccaccio, V. Saldo, J.-M. Bonnet, S. Malaval, L. Carénini, and L. Brissonneau. Two-dimensional interaction of oxidic corium with concretes: The vulcano vb test series. *Ann. Nucl. Energy*, 36(10):1597–1613, 2009.

[117] L. P. Kadanoff. *Statistical Physics, Statics, Dynamics and Renormalization.* World Scientific, Singapore, 2000.

[118] J.-P. Kahane and J. Peyrière. Sur certaines martingales de Benoit Mandelbrot. *Advances in Mathematics*, 22(2):131–145, 1976.

[119] Y. Kaneda, T. Ishihara, M. Yokokawa, K. Itakura, and A. Uno. Energy dissipation rate and energy spectrum in high resolution direct numerical simulations of turbulence in a periodic box. *Phys. Fluids*, 15(2):L21–L24, 2003.

[120] E. E. Keaveny and M. R. Maxey. Modeling the magnetic interactions between paramagnetic beads in magnetorheological fluids. *J. Comput. Phys.*, 227(22):9554 – 9571, 2008.

[121] O. Keplinger, N. Shevchenko, and S. Eckert. Visualization of bubble coalescence in bubble chains rising in a liquid metal. *Int. J. Multiphase Flow*, 105:159–169, 2018.

[122] O. Keplinger, N. Shevchenko, and S. Eckert. Experimental investigation of bubble breakup in bubble chains rising in a liquid metal. *Int. J. Multiphase Flow*, 116:39–50, 2019.

[123] A. R. Kerstein. One-dimensional turbulence: model formulation and application to homogeneous turbulence, shear flows, and buoyant stratified flows. *J. Fluid Mech.*, 392:277–334, 1999.

[124] A. N. Kolmogorov. Decay of isotropic turbulence in an incompressible viscous fluid. *Dokl. Akad. Nauk SSSR*, 31:538–41, 1941.

[125] A. N. Kolmogorov. Dissipation of Energy in the Locally Isotropic Turbulence. *Dokl. Akad. Nauk SSSR*, 32:1, 1941. Translation by V. Levin in Philos. Trans. Roy. Soc. A 1991 vol. 434 p. 15-17.

[126] A. N. Kolmogorov. The Local Structure of Turbulence in Incompressible Viscous Fluid for Very Large Reynolds Numbers. *Dokl. Akad. Nauk SSSR*, 434:9–13, 1941. Translation by V. Levin in Philos. Trans. Roy. Soc. A 1991 vol. 434 p. 9-13.

[127] A. N. Kolmogorov. On the log-normal distribution of particles sizes during break-up process. *Dokl. Akad. Nauk SSSR*, 31:99, 1941.

[128] A. N. Kolmogorov. A refinement of previous hypotheses concerning the local structure of turbulence in a viscous incompressible fluid at high Reynolds number. *J. Fluid Mech.*, 13:82–85, 1962.

[129] R. H. Kraichnan. On Kolmogorov's inertial-range theories. *J. Fluid Mech.*, 62:305–330, 1974.

[130] R. H. Kraichnan and S. Nagarajan. Growth of turbulent magnetic fields. *Phys. Fluids*, 10(4):859–870, 1967.

[131] B. Kumar, J. Schumacher, and R. A. Shaw. Lagrangian mixing dynamics at the cloudy–clear air interface. *J. Atmos. Sci.*, 71(7):2564 – 2580, 2014.

[132] M. Kumar. *Magnetic flux distorsion in two-phase liquid metal flow.* PhD thesis, 2016.

[133] M. Kumar, W. Bergez, P. Tordjeman, R. Arinero, and K. Paumel. Magnetic flux distortion in two-phase liquid metal flow: Model experiment. *J. Appl. Phys.*, 119(18):pp. 185105/1–185105/7, 2016.

[134] A. La Porta, G. A. Voth, A. M. Crawford, J. Alexander, and E. Bodenschatz. Fluid particle accelerations in fully developed turbulence. *Nature*, 409:1017–1019, 2001.

[135] C. C. Lalescu and M. Wilczek. Acceleration statistics of tracer particles in filtered turbulent fields. *J. Fluid Mech.*, 847(R2), 2018.

[136] A. G. Lamorgese, S. B. Pope, P. K. Yeung, and B. L. Sawford. A conditionally cubic-Gaussian stochastic Lagrangian model for acceleration in isotropic turbulence. *J. Fluid Mech.*, 582:243–448, 2007.

[137] M. Lance and J. Bataille. Turbulence in the liquid phase of a uniform bubbly air–water flow. *J. Fluid Mech.*, 222:95–118, 1991.

[138] L. D. Landau and E. M. Lifshitz. *Fluid Mechanics (Volume 6 of A Course of Theoretical Physics).* Pergamon Press, 1959.

[139] A. Lanotte, L. Biferale, G. Boffetta, and F. Toschi. A new assessment of the second-order moment of lagrangian velocity increments in turbulence. *J. Turbul.*, 14(7):34–48, 2013.

[140] A. Lanotte, E. Calzavarini, T. Federico, B. Jeremie, B. Luca, and C. Massimo. Heavy particles in turbulent flows. International CFD Database, 2011.

[141] A. Lanotte, E. Calzavarini, F. Toschi, J. Bec, L. Biferale, and M. Cencini. Heavy particles in turbulent flows rm-2007-grad-2048.st0, 2011.

[142] F. Laurent and M. Massot. Multi-fluid modeling of laminar poly-dispersed spray flames: origin, assumptions and comparison of section al and sampling methods. *Combust. Theor. Model.*, 5:537–5 72, 2001.

[143] J. M. Lawson, E. Bodenschatz, A. N. Knutsen, J. R. Dawson, and N. A. Worth. Direct assessment of Kolmogorov's first refined similarity hypothesis. *Phys. Rev. Fluids*, 4(2), 2019.

[144] F. Le Roy De Bonneville, R. Zamansky, F. Risso, A. Boulin, and J.-F. Haquet. Numerical simulations of the agitation generated by coarse-grained bubbles moving at large Reynolds number. *J. Fluid Mech.*, 926:A20, 2021.

[145] C. Lee, K. Yeo, and J.-I. Choi. Intermittent nature of acceleration in near-wall turbulence. *Phys. Rev. Lett.*, 92(14):144502, 2004.

[146] R. Letournel, L. Goudenège, R. Zamansky, A. Vié, and M. Massot. Reexamining the framework for intermittency in Lagrangian stochastic models for turbulent flows: A way to an original and versatile numerical approach. *Phys. Rev. E*, 104:015104, 2021.

[147] V. G. Levich. *Physicochemical hydrodynamics*. Prentice-Hall, 1962.

[148] R.-C. Lien, E. A. D'asaro, and G. T. Dairiki. Lagrangian frequency spectra of vertical velocity and vorticity in high-Reynolds-number oceanic turbulence. *J. Fluid Mech.*, 362:177–198, 1998.

[149] D. Lohse. Bubble puzzles: From fundamentals to applications. *Phys. Rev. Fluids*, 3(11), 2018.

[150] A. Loisy and A. Naso. Interaction between a large buoyant bubble and turbulence. *Phys. Rev. Fluids*, 2:014606, 2017.

[151] Z. Lyu, T. Boeck, and C. Karcher. Electromagnetic interaction between a permanent magnet and a sphere moving in liquid metal. *Exp. Fluids*, 62(5):109, 2021.

[152] J. Magnaudet. The forces acting on bubbles and rigid particles. *ASME Fluids Engineering Division Summer Meeting, FEDSM*, 3522(97), 1997.

[153] J. Magnaudet and I. Eames. The motion of high-Reynolds-number bubbles in inhomogeneous flows. *Annu. Rev. Fluid Mech.*, 32:659–708, 2000.

[154] J. Magnaudet and L. Thais. Orbital rotational motion and turbulence below laboratory wind water waves. *J. Geophys. Res.: Oceans*, 100(C1):757–771, 1995.

[155] B. B. Mandelbrot. Some noises with 1/f spectrum, a bridge between direct current and white noise. *IEEE Transactions on information theory*, IT13(2):289, 1967.

[156] B. B. Mandelbrot. Possible refinement of the lognormal hypothesis concerning the distribution of energy dissipation in intermittent turbulence. In M. Rosenblatt and C. Van Atta, editors, *Statistical Models and Turbulence*, pages 333–351, Berlin, Heidelberg, 1972. Springer Berlin Heidelberg.

[157] B. B. Mandelbrot. Intermittent turbulence in self-similar cascades: divergence of high moments and dimension of the carrier. *J. Fluid Mech.*, 62(2):331–358, 1974.

[158] B. B. Mandelbrot, J. Berger, J.-P. Kahane, and J. Peyriere. *Multifractals and 1-f noise*. Springer, 1999.

[159] B. B. Mandelbrot and J. W. Van Ness. Fractional brownian motions, fractional noises and applications. *SIAM Rev.*, 10(4):422–437, 1968.

[160] E. Marinari, G. Parisi, R. D., and P. Windey. On the interpretation of 1/f noise. *Commun. Math. Phys*, 89:1–12, 1983.

[161] J. Martínez Mercado, C. Palacios-Morales, and R. Zenit. Measurement of pseudo-turbulence intensity in monodispersed bubbly liquids for $10 < Re < 500$. *Phys. Fluids*, 19(10):103302, 2007.

[162] V. Mathai, E. Calzavarini, J. Brons, C. Sun, and D. Lohse. Microbubbles and microparticles are not faithful tracers of turbulent acceleration. *Phys. Rev. Lett.*, 117:024501, 2016.

[163] M. R. Maxey. The gravitational settling of aerosol particles in homogeneous turbulence and random flow fields. *J. Fluid Mech.*, 174:441–465, 1987.

[164] M. R. Maxey and J. J. Riley. Equation of motion for a small rigid sphere in a nonuniform flow. *Phys. Fluids*, 26(4):883–889, 1983.

[165] T. Maxworthy, C. Gnann, M. Kürten, and F. Durst. Experiments on the rise of air bubbles in clean viscous liquids. *J. Fluid Mech.*, 321:421–441, 1996.

[166] R. Mei. Velocity fidelity of flow tracer particles. *Exp. Fluids*, 22(1):1–13, 1996.

[167] S. Mendez-Diaz, J. C. Serrano-García, R. Zenit, and J. A. Hernández-Cordero. Power spectral distributions of pseudo-turbulent bubbly flows. *Phys. Fluids*, 25(4), 2013.

[168] C. Meneveau. Lagrangian Dynamics and Models of the Velocity Gradient Tensor in Turbulent Flows. *Annu. Rev. Fluid Mech.*, 43:219–245, 2011.

[169] C. Meneveau and T. S. Lund. On the lagrangian nature of the turbulence energy cascade. *Phys. Fluids*, 6(8):2820–2825, 1994.

[170] D. Mercier. *Large eddy simulation of coupled dispersed phase flows: a statistically-consistent formalism*. PhD thesis, Ecole Centrale Paris, 2020.

[171] A. Merle, D. Legendre, and J. Magnaudet. Forces on a high-Reynolds-number spherical bubble in a turbulent flow. *J. Fluid Mech.*, 532:53–62, 2005.

[172] J.-P. Minier, S. Chibbaro, and S. Pope. Guidelines for the formulation of lagrangian stochastic models for particle simulations of single-phase and dispersed two-phase turbulent flows. *Phys. Fluids*, 26(113303), 2014.

[173] S. Miralles, N. Plihon, and J.-F. Pinton. Lorentz force effects in the bullard–von kármán dynamo: saturation, energy balance and subcriticality. *J. Fluid Mech.*, 775:501–523, 2015.

[174] S. Miralles, G. Verhille, N. Plihon, and J.-F. Pinton. Mhd turbulence at high interaction parameter. In *14 th european turbulence conference*, 1–4 SEPTEMBER 2013, LYON, France, 2013.

[175] H. K. Moffat. Interaction of turbulence with strong wind shear. In A. M. Yaglom and V. I. Tatarsky, editors, *Atmosphere Turbulence and Radio Wave Propagation*, pages 139–156, Nauka, Moscow, 1967.

[176] H. K. Moffatt. On the behaviour of a suspension of conducting particles subjected to a time-periodic magnetic field. *J. Fluid Mech.*, 218:509–529, 1990.

[177] H. K. Moffatt. Electromagnetic stirring. *Phys. Fluids A*, 3(5):1336–1343, 1991.

[178] A. S. Monin and A. M. Yaglom. *Statistical Fluid Mechanics: Mechanics of Turbulence*, volume 2. MIT Press, Cambridge, MA, 1981.

[179] D. W. Moore. The boundary layer on a spherical gas bubble. *J. Fluid Mech.*, 16(2):161–176, 1963.

[180] N. Mordant, A. M. Crawford, and E. Bodenschatz. Experimental lagrangian acceleration probability density function measurement. *Physica D*, 193(1-4):245–251, 2004.

[181] N. Mordant, A. M. Crawford, and E. Bodenschatz. Three-dimensional structure of the lagrangian acceleration in turbulent flows. *Phys. Rev. Lett.*, 93(21):214501, 2004.

[182] N. Mordant, J. Delour, E. Lévêque, A. Arnéodo, and J.-F. Pinton. Long time correlations in lagrangian dynamics: a key to intermittency in turbulence. *Phys. Rev. Lett.*, 89(25):254502, 2002.

[183] N. Mordant, E. Lévêque, and J.-F. Pinton. Experimental and numerical study of the Lagrangian dynamics of high Reynolds turbulence. *New J. Phys.*, 6:116, 2004.

[184] N. Mordant, P. Metz, and O. Michel. Measurement of Lagrangian velocity in fully developed turbulence. *Phys. Rev. Lett.*, 21:214501, 2001.

[185] R. Moreau. *Magnetohydrodynamics*. Springer, Dordrecht, 1990.

[186] G. Mougin and J. Magnaudet. Path instability of a rising bubble. *Phys. Rev. Lett.*, 88(1), 2001.

[187] R. F. Mudde. Gravity-driven bubbly flows. *Annu. Rev. Fluid Mech.*, 37(1):393–423, 2005.

[188] A. Naert, B. Castaing, B. Chabaud, B. HÈbral, and J. Peinke. Conditional statistics of velocity fluctuations in turbulence. *Physica D*, 113(1):73 – 78, 1998.

[189] A. Naert, R. Friedrich, and J. Peinke. Fokker-Planck equation for the energy cascade in turbulence. *Phys. Rev. E*, 56(6):6719–6722, 1997.

[190] C. L. M. H. Navier. Sur les lois du mouvement des fluides. *Mémoire de l'Académie Royale des Sciences*, 6:389–416, 1823.

[191] E. A. Novikov and R. W. Stewart. The intermittency of turbulence and the spectrum of energy dissipation fluctuations. *Izv. Geophys. Ser*, 3:408–413, 1964.

[192] A. M. Oboukhov. Some specific features of atmospheric tubulence. *J. Fluid Mech.*, 13(01):77–81, 1962.

[193] S. A. Orszag and G. S. Patterson. Numerical simulation of three-dimensional homogeneous isotropic turbulence. *Phys. Rev. Lett.*, 28:76–79, 1972.

[194] G. I. Park, M. Bassenne, J. Urzay, and P. Moin. A simple dynamic subgrid-scale model for les of particle-laden turbulence. *Phys. Rev. Fluids*, 2(4):044301, 2017.

[195] R. M. Pereira, L. Moriconi, and L. Chevillard. A multifractal model for the velocity gradient dynamics in turbulent flows. *J. Fluid Mech.*, 839:430–467, 2018.

[196] C. S. Peskin. A random-walk interpretation of the incompressible Navier-Stokes equations. *Communications on Pure Appl. Math.*, 38(6):845–852, 1985.

[197] J. R. Picardo, A. Bhatnagar, and S. S. Ray. Lagrangian irreversibility and Eulerian dissipation in fully developed turbulence. *Phys. Rev. Fluids*, 5:042601, 2020.

[198] Y. Pomeau. Symétrie des fluctuations dans le renversement du temps. *J. Phys.*, 43(6):859–867, 1982.

[199] S. B. Pope. Lagrangian Microscales in Turbulence. *Philos. Trans. Roy. Soc. London*, 333(1631):309–319, 1990.

[200] S. B. Pope. On the relationship between stochastic lagrangian models of turbulence and second-moment closures. *Phys. Fluids*, 6(2):973–985, 1994.

[201] S. B. Pope. *Turbulent Flows*. Cambridge University Press, 2000.

[202] S. B. Pope. A stochastic Lagrangian model for acceleration in turbulent flows. *Phys. Fluids*, 14(7):2360, 2002.

[203] S. B. Pope and Y. L. Chen. The velocity-dissipation probability density function model for turbulent flows. *Phys. Fluids*, 2(8):1437–1449, 1990.

[204] J. Pozorski and S. V. Apte. Filtered particle tracking in isotropic turbulence and stochastic modeling of subgrid-scale dispersion. *Int. J. Multiphase Flow*, 35(2):118–128, 2009.

[205] V. N. Prakash. *Light particles in turbulence*. PhD thesis, University of Twente, Enschede, 2013.

[206] V. N. Prakash, J. Martínez Mercado, L. van Wijngaarden, E. Mancilla, Y. Tagawa, D. Lohse, and C. Sun. Energy spectra in turbulent bubbly flows. *J. Fluid Mech.*, 791:174–190, 2016.

[207] A. Prosperetti. Vapor bubbles. *Annu. Rev. Fluid Mech.*, 49(1):221–248, 2017.

[208] A. Pumir, H. Xu, G. Boffetta, G. Falkovich, and E. Bodenschatz. Redistribution of kinetic energy in turbulent flows. *Phys. Rev. X*, 4:041006, 2014.

[209] N. M. Qureshi, U. Arrieta, C. Baudet, A. Cartellier, Y. Gagne, and M. Bourgoin. Acceleration statistics of inertial particles in turbulent flow. *Eur. Phys. J. B*, 66(4):531–536, 2008.

[210] N. M. Qureshi, M. Bourgoin, C. Baudet, A. Cartellier, and Y. Gagne. Turbulent tranport of materials particles: an experimental investigation of finite size effect. *Phys. Rev. Lett.*, 99:184502, 2007.

[211] M. W. Reeks. On a kinetic equation for the transport of particles in turbulent flows. *Phys. Fluids A*, 3(3):446–456, 1991.

[212] S. Renaudière de Vaux. *Convection thermique en présence d'un champ magnétique constant, alternatif, ou d'une source de chaleur dispersée.* PhD thesis, Institut National Polytechnique de Toulouse, 2017.

[213] J. Rensen, S. Luther, and D. Lohse. The effect of bubbles on developed turbulence. *J. Fluid Mech.*, 538:153–187, 2005.

[214] A. Reynolds. Superstatistical lagrangian stochastic modeling. *Physica A*, 340(1):298 – 308, 2004. News and Expectations in Thermostatistics.

[215] A. M. Reynolds. On the application of nonextensive statistics to lagrangian turbulence. *Phys. Fluids*, 15(1):L1–L4, 2003.

[216] A. M. Reynolds. Superstatistical mechanics of tracer-particle motions in turbulence. *Phys. Rev. Lett.*, 91:084503, 2003.

[217] A. M. Reynolds, N. Mordant, A. M. Crawford, and E. Bodenschatz. On the distribution of lagrangian accelerations in turbulent flows. *New J. Phys.*, 7(1):58, 2005.

[218] A. M. Reynolds, K. Yeo, and C. Lee. Anisotropy of acceleration in turbulent flows. *Phys. Rev. E*, 70(1):017302, 2004.

[219] G. Riboux, D. Legendre, and F. Risso. A model of bubble-induced turbulence based on large-scale wake interactions. *J. Fluid Mech.*, 719:362–387, 2013.

[220] G. Riboux, F. Risso, and D. Legendre. Experimental characterization of the agitation generated by bubbles rising at high Reynolds number. *J. Fluid Mech.*, 643:509–539, 2010.

[221] S. F. Richardson. *Weather prediction by numerical process.* Cambridge University Press, 1922.

[222] F. Risso. Physical interpretation of probability density functions of bubble-induced agitation. *J. Fluid Mech.*, 809:240–263, 2016.

[223] F. Risso. Agitation, mixing, and transfers induced by bubbles. *Annu. Rev. Fluid Mech.*, 50(1):25–48, 2018.

[224] F. Risso and K. Ellingsen. Velocity fluctuations in a homogeneous dilute dispersion of high-Reynolds-number rising bubbles. *J. Fluid Mech.*, 453:395–410, 2002.

[225] F. Risso, V. Roig, Z. Amoura, G. Riboux, and A.-M. Billet. Wake attenuation in large Reynolds number dispersed two-phase flows. *Philosophical Transactions of the Royal Society A: Mathematical, Physical and Eng. Sci.*, 366(1873):2177–2190, 2008.

[226] R. S. Rogallo. Numerical experiments in homogeneous turbulence. Technical report, NASA Technical Memorandum, 1981.

[227] W. Rybczynski. On the translatory of a fluid sphere in a viscous medium. *Bull. Acad. Sci de cracovie*, A:40–46., 1911.

[228] V. Sabelnikov, A. Barge, and M. Gorokhovski. Stochastic modeling of fluid acceleration on residual scales and dynamics of suspended inertial particles in turbulence. *Phys. Rev. Fluids*, 4(4):044301, 2019.

[229] V. Sabel'nikov, A. Chtab, and M. Gorokhovski. The coupled LES - sub-grid stochastic acceleration model (LES-SSAM) of a high Reynolds number flows. In *Advances in Turbulence XI*, volume 117, pages 209–211, 11th EUROMECH European Turbulence Conference, June 25-28, 2007, Porto, Portugal, 2007. Springer Proceedings in Physics.

[230] V. Sabel'nikov, A. Chtab-Desportes, and M. Gorokhovski. New sub-grid stochastic acceleration model in LES of high-Reynolds-number flows. *Eur. Phys. J. B*, 80(2):177–187, 2011.

[231] P. G. Saffman. On the settling speed of free and fixed suspensions. *Stud. Appl. Math.*, 52(2):115–127, 1973.

[232] P. Sagaut. *Large Eddy Simulation for Incompressible Flows: An introduction.* Springer Verlag, 2nd edition, 2002.

[233] P. Sagaut and C. Cambon. *Homogeneous Turbulence Dynamics.* Cambridge University Press, 2008.

[234] T. Sanada. Cluster statistics of homogeneous fluid turbulence. *Phys. Rev. A*, 44:6480–6489, 1991.

[235] V. L. Saveliev and M. A. Gorokhovski. Description of group-theoretical model of developed turbulence. *Phys. Scr.*, T132:014005 (6pp), 2008.

[236] B. Sawford and F. Guest. Lagrangian statistical simulation of the turbulent motion of heavy particles. *Boundary Layer Meteorol.*, 54(1-2):147–166, 1991.

[237] B. L. Sawford. Reynolds number effects in Lagrangian stochastic models of turbulent dispersion. *Phys. Fluids A*, 3:1577, 1991.

[238] B. L. Sawford and P. K. Yeung. Kolmogorov similarity scaling for one-particle Lagrangian statistics. *Phys. Fluids*, 23(9):091704, 2011.

[239] B. L. Sawford and P. K. Yeung. Turbulent lagrangian velocity statistics conditioned on extreme values of dissipation. *Procedia IUTAM*, 9:129–137, 2013. IUTAM Symposium on Understanding Common Aspects of Extreme Events in Fluids.

[240] B. L. Sawford and P. K. Yeung. Direct numerical simulation studies of Lagrangian intermittency in turbulence. *Phys. Fluids*, 27:065109, 2015.

[241] B. L. Sawford, P. K. Yeung, M. S. Borgas, P. Vedula, A. La Porta, A. M. Crawford, and E. Bodenschatz. Conditional and unconditional acceleration statistics in turbulence. *Phys. Fluids*, 15(11):3478–3489, 2003.

[242] L. Schiller and A. Nauman. A drag coefficient correlation. *V.D.I. Zeitung*, 77:318–320, 1935.

[243] Z.-S. She, S. Chen, G. Doolen, R. H. Kraichnan, and S. A. Orszag. Reynolds number dependence of isotropic navier-stokes turbulence. *Phys. Rev. Lett.*, 70:3251–3254, 1993.

[244] J. A. Shercliff. *The theory of electromagnetic flow-measurement.* Cambridge University Press, 1962.

[245] O. Simonin. Continuum modelling of dispersed two-phase flows. *Lecture series-van Kareman Institute for Fluid Dyn.*, 2:1–47, 1996.

[246] K. D. Squires and J. K. Eaton. Preferential concentration of particles by turbulence. *Phys. Fluids A*, 3(5):1169–1178, 1991.

[247] S. Subramaniam, M. Mehrabadi, J. Horwitz, and A. A. Mani. Developing improved lagrangian point particle models of gas-solid flow from particle-resolved direct numerical simulation. In *Proceedings of the summer program 2014*. Center for Turbulence Research - Stanford University, 2014.

[248] E. Taberlet and Y. Fautrelle. Turbulent stirring in an experimental induction furnace. *J. Fluid Mech.*, 159:409–431, 1985.

[249] S. Tang, R. Antonia, L. Djenidi, and Y. Zhou. Scaling of the turbulent energy dissipation correlation function. *J. Fluid Mech.*, 891:A26, 2020.

[250] G. I. Taylor. Diffusion by continuous movements. *Proceedings of the London Mathematical Society*, s2-20(1):196–212, 1922.

[251] G. I. Taylor. Statistical theory of turbulence. *Proc. R. Soc. London, Ser. A*, 151(873):421–444, 1935.

[252] T. D. Taylor and A. Acrivos. On the deformation and drag of a falling viscous drop at low Reynolds number. *J. Fluid Mech.*, 18(3):466–476, 1964.

[253] C. M. Tchen. *Mean value and correlation problems connected with the motion of small particles suspended in a turbulent fluid.* PhD thesis, Delft University, Netherlands, 1947.

[254] M. A. C. Teixeira and C. A. Mériaux. Estimating the filtering of turbulence properties by finite-sized particles using analytical energy spectra. *Phys. Fluids*, 34(4):045117, 2022.

[255] H. Tennekes. Eulerian and lagrangian time microscales in isotropic turbulence. *J. Fluid Mech.*, 67(3):561–567, 1975.

[256] H. Tennekes and J. L. Lumley. *A First Course in Turbulence*. MIT Press, 1972.

[257] L. Thais and J. Magnaudet. A triple decomposition of the fluctuating motion below laboratory wind water waves. *J. Geophys. Res.: Oceans*, 100(C1):741–755, 1995.

[258] A. Tsinober. *An Informal Conceptual Introduction to Turbulence*. Springer, 2nd edition, 2009.

[259] A. Tsinober, P. Vedula, and P. K. Yeung. Random taylor hypothesis and the behavior of local and convective accelerations in isotropic turbulence. *Phys. Fluids*, 13(7):1974–1984, 2001.

[260] A. Vié, F. Doisneau, and M. Massot. On the anisotropic gaussian velocity closure for inertial- particle laden flows. *Comm. Comput. Phys.*, 17:1–46, 2015.

[261] B. Viggiano, J. Friedrich, R. Volk, M. Bourgoin, R. B. Cal, and L. Chevillard. Modelling Lagrangian velocity and acceleration in turbulent flows as infinitely differentiable stochastic processes. *J. Fluid Mech.*, 900:A27, 2020.

[262] A. Vincent and M. Meneguzzi. The spatial structure and statistical properties of homogeneous turbulence. *J. Fluid Mech.*, 225:1–20, 1991.

[263] R. Volk, E. Calzavarini, E. Lévêque, and J.-F. Pinton. Dynamics of inertial particles in a turbulent von kármán flow. *J. Fluid Mech.*, 668:223–235, 2011.

[264] G. Voth, A. La Porta, A. Grawford, J. Alexander, and E. Bodenschatz. Measurements of particle accelerations in fully developed turbulence. *J. Fluid Mech.*, 469:121, 2002.

[265] L. V. Wijngaarden. Bubble velocities induced by trailing vortices behind neighbours. *J. Fluid Mech.*, 541:203–229, 2005.

[266] M. Wilkinson and A. Pumir. Spherical Ornstein-Uhlenbeck processes. *J. Stat. Phys.*, 145:113–142, 2011.

[267] H. Xu and E. Bodenschatz. Motion of inertial particles with size larger than Kolmogorov scale in turbulent flows. *Physica D*, 237(14–17):2095 – 2100, 2008. Euler Equations: 250 Years On Proceedings of an international conference.

[268] H. Xu, A. Pumir, G. Falkovich, E. Bodenschatz, M. Shats, H. Xia, N. Francois, and G. Boffetta. Flight–crash events in turbulence. *Proc. Natl. Acad. Sci. U.S.A.*, 111(21):7558–7563, 2014.

[269] Y. Xu and S. Subramaniam. Consistent modeling of interphase turbulent kinetic energy transfer in particle-laden turbulent flows. *Phys. Fluids*, 19(8):085101, 2007.

[270] A. M. Yaglom. The Influence of Fluctuations in Energy Dissipation on the Shape of Turbulence Characteristics in the Inertial Interval. *Soviet Physics Doklady*, 11:26–29, 1966.

[271] P. K. Yeung, S. B. Pope, A. G. Lamorgese, and D. A. Donzis. Acceleration and dissipation statistics of numerically simulated isotropic turbulence. *Phys. Fluids*, 18:065103, 2006.

[272] P. K. Yeung, K. R. Sreenivasan, and S. B. Pope. Effects of finite spatial and temporal resolution in direct numerical simulations of incompressible isotropic turbulence. *Phys. Rev. Fluids*, 3(6), 2018.

[273] L. I. Zaichik and V. M. Alipchenkov. A model for predicting the acceleration variance of arbitrary-density finite-size particles in isotropic turbulence. *Int. J. Multiphase Flow*, 37(3):236–240, 2011.

[274] R. Zamansky. Acceleration scaling and stochastic dynamics of a fluid particle in turbulence. *Phys. Rev. Fluids*, 7:084608, 2022.

[275] R. Zamansky, F. Coletti, M. Massot, and A. Mani. Turbulent thermal convection driven by heated inertial particles. *J. Fluid Mech.*, 809:390–437, 2016.

[276] R. Zamansky, I. Vinkovic, and M. Gorokhovski. Acceleration in turbulent channel flow: universalities in statistics, subgrid stochastic models and an application. *J. Fluid Mech.*, 721:627–668, 2013.

[277] R. Zenit, D. Koch, and A. Sangani. Measurements of the average properties of a suspension of bubbles rising in a vertical channel. *J. Fluid Mech.*, 429:307–342, 2001.

[278] R. Zenit and J. Magnaudet. Path instability of rising spheroidal air bubbles: A shape-controlled process. *Phys. Fluids*, 20:061702, 2008.

[279] Z. Zhang, D. Legendre, and R. Zamansky. Model for the dynamics of micro-bubbles in high Reynolds number flows. *J. Fluid Mech.*, 879:554–578, 2019.

[280] Z. Zhang, D. Legendre, and R. Zamansky. Fluid inertia effects on the motion of small spherical bubbles or solid spheres in turbulent flows. *J. Fluid Mech.*, 921:A4, 2021.

[281] T. Zürner, W. Liu, D. Krasnov, and J. Schumacher. Heat and momentum transfer for magnetoconvection in a vertical external magnetic field. *Phys. Rev. E*, 94(4), 2016.